Micromachined Capacitive Long-Range Displacement Sensor for Nano-Positioning of Microactuator Systems

Toon Kuijpers

Promotiecommissie

Voorzitter:	Prof.dr. W.H.M. Zijm	Universiteit Twente
Secretaris	Prof.dr. W.H.M. Zijm	Universiteit Twente
Promotoren:	Prof.dr. M.C. Elwenspoek	Universiteit Twente
Leden:	Dr.ir. G.J.M. Krijnen	Universiteit Twente
	Prof.dr.A.G.R. Evans	University of Southampton
	Prof. ir. H.M.J.R. Soemers	Universiteit Twente
	Prof. dr. ir. J van Eijk	Philips CFT Eindhoven
	Prof. dr. P.J. French	Technische Universiteit Delft
	Prof.dr.ir. L. Abelmann	Universiteit Twente
	Prof.dr.ir. P.P.L. Regtien	Universiteit Twente

The research described in this thesis was carried out at the Transducers Science and Technology Group of the MESA+ research institute, University of Twente, the Netherlands. It was performed within the framework of the STW project 'Microactuator systems for nano-position control'.

CIP-GEGEVENS KONINKLIJKE BIBLIOTHEEK, DEN HAAG

Kuijpers, Toon A.A.
Micromachined Capacitive Long-Range Displacement Sensor for Nano-Positioning of Microactuator systems
[S.I. : s.n.]
Ph.D. thesis University of Twente, Enschede, The Netherlands

ISBN 90-365-2119-X

Subject headings: displacement sensor, microactuator, micromachining technology

© A.A. Kuijpers, Enschede, 2004
No part of this work may be reproduced by print, photocopy or any other means without the permission in writing from the publisher.

Print: Wöhrmann Print Service, Zutphen

MICROMACHINED CAPACITIVE LONG-RANGE DISPLACEMENT SENSOR FOR NANO-POSITIONING OF MICROACTUATOR SYSTEMS

PROEFSCHRIFT

ter verkrijging van
de graad van doctor aan de Universiteit Twente,
op gezag van de rector magnificus,
prof.dr. F.A. van Vught,
volgens besluit van het College voor Promoties
in het openbaar te verdedigen
op woensdag 8 december 2004 om 13.15 uur

door

Anton Adriaan Kuijpers
geboren op 27 september 1970
te Zwolle

Dit proefschrift is goedgekeurd door de promotor:

Prof.dr. M.C. Elwenspoek

en de assistent promotor:

Dr.ir.G.J.M.Krijnen

Aan mijn ouders,
Enno en Ans Kuijpers - Kirchner

Contents

1 INTRODUCTION 1

References 8

2 NANO-POSITION SENSING CONCEPTS 11

2.1 Two Measurement Principles 12

2.1.1 Non-incremental measurement principle 13

2.1.2 Incremental measurement principle 13

2.2 Displacement sensing principles 16

2.2.1 Probe-based sensing 17

2.2.2 Integrated optical displacement sensing 19

2.2.3 Thermal displacement sensing 22

2.2.4 Capacitive displacement sensing 22

2.3 Digital microactuator displacement 25

2.4 Conclusion 25

References 26

3 CAPACITIVE INCREMENTAL POSITION SENSOR FOR MICROACTUATORS 29

3.1 Introduction 29

3.2 Basic periodic capacitive sensing structure 30

3.2.1 Incremental Capacitance Measurement Mode ICMM 30

3.2.2 Constant Capacitance Measurement Mode CCMM 31

3.2.3 Estimation of SNR for ICMM and CCMM 31

3.3 Quadrature detection 36

3.4 Possible Capacitance measurement methods 37

3.5 Noise limits for incremental capacitive sensor 40

3.5.1 Limitations by thermal electric noise 41

3.5.2 Limitations by thermal mechanical noise 41

3.5.3 Limitations by Electrostatic forces due to signal voltage U_s 43

3.5.4 Limitations by Electrostatic forces due to capacitance change ΔC_{sens} 44

3.6 Conclusions 45

References 46

4 2D-FE SIMULATIONS FOR A CAPACITIVE INCREMENTAL POSITION SENSOR 47

4.1 Introduction 47
4.2 FEM simulations for a capacitive long-range position sensor 48
4.3 Simulations Incremental Capacitance mode 50
4.4 2D-FE Simulations Constant capacitance mode (CCMM) 54
4.5 Simulation results for CCMM 55
4.6 Simulations for CCMM for rounded vs sine geometry 57
4.7 Discussion 63
4.8 Conclusions 65
References 66

5 DESIGN AND FABRICATION 67

5.1 Introduction 67
5.2 Typical Fabrication steps in poly-process 68
5.2.1 Examples of devices made with the poly-process 76
5.3 Further improvements: Twin process 79
5.3.1 Examples of devices made with the TWIN bulk-process 83
5.4 Conclusions 85
References 86

6 ASSESSMENT OF MICROMACHINED CAPACITIVE LONG-RANGE POSITION SENSOR 87

6.1 Introduction 87
6.2 Measurement method: Synchronous detection 88
6.2.1 Implementation of the charge-amplifier 91
6.2.2 Implementation of the synchronous detector 92
6.2.3 Conversion of measured voltage to capacitance 94
6.2.4 Connection of device under test 95
6.2.5 Actuation methods for quasi static and dynamic measurements 97
6.3 Quasi-static experiments for Incremental capacitance measurement Mode 100
6.3.1 Measurements for different periodic geometries 100
6.3.2 Quasi-static experiments with active gap-adjustment 108
6.4 Quasi-Static Experiments for Constant Capacitance measurement Mode 115
6.4.1 Operation of constant capacitance measurement mode 115
6.4.2 Implementation of constant capacitance measurement mode 116
6.4.3 Results of constant capacitance measurement mode 117

6.5 Dynamic experiments for ICMM with active gap-adjustment 125
6.6 Dynamic experiments using a comb-drive actuator as position sensor 129
References 141

7 CONCLUSIONS AND DISCUSSION 143
7.1 Capacitive incremental position sensing 143
7.2 Conclusions experimental results 145
7.3 Discussion on experimental results 147

APPENDIX 1 EXAMPLES 2D-FE SIMULATION RESULTS 151

APPENDIX 2 DESIGN AND FABRICATION 155
2.1 Poly-process: Design RectP12 (generation 1) 155
2.2 Poly process: redesign SinP10 generation II 156
2.3 TWIN process: design SinP10 159
2.4 Design calculations 162
2.5 Process outline surface-micromachined integrated capacitive position sensor for microactuators 166
2.6 Conduction measurement Chrome Platinum pads 175

APPENDIX 3 EXPERIMENTS AND SETUP DATA 177
3.1 Measurement setup and electronics 177
3.2 Measurement data Calibration 179
3.3 Additional measurement results for ICMM 180
3.4 Additional results comparison simulations and measurements 183
3.5 Additional results for CCMM 184
3.6 Frequency response pull-pull actuation electronics 186

SUMMARY 189

SAMENVATTING 191

DANKWOORD 193

BIOGRAFIE 195

1 Introduction

This thesis is the result of the Ph.D. project “Microactuator systems for Nano-Position control”, financed by the Dutch technology foundation STW. This project is part of the ongoing research on design and fabrication of Micro Electro Mechanical Systems (MEMS) of the Transducers, Science and Technology group at the University of Twente. The group is a contributing party of the MESA+ research institute and one of the leading groups in the world in the field of Micro System Technology (MST) [1].

Aim of the project

Within this project and thesis the focus has been on developing a displacement sensor for MEMS devices containing a linear displacement microactuator. Such devices are used in applications, which require the displacement of small objects or masses (e.g. probes, lenses, mirrors, cells) and sub-mm sized miniaturized sensors and actuators. For applications that require high-precision displacements over a long-range, which may not be obtained using open-loop operation, a combination of position sensing and control is necessary. In general, with the addition of position control the performance of a system can be improved and the sensitivity for parameter variations and external disturbances (e.g. noise, vibrations) can be reduced. To enable position control with nanometer accuracy over 10’s of micrometers displacement a position sensor is required that has a high dynamic range of displacement over resolution.

Application areas for MEMS Position sensing

The miniaturization and development of more complex displacement generating microsytems has led to a need for an increase in performance of such systems in terms of displacement range, accuracy, velocity (bandwidth) etc. Provided that nanometer position accuracy can be obtained over 10’s of µm displacement range, microactuators have a high potential in future probe memory applications [2, 3, 4, 5, 6, 7], scanning probe microscopy [8, 9, 10, 11, 12], medical analysis [13], cell manipulation (e.g. DNA analysis [14], neuron analysis in neurophysiology [15], microbiology applications [16]), optical mirror manipulation [17], microtooling and robotics [18] (e.g. microgripper) etc,

Scanning probe applications

As demonstrated by Binnig et al in 1986, scanning-probes are useful tools to observe, measure and modify surfaces at the atomic scale [8, 9]. This capability has been recognized and many efforts are underway to develop both MEMS-based Scanning probe microscopy applications and future MEMS-based data-storage devices using scanning probe techniques.

These storage devices are emerging as potential, ultra-high-density, fast, low-power alternatives to conventional data storage systems. The areal densities of the conventional magnetic recording techniques will eventually reach a maximum density of about 250 Gbit in^{-2} or 38 Gbit cm^{-2} imposed by the well known super paramagnetic effect [2,5,19,20].

An example of one of the first concepts for a MEMS-based scanning-probe data storage device is given in Fig. 1.

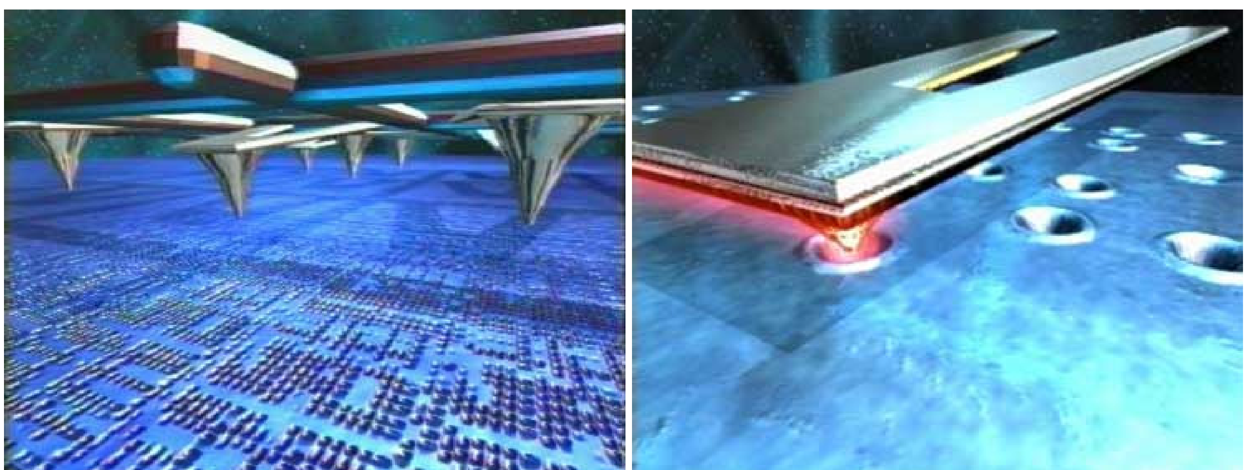

Fig. 1: An impression of the thermo-mechanical data-storage concept called the Millipede. A large number of parallel cantilever / probe-tips read/write and erase data in the form of nanometer scale indentations in thin polymer films reaching future storage capacities of Tbit / in^2. (Courtesy of International Business Machines Corporation. Unauthorized use not permitted)

This datastorage device is well known under the name of Millipede. In this concept digital data is recorded by writing indentations into a thin polymer film [3,5] in a thermomechanical approach. A nanometre-sharp tip is heated to a relatively high temperature of about 400 °C to soften the polymer locally. By applying a local force through cantilever/tip to the softened polymer a thermomechanical write action is achieved. Recent results have been reported on single-probe experiments using the thermomechanical write / read process to record data at 641 Gbit/in^2 and read them back at a raw error rate of better than 10^{-4}. It was demonstrated that at pit and track pitch of 37 nm, an indentation has a conical shape with an average depth of 3 nm and an average diameter at 50 % of the maximum depth of 15 nm [19, 21]. The error-rate performance depends on the indentation shape and dimensions and rapidly deteriorates as the probe-tip distance from the centre of the indentation increases. Therefore, the requirements for tracking performance are in the nanometre range for nanometre-sharp probe tips [20].

Besides the above-described thermomechanical storage concepts also MEMS-actuated magnetic probe-based storage concepts are reported [7,22]. Fig. 2 gives an impression of the magnetic storage concept called μSPAM (i.e. micro Storage Probe Array Memory). This project is part of the ongoing research by the Systems and Materials for Information storage group (SMI) at the University of Twente.

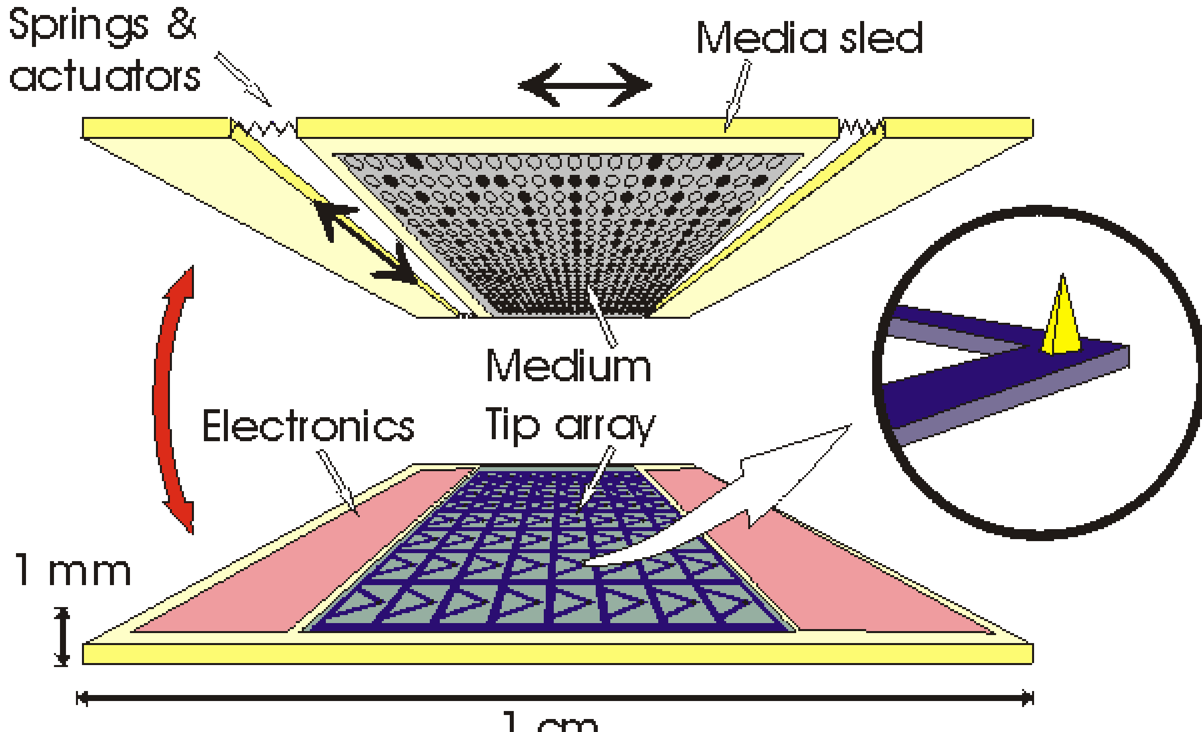

Fig. 2: Impression of a MEMS-based Scanning Probe Memory Array (μSPAM). In this concept data is stored in a large array of magnetic dots on a media sled and the read/write actions are performed by parallel operating cantilever probes. (Courtesy of Prof. Abelmann, SMI group. Unauthorized use not permitted)

The previous examples show that the probe-based data-storage concepts are based on the positioning in the x/y plane of a storage medium and the fine-tracking of each individual cantilever tip in the y/z direction. The concepts in the given references report on the use of a storage field with an area of 100 x 100 μm^2 [9, 23].

Very recently Pantazi et al [20] have reported on a servo-tracking control mechanism for the 'Millipede' project. A media sled or storage medium scanner is positioned with x/y-motion capabilities on the order of 120 μm [5, 20,23]. The mobile platform is fabricated from a 400 μm thick single-crystal silicon wafer using a deep-trench-etching process and actuated using miniature electromagnetic actuators using permanent magnets attached to the silicon scanner i.e. voice-coil-type actuators. Two pairs of thermal position sensors provide x/y-position information to the servo controller during closed-loop operation of the scanner. The sensors consist of thermally isolated resistive strip heaters made from locally doped silicon. Each sensor is positioned above an edge of the scan table and heated by applying a current. Part of the generated heat is conducted through the ambient air into the scan table, which acts as a heat sink. A displacement of the scan table results in a change in the temperature of the heater and thus in the electrical resistance. The time response is well modelled by a first-order low-pass filter with a time constant of 100 μs. Pantazi [20] reports on experimental results that show the feasibility of closed-loop track following using thermal position sensor signals yielding a position-error standard deviation of approximately 2 nm.

These examples clearly illustrate typical application areas for the displacement sensor presented in this thesis. They are also example of applications with an increasing demand for further miniaturation of (parts of) products and a need for accurate nano-positioning over a long-range of displacement of microactuator systems. Typically the performance of these MEMS-based devices will increase if the position sensor is fully integrated with the device in combination with position control. In order to make such systems both economically viable as well as compact, on-chip position sensing appears to be a requirement. This may not mean the full integration of sensing electronics with the MEMS device because as reported by Elwenspoek [24], it seems that the hybrid integration of several electromechanical and electronic functions is sometimes simpler and economically more feasible.

Silicon Micromachining Technology

The technology for miniaturization of systems develops from a number of fabrication methods. Precision engineering uses more conventional machining processes, which include cutting, drilling, sand blasting, spark erosion, mould injection etc. This work concentrates on the silicon micromachining fabrication process derived from the widely available Integrated Circuit (IC) fabrication processes. In addition to photolithography this high-precision micromachining technology includes etching techniques, thin film deposition and waferbonding.

These processes enable the simultaneous fabrication of many devices in parallel on one silicon wafer. The technology can be under certain restrictions CMOS compatible and therefore also allows in principle the monolithic integration of mechanical microsystem and electronics in one and the same chip. This aspect offers a high potential for both cheap and advanced microsystems.

A large variety of microsystems including pressure sensors, accelerometers, angular rate, fluid flow, and resonant sensors have been developed with micromachining technology.

Micromachining is quite complex and in contrast to the technology of CMOS IC's, it has hardly been developed to a standard technology. However, the micromachining techniques have become reliable and this is an important reason for the commercial success of microsensors. Large numbers of these sensors are applied foremost in the automobile industry, process control, medical applications and for scientific instrumentation [24].

Silicon micromachining can be divided into bulk micromachining and surface micromachining. Madou [25] and Elwenspoek and Jansen [26] give an overview of a variety of known processes for bulk- and surface micromachining.

Although MEMS technology is not restricted to silicon, most of the MEMS devices are made on silicon wafers as the starting substrate. This is because of the available technology but also because single-crystalline silicon has a number of remarkable mechanical properties in combination with a small thermal expansion coefficient and high stability to high temperatures. It is a very brittle material in contrast to (ductile) metals. Silicon has very low hysteresis and creep, and therefore the possibility to achieve high reproducibility of silicon sensor signals that rely on mechanical deformation (e.g. bending of membranes, deflection of beams). Silicon fails before it is deformed

plastically at much higher yield stress than for e.g. stainless steel. After releasing the load on an elastically deformed spring a small residual length remains and from this length it creeps slowly to its original length. [24, 26].

Micromechatronics and MEMS

There is an important systems aspect of microsensors: being small, and generally producing small signals, they do not trivially interface with the macro-world. Therefore, micromechanical sensors cannot be viewed as separate entities or components but they should actually be considered as microsystems involving not only the sensing microstructure but the interfacing and packaging as well. Hence, the design and development-process of microsensors should simultaneously include the interfacing and packaging aspects in order to successfully come to a working micro-sensor-system. In some cases, where one cannot rely on standard technology (i.e. in the form of foundry-processes), it may be even necessary to design the microfabrication processes hand in hand with the microsystems. The foregoing also reveals the multi-disciplinary nature of micro-sensor-systems; not only are the mechanical properties of structures important, but generally all the physical domains that take part in the transduction of the measurand to the eventual signal. This may involve such things as mechanics, for the actual response of the sensor (i.e. a bending membrane), optics (for read-out of a displacement), opto-electronic conversion and electronics for further signal processing. Moreover, the sensor system needs to be packaged. Although packaging of electronic integrated circuits is not a trivial thing, packaging a microsensor may even be more challenging by the very sole reason that a sensor should somehow "be open" to the environment in order to measure the measurand e.g. light, pressure, humidity, temperature. This means, that apart from an electrical interconnection, it needs at least one other physical connection called a port.

However, these micro-sensors are a subset and quite often a part of Micro Electro Mechanical Systems (MEMS) and Micro Systems Technology (MST). The denotion of MST is sometimes used as an extension of the Micro Electro Mechanical transducers with optical, thermal, magnetic, chemical and (fluidic) analysis micro systems. However, both MEMS and MST have a large overlap [24]. Within these systems a form of actuation in addition to sensing is present e.g. microactuators generating small forces and displacements, micro pumps in micro fluid handling systems, microrobots, etc.

The design and development of such a MEMS device calls for a synergetic approach because the physical properties of the sensing element, the actuator, the electronic interfacing and the packaging have to be understood and designed as a whole. Designing such a system by designing the separate parts will not lead to an optimal performing system. This multidisciplinary approach is often denoted as micromechatronics.

Feedback control in MEMS: Examples

In general feedback control can improve the performance of a dynamic system. Normally, systems are underdamped. For a control of the position a Proportional, Integrating, and Differentiating PID controller can be used, which increases the system damping and results in zero steady-state error. However, the introduction of the Integration-part, will lead to a loss in stability and increased time response. Legtenberg et al [27] performed a study towards PID position control of electrostatic comb drives using the comb-actuators simultaneously as capacitive sensor.

Cheung and Horowitz [28] describe a Kalman filtering scheme, which achieves a

position estimation error covariance below 0.01 µm (rms) for a comb-drive microactuator. Experiments demonstrate a state variable feedback loop operating at a closed loop bandwidth of over 11 KHz. The device has linear dimensions of 310 µm x 340 µm x 1.7 µm and a range of motion of ±4 µm and a force up to 0.3 µN. The dynamic range was therefore limited to ~ 400.

Horsley et al [29] presented a microfabricated actuator designed for high precision servo-positioning in a magnetic hard disk drive. With capacitive sensing and closed loop control a prototype device was used to actuate a 1.6 mg ceramic slider over a 1.2 KHz bandwidth with a sensing resolution of about 20 nm.

Finally, the earlier described results of Pantazi [20] of a servo-tracking control system for a MEMS-based x/y stage are a good example of the ongoing efforts to improve system performance of MEMS devices through feedback control.

Setting of the Project

This thesis focuses on the concept, design, fabrication and testing of a displacement sensor integrated with a MEMS device generating long-range one-dimensional linear displacements in the order of 50-100 µm. The target specification for the accuracy is set to 1 – 10 nm. The bandwidth is initially considered to be less decisive.

This research started with the consideration and choice of sensing principle, microactuator and process design to enable a full integration and meet the target specifications.

In an early stage of the project it was decided to concentrate on the (polysilicon) surface micromachining and on electrostatic microactuators because these microactuators have good scaling properties [24]. Moreover, in the TST group there is ample experience and facilities for successful fabrication and characterization of e.g. surface micromachined devices.

This research has already resulted in the successful fabrication of electrostatic actuators by Legtenberg [30] and Tas [31] and the complete process sequences are more or less standard available in the MESA$^+$ clean room laboratory.

The work of Legtenberg in 1996 [30] included the development of polysilicon surface micromachining technology and various electrostatic actuators including the commonly known comb-drive actuator.

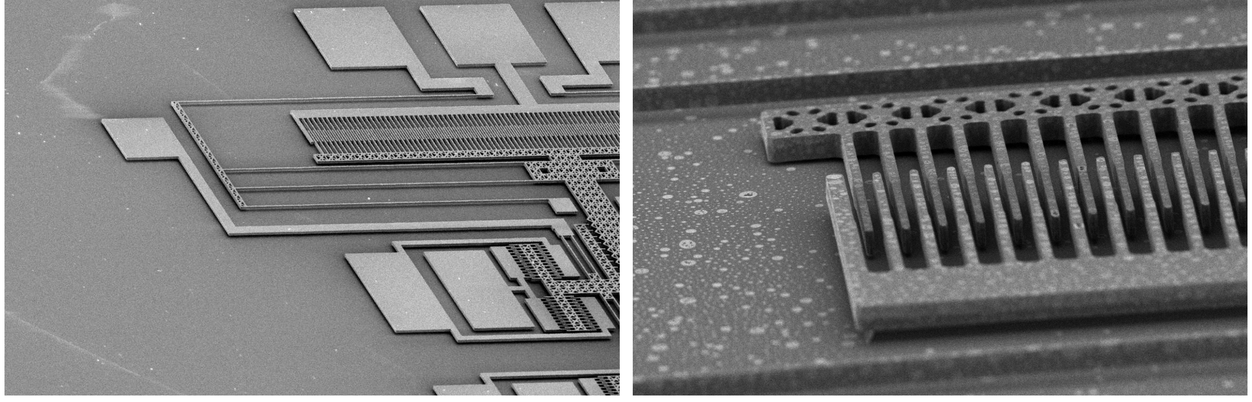

Fig. 3: Two examples of a comb-drive and folded flexure spring. Finger width and gap-size are 2 µm, the height is 5 µm

The work of Tas in 2000 [31] was a continuation of the research for surface micromachining technology and strong electrostatic actuators. Tas gives an overview of various propulsion principles for linear micromotors including piezoelectric and electrostatic motors fabricated by 'traditional' precision-mechanical, bulk- and surface micromachining fabrication processes. The use of thin film piezoelectric actuators (e.g. zinc-oxide, PZT) was avoided because of the problematic compatibility of this material with surface micromachining. Using the surface micromachining process Tas realized the so-called electrostatic shuffle motor and demonstrated the high future potential of this device. It is a linear (i.e. not rotating) walking or stepping motor which in theory can deliver up to 1 mN force in an actuator volume of 100 x 200 x 2 μm^3 at 30 V driving voltage. Tests showed an effective step size of 85 nm with a total reach of 43 µm and a produced force of 43 µN at 40 V driving voltage. Special attention should be paid to the design to minimize adhesion forces and tribology aspects of contacting surfaces.

The fabrication process scheme for the microwalker described by Tas turned out to be quite complex. The process scheme involved three polysilicon layers, two silicon nitride layers and 8 masks and photolithography steps. The process described by Legtenberg for the comb-drive actuators used only one polysilicon layer with thickness of about 5 µm and one photolithography mask.

Constraints for the work in the MESA+ laboratory is that the structural poly silicon layer has a maximum height of 5 µm. Possible stress gradients will result in a deflection for increasing lateral sizes of structural elements. As a rule of thumb, the maximal lateral size of elements or parts should be less than 1 mm, in order to keep the deflection due to out-of –plane bending below 1 µm. The resolution of the standard available photolithography determines the minimum lateral sizes of gaps and beams to about 2 µm [31].

As a starting point it was decided to investigate sensing principles that can be combined with electrostatic comb-drive microactuators. This would enable relative easy design, fabrication and experiment possibilities and a sufficiently strong actuator. The optimal sensor principle can be integrated but is not essentially bounded by the choice for a surface micromachined electrostatic comb-drive actuator.

Such a device containing sensor and actuators may have dimensions typically in the order of 1000 x 1000 x 5 μm^3 and minimum feature sizes in the µm-range. A rather straightforward idea is to consider a surface micromachined device with a mass displaced by comb-drive microactuators over a range of 10's of µm and capable of nm-resolution.

Thesis outline

The outline of this thesis is as follows: The next chapter describes the sensing principles that could potentially meet the target specifications for a displacement range of 100 µm with an accuracy of 1 – 10 nm. Other criteria will be described and discussed further in chapter 2 as well. The reason to select a capacitive position sensing principle will be given. Two concepts of an incremental position sensor will be examined in chapter 3. Also, the possible methods, difficulties and limitations to measure very small changes in capacitance will be discussed.

In chapter 4 the capacitive sensing principle will be numerically evaluated using 2D-Finite Element simulations.

Chapter 5 presents two micro fabrication processes with which the capacitive sensor can be integrated with electrostatic microdevices. A poly-silicon surface micromachining process and a bulk micromachining process are developed. This chapter will compare and discuss the benefits of the two processes. With the poly-silicon process various devices are made.

Chapter 6 presents the assessment of quasi-static and dynamic experimental results with these devices. The aim is to proof that the concept potentially can have nanometer accuracy, with high bandwidth and long travel range.

Chapter 7 ends this thesis with conclusions and discussions.

References

[1] http://www.el.utwente.nl/tt/, 2004

[2] S.Hoen, H.J.Mamin, D.Rugar, Thermo-mechanical data storage using a fiber optic styles, Appl.Phys.Lett. 64(3), jan 1994,

[3] H.J.Mamin, L.S.Fan, S.Hoen, D.Rugar, Tip-based data storage using micromechanical cantilevers, Sensors and Actuators A48, 215-219, 1995

[4] M. I. Lutwyche, C. Andreoli, G. Bennig, J. Brugger, U. Drechsler, W. Haeberle, H. Rohrer, H. Rothuizen, and P. Vettiger, “Microfabrication and parallel operation of 5 x 2D AFM cantilever arrays for data storage and imaging,” in Proc. IEEE Workshop on MEMS (MEMS98), Heidelberg, Germany, pp. 8-l 1, Jan. 1998

[5] P. Vettiger, M. Desmont, U.D. Drechsler, U.H. Ürig, W. Äberle, M.I. Luwyche, H.E. Rothuizen, R. Stutz, R.Widmer and G.K.Binnig, The “Millipede” – More than one thousand tips for future AFM data storage, IBM J.Res.Dev. 44 (3), 323-340,2000.

[6] J.L.Griffin, S.W.Schlosser, G.R.Ganger, D.F.Nagle, Modeling and performance of MEMS-Based storage devices, Proc.ACM Sigmetrics June 2000.

[7] L. Abelmann, T. Bolhuis, A. M. Hoexum, G. J. M. Krijnen, J. C. Lodder "Large capacity probe recording using storage robots" IEE Proceedings-Science Measurement and Technology, 150 (2003), no 5, Page 218-221

[8] G.Binnig, C.F.Quate, C.Gerber, Atomic force microscope, Phys.Rev Lett. 56, 930, 1986.

[9] H.J. Mamin, D.Rugar, Thermomechanical writing with an atomic microscope tip, Appl. Phys. Lett. 61,1003, 1992

[10] S. Deladi, J.W. Berenschot, M.J. de Boer, G.J.M. Krijnen and M.C. Elwenspoek, An AFM-based device for in-situ characterization of nano-wear, Proc. of MEMS2004, Maastricht, Netherlands, pg 181, January 2004.

[11] H.Toshiyoshi, M.Goto, M.Mita, H.Fujita, D. et al., Fabrication of micromechanical tunneling probes and actuators on a silicon chip, Jpn J.Appl.Phys. (38), 7185-7189, dec 1999,

[12] T.W.Kenny, S.B. Waltman, J.K.Reynolds, W.J.Kaiser, “Micromachined silicon tunnel sensor for motion detection”, Appl. Phys. Lett., (58), pp.100, 1991

[13] G. Lim, K. Minami, M. Sugihara, M. Uchiyama, and M. Esashi, “Active catheter with multi-link structure based on silicon micromachining,” in Proc. 8th IEEE Workshop Micro Electra Mechanica Systems, Amsterdam, The Netherlands, p. 116, Jan. 1995

[14] C. H. Mastrangelo, M.A. Burns, and D. T. Burke, “Microfabricated devices for genetic diagnostics,” Proc. IEEE, 86, 8, 1769-1787, 1998

[15] J.Muthuswamy, D.Salas, M.Okandan, A chronic Micropositioning system for neurophysiology, Proc. Of second joint EMBS/BMES conf., Houston, oct 23-26, 2002.

[16] A.Bergander, Micropositioners for microscopy applications and microbiology based on piezoelectric actuators, Journ. Of micromechatronics, 2,1, 65-76, 2003.

[17] J.D.Grade, Advanced, vibration resistant, comb-drive actuators for use in a tunable laser source, Sensors and Actuators A, 114, 413-422, sept 2004 .

[18] A.Ferreira, j.Agnus, N.Chaillet, JM Breguet, A smart microrobot on chip: design, fabrication and control, IEEE- ASME Trans. On Mechatronics, 9 (3), 508-519, sept 2004.

[19] D.A.Thompson, J.S. Best, The future of magnetic data storage technology, IBM J RES Develop.,44,3, 2000

[20] A Pantazi,MA Lantz, G Cherubini, H Pozidis and E Eleftheriou, A servomechanism for a micro-electromechanical-system-based scanning-probe data storage device, Nanotechnology, (15), S612–S621, 2004

[21] H.Pozidis, W.Hëberle, D.Wiesmann, U.Drechsler, M.Despont, T.E.Albrecht, E.Eleftheriou, Demonstration of thermomechanical recording at 641 Gbit/in^2, IEEE Trans.Magnetics, 40, 4, 2004.

[22] L.R.Carley, J.A.Bain, G.K.Fedder, D.W.Greve, D.F. Guillou, M.S.C.Lu, T.Mukherjee, S.Santhanam, L.Abelmann, S.Min, Single-chip computers with microelectromechanical systems-based magnetic memory (invited), J.of Applied Phys., 87, 9,may 2000

[23] E.Eleftheriou, T.Antonakopoulos, G.K.Binnig, G.Cherubini, M.Despont, A.Dholakia, U.Dürig, M.A.Lantz, H.Pozidis, H.E.Rothuizen, P.Vettiger, Millipede—A MEMS-based Scanning-Probe Data-Storage System, IEEE Trans. On Magnetics, 39, 2, 2003

[24] M.Elwenspoek, R.J.Wiegerink, Mechanical Microsensors, Berlin Heidelberg New York, Springer-Verlag, 13-21, 2000.

[25] M.Madou, Fundamentals of Microfabrication, CRC-press, New York,1997

[26] M.Elwenspoek, H.Jansen, Silicon Micromachining, Cambridge University Press, 1998

[27] R.Legtenberg, A.W.Groeneveld, M.Elwenspoek, Towards Position control of electrostatic comb drives, Proc. Micromech. Microeng. (MME’95), Copenhagen, 3-5 Sept., 1995.

[28] P.Cheung, R.Horowitz, Design, Fabrication, Position Sensing and Control of an Electrostatically-driven Polysilicon Microactuator, *IEEE Trans. Magnetics*, **32-**1, 122-128, 1996

[29] D.A.Horsley, N.Wongkomet, R.Horowitz, A.P.Pisano, Precision positioning using a microfabricated electrostatic actuator, IEEE Trans. On Magnetics, (35), 2, march 1999

[30] R.Legtenberg, Electrostatic actuators fabricated by surface micromachining techniques, Ph.D.thesis, Twente University, Enschede, 1996

[31] N.R.Tas, Electrostatic Micro Walkers, micro electromechanics and micro tribology, Ph.D. Thesis, Twente University, Enschede, 2000.

2 Nano-position sensing concepts

This chapter will further briefly discuss various general nano-position sensing concepts for large displacement microsystems. In the broader context of this work, the interest for accurate-positioning over a long range of displacement by means of a relative small integrated micromachined position sensor has been the basic objective and motivation for this research. Because of the choice for silicon-based fabrication technology, microactuators that are capable of producing 100 µm displacement-ranges are confined to in-plane motion, i.e. parallel to the substrate. This aspect will naturally also influence the possible options for sensing concepts.

The target specifications for the micromachined integrated position sensor are to obtain nanometer accuracy over a range of 50 – 100 µm of in-plane displacement, which implies a dynamic sensing range in the order of 10^5 (i.e. 100 µm / 1nm). The demands for bandwidth or velocity are not easy to establish without an immediate application and it is decided to be at this point less decisive.

However, taking the context of a probe memory system as described in the introduction and the aim for strong actuators capable of forces in the order of 1 mN [24], an estimation of the velocity can be made. For a cubic silicon mass of dimensions 1 x 1 x 0.5 mm^3, the maximum acceleration is determined by $a_{max} = F / M$. Assuming a sinusoidal position function $x(t) = x_{max} \cdot \sin(\omega \cdot t)$, determines the maximal acceleration by $|a_{max}| = \omega^2 \cdot x_{max}$. This means that the maximum velocity and the related frequency for these conditions are given by:

$$v_{max} = \omega \cdot x_{max} = \left(\sqrt{\frac{a_{max}}{x_{max}}}\right) \cdot x_{max} = \sqrt{a_{max} \cdot x_{max}} = \sqrt{\frac{F \cdot x_{max}}{M}}$$

$$f = \frac{1}{2\pi}\sqrt{\frac{a_{max}}{x_{max}}} = \frac{1}{2\pi}\sqrt{\frac{F}{M \cdot x_{max}}} \qquad \text{(Eq.2.1)}$$

For a maximal displacement amplitude x_{max} = 50 µm, the maximal velocity v_{max} = 207 mm/s and frequency f = 659 Hz for a force F = 1 mN and mass M = 1.16e-6 Kg, This calculation illustrates the relation between force, mass, displacement and velocity for a MEMS-based scanning probe device.

Measuring a position is always done with respect to a chosen or designed reference frame and origin. A displacement indicates both a direction and a length or distance between two positions. Because of the condition of one-dimensional motion, measuring a position is the same as measuring a displacement in this project.

It is only briefly noted here, that in practice pure 1-dimensional motion of an object/body or mass having 6 degrees of freedom (6-Dof) is very hard if not impossible to realize. It means infinitely good restraint of motion in 5 Dof and no restraint in the desired direction of motion. Any unwanted motion along or about a given axis, caused by a motion in the desired direction, is denoted as cross-talk. Atherton [1] describes in detail

the position measurement errors due to, misalignment of measurement axis and motional axis, cross-talk and parasitic angular motions. Without a sensing principle, sensor or actual system at hand these errors cannot be assessed seriously.

Therefore, first the different position measurement principles and then transducer sensing principles that have the potential for nm-accuracy over a long-displacement range will be described.

2.1 TWO MEASUREMENT PRINCIPLES

For a given maximum range of displacement and desired accuracy, two measurement principles can be distinguished.

- Non-incremental measurement (absolute)
- Incremental measurement (counting)

A non-incremental measurement method measures the (change in) displacement x and results in an output function $f(x)$, preferably linear over the full range X_{max} as indicated in Fig. 4. Taking the inverse function $f^{1}(x)$ gives an absolute value for position x, provided that f^{1} exists and gives an unambiguous of f^{1} to x

An incremental measurement method has a periodic output function $g(x)$ e.g. sine. The total range of displacement X_{max} is divided in N units or periods P. Counting the number of units is a relatively more simple measurement method than a non-incremental absolute measurement method. The function $g(x)$ is used to determine the position x relative to the starting point of the actual period. The design has to be such that each period gives the same output function $g(x)$. This principle reduces the demands for dynamic range.

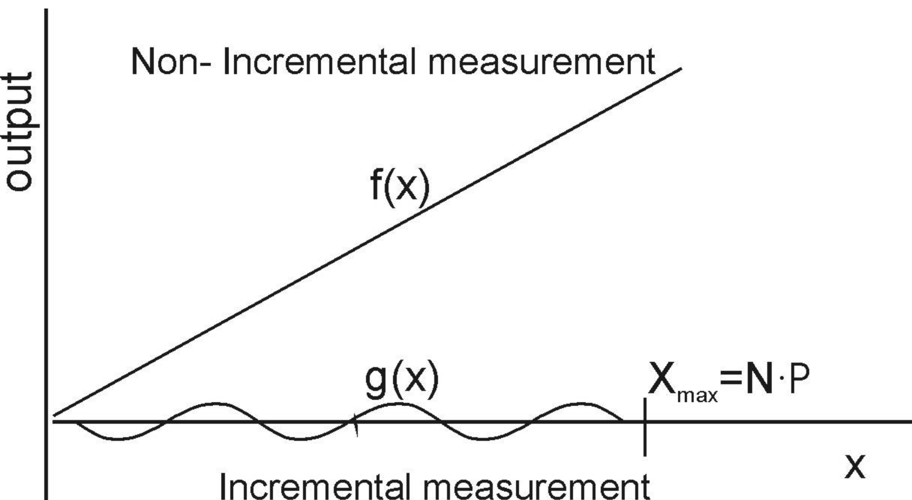

Fig. 4: Two measurement principles are discriminated: A non-incremental measurement and an incremental measurement principle. The maximum range is indicated by X_{max}.

2.1.1 Non-incremental measurement principle

For a non-incremental principle the demands for dynamic range are very severe if the position has to be measured with nm accuracy over 100 µm range or more. Assume a sensor or a measurement system with a transfer function depending on position, temperature, humidity, pressure, noise, etc. $f(x, T, H_r, p,..)$. A total range of position X_{max} results in a full scale output of Δf_{fso}. The other variables should be kept constant if possible, because they are a kind of error sources. If Δx_{max} = 100 µm and the accuracy is 1 nm, then the required dynamic range D_R is 10^5. The required maximum resolution, is $R_{max} = x_{max} / \Delta x$, where Δx is the smallest detectable change in x in the presence of noise and disturbance [2, 3]. Accurate measurement depends on elimination, reduction and compensation of error sources and error sensitivities. Commonly this is achieved by careful designing of the measurement system and maintaining environmental measurement conditions constant. The larger the dynamic range D_R the more difficult it becomes to meet the specification.

2.1.2 Incremental measurement principle

In the field of measurement and instrumentation the concept of an incremental position sensor is quite common. It is the solution for the combination of a desired very high dynamic range and a high accuracy. By dividing the maximum range of displacement into a discrete number of units of length, the problem of measuring a certain displacement (position) is reduced to (simply) counting the number of units starting from a reference or initial position. From one periodic sensor signal $s(x)$ only the count or speed information, which is the basic sensing of movement can be derived [3].To measure velocity, direction and incremental position, two periodic sensor signals $s_1(x)$ and $s_2(x)$ are necessary to unambiguously determine the position within each position.

With two rectangular signals, increments in position of dx-size can be unambiguously detected. Commonly, this principle is implemented by a mechanical offset of a quarter period P/4 between two rectangular signals. This principle is called quadrature detection [3]. In this way the period P is divided into four quadrants to determine the actual position unambiguously with the smallest detectable increment of displacement equal to dx = P/4. The dynamic sensing range (DR) within each period is then determined by the ratio of period P and smallest increment dx i.e. DR = P / (P/4) = ¼. For the maximum range X_{max}, which equals N periods of length P, the dynamic range D.R. = N·P / (P/4) = 4·N. An example is given in Fig. 5.

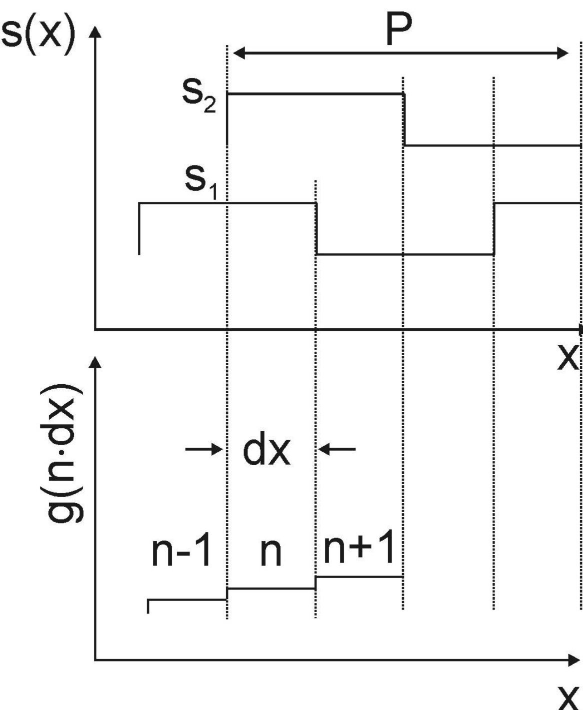

Fig. 5: (Left) An incremental measurement principle discretizes a displacement into a number of units dx or (half) periods P. Two signals *s(x)* are needed for unambiguous quadrature displacement detection.

In addition to this coarse measurement, a fine position measurement principle is possible using an interpolation or analog measurement technique. Any residual distance between actual 'true' displacement and the number of counted units can be determined with sub-unit accuracy, provided that the signals $s_1(x)$ and $s_2(x)$ allows for an (linear) interpolation within each unit (i.e. s_1 and s_2 should not be rectangular). With the use of sinusoidal or triangular functions as given in Fig. 6 and an *arctan* calculation given in (Eq.2.2), the displacement can be detected with a resolution limited by noise and stability [4].

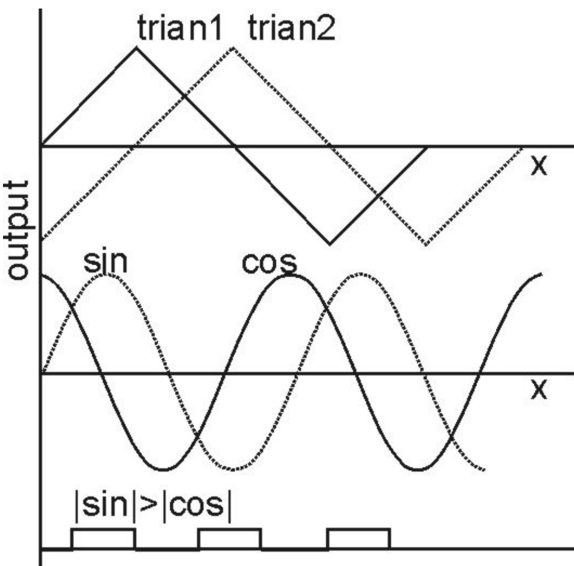

Fig. 6: Both triangular and sine signals can be used for quadrature position detection with interpolation between counts. Commonly, an arctan calculation is used.

$$x = arctan\left[\frac{sin(x)}{cos(x)}\right] \quad if\ |sin| < |cos|$$

$$x = \frac{\pi}{4} - arctan\left[\frac{sin(x)}{cos(x)}\right] \quad if\ |sin| > |cos| \qquad \text{(Eq.2 2)}$$

A coarse position detection is established by counting the half periods of each signal with an up-down counter e.g. *sin(x)* >0, *cos(x)* >0 or *|sin(x)|* > *|cos(x)|* and discrete increments of a quarter period can be detected. The more precise position detection combines the coarse position detection with a fine analog measurement of the distance to the last counter increment using an arctan calculation (Eq.2.2) or a look-up table [4].

This quadrature detection technique is commonly used with optical interferometers, incremental optical and capacitive encoders, rotary shaft encoders and resolvers [4,5,6,7,8]. Strictly speaking, the term incremental only accounts for the discrete / counting technique. In this thesis, the combination of an incremental and interpolating analog measurement is loosely denoted as an incremental position sensor.

A triangular shaped signal as in Fig. 6 is interesting for detection because of its linearity and it therefore has a constant differential change $\partial Trian(x)/\partial x$ = constant. Hence, the sensitivity for this type of sensor signal is constant. A saw tooth-shaped signal would be interesting to consider too. For a sine-function the differential change is continuous but not linear.

According to Baxter [4] an inverse tangent calculation is preferred above choosing either *sin(x)* or *cos(x)* separately. It is insensitive to absolute changes in amplitude if both quadrature signals are well matched to have equal amplitude. Taking the ratio between *sin(x)* and *cos(x)* will compensate for any variations in temperature and relative humidity. The *arctan* calculation may be done by using a lookup table which also can compensate for nonlinearities like rounded corners on the triangular output signals. With two lookup tables, the effects caused by a mismatch in amplitude can be compensated as well [4].

However, if both the *sin(x)* and *cos(x)* are afflicted by a contribution of position dependent noise then the use of an *arctan* calculation may not be beneficial. If one considers the positions for which the *cos(x)* is minimal in Fig. 6 but the most influenced by noise, then for these positions the method of choosing between two look-up tables for the *sin(x)* and *cos(x)* separately may give better results than the *arctan* calculation.

To obtain a periodic read-out signal, one way of approach is to divide the total displacement range into a physical repetitive pattern with a large number of units or dots with a physical property e.g. magnetic, optical, thermal, electrostatic, or chemical labeling. Alternatively the pattern may contain a specific geometric property e.g. holes, indentations or dimples. This pattern may be read out with probes similar to the probes discussed for the SPM techniques in chapter 1.

With the use of an inverse tangent calculation the demands for fabrication accuracy in terms of unit size and alignment accuracy are less stringent. Otherwise, for pure rectangular read-out signals, the coarse quadrature detection principle would require the spatial displacement offset between the two sensor signals to be $dx = P/4 = 1$ nm. This corresponds to a Minimum Feature Size (MFS) of the units of $P/2 = 2$ nm.

With larger period sizes, more emphasis is put on the accuracy of the look-up table or

the inverse tangent calculation. An overview of the consequences of the two measurement principles is given in Fig. 7.

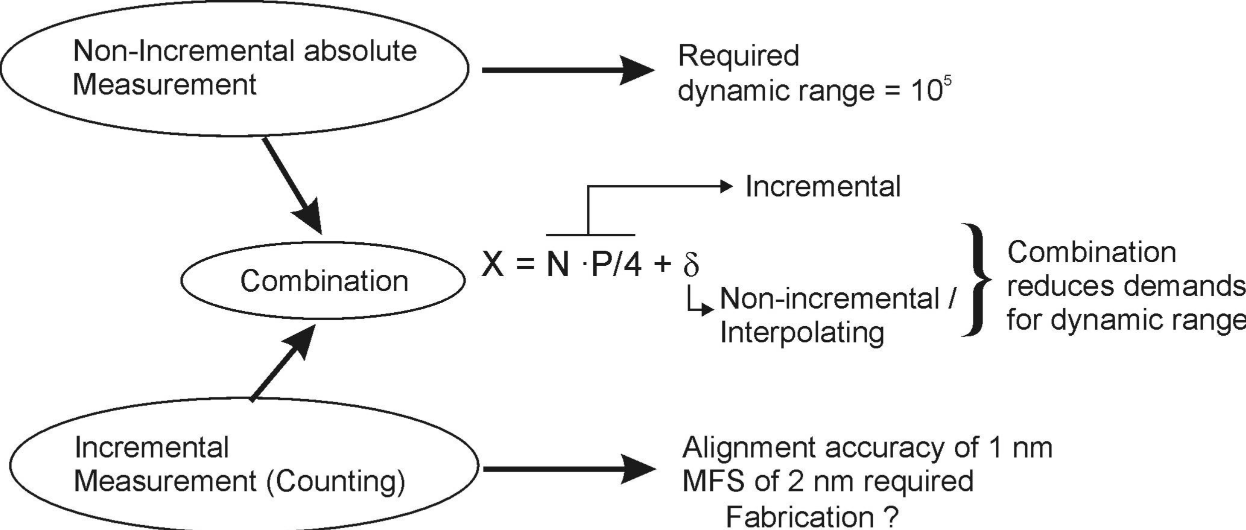

Fig. 7: Two general measurement principles: A non-incremental absolute measurement principle and incremental measurement principle. A combination of both methods reduces the demands for dynamic range and fabrication accuracy.

2.2 DISPLACEMENT SENSING PRINCIPLES

A brief survey has been carried out to consider the possibilities of transducer principles including optical, thermal, capacitive and probe-based principles (e.g. Scanning Tunneling Microscopy and Atomic Force Microscopy) in terms of nm-accuracy, fabrication / micromachining and integration with a MEMS device, interfacing with electronics, parasitic forces and power consumption. This is depicted in Table 1.

	Transducer principles			
Criteria	**Probe-based**	**Optical**	**Capacitive**	**Thermal**
Accuracy	++	++	+ / ++	+ /++
Range	- / +	++	+/++	+/ ++
Speed	+	+	+	-
Fabrication/ Micromachining	-	--	++	++
Electronics / Integration	+	-	++	++
Parallelism	-/+	--	+/++	+/++
Parasitic forces	-/+	++	--	-/+
Power consumption	+/++	-/+	++	+

Table 1: For the possible implementation and integration of a position sensor within a MEMS device to enable nm-accuracy over a 100 µm-range, four transducer principles are compared in the following sections on a number of criteria.

2.2.1 Probe-based sensing

Many transducer principles can be employed for probe-based position sensing using a periodic geometrical function or a periodic pattern of dots with a physical or a geometrical property.

A macro world probe-sensing principle is presented by Ohara [9] for a scanning probe position encoder (SPPE). It is a real-time position measurement device with target specifications of 1 nm precision over 300 mm, 0.01nm resolution and a detection speed of 5 – 10 m/s. The SPPE sensor probe is oscillating above a grating surface (sine pattern) with 100 nm – 300 nm period in the direction of the period-axis. For experimental testing a chemically etched tungsten wire was used as capacitance sensing probe. Actual characterization of the achieved accuracy is not reported.

Examples of other probe scanning principles are found in the probe-based data storage devices described in the introduction (chapter 1) and in the research fields of a.o. Scanning Tunneling Microscopy (STM) [10,11], Electric Field Microscopy (EFM) [12], Atomic Force Microscopy (AFM) [13], Scanning Capacitance Microscopy [14,15], Thermal Scanning Microscopy [16].

For applications such as the probe-based memory devices reading a repetitive pattern of magnetic dots [17] or mechanical indentations [18,19] is possible since the facility to make and read these patterns is already present to store data on a scanning medium or x/y stage. Different storage concepts are reported, ranging from magnetic-probe-based storage to thermomechanical probe-based data-storage. Dot or bitsizes of 30-40 nm with two times larger pitch sizes have been reported by Vettiger using this thermomechanical technique [19,19]. More recently pit-sizes of about 7 - 8 nm have been reported by Pantazi et al [20]. They demonstrated a servo mechanism for the scanning x/y stage using dedicated storage fields for timing information and track following servo-control. A special technique is implemented to achieve quadrature position measurement. The cantilever deflection is in this case measured using a thermal-resisitive principle.

More commonly used for probe scanning microscopy are the AFM and the STM. The STM can only be used to study conducting surfaces. Both principles are capable of extremely high spatial resolution in three dimensions. The small forces near the surface of the sample act on the tip and cause minute deflections of the cantilever, which are measured with sub-angstrom (Å) sensitivity by e.g. an optical or tunneling displacement detector [11].

The key aspect to achieve angstrom scale resolution in scanning probe microscopes such as the STM and AFM is the use of nm-sharp tips in combination with an extremely strong distance dependence. For example with STM the tunneling current between tip and sample is exponentially decreasing as the tunneling gap is increased as given by $I(s) = I_0 \cdot e^{-ks}$ where **s** is the gap spacing. With typical values of **k**, an increase of **s** by 1 Å typically decreases **I** by a factor of 10. At very close range the AFM (contact or repulsive mode) exhibits an even stronger distance dependence though this results in a similar lateral resolution as that of STM. For non-contacting modes the tip is held at a larger distance (~ 5 nm) above the sample surface which reduces the chances of damaging the sample or probe tip. Albrecht reports on a lateral resolution for this mode in the order of 5 nm [11].

Meli and Thalmann [13] report on a long-range AFM profiler used for accurate pitch measurements. With AFM tapping mode measurement on a standard holographic calibration grating a small combined standard uncertainty of only 32 pm for the average pitch of 700.989 nm is reported.

Eagle and Fedder [21] report on a reproducible method to write nanometer-sized pits in a sputtered carbon film scanning tunneling microscope (STM) with a platinum iridium tunneling tip. By applying a 4 V, 250 ns voltage pulse across the tunneling gap a 3.5 nm diameter pit is demonstrated with a depth of roughly 4 nm. Overall surface roughness of the carbon films is under 3 Å (rms) on 100 nm x 100 nm scanned areas. An array of holes written in the carbon demonstrates reproducibility and the feasibility to use this technique in lithography and data storage applications.

Matey and Blanc [15] demonstrated using Scanning Capacitance microscopy the capability to detect variations in topography of about 0.3 nm over areas of the order of 0.5 μm^2 with a lateral resolution of about 100 nm. The capacitance probe is some 20 nm in height above the sample surface. For the demonstrated system the oscillator noise in a 30 KHz bandwidth centered around 5 MHz limits the resolution of the system to ~ 0.5 aF for about 0.1 nm change in height. With a relative electrode to sample velocity of 5 m/s, features with lateral dimensions of 0.1 – 10.0 µm (i.e. Lateral resolution) and heights of more than 0.2 nm are resolved.

Barret and Quate [22] demonstrate a scanning capacitance microscope which is based on the atomic force microscope. The tip-sample capacitance as a function of lateral position is employed to study dielectric properties of nitride-oxide-silicon (NOS) films. This system has the ability to store information by trapping charge in the silicon nitride with the cantilever tip in contact with the dielectric nitride film. It is reported that there appears to be no restriction to achieve data reading rates of 1 MHz or better for minimum detectable bitsizes of about 20 nm and scan speeds of more than 1 cm/s. However, strong challenges will probably be material and tribology problems because of the contact forces (i.e. friction) between tip and sample.

It is known that adsorbed thin-films of contaminants (e.g. adsorbed H_2O molecules) are present on most surfaces in air, although the physical parameters depend on environmental conditions and the nature of the surface. These contaminants can cause large forces on the tip and cantilever and causes a strong reduction in sensitivity, especially for STM [10]. This aspect is important for a successful operation of an implemented probe sensing concept for incremental displacement sensor based on the periodic pattern scanning with nm accuracy.

Tabib-Azar [21] gives an overview of various cantilever deflection sensing methods including capacitive, piezo electric and piezo resistive, tunneling current, magnetic field, optical Michelson interferometry, beam deflection methods. The capacitive and piezoresistive methods seem most suitable for integration with a MEMS actuator.

Some examples of MEMS-based tunneling sensing are found in [23] for a high-sensitivity micromachined tunneling accelerometer with micro-g resolution. Tunnelling is

often combined with an actuator to form a feedback control keeping the gap distance constant. This offers a convenient way of detection, [24].

From this brief survey it is illustrated that it is in principle possible to make and scan periodic patterns with probe-based sensing methods. In general however, these probe sensing principles have a very high resolution (atomic scale) in the out-of plane direction (perpendicular to the substrate surface), but the lateral resolution can be orders of magnitude less. Some of these probe sensing principles e.g. STM are operating with a gap-distance between tip and surface within a range of 10 Å (i.e. 1 nm). This puts a big pressure on the performance of the microsystem and the tip-actuators. The integration with a microactuator system, and the compatibility within a micromachining process is less favorable. Any additional manual assembly of a probe-sensor after the processing of the microactuator system is undesirable.

Dot-sizes of 2 nm diameter have not been demonstrated to our knowledge. Therefore, an incremental quadrature displacement technique by dividing a period into 4 quadrants using two periodic read-out signals is very difficult to accomplish. For larger dot sizes (e.g. 40-50 nm) a bit counting concept and an analog measurement technique (e.g. interpolation, look-up table) has to be combined if an accuracy or precision of 1 nm is required for specific applications.

Furthermore, it may not always be possible to detect the position from the information stored on the table of an x/y-stage or scanning medium. Particularly, for applications such as Surface scanning probe microscopy or Protein and DNA scanning microscopy the table or medium does not contain an array of bits or dots. And it may not be possible or desirable to add these bits with extra fabrication steps because these steps could alter the surface properties, which may just be the object of research interest.

Referring back to Table 1 it seems that the complexity of the fabrication, the integration through micromachining processes and the complex tribology aspects due to tip-sample interactions makes these sensing schemes relatively less advantageous than other transduction or sensing principles, described in the following sections.

2.2.2 Integrated optical displacement sensing

Optical sensors are popular for measuring position and displacement. The advantages are simplicity of application and relative long operating distances. They are relatively insensitive to stray magnetic fields and electrostatic interferences and therefore quite suitable for many sensitive applications.

In general an optical position sensor requires three essential components: A light source, a photodetector and a light guidance or transport medium, which may include lenses, mirrors, optical fibers, polarizers, etc.

Within the field of optical sensing principles, laser interferometry has a long tradition of combining high accuracy over a very large range because this is intrinsically an incremental sensing principle due to the periodic nature of interfering light. An example that shows the strength of the interferometric principle is the fact that the meter is defined by a laser light in vacuum with an accuracy of better than a few parts in 10^{11} [25]. For He-Ne laser light (λ ~ 632 nm) operated in air the accuracy will be at least one part in 10^7 which is 0.01 nm in 100 μm [1].

This principle is interesting for characterization of the integrated displacement sensor that is developed in this work. However, the measurement of in-plane displacements appears to be particularly difficult for MEMS devices with very limited accessibility and structure height (~ 5 μm). For example Cho et al [26] report on a modified Mach-Zehnder Interferometer that is used for the characterization of a nonlinearly modulated actuator capable of producing high-precision digital stroke. A laser beam is focused on a micromirror situated on the outer rim of the device and with a mirrorplane perpendicular to the in-plane motional direction. The cross-section of the laser spot is in the order of 30 μm. A repeatability of 12.3 ± 2.9 nm is demonstrated.

Another possible optical displacement transducer can be fabricated with two overlapping gratings which modulate the light intensity of the transmitted light. Very popular in macro-world applications are the optical encoders using an incremental quadrature measurement principle [3, 7].

Probably the most common integrated optic elements are waveguides. They are fabricated using a variety of methods, including standard photo-lithography and wet and dry etching [27].

Ura et al [28] give several references to integrated Michelson. They further describe and experimentally verify an integrated optic sensor head for sensing a two-dimensional displacement of a scale consisting of crossed gratings with a grating scale of 3.2 μm period. The device was designed and fabricated on a Si substrate with integrated waveguides and 4 photo detectors. The size was 2 mm x 15 mm. A complete combination and integration of this encoder-like technique to measure the displacement of a laterally moving MEMS actuator seems rather complicated.

A concept for an in-plane displacement sensor using optical waveguides is given in Fig. 8. A light source is connected to a waveguide. Simple V- or U-grooves enable the insertion of fibers into the Integrated Optics circuits and simplify alignment procedures.

An optical wave in a dielectric guide has an exponentially decaying evanescent field outside the waveguide. The length of the evanescent tail depends on the refractive index of the waveguiding structures (core and surrounding), polarization direction, wavelength and on the particular mode of the propagating light. Typically the decay length is in the order of the wavelength λ [27].

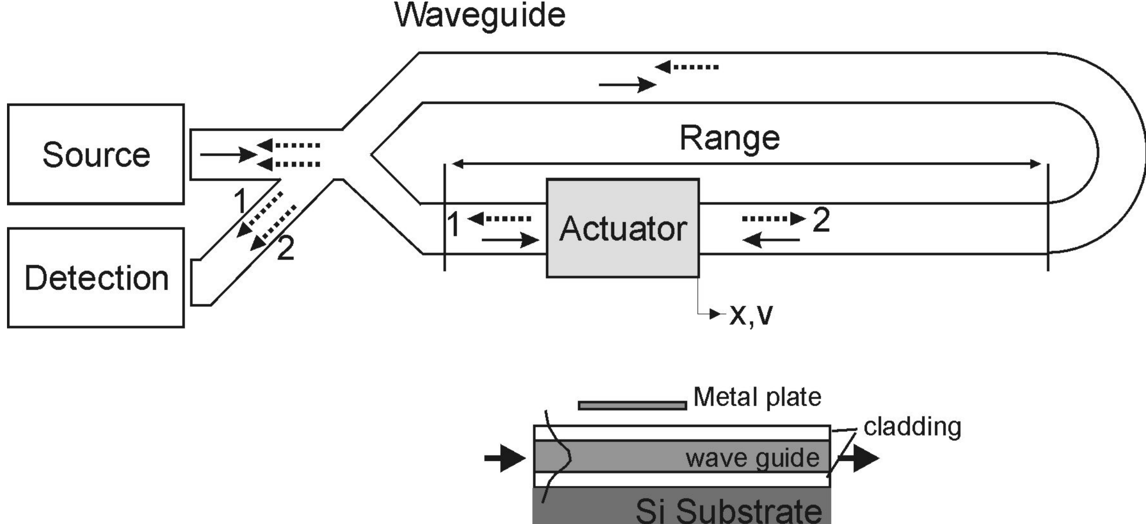

Fig. 8: Concept for a long-range displacement sensor based on integrated optical waveguides with a MEMS device.

A plate brought within the reach of the evanescent field (~ λ) of the waveguide core, imposes new boundary conditions on the propagating wave. This will modify the effective refractive index of the mode and cause reflections on both sides of the plate. Beyond the X-junction both reflections r1 and r2 will give an interference pattern at the photo detector input. The phase difference between reflections r1 and r2 is a measure of the difference in path lengths and hence of the position of the metal plate or actuator. With two reflections the influence of the temperature and humidity on the refractive index can be reduced or even eliminated. An example is given by Tabib-Azar [27] for a Mach-Zehnder displacement sensor which measures the deflection of a cantilever beam suspended above an optical waveguide. Another example of this concept of Evanescent Field Modulation is extensively described by Heideman and Lambeck [29] for a remote opto-chemical sensing with extreme sensitivity using a phase-modulated Mach-Zehnder interferometer system.

The given concepts, examples and references for optical displacement sensing are illustrative to make a decision based on the criteria given in Table 1.

Integration of optical waveguide sensors with electrostatic microactuator systems to detect in-plane long-range displacements is possible in principle but fabrication through micromachining technology is complex.

Interfacing with electronics is also a disadvantageous aspect because the light has to be converted to an electric signal. For some other sensing principles (e.g. capacitive) the electric signals are immediately available.

In terms of parallelism the optical sensing principle may be disadvantageous too. For example if 1000 medium scanners for a probe memory device have to be connected and aligned to an individual optical fiber, laser source and photo detector than this option may be less favorable than other sensing principles. The power consumption is indecisive. Probably a laser diode will dissipate more power than the other sensing principles.

2.2.3 Thermal displacement sensing

Thermal displacement sensing is another option to consider. Fig. 9 gives an example for a concept based on the change in resistance of a temperature dependent resistive heating element due to a change in heat flow. The heat flow Q_h is proportional to surface area and inversely proportional to the gap distance. A larger gap distance will decrease the heat flow, the heater temperature will increase and thus the heater resistance will increase.

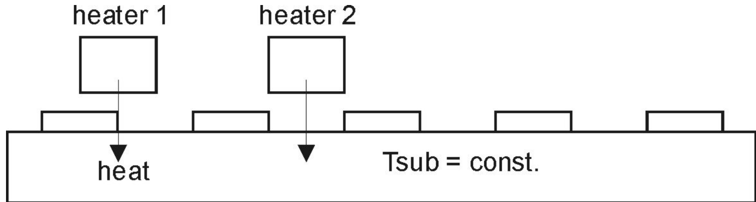

Fig. 9: Example of thermal displacement sensing concept based on a change in heat flow which results in changes in heater resistance.

The thermal sensing principle does not have the parasitic forces as present with capacitive sensing, only possible mechanical deformation effects due to thermal expansion. Similar to parasitic capacitance with capacitive sensing, the thermal sensing principle is always accompanied with parasitic effects e.g. changing heatsink temperature, heat leaks and drift. The obtainable speed is unclear. The thermo-mechanical probe-based sensing as seen with the earlier described Millipede [18,20] show fast time-responses. Also the thermal position sensor for a MEMS based x/y stage described by Pantazi [30] (see chapter 1) showed a position-error standard deviation of approximately 2 nm and a response time of 100 µs. i.e. bandwidth of 10 KHz. A DC drift of this sensor of less than 6 nm in 1 h is reported. However, in general thermal transducer principles are considered to be relatively slow principles. The power consumption is uncertain and likely to be higher than with the use of capacitive sensing.

2.2.4 Capacitive displacement sensing

The capacitive displacement sensing principle is a very well known principle with a long history [4]. Fig. 10 shows the most basic parallel-plate configurations used for displacement measurement. Ignoring electrostatic field fringing, the capacitance for two parallel plates much larger than the gap between them is given by:

$$C = \frac{\varepsilon_0 \cdot \varepsilon_r \cdot A}{g} \qquad \text{(Eq.2.3)}$$

With dielectric constant ε_0 for vacuum, relative dielectric constant ε_r, surface area A and gap distance g. The capacitive impedance is given by:

$$|Z| = \frac{1}{2\pi \cdot f \cdot C} \qquad \text{(Eq.2.4)}$$

Configuration a) is a changing gap capacitance. This configuration forms a non-incremental absolute measurement principle, as described in section 2.1.1.

The displacement range is limited compared to the change in area configuration b). However, the changing gap-configuration is relatively more sensitive than the changing area configuration [4].

With a three-plate configuration as in Fig. 8(b) a change in displacement of the pick-up plate gives a differential change in capacitance: $\Delta C_1 = - \Delta C_2$. The position for which $C_1 = C_2$ is taken as initial position. At this position, changes in geometry parameters due to temperature changes, do not introduce a zero error as long as $C_1 = C_2$. The initial output signal is zero at position $x = 0$ (because $\Delta C = 0$). Only differences in C_1 and C_2 are processed to an output signal without bias component as is present with the 2-plate configuration. Hence, the differential concept of a 3-plate configuration increases the dynamic measurement range relative to a 2-plate configuration.

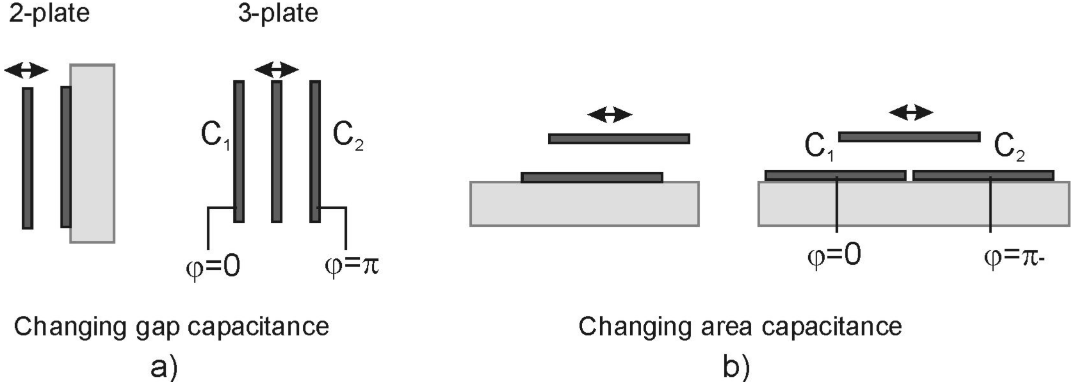

Fig. 10: Basic capacitive displacement sensing configurations. With a two plate configuration, changes in absolute capacitance are measured. Differential changes in capacitance can be measured with a three-plate configuration.

An example of a macro-world application using the 2-plate gap-closing configuration is the position sensor for the xyz-stages manufactured by companies as PI instruments [31] and Queensgate [32]. These stages are commonly used for various kinds of probe-based microscopy described in previous sections. These manufacturers report for their capacitive position sensors, resolutions of 0.01 nm over 1 mm range, extremely high long term stability of 0.1 nm/3 hours and bandwidth of 10 KHz. The nominal capacitance is ~ 10 pF. They use active guarding techniques to reduce the fringing fields. (i.e. stray capacitance) [1,4,32]. For three different sensor models the active surface area ranges from 17 to 113 mm^2 depending on the nominal gap and displacement range.

The design challenge for an ultrasensitive capacitive micrometer is to eliminate all unwanted environmental variations due to pressure, temperature and electric component changes and be able to detect very small variations of plate capacitance. For a 3-plate changing gap configuration Jones and Richards [33] have demonstrated in 1973 a detectable static displacement of 10^{-13} m and a corresponding resolution limited to 0.3 aF (0.3×10^{-18} F). However, this concept is very limited in range of motion. This is a common trade-off between high resolution and large-displacement range

For large-range displacement sensing, configuration b) with a changing area is regularly used as an absolute non-incremental displacement sensor. If this configuration is not accurate enough or the demands for dynamic range are too high, the configuration can be replicated many times with the addition of a counting circuit to count the plates or half periods.

Baxter [4] reports on various macro scale capacitive multiple plate systems which combine high resolution with long measurement range. A linear capacitive transducer described by Kosel [5] has a resolution of 4 pm and a 3 cm range. Zhu describes a capacitive multiple plate sensor with a resolution of 1 nm of over a meter. The common vernier caliper has a resolution of 2 $\times 10^{-4}$ mm and a 15 cm range. Klaasen and van Peppen [6] describe a printed circuit board realization of a multiple plate capacitive displacement sensor using a phase read-out technique. A resolution of better than 25 nm in a measurement span of about 1 cm and a non-linearity smaller than 2 µm is reported.

In an attempt for further miniaturization, Pedrocchi et al [34] describe a novel capacitive position micro sensor based on a multiple plate sensor with phase detection. A PC board 10x model for a long-range micromachined capacitive position sensor was demonstrated with an optimized pitch to spacing ratio. Measurement results were limited by Johnson (thermal) noise to 63 nm sensitivity. Because of the geometry of the capacitance this concept suffers from out-of-plane forces.

Fig. 1 depicts two basic operation modes for comb-structures, commonly used in MEMS as actuator and as sensor. Configuration c) corresponds to a changing gap capacitance as given earlier. This configuration can be very sensitive but it is limited in range and is found e.g. in accelerometers. Configuration d) corresponds to the change in area configuration b) in Fig. 10.

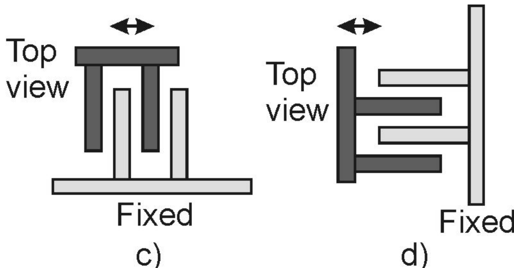

Fig. 11: Examples of comb-structures operated in changing gap mode or changing area mode. These structures are commonly used in MEMS.

Cheung et al [35] and Legtenberg [36] have used micromachined comb-sensors to detect displacements. Comb-sensors are however not incremental and therefore always limited in dynamic sensing range i.e. ratio of range over resolution. Cheung was able to measure lateral positions with 0.01 µm estimation error using Kalman state-variable feedback control. Legtenberg measured a linear change $\Delta C/\Delta x \approx 2.67$ [fF/µm] with initial capacitance $C_{comb} \approx 300$ fF ($\Delta C_{max} \approx 80$ fF) over a deflection range of 30 µm.

Kung et al [37] have reported an air-gap-capacitor pressure sensor with integrated NMOS circuits where a 100 fF air-gap-capacitor could be measured with a resolution of less than 30 aF and several nm of deflection.

A capacitive sensing principle seems most favorable in terms of obtainable accuracy, displacement range, and compatibility of the micromachining and fabrication process, the wide range of interfacing possibilities and electronic signal manipulation and the

potential for parallelism. A less favorable property of capacitive sensors is the occurrence of parasitic electrostatic forces between sensor plates and the ever present parasitic capacitances. These effects can sometimes be reduced or compensated with special techniques [4]. Ultimately the resolution is limited by noise and stability.

Using repetitive patterns with periods down to e.g. 8 micrometer and combined with quadrature detection, 2 micrometer periodicity is obtained. Hence the dynamic range requirement of 10^5 (X_{max} = 100 µm / δx =1 nm) is reduced to P/δ_x, by a factor of 50. The required bandwidth is of course related to the maximum speed of the microactuator. If the incremental sensor generates a sensor signal with a period size of P_x = 8 µm, a velocity of e.g. v = 50 mm/s would mean a required bandwidth of v / P_x = 6.5 KHz. Possibly even more because detection of the higher order harmonics can be important too.

2.3 DIGITAL MICROACTUATOR DISPLACEMENT

A different approach could be to digitize the microactuator displacement as is done with the so called MicroElectroMechanical Digital-to-Analog converter (MEMDAC) [38,39]. This is a novel micromechanism for precise positioning by using an N-bit digital code. The mechanism is an N-stage network of connected suspensions connected with electrostatic actuators. The N-bits of local displacement accumulate in the suspension network to synthesize an analog output, which is proportional to the analog value coded with the N-bit input. The output displacement is independent of the fluctuation of the driving voltage since the traveling distance of the shuttle is clipped by mechanical stoppers.

Toshiyoshi successfully demonstrated with a 4-bit MEMDAC with a total stroke of 5.8 µm and a step of 0.38 µm with less mechanical nonlinearity than a MEMDAC developed by Yeh [40]. The positioning resolution of an 8-bit MEMDAC is expected to be as small as 20 nm. The total stroke can be expanded, but it degrades the positioning resolution unless the number of bits is increased in accordance. The fundamental mechanical resonance was found to be in the range of 2–10 kHz depending upon the input code, the load and the generated force.

However, digitizing a displacement range of 100 µm into an N-bits code seems not very favorable in terms of accuracy, dynamic properties and the aim for nanopositioning.

2.4 CONCLUSION

It is decided to further investigate the combination of a capacitive incremental position sensing principle and an electrostatic microactuator. The combination of fabrication, electronics, parallelism and accuracy, range and speed appears to be favorable to achieve the target specifications of range (~100 µm) and accuracy (1-10nm). A drawback may be the presence of electrostatic forces and parasitic capacitances.

In the next chapter two related concepts for a micromachined integrated capacitive incremental position sensor will be given. The concepts are based on the change in capacitance for a relative displacement between 2 periodic geometries. Analysis will be given of the SNR for the two concepts. Furthermore, an investigation is given of possible

limitations or drawbacks due to electrostatic forces and thermal electrical and mechanical noise. Also the possibilities reported in literature for the measurement of small capacitances and the reduction or elimination of afflicting parasitic capacitances is evaluated.

References

[1] T.R.Hicks, P.D. Atherton, The nano positioning book, Queensgate instruments, Penton Press, 1997

[2] P.P.L.Regtien, F. van der Heijden, M.J.Koster, W.Olthuis, Measurement Science for Engineers, Kogan Page Science, London, UK; August 2004

[3] J.Fraden, Handbook of Modern Sensors, physics, designs and applications, Spinger-Verlag, New York, 1996

[4] L.K.Baxter et al., *Capacitive Sensors: Design and Applications*, IEEE Press, New York, 1997.

[5] P.B.Kosel, G.S.Munro, R.Vaughan, Capacitive Transducer for Accurate Displacement Control, IEEE Trans. On Instrumentation and Measurement, (IM-30),2,114, June 1981

[6] K.B.Klaassen, J.C.L.van Peppen, Linear capacitive microdisplacement transduction using phase read-out, Sensors And actuators, 3, 209-220, 1982/83

[7] www.opticalencoder.com

[8] www.GlobalSpec.com

[9] T.Ohara (NanoWave Inc., USA), Scanning Probe Position Encoder (SPPE) – a new approach for a high precision and high speed position measurement system, Proceedings of the SPIE - The International Society for Optical Engineering, v 4344, 2001, p 552-61

[10] G.Binnig, H.Rohrer, Scanning Tunneling Microscopy, IBM J. of Res. And Dev., 44, 279-293, 2000

[11] T.R.Albrecht, Advances in Atomic Force Microscopy and Scanning Tunneling Microscopy, Dissertation, Stanford University, California, USA, June 1989

[12] Nyffenegger RM, Penner RM, Schierle R, Electrostatic force microscopy of silver nanocrystals with nanometer-scale**,** Appl. Phys. Lett., 71 (13): 1878-1880, 1997

[13] F.Meli, R.Thalmann, Long-range AFM profiler used for accurate pitch measurements, Meas.Sci Technol.,(**9**),1998, 1087-1092

[14] Restagno F., J.Crassous, E.Charlaix, M.Monchanin, A new capacitive sensor for displacement measurement in a surface force apparatus, Meas.Sci.Technol., 12, 16-22, 2001

[15] J.R.Matey, J.Blanc, Scanning capacitance microscopy, J.Appl.Physics, 57,(5) 1985

[16] H.M.Pollock, A.Hammische, Micro-Thermal analysis: techniques and applications, J.Phys.D: Appl.Phys., 34, p23, 2001

[17] L.R.Carley, J.A.Bain, G.K.Fedder, D.W.Greve, Guillou D.F., M.S.C. Lu, T.Mukherjee, S.Santhanam, L.Abelmann, S.Min, J.Appl.Phys., 87, 6680, 2000

[18] P. Vettiger, M. Desmont, U.D. Drechsler, U.H. Ürig, W. Äberle, M.I. Luwyche, H.E. Rothuizen, R. Stutz, R.Widmer and G.K.Binnig, The “Millipede” – More than one thousand tips for future AFM data storage, IBM J.Res.Dev. 44 (3), 323-340,2000.

[19] P. Vettiger, M. Desmont, U.D. Drechsler, U.H. Ürig, W. Äberle, M.I. Luwyche, H.E. Rothuizen, R. Stutz, R.Widmer and G.K.Binnig, The "Millipede" – More than one thousand tips for future AFM data storage, IBM J.Res.Dev. 44 (3), 323-340,2000.

[20] A. Pantazi, M.A. Lantz, G. Cherubini, H. Pozidis and E.Eleftheriou, A servomechanism for a micro-electromechanical-system-based scanning-probe data storage device, Nanotechnology, (15), S612–S621, 2004

[21] S.C.Eagle, G.K.Fedder, Writing nanometer-scale pits in sputtered carbon films using scanning tunneling microscope, Appl.Phys Lett., 74, 25, 1999

[22] R.C.Barrett, C.F.Quate, Charge storage in a nitride-oxide-silicon medium by scanning capacitance microscopy, J.Appl.Phys., 70 (5), 2725,1991

[23] C. Liu, A. Barzilai, J. Reynolds, A. Partridge, T. Kenny, J. Grade, H. Rockstad, "Characterization of a high-sensitivity micromachined tunneling accelerometer with micro-g resolution", J. Micro. Elect. Mech. Syst., Vol-7, 1998, pg 235-244

[24] M.A. McCord, A. Dana and R.F.W. Pease, "The micromechanical tunnelling transistor", J. Micromech. Microeng., Vol-8, 1998, pg 209-212

[25] P.Hariharan, Basics of Interferometry, Academic Press Inc., San Diego, USA,1992

[26] Y.H.Cho, W.C.Lee, K.H.Han, Fabrication Uncertainty and Noise Issues in High-Precision MEMS Actuators and Sensors, J.of Semiconductor Technology and Science, 2,280,2002

[27] M.Tabib-Azar, Microactuators, electrical, magnetic, thermal, optical, mechanical, chemical and smart structures, Kluwer Academic Publishers, 1998

[28] S.Ura, T. Endoh, T.Suhara, H.Nishihara, Integrated optic head for sensing a two-dimensional displacement of a grating scale, Applied optics, 35, 31, 6261, 1996.

[29] R.G.Heideman, P.V.Lambeck, Remote opto-chemical sensing with extreme sensitivity: design, fabrication and performance of a pigtailed integrated optical phase-modulated Mach-Zehnder interferometer system, Sens. And Act. B, 61, 100-127,1999.

[30] A Pantazi,MA Lantz, G Cherubini, H Pozidis and E Eleftheriou, A servomechanism for a micro-electromechanical-system-based scanning-probe data storage device, Nanotechnology, (15), S612–S621, 2004

[31] http://www.physikinstrumente.de/products/ c) 2004

[32] http://www.nanopositioning.com/products/NanoSensors/specification.aspx, c) 2003

[33] R.V.Jones, J.C.S.Richards, The Design and some Applications of Sensitive Capacitance Micrometers, J.of Physics E: Scientific Instruments 6: 589-600.

[34] A.Pedrocchi, S.Hoen et al, Perspectives on MEMS in Bioengineering: A novel Capacitive Position Micro-sensor, *IEEE Trans. Biomedical Eng*., **47-**1, 8-11, 2000.

[35] P.Cheung, R.Horowitz, Design, Fabrication, Position Sensing and Control of an Electrostatically-driven Polysilicon Microactuator, *IEEE Trans. Magnetics*, **32-**1, 122-128, 1996.

[36] R.Legtenberg, A.W.Groeneveld, Towards Position control of electrostatic comb drives, *Proc. Micromech. Microeng. (MME'95)*, Copenhagen, 3-5 Sept., 1995.

[37] J.T.Kung, H.S.Lee, An integrated Air-Gap-Capacitor Pressure sensor and digital readout with sub-100 attofarad resolution, *J. of MEMS*, **1**(3), 121-128, 1992.

[38] H. Toshiyoshi, D. Kobayashi, M. Mita, G. Hashiguchi, H. Fujita, J. Endo, Y. Wada, Microelectromechanical Digital-to-Analog Converters of Displacement for Step Motion Actuators, J. of MEMS, (9),no. 2, June 2000

[39] H.Fujita, Microactuators and micromachines, Proc. IEEE, 86, 8, 1721-1732, Aug.1998,

[40] R. Yeh, R. A. Conant, and K. S. J. Pister, "Mechanical digital to analog converters," in 10th Int. Solid-State Sens. Actuators Conf., Sendai, Japan, June 7–10, 1999, 998–1001.

3 Capacitive Incremental Position Sensor for Microactuators

3.1 INTRODUCTION

In the previous chapter the motivation for a capacitive sensing principle was given. We will investigate a capacitive position sensor integrated with a micromachined electrostatic microactuator to facilitate nano-positioning through nano-position sensing. The aim is to investigate a position sensor with nanometer accuracy over a displacement range of 50-100 micrometers. To achieve this while keeping the demands on the dynamic sensing range of the sensor modest, a combination of discrete (counting) and analog measurement techniques is investigated i.e. a incremental position sensor [1,2,3,4,5,6]. The advantage of this incremental sensing concept is that the desired position accuracy is decoupled from the range of motion of the actuator that is used for generating displacements.

In the next section a novel incremental capacitive position sensor is presented based on two related concepts explained in the next section:

- Incremental Capacitance Measurement Mode ICMM (Open-Loop)
- Constant Capacitance Measurement Mode CCMM (Closed-Loop)

In fact both concepts are incremental position sensors based on the measurement of (changes in) capacitance between two periodic geometries as a function of their relative displacement. The CCMM concept is expected to have a higher signal-to-noise ratio (SNR) than the ICMM concept. The sensor capacitance in the CCMM concept is held at a constant larger value and therefore gives a larger signal. For the same level of noise this means, a larger SNR is acquired.

Of course the aim in this work is to implement these concepts into a MEMS device and assess the quality of operation through experiments and preferably characterization. Therefore, the necessary steps are:

- to analyze the concepts and compare them in terms of expected SNR, expected periodic change in capacitance and the shape of the change in capacitance as a function of displacement for different combinations of periodic geometries.
- to develop the measurement methods for (small) capacitances with a strong focus on a possible integration of these concepts with a MEMS device
- to fabricate and integrate these sensors with a test device enabling the exploration of the performance of the designed capacitive position sensors.
- to develop an experimental setup and perform measurements in order to assess the functioning and performance of the designed incremental position sensor for microactuator systems

In this chapter are presented and analyzed, the concepts ICMM and CCMM for an incremental position sensor, an analysis to estimate the SNR for both concepts, the possible technique to measure the change in capacitance and detect displacement or position and the estimated limits for position detection in the presence of noise.

3.2 BASIC PERIODIC CAPACITIVE SENSING STRUCTURE

This section presents two concepts for a capacitive incremental position sensor. Both concepts are based on the change in capacitance between two periodic geometries for a relative displacement between the two. This principle is depicted in Fig. 1. Both slider and sense-structures have opposing periodic patterns. It is the position (x) of the slider that has to be measured by measuring the periodic change in capacitance $\Delta C_s(x)$. The sense-structures are driven by additional actuators and can move in y-direction only in order to decrease (but not close) the air-gap between the two geometries on slider and sense-structure and increase the (change in) capacitance between the two geometries (i.e. similar to the fact that decreasing the gap of a parallel plate capacitor would increase its capacitance).

The aim is to integrate this position sensing principle with a micromachined microactuator. Because it is instructive for the rest of the thesis, two examples of a realized device are given in Fig. 2 in advance.

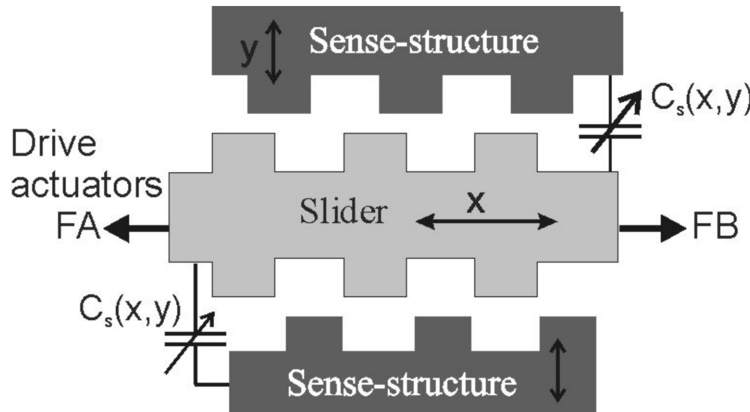

Fig. 1: Concept of the capacitive long-range incremental position sensor.

3.2.1 Incremental Capacitance Measurement Mode ICMM

In the Incremental Capacitance Measurement Mode ICMM (open-loop), the capacitance between slider and sense-structure changes periodically as the slider-beam moves (x-direction). By counting the number of periods as well as measuring the change in capacitance within one period, in principle a (infinitely) long-range position measurement is obtained with high resolution and high accuracy i.e. an incremental position sensor. Additional sense-actuators (comb-drives) are used to reduce the design-gap between slider and sense-structure, only once before the actual measurement operation starts, thus, increasing the capacitance $C_s(x)$ and capacitance variation $\Delta C_s(x)$ (i.e. $C_s(x) = C_{min} + \Delta C_s(x)$).

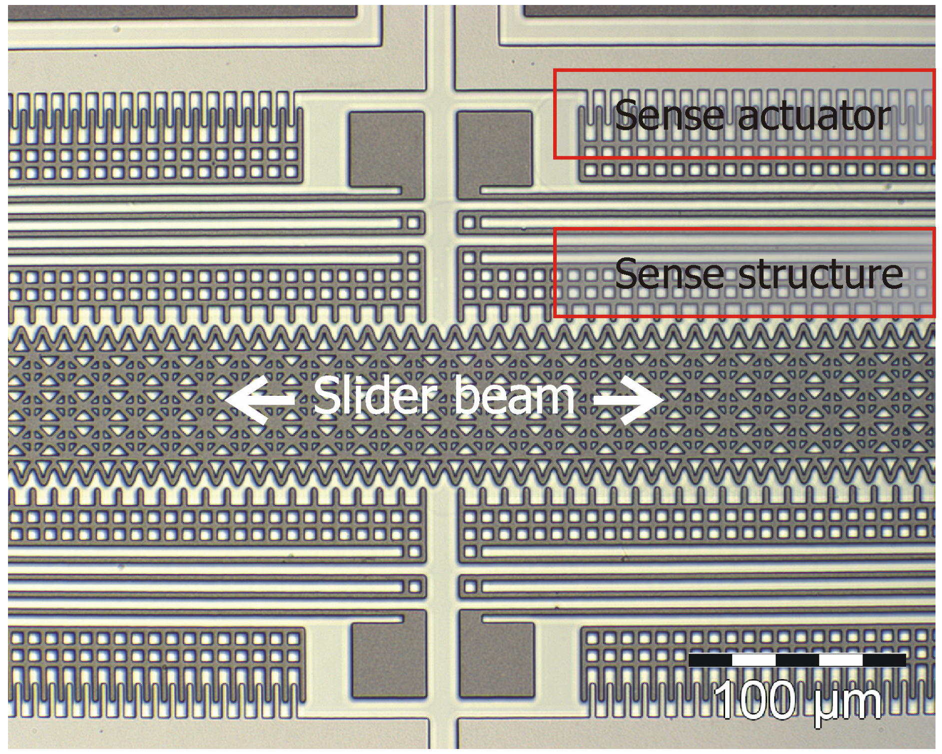

Fig. 2: Micromachined capacitive incremental position sensor. As the slider beam moves, the capacitance between opposing periodic patterns on the slider and the sense structure changes.

3.2.2 Constant Capacitance Measurement Mode CCMM

In Constant Capacitance Measurement Mode (CCMM) the sense-actuators are closed-loop controlled in order to keep the capacitance C_s constant, equal to a setpoint value C_{setp}. (i.e. $C_s = C_0$, $\Delta C_s = 0$). As a result the sense-structures will move in y-direction, closely following the pattern on the slider. The required sense-actuator voltage (i.e. the control voltage $U_{control}$, in short $U_c(x)$) will have the same period as the periodic geometry and becomes a measure for the slider displacement i.e. $U_c(x)$. This method is expected to give a better signal-to-noise ratio (SNR), because for all positions within a period the sensor-capacitance is kept at a larger constant value than is possible with open-loop operation.

3.2.3 Estimation of SNR for ICMM and CCMM

In the following part a derivation is given to estimate the increase in signal-to-noise ratio (SNR) for the CCMM concept over the ICMM concept, see Fig. 3.

- In the ICMM concept the capacitance between geometries S1 and S2 changes periodically for a relative displacement (x) between S1 and S2 and the gap y_0 is made smaller only once prior to the measurement operation.
- In the CCMM concept the periodic geometry S2 is displaced in y-direction for every x-position to keep the capacitance $C(x,y)$ equal to a setpoint value i.e. $C(x,y) = C_{set}$ or more precise $C(x,y(x)) = C_{set}$.

In practice the situation given in Fig. 3 will be in between two extremes depicted in Fig. 4. As a first order approximation a correspondence with the probe-like capacitance model in Fig. 4 is assumed. Only the distance $d(x)$ between the tip or fingers and the geometry S1 is

important if the width of the fingers is small with respect to the period size. For the probe-like geometry in Fig. 4, the ratio of the width of the tip (3D) or plate (2D) to the distance d between probe and plate is infinitely small ($w/d \rightarrow 0$), the field intensity will be mostly non-uniform and concentrated between tip and the bottom surface area (plate) and the shape of the probe, rounded or rectangular is not important anymore. If the fingers in Fig. 3 have a certain limited width then continuously decreasing the gap d will end up with a situation depicted by the parallel plate-like geometry in Fig. 4. The field intensity will be mostly uniform and concentrated between top plate and bottom plate. Here, the average width d_{mean} is important if the top or bottom surface is curved or under an angle.

So the assumption of probe like dimensions in Fig. 3 means for ICMM that the ratio of period size P_x over the width of the fingers w (i.e. $\alpha = P_x/w >> 1$) is large and for CCMM an additional assumption is that finger length ℓ_f is much larger than the amplitude of geometry S1 i.e. $\ell_f >> 2A$.

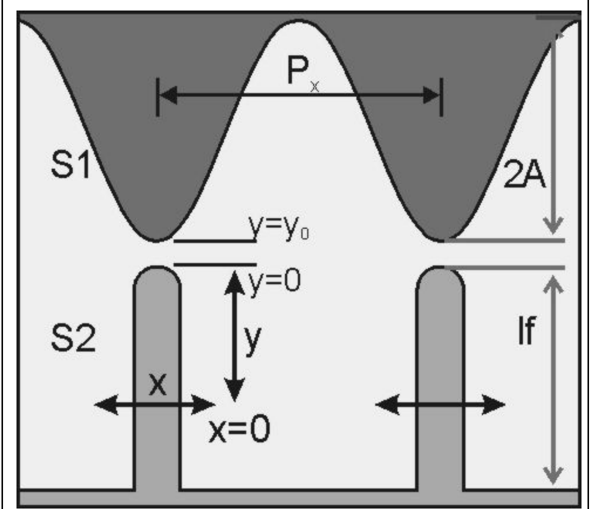

Fig. 3: In constant capacitance mode, the periodic geometry S2 with rounded fingers is moved in *y*-direction for every x-position to keep the capacitance *C(x, y(x)) = Cset.*

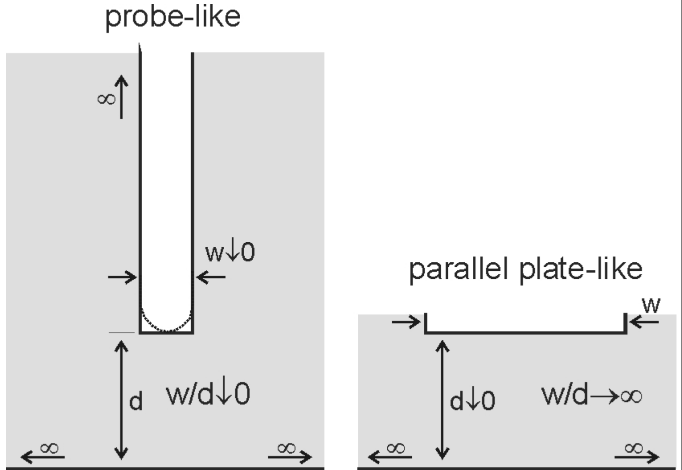

Fig. 4: A probe-like capacitance and a parallel plate-like capacitance; Two basic capacitance models are considered as two extreme situations, with in between the model for a more practical situation in Fig. 3

For the capacitance in ICMM (open-loop) between geometry S1 and S2 assuming probe-like dimension ratios the expression is:

$$C(x) = C_p + \frac{C_0}{y_0 + A(1 - \cos kx)}, \quad C_0 = [Fm], k = \frac{2\pi}{P_x} \qquad \text{(Eq.3.1)}$$

The parasitic capacitance Cp is included because in practice this capacitance will always be present and unknown. For position detection only the change in capacitance ΔC versus displacement (x) is relevant, assuming constant parasitic capacitance C_p.

$$\Delta C(x) = \frac{C_0}{y_0 + A(1 - \cos kx)} \qquad \text{(Eq.3.2)}$$

Any noise contribution δC leads to a finite Signal-to-Noise ratio (SNR$_c$).

$$\Delta C(x) = \frac{C_0}{y_0 + A(1 - \cos kx)} \cdot \frac{1}{\delta C} \quad \text{(Eq.3.3)}$$

Taking the amplitude of ΔC gives for the SNR for ICMM:

$$S/N_c = \frac{\Delta C}{\delta C} = \left[\frac{C_0 \cdot A}{y_0 \cdot (y_0 + 2A)}\right] \cdot \frac{1}{\delta C} \quad \text{(Eq.3.4)}$$

In CCMM the geometry S2 is moveable in y-direction by an additional comb-drive actuator. For a comb-drive actuator the displacement y is proportional to the square of the applied voltage U. This means that reducing the gap between S1 and S2 will increase the capacitance. The capacitance between S1 and S2 becomes:

$$C(x, U_c) = C_p + \frac{C_0}{y_0 + A(1 - \cos kx) - KU_c^2},$$
$$C_0 = [Fm], k = \frac{2\pi}{P_x}, K = [m/V^2] \quad \text{(Eq.3.5)}$$

Suppose a setpoint is taken at position $x = P_x/4$:

$$C_{setp}(x = \frac{P_x}{4}, U_c = U_r) = C_p + \frac{C_0}{y_0 + A - KU_{set}^2} \equiv C_{set} \quad \text{(Eq.3.6)}$$

and for the voltage U_{set} for which the capacitance $C(P_x/4, U_r) = C_{set}$:

$$U_{set}^2 = \frac{1}{K}\left[y_0 + A - \left[\frac{C_{set} - C_p}{C_o}\right]^{-1}\right] \quad \text{(Eq.3.7)}$$

For position detection the control-voltage $U_c(C_{set}, x)$ is needed. For an arbitrary position $0 < (x) < P_x$, U_c is such that $C(x, U_c) + C_p = C_{set}$:

$$\frac{C_0}{y_0 + A(1 - \cos kx) - KU_c^2} + C_p = C_{set} \quad \text{(Eq.3.8)}$$

Thus, we can write for the voltage U_c:

$$U_c^2 = \frac{1}{K}\left[y_0 + A(1 - \cos kx) - \left[\frac{C_{set} - C_p}{C_o}\right]^{-1}\right] \quad \text{(Eq.3.9)}$$

The voltage change $\Delta U_c(x)$ is the difference between $U_c(x)$ and U_{set} Combination with

Eq.3.7 gives an expression for the change in voltage $\Delta U_c(x)$ versus displacement (x), where in the derivation a term ΔU_c^2 is neglected:

$$U_c^2 - U_{set}^2 \approx 2 \cdot \Delta U_c(x) \cdot U_{set} = \frac{1}{K}\left[-A\cos kx\right]$$
$$\Delta U_c(x) = \frac{1}{2KU_{set}}\left[-A\cos kx\right] \qquad \text{(Eq.3.10)}$$

Equation Eq.3.10 shows that the change in control voltage will have the same shape as the periodic geometry S1.

A disturbance of the capacitance with δC due to noise, or changes in humidity or temperature will lead to a change in voltage ΔU_c with δu to compensate the change δC.

$$U_c^2 = (U_{set} + \Delta U_c(x) + \delta u)^2 = \frac{1}{K}\left[y_0 + A(1 - \cos kx) - \left[\frac{C_{set} - C_p - \delta C}{C_o}\right]^{-1}\right] \qquad \text{(Eq.3.11)}$$

Neglecting a term δu^2 in (Eq.3.11), U_c^2 is written as:

$$U_c^2 \approx U_{set}^2 + 2\Delta U_c(x) \cdot U_{set} + 2\delta u \cdot U_{set} =$$
$$= \frac{1}{K}\left[y_0 + A(1 - \cos kx) - \left[\frac{C_o}{C_{set} - C_p - \delta C}\right]\right] \qquad \text{(Eq.3.12)}$$

With a Taylor approximation for the last term in (Eq.3.12) as a function of δC we get:

$$U_c^2 \approx U_{set}^2 + 2\Delta U_c(x) \cdot U_{set} + 2\delta u \cdot U_{set} =$$
$$= \frac{1}{K}\left[y_0 + A(1 - \cos kx) - \left[\frac{C_o}{C_{set} - C_p}\right] - \left[\frac{C_o}{(C_{set} - C_p)^2} \cdot \delta C\right]\right] \qquad \text{(Eq.3.13)}$$

and combination of (Eq.3.13) with (Eq.3.7), (Eq.3.8) and (Eq.3.10) gives:

$$U_c^2 - U_{set}^2 = +2\Delta U_c(x) + 2 \cdot \delta u = \frac{1}{K \cdot U_{set}}\left[-A\cos kx - \left[\frac{C_o}{(C_{set} - C_p)^2} \cdot \delta C\right]\right] \qquad \text{(Eq.3.14)}$$

Therefore, the additional voltage δu_c to compensate a change in capacitance by δC by disturbance or noise can be written as:

$$\delta u_c = \frac{1}{2K \cdot U_{set}}\left[\frac{C_o}{(C_{set} - C_p)^2} \cdot \delta C\right] = \frac{1}{2K \cdot U_{set}}\left[\frac{\left(y_0 + A - KU_{set}^2\right)^2}{C_o} \cdot \delta C\right] \qquad \text{(Eq.3.15)}$$

The S/N_u ratio for CCMM with the amplitude ΔU_c in Eq.3.10 and Eq.3.15 is given by:

$$S/N_u = \frac{\Delta U_c}{\delta u_c} = \frac{\frac{1}{2KU_{set}}[A]}{\frac{1}{2KU_{set}}\left[\frac{C_o}{(C_{set}-C_p)^2}\cdot\delta C\right]} = \tag{Eq.3.16}$$

$$= \frac{[A]\cdot(C_{set}-C_p)^2}{C_o\cdot\delta C} = \frac{[A]\cdot\left[\frac{C_0}{y_0+A-KU_{set}^2}\right]^2}{C_o\cdot\delta C}$$

The final expression for the SNR for CCMM becomes (SNR_u):

$$S/N_u = \frac{\Delta U_c(x)}{\delta u_c} = \frac{[A]}{\left(y_0+A-KU_{set}^2\right)^2}\cdot\frac{C_0}{\delta C} \tag{Eq.3.17}$$

In the following part an estimation is given for the SNR improvement of CCMM in comparison with ICMM. The ratio between the SNR_c for ICMM (Eq.3.4) and the SNR_u for CCMM (Eq.3.17) is:

$$\frac{S/N_u}{S/N_c} = \frac{y_0\cdot(y_0+2A)}{\left(y_0+A-KU_{set}^2\right)^2} \tag{Eq.3.18}$$

For x=0, amplitude A = 4 [µm], y_0 = 2 [µm], and a controlled gap between geometry S1 and S2 of $g = y_0 + A - K\cdot U_{set}^2 = 0.25$ [µm], gives an improvement of SNR_u for CCMM of ~320x SNR_c for CCMM.

To conclude this analysis, the following conclusions are drawn:

- From the expression in (Eq.3.17) it can be concluded that the Signal-to-Noise Ratio (SNR) is increased when (apart from minimizing δC)
    1) The amplitude A of the periodic geometry S1 is large, and the term C_0 which includes the structure height h is large
    2) $KU_{ref}^2 \sim y_0 + A$

- Parameter K is not really important for the SNR but a larger K means a lower U_{set} is necessary for a certain displacement y. For the dynamic response the value of K is naturally very important.
- More importantly, it is repeated that with closed-loop Constant Capacitance Measurement Mode the shape of the geometry S1 is reflected in the control voltage U_c as expressed by equation (Eq.3.10) and ideally, geometry S1 would be pure sine or triangular shaped. The periodic change in control voltage U_c becomes a measure for the relative displacement *(x)*.

3.3 QUADRATURE DETECTION

So far the desired shape of $\Delta C_s(x)$ for ICMM or of $U_c(x)$ for CCMM has not been discussed apart from the periodicity. Either a pure sine or a triangular shaped detection signal as given in Fig. 5 would be interesting and favourable as discussed in the previous chapter. However, if for CCMM the control voltage $U_c(x)$ would be a triangular signal this would mean, the sense-structures would have to respond to an impulse-function at the positions of discontinuous differential change in $U_c(x)$ i.e. the peak-amplitudes of the triangular functions. In practice the peaks will be rounded and thus an impulse function will be rather theoretical. However, since any periodic signal can be written as an infinite Fourier Series, one could say that the triangular signal functions contain much more (infinitely) higher order harmonics than pure sine-signal functions. Looking at it in this way, sine-shaped detection signals may be considered as favourable because, they reduce the demands for required bandwidth for the sensor electronics and the dynamic mechanical response of the sense-structures.

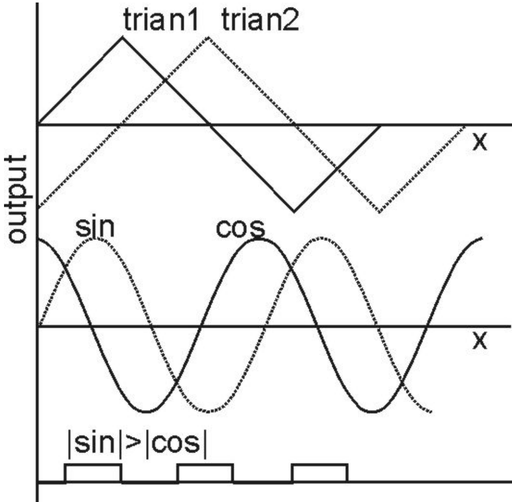

Fig. 5: Both triangular and sine signals can be used for quadrature position detection with interpolation between counts. Commonly, an arctan calculation is used.

The displacement can be detected using (Eq.3.19) [1]:

$$x = arctan\left[\frac{sin(x)}{cos(x)}\right] \quad if\ |sin| < |cos|$$

$$x = \frac{\pi}{4} - arctan\left[\frac{cos(x)}{sin(x)}\right] \quad if\ |sin| > |cos| \qquad \text{(Eq.3. 19)}$$

For multiple plate capacitive sensors this technique works well since the analog outputs are quite stable while optical encoders with light source aging, dust, and photodevice tolerances can make analog interpolation inaccurate [1, 3]. However, the electronics for these signals must be designed carefully to avoid miscounts which can happen if noisy edges are present [1, 7].

3.4 POSSIBLE CAPACITANCE MEASUREMENT METHODS

As explained in detail in [8] to measure capacitance changes, two techniques are commonly used:

- In a bridge configuration capacitance changes just like resistance changes can be measured
- In a sinusoidal or relaxation oscillator circuit the capacitance change can be used to control the oscillation frequency

Simple oscillator circuits producing an output frequency which is dependent on a capacitor value are quite frequently used in. e.g pressure sensors [9], accelerometers [10], load cells [11]

In general, the difficulty with oscillator circuits is that (changing) parasitic capacitances can directly change the frequency. However, Toth and Meijer (12,13) employ a modified martin oscillator where all additive and multiplicative errors due to non-idealities and temperature dependencies in the circuit have been eliminated. Only nonlinearity and random errors remain.

The accuracy of the modified martin oscillator for the high capacity load cell sensor reported by Zwijze [11] was limited by the variation in the amplitude of square wave driving signals and by the steepness of the side edges of these driving signals.

Therefore, sinusoidal signals are preferred, but sinusoidal oscillators are much harder to realize such that they are independent of parasitic capacitance.

A standard Wheatstone bridge is often used for low noise instrumentation [1]. To measure capacitors an alternating supply has to be used with a capacitance bridge configuration and usually results in a very simple circuit. This technique can also be integrated on the sensor die.

Baxter [1] reports that the most flexible and accurate method of measuring capacitance is to first apply a high frequency signal in the 10KHz – 1 MHz range through a known impedance to the capacitor under test (i.e. C_{sens}). The signal (current) is amplified and converted to voltage and applied to a synchronous demodulator which produces a DC-level signal U_{out} after low-pass filtering. The voltage Uout is proportional to the capacitance C_{sens} and the change in capacitance ΔC_{sens}. The higher the frequency, the lower the capacitive impedance as can be seen from the equation for a capacitive impedance:

$$|Z| = \frac{1}{2\pi f C_{sens}} \quad ,$$

The lower the capacitive impedance, the more current will go through C_{sens}, the higher the DC-ouput voltage of the synchronous demodulator will be.

The circuit in Fig. 6 is based on a capacitance bridge and shows a simple capacitive voltage divider, a charge amplifier, a synchronous demodulator (multiplier/mixer) and a low-pass filter.

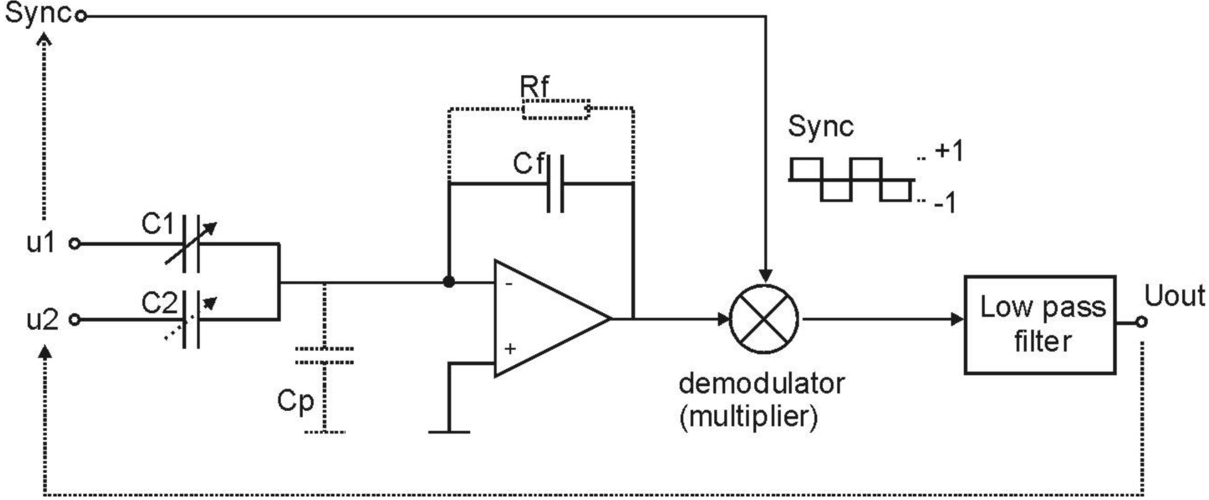

Fig. 6: Basic Synchronous demodulator circuit with a charge-amplifier and two sensor capacitances C_1 and C_2

With voltage $u_2 = - u_1$ the capacitive voltage divider formed by elements C_1,C_2, is driven symmetrically. The shape of u_1 and u_2 is not important, usually a square wave signal is used, but for high frequency excitation (above 1 MHz) sine wave signals are preferred because of better amplifier performance.
For the capacitive voltage divider, neglecting the parasitic capacitance C_p the output voltage is given by:

$$U_{cvd} = \left(\frac{2 \cdot C_2}{C_1 + C_2} - 1 \right) \cdot U_1 \qquad \text{(Eq.3. 20)}$$

With a differential change in capacitance ($C_1 = C - \Delta C$, $C_2 = C + \Delta C$) the output voltage is given by:

$$U_{cvd} = \left(\frac{\Delta C}{C} \right) \cdot U_1 \qquad \text{(Eq.3. 21)}$$

Usually in micromachined devices the sensor capacitances are very small and the influence of parasitic capacitance C_p cannot be neglected.

The charge amplifier consists of an operational amplifier (OPAMP) with a feedback capacitor C_f. Resistance R_f is required to define the dc output voltage and should be significantly larger than the impedance of capacitor C_f (i.e. Z_f = 160 KΩ) for a signal frequency of 1 MHz.

In principle the OPAMP will adjust the output voltage such that the differential input voltage and the voltage across parasitic capacitance C_p remains virtually zero i.e. the – input becomes a virtual ground potential. Thus C_p is effectively eliminated.
The output voltage of the charge-amp is (in first order with ideal OPAMP) given by:

$$U_{ca} = \left(\frac{C_2 - C_1}{C_f} \right) \cdot U_1 \qquad \text{(Eq.3. 22)}$$

Or for a differential change in capacitance ($C_1 = C - \Delta C$, $C_2 = C + \Delta C$):

$$U_{ca} = \left(\frac{2\Delta C}{C_f} \right) \cdot U_1 \qquad \text{(Eq.3. 22}_b\text{)}$$

The synchronous detection circuit is used to eliminate noise and drift from the amplifier. The output of the amplifier is multiplied by a square wave (Sync) with the same frequency and in phase with the input signal and subsequently low-pass filtered. With the first harmonic of the square wave as an example the output of the LP-filter becomes:

$$U_{out} = \frac{1}{T} \int_0^T A\,cos(\omega t) \cdot \left(cos(\omega t + \phi) \right) dt = \frac{A}{2} cos(\phi) \qquad \text{(Eq.3. 23)}$$

with phase shift ϕ between input signal $A \cdot cos(\omega t)$ and the first harmonics of the square wave $cos(\omega t + \phi)$. For maximum DC output signal, ϕ should be 0 or π [rad]. Therefore, the phase of the square wave or the synchronizing signal (SYNC) is adjusted, sometimes automatically, to compensate any phase difference between the sync-signal and the input of the demodulator.

For the demodulator circuit in Fig. 6, positive and rectified negative half-cycles of the signal will contribute to the output DC level. Often the multiplier is implemented with solid state (CMOS) switches to replace a linear (analog) multiplier and the input of the low-pass filter is rich with harmonics, but the signal linearity and stability can be better than with a conventional two-port linear (analog) multiplier. The disadvantage of the multiplier implemented with switches is the possible charge injection produced by the switches. The switches can pick-up some (residual) charge, which is passed on when closing the switches [1]. Furthermore, any latency between the switching will also cause small glitches in the signal which will be filtered to a non-zero dc-voltage. However, the implementation through switches is chosen because of its simplicity.

The ouput voltage U_{out} of the synchronous detector can be used to adjust the amplitude of voltage u_2. With initial position $x = 0$ and so $\Delta C = 0$ in Eq.3.22, the change in ouput voltage ΔU_{out} should be zero. If it is not required to measure absolute capacitance but only the change in capacitance the use of two capacitances offers the possibility to eliminate (paracitic) changes in humidity, temperature etc. and any static differences between C_1 and C_2. To this end the amplitude of signal voltage u_2 is continuously adjusted such that the ouput voltage of the synchronous detector $U_{out} = 0$. A similar approach is reported by [14]. The current I_1 through C_1 is made equal to the current I_2 through C_2:

$$I_1 + I_2 = \frac{U1}{/Z1/} + \frac{U2}{/Z2/} = 0 \qquad \text{(Eq.3. 24)}$$

It follows that the ratio between signal voltages U_1 and U_2 is given by:

$$\frac{U1}{U2} = \frac{C2}{C1} \qquad \text{(Eq.3. 25)}$$

Both capacitances should be situated close to each other and undergo the same relative parasitic changes due to a change in relative humidity ΔH_r, temperature ΔT and pressure ΔP i.e. $C_1 = C_1 \cdot (1 + \Delta_1)$ and $C_2 = C_2 \cdot (1 + \Delta_2)$ with $\Delta_1 = \Delta_2$. Then, the elimination of these changes will be optimal. With this method of feedback also the changes in amplifier gain and feedback capacitance C_f can be compensated.

3.5 NOISE LIMITS FOR INCREMENTAL CAPACITIVE SENSOR

The design challenge for the presented concept with a capacitive position sensor is to be able to detect very small variations of capacitance and eliminate or keep constant unwanted environmental or external variations due to temperature, pressure, humidity an electronic component changes. In their important paper of 1973, Jones and Richards [15] describe 15 years of research and they have achieved remarkable results. They report on a few instruments which at maximum sensitivity give full output ~5V for ~ 10 aF. This results in a detectable displacement of 10^{-14} m and a limiting resolution corresponding to a capacitance change of 0.3 aF (0.3 x 10^{-18} F) due to an equivalent noise current of about 10 pA in a bandwidth of 1 Hz. Jones and Richards further describe a measurement system (built) with a typical three plate transducer (typically surface area A might be 300 mm^2). The RMS electrical noise on the output was equivalent to a capacitance change of 0.01 aF in a noise bandwidth of 1 Hz.

In the next chapter the change in capacitance for different combinations of opposing periodic geometries is simulated with 2D-Finite Element simulations. For a combination of 2 opposing infinite periodic geometries with rectangular fingers with period P_x = 12µm, finger length l_f = 6, width w = 2, and gap between fingers g = 1 or 0.5 µm, the maximum change in capacitance per finger-pair is ΔC ~ 70aF or respectively ΔC ~ 170 aF per 5 µm, thus 0.014 aF nm^{-1} or 0.034 aF nm^{-1}.

Thus, if the sensitivity can be as good as 0.01 aF as reported by Jones and Richards [15] the preliminary conclusion is that an accuracy of 1 nm seems feasible, but far from straightforward.

A limit to measurement precision in a capacitive sensor may be the number of electrons to charge the capacitance. Baxter calculates for a 1 cm disk a capacitance of C_{disk} ~345 fF and 2.27 x 10^6 electrons needed to charge it with 1V. (This corresponds to a parallel plate capacitor with A = 100 mm^2 and a gap distance of 2.6 mm)

For a micromachined parallel plate capacitor with dimensions L x H = 600 x 5 µm^2 and a gap-size of 1 µm, the capacitance would be C_{mm} = 27 fF and 1.7 x 10^4 electrons would be needed for 1V of voltage difference.

Applying 1V to C_{disk} would give a signal current of 2 µA and 0.2 µA for C_{mm}. As an example, for an input current noise of 10^{-12} A/Hz^{-1} for the ultra low-noise wideband OPAMP (e.g. CLC425) or 10^{-15} A/Hz^{-1} for a FET-input OPAMP's (e.g. AD823) a signal to noise ratio SNR of 2 x 10^6 – 2 x 10^9 for the disk capacitor and a SNR ~ 2 x 10^5 – 2 x 10^8 can be expected.

Therefore, the resolution or measurement precision for a typical micromachined capacitive sensor appears not to be limited by the current noise of the amplifier or on the number of charged particles or on the applied circuitry with careful circuit design, and high environmental, and mechanical stability.

3.5.1 Limitations by thermal electric noise

Another limit to measurement precision may be the thermal electric and mechanical noise present in every physical system with electronics. This aspect is only briefly addressed here as an illustration and estimation of the influence of these noise sources on the measurement precision.

The noise in electronic circuits is caused by several physical random fluctuation mechanisms. The random motion of electrons in a conductor with a resistance *R* due to thermal agitation is called thermal noise. It implies the occurrence of random currents and voltages between the terminals of resistance *R*. The noise voltage generated by this mechanism is given by:

$$\overline{v^2{}_n} = 4kTR\Delta f \qquad \text{(Eq.3. 26)}$$

With Boltzmann's constant k = 1.38 $\cdot 10^{-23}$ [J/K], absolute temperature T [K]. Eq.3.24 implies a flat spectral power density and therefore thermal noise is also called white noise.

Although ideal reactive components (*L* and *C*) are free of noise sources these components are not free of noise. The total noise voltage squared for the simple low-pass RC-combination in Fig. 7 is given by (Eq.3.17) [16]:

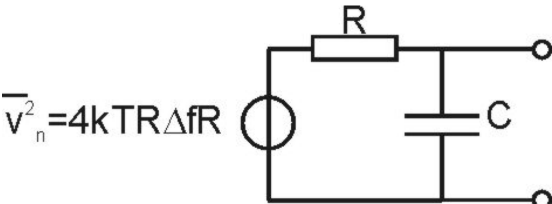

Fig. 7: Equivalent circuit for the calculation of the noise voltage for the noise generated by R.

$$\overline{v^2{}_{nc}} = \int_0^\infty \frac{4kTR}{1 + 4(fRC)^2} df = \frac{kT}{C} \qquad \text{(Eq.3. 27)}$$

Thus, a larger capacitance reduces the noise voltage over the capacitance due to the thermal noise produced by a resistor *R* which is buffered by the capacitor. The first term in the integral of equation (Eq.3.17) can be seen as a spectral noise density. It is clear that the noise voltage produced in a narrow bandwidth around a higher carrier frequency e.g. 1MHz is much less than *kT/C*. To illustrate this, the average noise voltage squared is calculated to v_{nc}^2 ~ 0.6 pV^2 or $\overline{v_{nc}}$ ~ 0.8 µV for a resistance *R* = 200KΩ, capacitance *C* = 1 pF, and a bandwidth BW = 200 Hz at a center frequency of *f* = 1 MHz. The values for the capacitance is quite realistic for capacitive sensors. A resistance of *R* = 200 KΩ is quite large. For a bandwidth of ~12.5 KHz, $\overline{v_{nc}}$ ~ 8 µV. Reducing the resistance by a factor 100, reduces the noise voltage for this BW to $\overline{v_{nc}}$ ~ 0.9 µV.

3.5.2 Limitations by thermal mechanical noise

The thermal mechanical noise due to the Brownian motion of the atoms is present in any material and ultimately forms a limit to the sensitivity. The spectral force density for the thermal mechanical noise is, similar to the electrical thermal noise, equal to:

$$\overline{x^2 n} = \frac{Fn}{Kx} = \frac{4kTD}{Kx} = \frac{4kT\sqrt{Kx \cdot M}}{Kx \cdot Q} = \frac{4kT}{Q \cdot \omega x} \quad \text{(Eq.3.28)}$$

For a typical device with a slider as in Fig. 1 and Fig. 2 made of poly-Silicon through surface-micromaching with dimensions L = 1500 µm, W = 50 µ and height H = 5 µm the mass of silicon is $M \sim 1 \times 10^{-9}$ Kg. Assuming a stiffness in x, y and z-direction as indicated in Fig. 8 to have resonance frequency's in the order of resp. f_x = 1 KHz, f_y = 250 KHz, f_z = 2.5 KHz, it is possible to estimate the Total Noise Equivalent Displacement (TNED) [8]. With a Q factor of 5, the TNED in a 1 Hz bandwidth becomes:

x_n = 0.73 pm/√Hz, y_n = 46 fm/ √Hz, z_n = 0.46 pm/ √Hz

The same reasoning is followed for the sense-structures with a length L, width W and Height H. The TNED for the dominant y-motion with the assumption of a resonance mode of f_{ssy} = 50 KHz and a damping factor Q ~ 5 becomes:

y_{ss_n} = 0.1 pm/√Hz

For a bandwidth BW = 1 KHz for the slider, this would mean a TNED of resp. x_n = 22 pm (i.e. 2% of 1 nm). The sense-structure must follow the periodic pattern on the slider and thus requires a higher bandwidth in the order of 15 – 20 KHz. Therefore, the TNED for the sense-structure is y_{ss_n} ~ 15 pm (i.e. 1.5 % of 1 nm), which is ~0.7x the TNED for x_n of the slider.

These figures show that thermal mechanical noise may be neglected in practice for the specifications of nm-accuracy for the concepts as presented here.

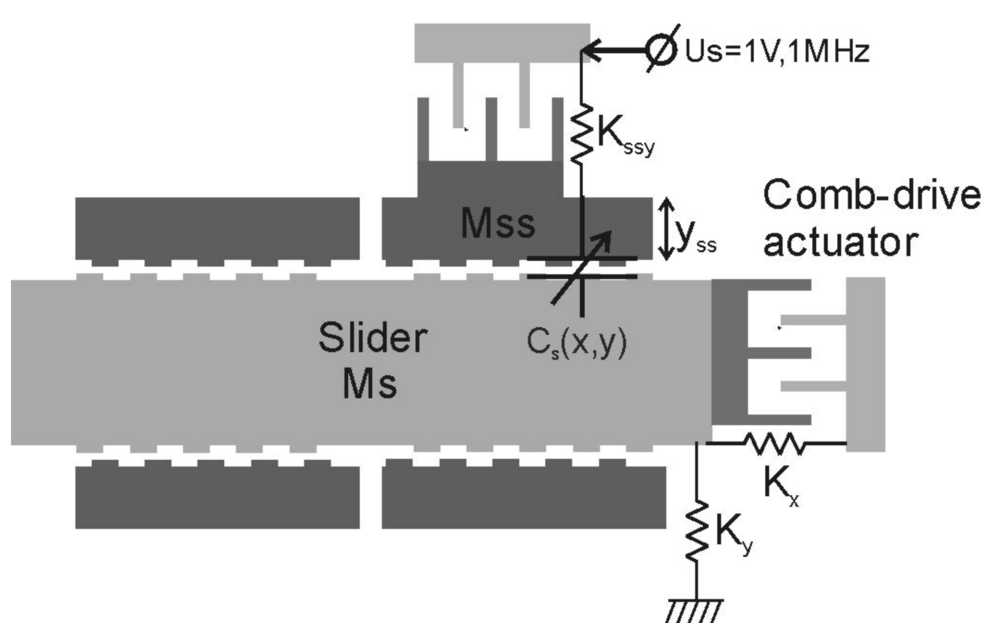

Fig. 8: A sketch of a device for the concepts ICMM and CCMM. Indicated are comb-drives as drive actuators for the slider mass and sense-actuators for the sense-structures which can be used for quadrature detection.

Next, it is estimated if the electrostatic forces on sense-structures and slider for small gap-sizes can cause pull-in of the sense-structures on to the slider.

3.5.3 Limitations by Electrostatic forces due to signal voltage U_s

Of course, the strong aspect of the presented concepts for an incremental capacitive position sensor is the symmetric design. The sense-structures have the same periodicity as the slider and thus the electrostatic forces on the slider caused by the sense-structures are balanced. However, the forces exerted on the sense-structures are not balanced.

If we assume the sense-structure and slider as a gap-closing capacitive transducer with two electrode plates formed by the side walls with surface area L x H = 600 µm x 5 µm. A stiffness or spring K_{ssy} is needed to balance the electrostatic force caused by the applied signal voltage $U_s = U_s{\cdot}cos(\omega_s{\cdot}t)$ of e.g. 1 V at a frequency fs = 1 MHz to measure the change in sense-capacitance $C_s(x, y)$.
The external force needed for equilibrium has a y-dependency given by:

$$F_{ext} = \left(\frac{\partial W'}{\partial y}\right)_u = \frac{1}{2}\frac{\varepsilon_0 LH}{y^2}u^2 + Ky \qquad \text{(Eq.3.29)}$$

The effective spring constant has a voltage dependency given by:

$$K_u = \left(\frac{\partial^2 W'}{\partial y^2}\right)_u = K - \frac{\varepsilon_0 LH}{y^3}u^2 \qquad \text{(Eq.3.30)}$$

There is a voltage u_{pi} at which the effective spring constant K_u is zero. Therefore, setting (Eq.3.30) to zero and substituting $U_s = U_s{\cdot}cos(\omega_s{\cdot}t)$ with U_s = 1 V it is calculated that the mechanical spring constant $K = K_{ssy}$ should be larger than 7 mN/m for a gap-size of 1 µm or 50 mN/m for a gap-size of 0.5 µm, as expressed by Eq.3.31:

$$K > \frac{\varepsilon_0 LH}{y^3}(U_s \cdot cos(\omega t))^2 \sim \frac{\varepsilon_0 LH}{y^3}(U_s^2/2) \qquad \text{(Eq.3.31)}$$

These figures do not seem to limit the operation of the concepts ICMM and CCMM. Particularly because, the gap between slider and sense-structure is only at the finger edges for some positions of the slider, equal to g ~ 1 µm or less.

3.5.4 Limitations by Electrostatic forces due to capacitance change ΔC_{sens}

We can derive forces in two directions: A force acting on the slider in x-direction, and a force acting on the sense-structure(s) in y-direction. The forces on the slider have opposite directions and they are assumed to compensate each other.
The force on the slider depends on the change in capacitance as given in equation Eq.3.32:

$$F_{ext} = \left(\frac{\partial W'}{\partial x}\right)_u = -\frac{1}{2}\frac{\partial C(x,y)}{\partial x}\cdot U^2 + Kx \qquad \text{(Eq.3.32)}$$

Assume for ICMM, $C(x,y) \sim \Delta C{\cdot}sin(k_x x)$ and y = constant and not a function of x.
Then, the force on the slider is given by Eq.3.33:

$$F_x = \left(\frac{\partial W'}{\partial x} \right)_u = -\frac{1}{2} \frac{\partial C(x,y)}{\partial x} /_y \cdot U_s^2 + Kx \qquad \text{(Eq.3.33)}$$

With $U_s = 1$ V, $f_s = 1$ MHz, a change in capacitance $\Delta C / (P_x/2) \sim 10$ fF, period size $P_x = 10$ µm and stiffness $K \sim M\ \omega_x^2 \sim 0.04 - 0.13$ [N/m], the displacement in x-direction is calculated using (Eq.3.32):

$$F_{ext} = -\frac{1}{2} \cdot 10^{-14} \cdot \frac{2\pi}{5 \cdot 10^{-6}} \cdot 1/2 + Kx = 0 \qquad \text{(Eq.3. 34)}$$

$x = 2.4 - 7.9$ nm for resp. $K_x \sim 0.13$ and 0.04 [N/m] !!

Also the electrostatic force on the sense-structure in y-direction is given by:

$$F_{ext_y} = -\frac{1}{2} \frac{\partial C(x,y)}{\partial y} \cdot U^2 + K \cdot y = 0 \qquad \text{(Eq.3. 35)}$$

In y-direction of the sense-structure, if we use the values given earlier as 2D-FE simulation results for a combination of rectangular finger pairs, the maximum change in capacitance per finger-pair for a change in gap distance from $g = 1$ µm to $g = 0.5$ µm is circa $\Delta C(y)|_{x=0}$ =185 aF at slider position $x = 0$. For 100 fingers $\Delta C \sim 20$ fF for the given change in gap. If we assume a resonant frequency $f_y \sim 50$ KHz for a mass $M \sim 0.1$ µg (0.1 x Mass of slider), $K_{yy} \sim 10$ N/m.

Due to the sensor input voltage $U_s = 1$ V (1MHz) and the given change in capacitance the displacement of the sense-structure in y_{ss} direction is:
$y_{ss} \sim 1$ nm

3.6 CONCLUSIONS

Two related concepts for a capacitive incremental postion sensor are presented: Incremental Capacitive Measurement Mode (ICMM) and Constant Capacitance Mode (CCMM). Both concepts are based on the change in capacitance between two periodic geometries for a relative displacement between the two.
For CCMM an increase in SNR of 320x is predicted over ICMM concept. Together with quadrature detection and the discussed capacitance sensing electronics the measurement of nm-accuracy over infinite range appears feasible. Thermal electric and mechanical noise and the originating electrostatic forces do not seem to form a limitation to meet the specifications.

References

[1] L.K.Baxter et al., *Capacitive Sensors: Design and Applications*, IEEE Press, New York, 1997.
[2] P.B.Kosel, G.S.Munro, R.Vaughan, Capacitive Transducer for Accurate Displacement Control, *IEEE Trans. On Instrumentation and Measurement*, (IM-30),2,114, June 1981
[3] K.B.Klaassen, J.C.L.van Peppen, Linear capacitive microdisplacement transduction using phase read-out, *Sensors and Actuators*, 3, 209-220, 1982/83
[4] www.opticalencoder.com
[5] P.Hariharan, *Basics of interferometry*, Boston Academic press, 1992
[6] B.G.Zagar, 'A laser-interferometer measuring displacement with nanometer resolution, *IEEE Trans. On Instrumentation and Measurement*, 43, 2, 332-336, april 1994
[7] J.Kuzdrall, Build an error-free encoder interface, Sept. 17,1992, Electronic design
[8] M.Elwenspoek, R.J.Wiegerink, *Mechanical Microsensors,* Berlin Heidelberg New York, Springer-Verlag, 2000
[9] J.T.Kung, H.S.Lee, An integrated Air-Gap-Capacitor Pressure sensor and digital readout with sub-100 attofarad resolution, *J. of MEMS*, **1**(3), 121-128, 1992.
[10] Y.M.Matsumoto, M.Nishimura, M.Matsuura, M.Ishida, Three-axis SOI capacitive accelerometer with PLL C-|V converter, *Sensors and Actuators A*, 75, 77-85,1999
[11] A.F.Zwijze, *Micro-Machined high capacity silicon load cells*, Ph.D.thesis, University of Twente, Enschede, The Netherlands, 2000
[12] F.N.Toth, G.C.M.Meijer, A low-cost, smart capacitive position sensor, *IEEE Trans. Instrum. Meas.*, 41, 1992
[13] F.N.Toth, *A design methodology for low-cost, high-performance capacitive sensors*, Ph.D.thesis, Delft University Press, The Netherlands, 1997
[14] R.F.Wolffenbuttel, P.P.L. Regtien, Capacitance-to-Phase Angle Conversion for the detection of extremely small capacities, IEEE Trans. On Instr. And Meas., IM-36, 4, 1987
[15] R.V.Jones, J.C.S.Richards, The Design and some Applications of Sensitive Capacitance Micrometers, *J.of Physics E: Scientific Instruments* 6: 589-600.
[16] J.Davidse, *Analog Electronic Circuit Design*, Wood Lane End, Prentice Hall International, 1991

4 2D-FE simulations for a capacitive incremental position sensor[1]

4.1 INTRODUCTION

This chapter gives the results of 2D Finite-Element modeling and simulations for the two concepts ICMM and CCMM for a micromachined incremental capacitive position sensor as discussed in chapter 2 and given in Fig. 1.

ICMM: In the concept Incremental Capacitance Measurement Mode the displacement of the slider is detected by measuring the periodic change in capacitance for a relative displacement between two opposing periodic geometries.

CCMM: In the concept Constant Capacitance Measurement Mode, the sense-structure is continuously adjusted in *y*-direction by additional sense-actuators to keep the capacitance between the two periodic geometries constant as the slider moves in *x*-direction. The control voltage U_c for the sense-actuators becomes a measure for the slider displacement.

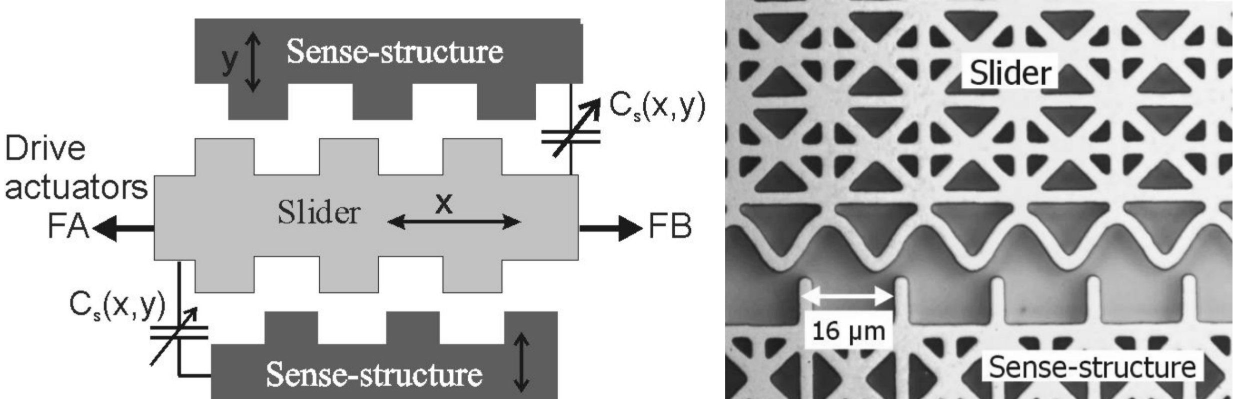

Fig. 1: (Left) the concept of an incremental capacitive position sensor. The displacement of the slider is detected by measuring the periodic change in capacitance which is a result of the relative displacement between two opposing periodic geometries. (Right) Example of a micromachined polysilicon structure forming a periodic capacitive position sensor.

In the next sections the influence of the combination of geometry on the shape and the change in capacitance ΔC as function of slider displacement (x) is examined through 2D-Finite Element simulations.

For both concepts the intention is to use quadrature position detection. Using two shifted periodic structures, delivering 90 degrees out of phase shifted signals it is possible to obtain a resolution that is ideally independent of position and that also allows for compensation of variations in temperature and relative humidity (by taking the ratio of the signals). Either a perfect sinusoidal $C(x)$ or $U_c(x)$ or a triangular function is desired, with the considerations given in chapter 3. However, it is difficult to determine which geometry combinations will produce such perfect functions. Naturally, the capacitance between two geometries S_1 and S_2 (see also chapter 3) is the result of a convolution between the two periodic functions, with

[1] Parts of this chapter are published in *J. Micromech. Microeng.*, **13,** S183–S189, 2003.

the amplitude approximately inversely related to the shortest distance between S1 and S2.

For a geometry combination of a sine pattern and sense-fingers with probe-like dimensions (large ratio of period size to finger width) the analysis for the CCMM concept given in chapter 2 predicts a better signal to noise ratio in combination with a sinusoidal function *y(x)*. Through Fourier analysis on simulated results for the combination of sense-fingers and sine pattern, the validity of the predictions will be examined in section 4.6.

The aim of the simulations has not only been the optimization of geometry combination and characteristics in order to produce the perfect sinusoidal *C(x)* function. The realizability through micromachining of such a perfect *C(x)* needs to be scrutinized as well as the measurability of the predicted capacitance changes.

In the discussion the simulated capacitance changes ΔC will be compared with measurement results reported in literature. With this comparison it is possible to determine the feasibility of the concepts.

4.2 FEM SIMULATIONS FOR A CAPACITIVE LONG-RANGE POSITION SENSOR

According to Feynman [1], the only general methods of solution of Laplace's equation are numerical. For analytical solutions of field distributions the complex variable technique is often powerful but limited to 2D problems, and it also is an indirect method [1]. Therefore, the approach has been to perform Finite-Element Model (FEM) simulations to study the concepts presented in this thesis. Fig. 2 presents the basic periodic geometry used in the program FEMLAB to run the FEM simulations.

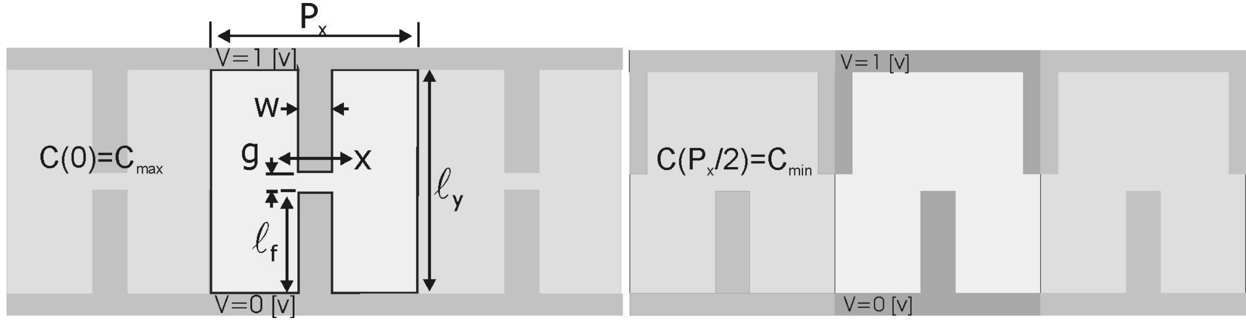

Fig. 2: Illustration of the basic periodic geometry as used in the FE model to simulate the change in capacitance vs. displacement (*x*) between two opposing periodic patterns. For *x* = 0 the capacitance C_s will be maximal, for *x* = *Px/2*, C_s will be minimal.

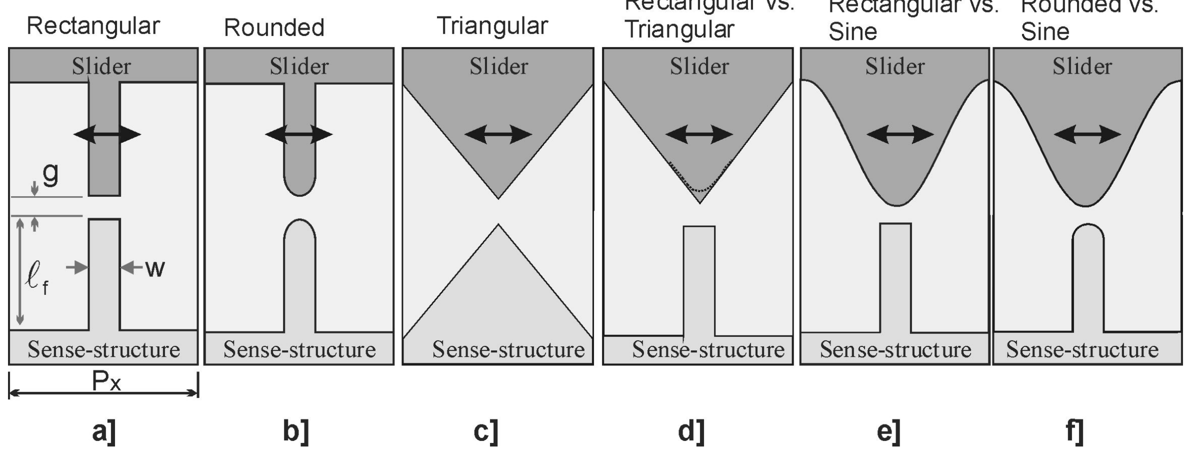

Fig. 3: This study includes simulations with different 'finger' shapes and different parameters e.g. gap *g*, vinger length l_f, ratio of period P_x - finger width *w*.

Initially, the parameters used in the 2D-simulations for the FE-model in Fig. 2 and Fig. 3 with rectangular fingers, assuming infinite structure height, are (in [μm]) given in Table 1:

Width of fingers **w**	2 [μm]
length fingers $\mathbf{l_f}$	6
gap distance **g**	1
(Lateral) period $\mathbf{P_x}$	12
bias-gap-distance $\mathbf{l_y}$	$2 \cdot l_f + g$
structure height of **h** for 2D-simulations for real structure	 Infinite 5

Table 1: Initial parameter values (in [μm]) for the FE-model with two opposing periodic patterns with rectangular 'fingers'

The width ***w*** of 2 μm comes from practical considerations concerning the minimum feature size that can be developed with standard available photo-lithography in the MESA+ laboratory. This will be explained more in chapter 5 about fabrication.

We have also simulated different shapes and combinations of dissimilar shapes of 'fingers' and patterns as well as for different period $\boldsymbol{P_x}$, length $\boldsymbol{l_f}$ and gap distance ***g*** as depicted in Fig. 3.

The capacitance (per meter of height) is calculated by calculating the electrostatic energy in the volume between the fingers with a given voltage difference U, i.e.

$$W_e = \tfrac{1}{2} \cdot C \cdot U^2 \qquad \text{(Eq.3 1)}$$

The electrostatic energy can also be expressed in terms of the electrostatic field strength:

$$W_e = \frac{1}{2} \int \varepsilon_0 \cdot E^2 \cdot dv \qquad \text{(Eq.3 2)}$$

Combination of Eq.4.1 and 4.2 gives for the capacitance:

$$C = \frac{1}{U^2} \int \varepsilon_0 \cdot E^2 \cdot dv \qquad \text{(Eq.3 3)}$$

After meshing the geometry into finite elements and defining boundary conditions (potentials) the electrostatic ***E***-vector is calculated by solving Laplace's equation $\nabla^2 V=0$ for all (area) elements. Dirichlet boundary conditions are used on the real geometric boundaries, by stating the potential i.e. $U(i)$ = 1 V or 0 V. The Neuman boundary conditions are used on the vertical 'artificial' segment boundaries. i.e. $\boldsymbol{n} \cdot \boldsymbol{D}=0$.

These conditions are implemented as periodic boundary conditions so that the calculated values for the E-field on the left side of the geometry in Fig. 2 are identical to values on the right side. This ensures the calculated field distribution corresponds to infinite repetition of a geometry segment.

The simulated capacitance per meter of height is multiplied with the structure height of ***h*** = 5 [μm] (i.e. poly-silicon layer thickness, see section fabrication). This results in the (approximate) capacitance per geometry-segment, containing one period of the geometry. Due to the scaling properties of the 2D-Laplace equation, the units of parameters w, P_x, L_f, g

are not important but only their relative proportions. Only important are the units of the dielectric permittivity ε_0 [F/m] and the structure height h [m] for calculation of the energy or capacitance (Eq. 3.1). It is preferred to have a unit-free normalized displacement ($x_n = x/P_x$), to better compare between geometries with different period (P_x).

4.3 Simulations Incremental Capacitance mode

Fig. 4 gives the simulated capacitances against normalized displacement (x/P_x) for 3 differently shaped finger-pairs with a lateral period of P_x=12 [µm]. As the displacement in x-direction between the pair of fingers is zero, the fingers are 'in-phase' and the capacitance is maximal. For a displacement of $½·P_x$ the fingers are 'out-of-phase' and the capacitance is minimum and rising again for larger displacements. For each shape of finger-pair the change in capacitance for every displacement is calculated i.e. $\Delta C(x) = C(x) - C_{min}$.

The simulation results for geometry combinations a, b, c in Fig. 3 are given first, and separated from combinations d, e, f, for clarity.

From Fig. 4 it is clear that the combination of two arrays of rectangular-shaped fingers has the largest absolute capacitance Fig. 4 (top) as well as the largest change in capacitance Fig. 4 (bottom) for each displacement of the arrays in respect to each other.

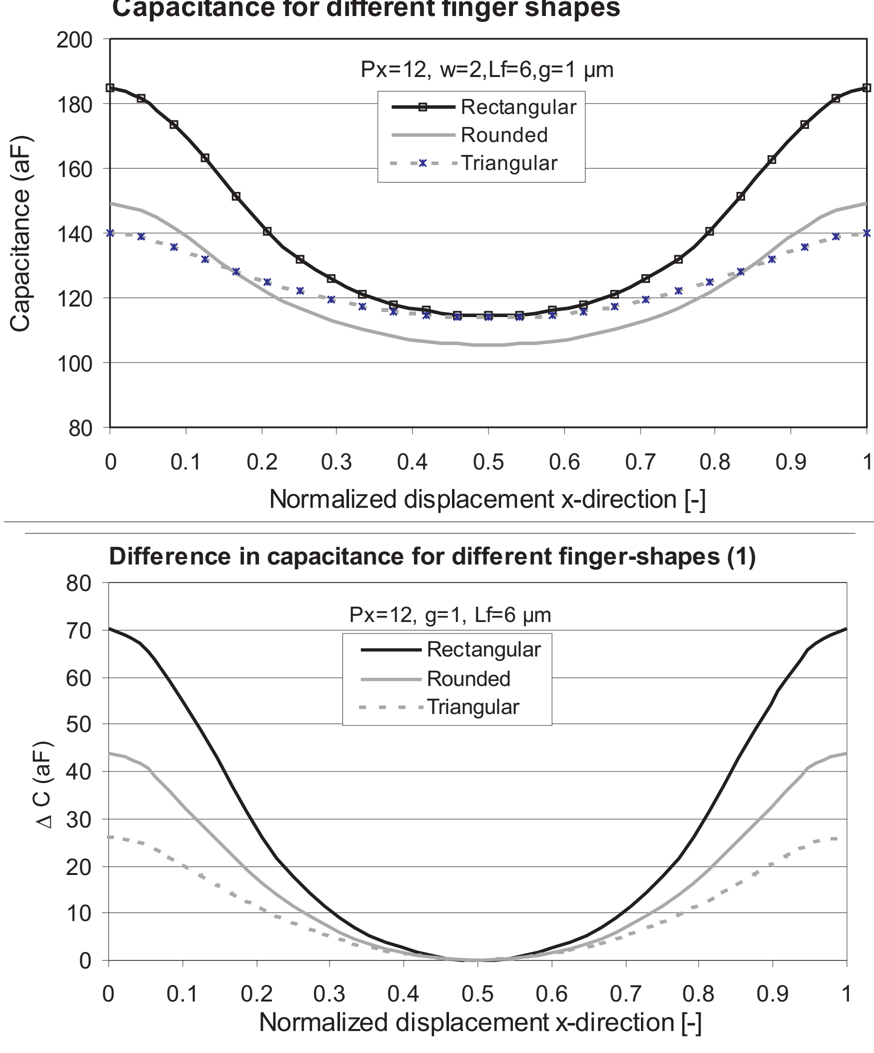

Fig. 4: (Top) Simulated capacitance per finger-pair versus displacement for 3 different shapes of finger-pairs. (Bottom) The calculated difference in capacitance $C(x) - C_{min}$.

We also examined the influence of combinations d, e, f in Fig. 3 with dissimilar ‘finger’-shapes. Fig. 5 gives the results of the FE-calculations for these combinations, with the same figures for width *w*, period P_x, finger-length l_f, gap *g* and with amplitudes A_s, $A_{tr} = l_f$. The combination of Sine- versus rectangular-shaped ‘finger’ is showing the largest difference in capacitance owing to the smallest “average gap distance”. The combination of rectangular fingers in Fig. 4 is showing a larger change, because of charge accumulation at the edges. Also the minimum value of the capacitance for this combination is lower, because the average distance l_y (Fig. 2, Fig. 3) is larger.

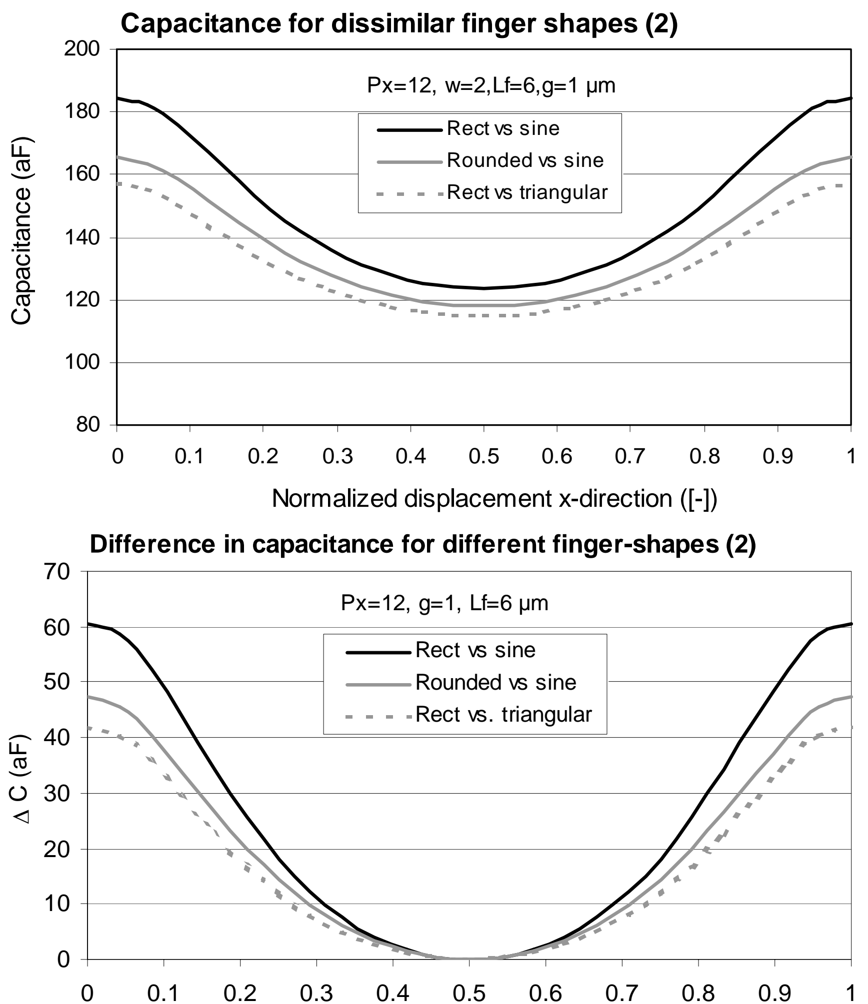

Fig. 5: (Left) Simulated absolute capacitance-values for dissimilar finger-shape combinations (see Fig. 3) (Right) calculated difference in capacitance $C(x) - C_{min}$.

Fig. 6 shows the results of the difference in capacitance versus displacement for rectangular fingers when the initial gap is changed from 2 to 0.5 µm (i.e. *g=w, ½ w, ¼ w*). Halving the gap increases the maximum difference by a factor larger than 2. Therefore, decreasing the gap by open-loop control of the sense-actuator provides a way to increase the change in capacitance $\Delta C(x)$ and therefore the position measurement signal. A larger ΔC means a higher average resolution and accuracy can be obtained. However, also the differential change $\partial_x C(x) = \partial \Delta C(x)/\partial x$ is important and this is determined by the shape of $C(x)$. Reducing the gap distance changes the shape of $C(x)$ and this means a non-linear

change in $\partial_x C(x)$. It could mean that $|\partial_x C(x)|_{max}$ is increased while the range of positions for which $\partial_x C(x) = 0$ or in practice too small to be detected is increased too.

Increasing the structure height ***h*** is more advantageous because then ΔC(x) and ∂_xC(x) are increased linearly. But, if $\partial_x C(x) = 0$ *and* $\partial^2_x C(x) = 0$ it means the position cannot be detected over a range dx and an increase in ***h*** would not change this.

In practice the height ***h*** is limited for the poly-silicon structural layer as explained in chapter 4 about design and fabrication. Therefore, reducing the gap is a good and only option to increase $\Delta C(x)$.

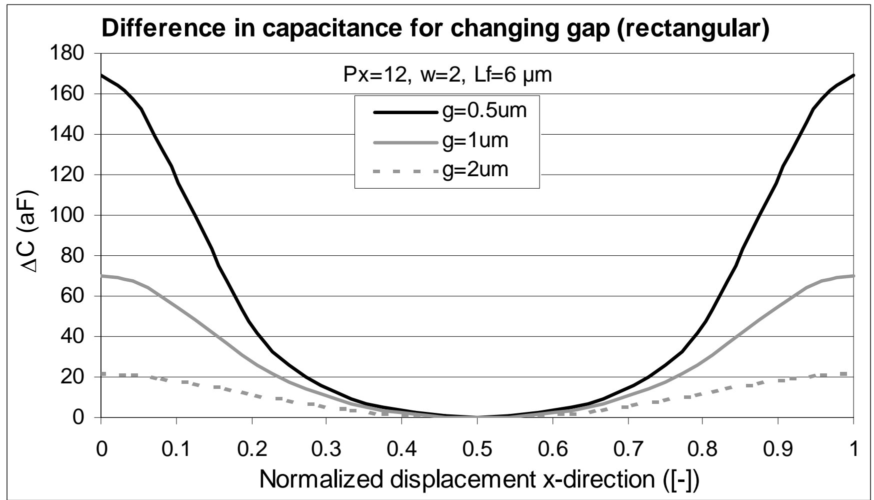

Fig. 6: Difference in capacitance for rectangular-shaped fingers and decreasing initial gap distance.

Fig. 7 gives the simulated difference in capacitance for rectangular-shaped fingers and for various values of the period P_x. Decreasing P_x does increase the sensor-density, and thus the discrete (counting) accuracy, but at the expense of decreasing ΔC when all other parameters remain the same (Fig. 7 top). However, a larger period P_x shows around $x = P_x/2$ (Fig. 7 bottom) a smaller dC/dx over a larger range. This means $C(x)$ will change less in this range, thus making it harder to detect this change in capacitance.

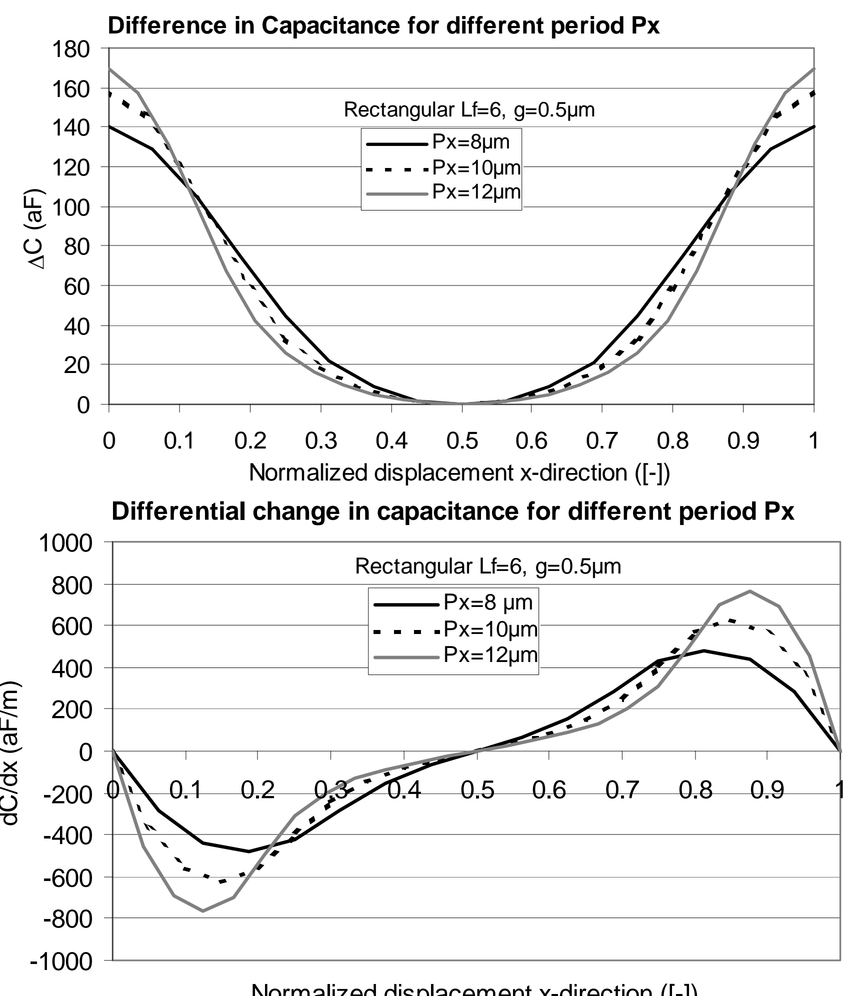

Fig. 7: (Top) For rectangular shaped fingers the difference in capacitance simulated for different period P_x and initial gap distance g = 0.5[µm]. (Bottom) The differential change in capacitance dC / dx

4.4 2D-FE Simulations Constant capacitance mode (CCMM)

In the next part we will give the results of simulations for a slightly different concept illustrated in Fig. 8. Here, the capacitance between Sense-structure and slider is held constant as the sliderbeam is moved by the drive-actuators (in *x*-direction). Each Sense-structure is driven in y-direction using a closed-loop control scheme.

In general this technique is used for larger dynamic range and minimization of the influence of parasitic capacitances e.g. accelerometers [2,3]. However, with these accelerometers, a test mass is held at a constant position by applying a closed-loop force-feedback concept.

In the closed-loop constant capacitance measurement mode presented here, the sense-structure(s) has to move in y-direction, while the slider is moving in *x*-direction, to keep the capacitance at a constant setpoint-value. The control signal for the Sense-Actuator becomes a measure for the x-displacement of the slider.

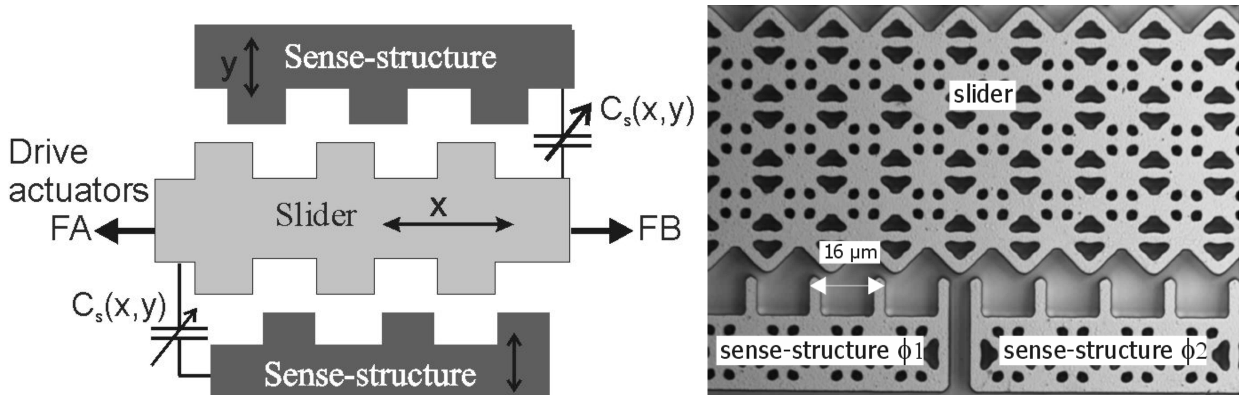

Fig. 8: (Left) Extension of the concept in Figure 1. For each displacement of the slider in x-direction the sense-structure is now actuated in y-direction to keep the sense-capacitance constant using closed-loop control. (Right) Photograph of micromachined periodic capacitance sense-structure.

4.5 SIMULATION RESULTS FOR CCMM

First we give results for a geometry combination with rectangular vs. rectangular (combination a] in Fig. 3). For an initial gap g_0 the capacitance is calculated at position x=0. Then, the top-finger in geometry a] in Fig. 3, is displaced in x-direction to position x_i and manually a new position in y-direction is found in order to make $C(x_i,y_j) = C_{set}(x_0, g_0)$. The remaining error or Error limit is 1% of C_{set} i.e. if $dC_e = C(x_i, y_j) - C_{set}) \leq 1\%$ a new position x_{i+1} is taken.

Fig. 9 gives the required motion in *y*-direction of the Sense-Actuator to keep the capacitance at the initial value $C_{set}(0)$ for $x = 0$. The $y = 0$ position is taken at the top of the moving finger for position $x = 0$, $g = g_0$.

If the initial gap g_0 for x=0 is made smaller, the initial capacitance C_{set} is larger. For a displacement of the slider the fingers of the Sense-actuator will have to follow the pattern on the slider more closely in order to keep the capacitance at the larger value of C_{set}. This increases the amplitude of the motion in *y*-direction and the SNR. Fig. 9 also shows that the *y*-displacement of the Sense-Actuator increases when the length of its fingers is increased from 6 to 8 µm. (The fingers on the slider remain 6 [µm]).

Fig. 10 gives the simulated y-displacement of the sense-actuator for 4 combinations of finger-shapes: a) rectangular-rectangular, b) rounded-rounded, c) triangular-triangular, d) rectangular- triangular. Combination a) in Fig. 10 shows the largest y-displacement but the differential change in y-motion (*dy/dx*) around $x = ½ \cdot P_x$ is slightly less than for combination d). This means that for combination d) at this position, a higher sensitivity is required to detect a displacement of the slider.

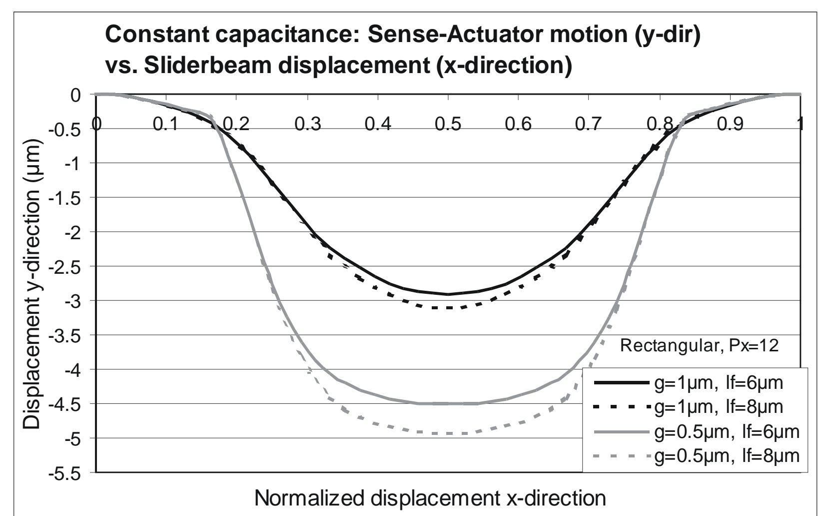

Fig. 9: Simulated displacement in y-direction, required to keep the capacitance equal to the initial capacitance C_0 *(x=0)*.

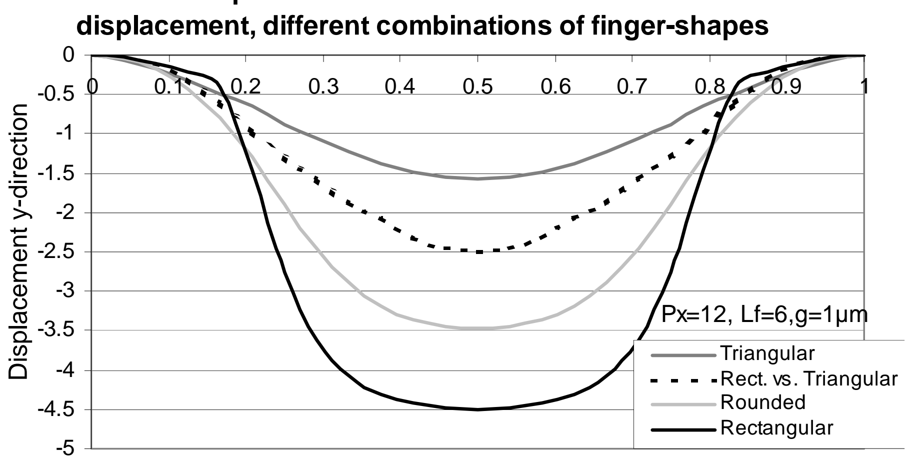

Fig. 10: *Y*-displacement of closed-loop controlled Sense-actuator for 4 combinations of dissimilar finger-shapes.

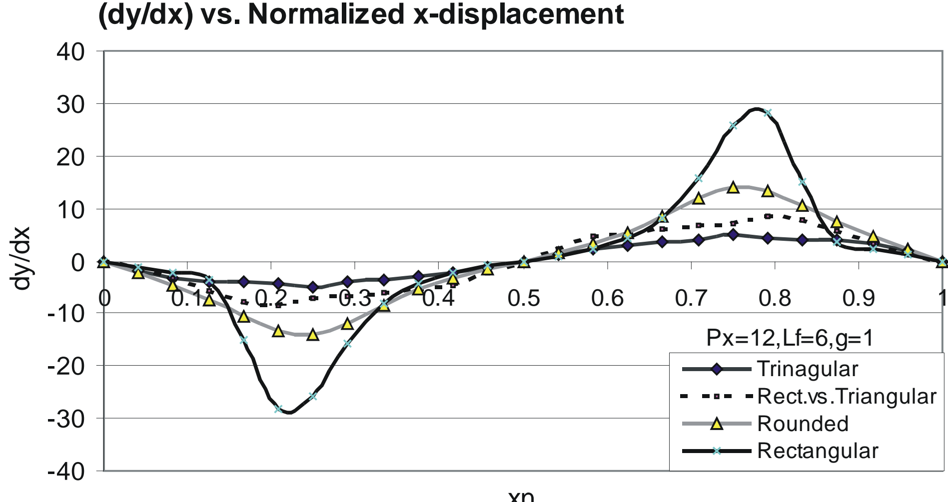

Fig. 11: differential change *dy/dx* versus normalized *x*-displacement based on Fig. 10.

Fig. 11 depicts the calculated differential change dy / dx versus displacement in x-direction for different finger-shapes. As mentioned in the introduction, ideally the capacitance function $C(x)$ or the displacement function $y(x)$ would be pure sinusoidal or triangular. The differential change for dy / dx would then be either sinusoidal or a constant. In practice however when it is not possible perhaps to realize the ideal geometries, there may be a trade off between large values of dy / dx for a range of positions versus zero dy / dx for a different range of positions. Such non-ideal functions are given in Fig. 11 for the geometry combinations a) to d) of Fig. 3.

Combination a) shows a large value of dy / dx around $x_n = 1/4$ and $x_n = 3/4$ in combination with a change dy / dx around $x_n = 0$, smaller than for the other geometries. The accuracy to detect changes in ΔC and to accuracy to produce a change in control voltage dU_c / dx determines the overall position accuracy.

One can try to find an ideal geometry combination which gives a large amplitude ΔC or Δy, in combination with a sinusoidal or triangular $\Delta C(x)$ or $y(x)$. However, a good alternative is to use two geometrically shifted arrays as in Fig. 8 (right), so that a minimum in sensitivity for one array is balanced by a maximum in sensitivity of the other (i.e. quadrature detection [4]). Implementation of this principle would require more space (area / volume), though.

4.6 SIMULATIONS FOR CCMM FOR ROUNDED VS SINE GEOMETRY

As mentioned in the introduction and in chapter 3 for quadrature detection two perfect sinusoidal signals or two perfect triangular signals with a phase shift of 90 [deg] are required. For ICMM these signals represent the capacitance functions $C_1(x)$ and $C_2(x)$. For CCMM these signals represent the control voltages for the sense-actuators $U_{c1}(x)$, $U_{c2}(x)$ or the positions of the sense-structures $y_1(x)$ and $y_2(x)$.

The analysis in chapter 3 predicts for the CCMM concept an improvement in SNR and a sinusoidal function $y(x)$ if a geometry combination of a sine on the slider and sense-fingers with probe-like dimensions is chosen.

In this section this prediction is examined through 2D-FE simulations and Fourier analysis for both ICMM and CCMM. The simulation method of the previous sections has been further developed and automated using a Matlab script file for FEMLAB software [5].

For the geometry given in Fig. 12 the resulting capacitance functions for ICMM for two gap sizes $g_1 = 0.5$ µm and $g_2 = 0.2$ µm, corresponding to a maximum capacitance of $C_1 = 200$ aF and $C_2 = 300$ aF are given in Fig. 13. Note that this is the capacitance per finger-pair segment, for a structure height of 5 µm.

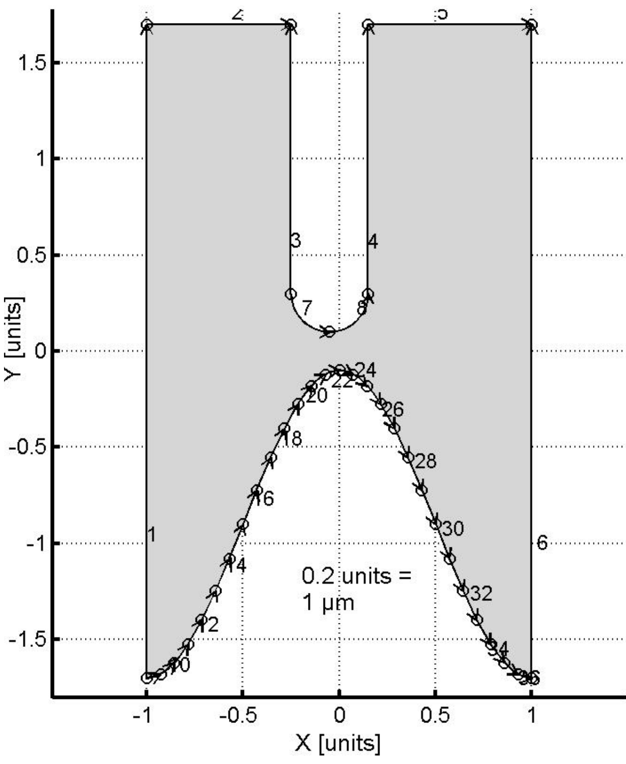

Fig. 12: Geometry for 2D-FE simulations the geometry combination sine – rounded finger and period P_x = 10 µm (= 2 units)

Again, it is noted that because of the scaling properties of the 2D-Laplace equation, the actual units for the x- and y-axis are not important but the ratio between period size and finger width, and other features are.

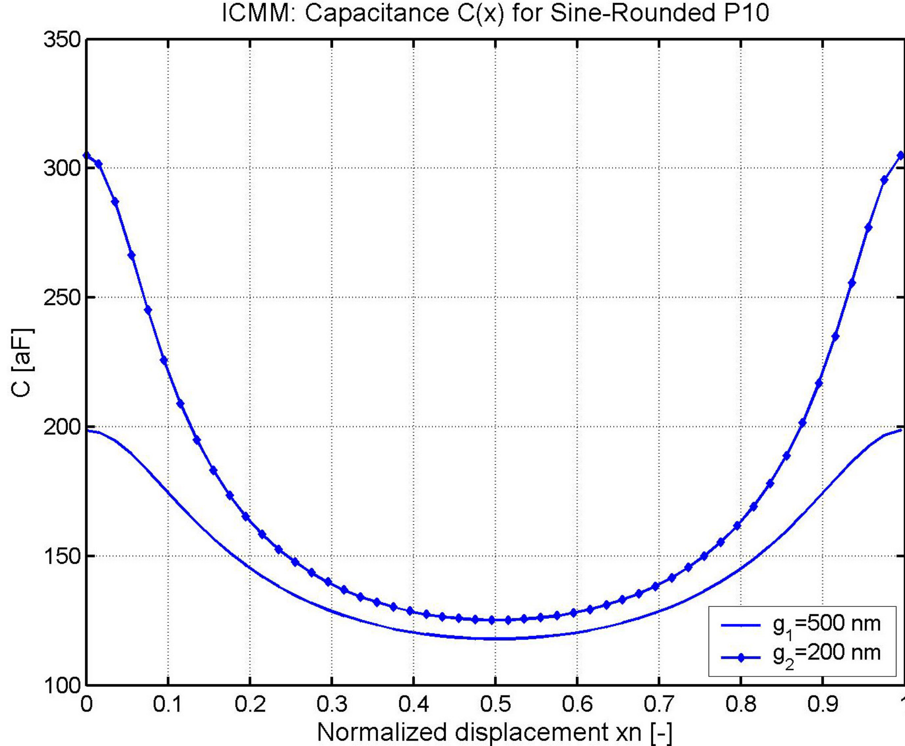

Fig. 13: The simulated capacitance function *C(x)* for 2 gaps g_1 = 500 nm and g_2 = 200 nm for the geometry in Fig. 12 with period size P_x = 10 µm

With FFT analysis the non-linearity due to higher order harmonics in $C(x)$ can be determined.

Because $C(x)$ is periodic it can be written as a Fourier series given by:

$$C(x) = \frac{1}{N}\sum_{n=0}^{N} A_n \cdot cos(n \cdot \omega_0 \cdot x) \qquad \text{(Eq.4 4)}$$

With $\omega_0 = 2\pi/P_x$ and $P_x = 10$ µm. The amplitudes A_n are given by the Fast Fourier Transform with $x = k{\cdot}\Delta x$:

$$A(n) = \sum_{n=0}^{N} C(k\Delta x) \cdot exp(-i \cdot 2\pi \cdot n \cdot k / N),\ 0 \le n \le N \qquad \text{(Eq.4 5)}$$

The first harmonic in space-domain $f_1(x) = f_{\omega 0}(x) = C_{\omega 0}(x) = A_1{\cdot}cos(\omega_0{\cdot}x)$. The residual spatial function $r_n(x)$ of all higher order harmonics is defined by:

$$r_n(x) = \frac{1}{N}\sum_{n=2}^{N} A_n \cdot cos(n \cdot \omega_0 \cdot x) \qquad \text{(Eq.4 6)}$$

The residual spatial function $r_n(x)$ is calculated using the inverse FFT algorithm (ifft) of Matlab.

$$r_n(k \cdot x) = \frac{1}{N}\sum_{n=2}^{N} A(n) \cdot exp(j \cdot 2\pi \cdot n \cdot k / N),\ 2 \le n \le N \qquad \text{(Eq.4 7)}$$

One can see the residual function $r(x_n)$ as the difference in space domain between the function $y(x)$ and a pure sine with amplitude $|f_1|$ and period P_x =10 µm i.e. P_{xn} =1. In other words this is the non-linearity due to higher order harmonics.

Because the capacitance functions in Fig. 13 are clearly far from sinusoidal, the spectrum is calculated without showing it here. Instead, Fig. 14 gives the result of the inverse FFT for all residual higher order frequency components of the capacitance functions. For comparison, also the first order harmonic $f_1(x) = A_1{\cdot}cos(\omega_0{\cdot}x)$ of the simulated $C(x)$ for a gap g_2 = 200 nm is given.

Table 2 gives the amplitudes and ratios of the first harmonic and higher order components in the FFT spectrum of the simulated functions $C(x)$ for different gaps g_1 = 500 nm and g_2 = 200 nm. The amplitudes in Table 2 are calculated as follows:

Amplitude $|f_{\omega 0}(x)| = 2A(1) / (N-1)$
Amplitude $|r_n(x)| = (max\,(r_n(x)) - min\,(r_n(x)))/2,\ for\ n \neq 0,1$

g [nm] / C [aF]	$f_{\omega 0}(x)$ [aF] $(\omega 0=0.1)$	$f_{(2\omega 0)}/f_{(\omega 0)}$	$f_{(3\omega 0)}/f_{\omega 0}(x)$	$r(x_n)$ [aF]	$r(x_n)/ f_{(\omega 0)}(x)$
500 / 200	36.9136	0.3012	0.0975	13.3589	0.3619
200 / 300	72.1783	0.4405	0.2105	45.0403	0.6240

Table 2: (ICMM) amplitudes and ratios for FFT components of simulated *C(x)* for different gaps *g*

For a smaller gap g_2 = 200 nm corresponding to a maximum capacitance C_2 = 300 aF, the contribution of the amplitude of the residual space domain function $r(x_n)$ is around 62% of the amplitude of the first harmonic $f_1(x)$ for g_2.

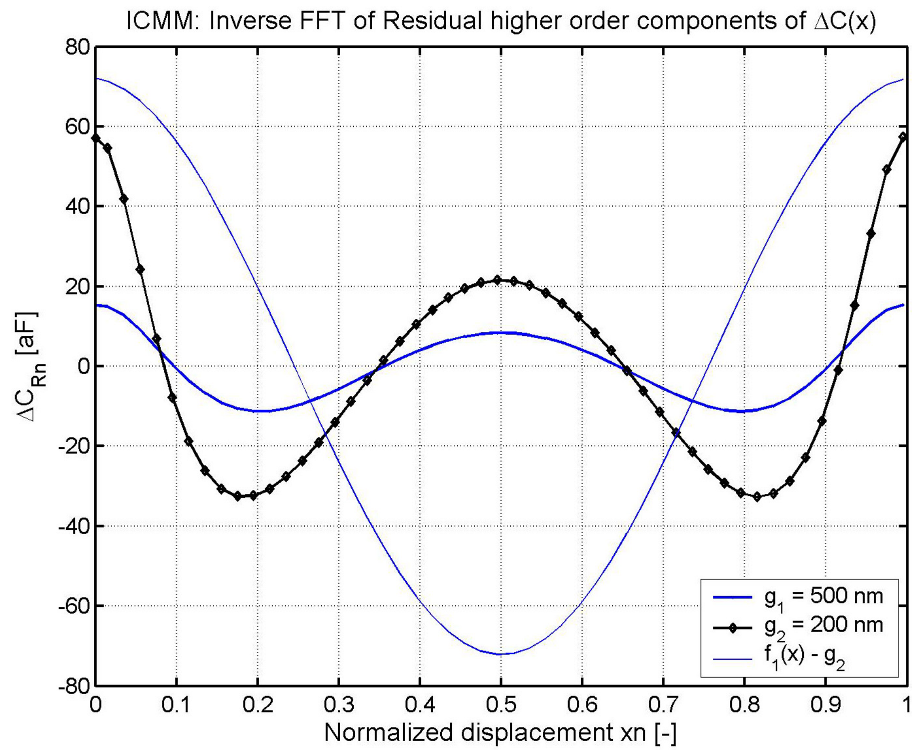

Fig. 14: Calculated inverse FFT of all residual higher order components in the FFT spectrum of the capacitance functions in Fig. 13. For comparison also the first order harmonic for g_2 is given.

These results are compared with simulation results for the CCMM concept. For every displacement of the rounded finger in Fig. 12 in x-direction a displacement in *y*-direction is calculated in order to keep the calculated capacitance $C(x,y)$ equal to the setpoint C_{set}, i.e. $dY = K_p \cdot (C(x,y) - C_{set})$, with $(C(x,y) - C_{set})$ < Error limit. The value for K_p is empirically found. The remaining error or Error limit is 1% of C_{set}. If $dC_e = C(x_i, y_j) - C_{set})$ < 1% a new position x_{i+1} is taken.

Apart from rounded fingers also rectangular-shaped fingers are used for the simulation and comparison. In Fig. 15 the displacement in Y-direction of the rounded finger is given for every displacement in X-direction for which $C(x, y(x)) = C_{setpoint}$. The $y = 0$ –line corresponds to the top of the sine geometry in Fig. 12. Therefore, the y-position for $x = 0$ corresponds to the minimum gap size between geometry S1 and S2. This reference position for $y = 0$ is a better choice than the $y = 0$ reference in Fig. 9.

As expected, for a higher setpoint capacitance C_{set} the larger the amplitude of *y(x),* but *y(x)* is limited by the function S_1 of the sine pattern. For rectangular fingers the amplitude of *y(x)* for a setpoint C_{set} = 250 aF, is less than for rounded fingers with the same setpoint. This is because, as we have seen with the simulations in section 4.3, the capacitance between rectangular shaped geometries is larger due to charge accumulation at sharp convex corners and an accompanying higher electric field intensity. Therefore, for the rectangular fingers to reach a certain setpoint capacitance a smaller displacement in *y*-direction is required. Because of the convolution nature of the capacitance between two geometries, the shape of *y(x)* for the rectangular finger is less corresponding to a sine than for the rounded finger. This is also clearly reflected in the amplitudes and ratios between first order and higher order harmonics of the simulated curves for *y(x)* given in Table 3 and Fig. 16. The inverse FFT of the residual higher order components of *y(x)* is $r(x_k)$ = Ifft $(A(n\cdot\omega 0))$ for $n \neq 0,1$ is given in Fig. 17.

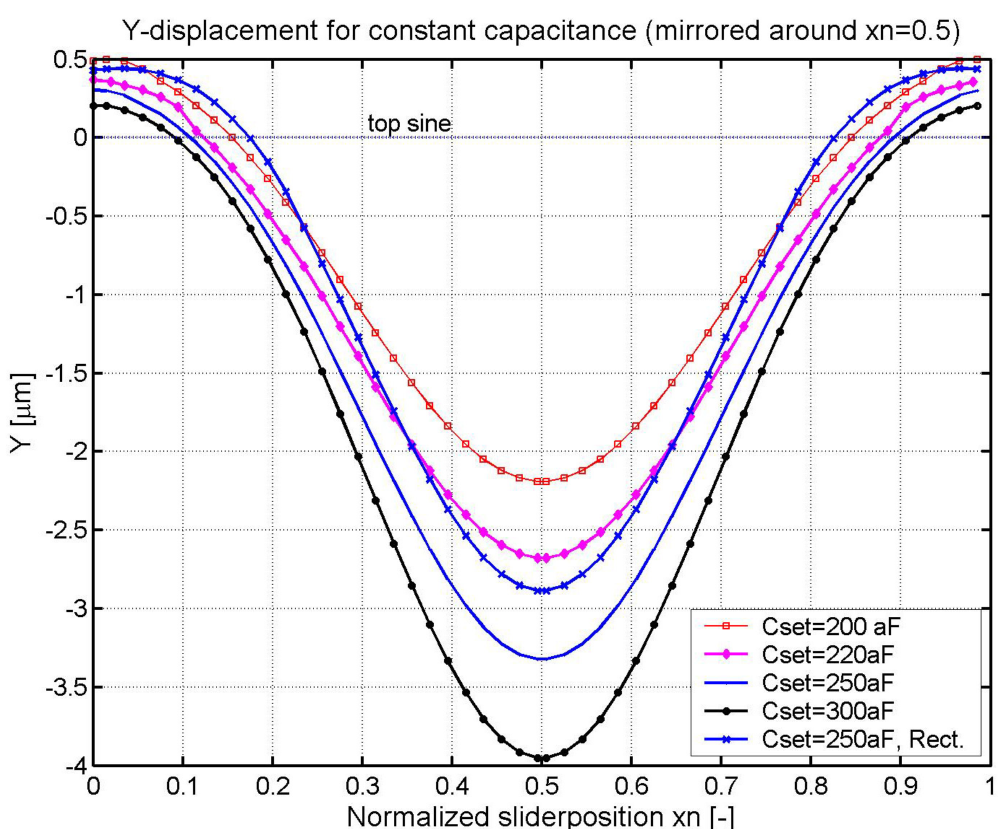

Fig. 15: Simulated y(x) for different setpoints C_{set}. The y=0 axis corresponds with the top of the sine geometry. The value *y(x=0)* is the minimum gap *g*.

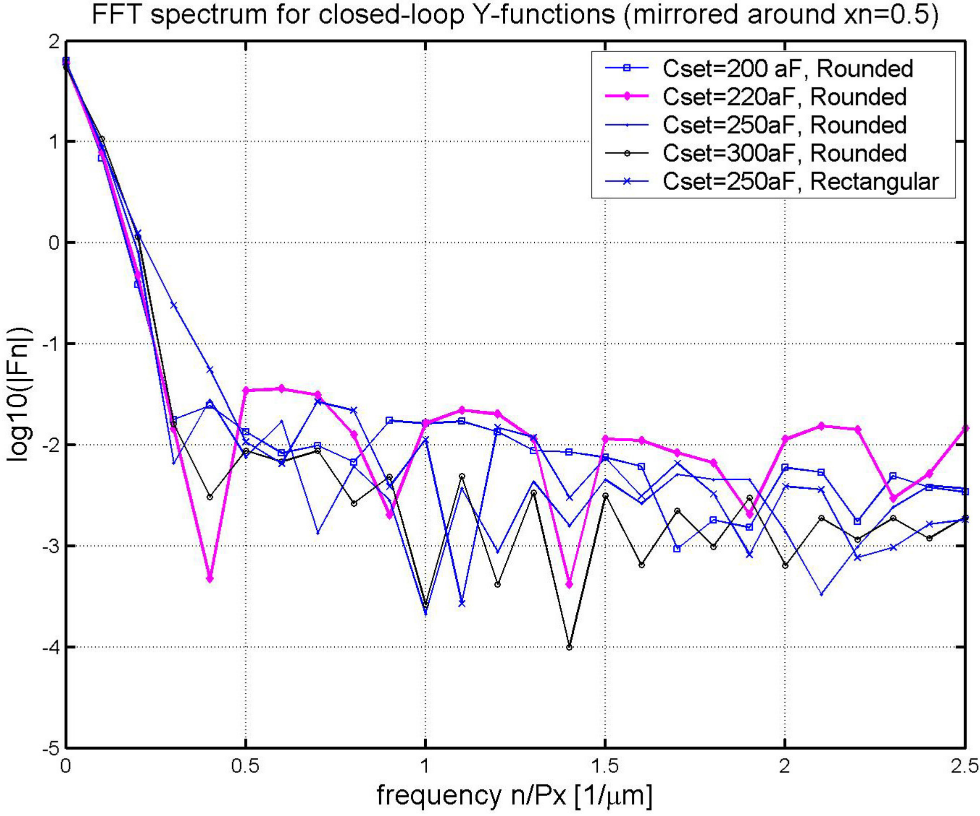

Fig. 16: FFT spectrum of simulated functions *y(x)* for different setpoints

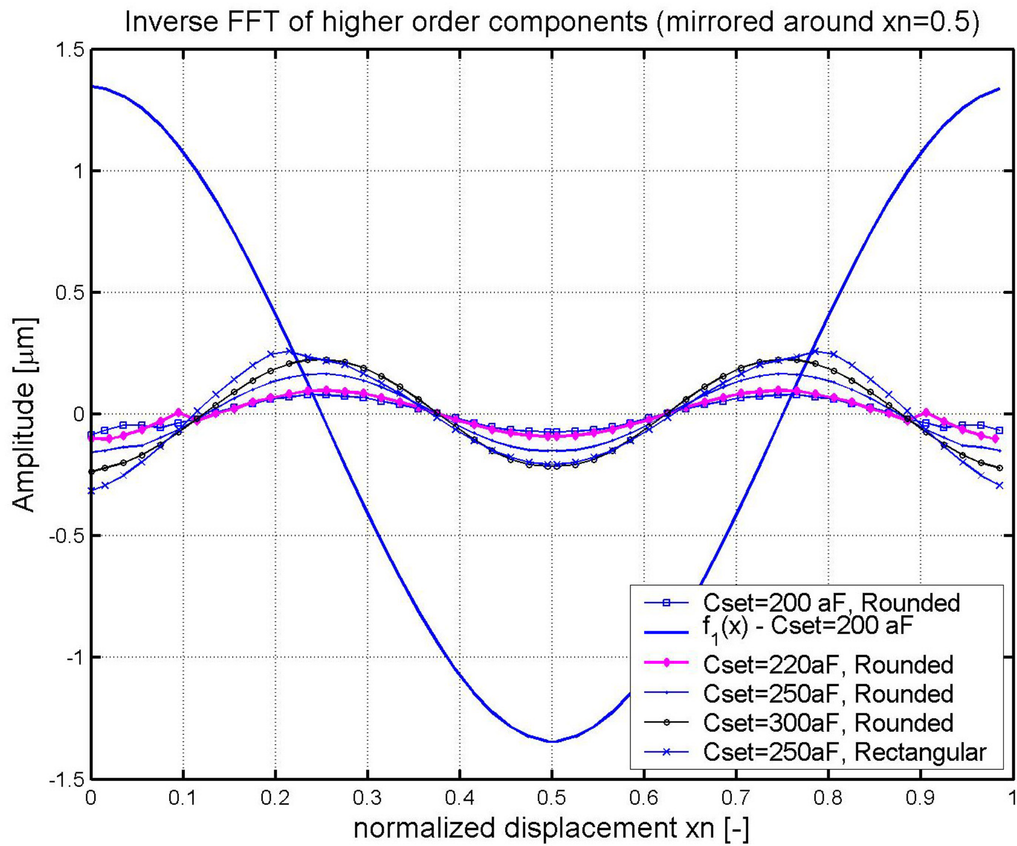

Fig. 17: The residual function $r(x_n)$ can be seen as the difference between $y(x)$ and a pure sine-function with amplitude $f_{\omega 0}$ and period P_x = 10 µm.

C_{set} [aF]	$f_{\omega 0}(x)$ [µm] ($\omega 0=0.1$)	$f_{(2\omega 0)}/f_{(\omega 0)}$	$f_{(3\omega 0)}/f_{\omega 0}(x)$	$r(x_n)$ [µm]	$r(x_n)/f(x)_{(\omega 0)}$
200	1.348	0.056	0.0026	0.0829	0.0615
250	1.8186	0.0895	7.12e-4	0.1616	0.0888
300	2.0919	0.1082	0.0015	0.2310	0.1104
250R	1.7143	0.1435	0.0276	0.2867	0.1576

Table 3: (CCMM) amplitudes and ratios for FFT components of simulated y(x) for different setpoints C_{set}

Table 3 shows, that the amplitudes of the higher order frequency components in the simulated Y(x) function for the geometry with rounded finger and sine pattern are about 11% of the first order harmonic, for a setpoint capacitance of C_{set} = 300 aF / period. This is for ICMM given in Table 2 about 62%. In other words, for CCMM the difference between Y(x) and a pure sine-function is less than the difference between *C(x)* and a pure sine for ICMM. This is also predicted by the analysis in chapter 3. Therefore, the ideal geometry combination that produces a pure sine-function *C(x)* for the ICMM concept will not be the same ideal geometry combination that produces a sine-function *Y(x)* for the CCMM concept.

However, for an increase in setpoint capacitance C_{set} for CCMM also the ratio between higher order frequency components and first order harmonic increases. This is very probably because the ratio between period size and rounded fingers is not exactly a situation with probe-like dimensions as discussed in chapter 3. Taking rounded fingers with a finger length $L_f > 2A$ (*A* = amplitude of sine pattern, chapter 3) gives a better result than rectangular fingers. 'Luckily', the fingers are rounded by the plasma etching process as given in Fig. 1, Fig. 8 and explained more in chapter 5 about design and fabrication.

The 2D-FE simulation results sustain the conclusion of the CCMM analysis in chapter 3 in terms of expected shape of *Y(x)* for the geometry combination of a sine with a finger-like pattern. The predictions for CCMM in terms of SNR improvement have not been examined. However, for all calculated positions for CCMM the capacitance can be $C(x, y(x)) = C_{set}$ = 300 aF while for ICMM the capacitance *C(x)* = 300 aF only around x = 0 and *C(x)* = 125 aF around $x = P_x /2$ for the given geometry and ratio of feature sizes. Therefore, in terms of signal amplitude of the capacitance measurement, the SNR can be higher for CCMM than for ICMM at given noise-levels.

4.7 Discussion

Although the FE-simulations are only 2D and the influence of parasitic capacitances is neglected, the results indicate that the periodic sensor-capacitance can be $C_s \approx 15$ [fF] and $\Delta C_{max} \approx 7$ [fF], if we apply 2 arrays of 50 finger-pairs along the sides of the slider. We think it should be possible to measure the change in capacitance versus displacement, using a charge amplifier and synchronous detection [2,4].

Using a modified Martin oscillator, Zwijze [6] and Toth [7] report that a capacitance of about 2 [pF] can be measured with an accuracy of 0.01% corresponding to an accuracy of 200 [aF]. They report that the resolution amounts to 50 [aF]. Kung et al [8]] have reported an integrated air-gap-capacitor pressure sensor where a 100 [fF] air-gap-capacitor could be measured with a resolution of less than 30 [aF].

We consider using the changing capacitance of the comb-actuators as a coarse displacement sensor. Legtenberg [9,10] has studied this before. He performed quasi-static measurements of capacitance versus dc-bias voltages, using a gain-phase/ impedance analyzer (HP4194A). Over a deflection range of 30 [µm], he measured a linear change $\Delta C/\Delta x \approx 2.67$ [fF/µm] versus squared voltage (V^2), with initial capacitance $C_{comb} \approx 300$ [fF] ($\Delta C_{max} \approx 80$ [fF]).

For a comb-structure the capacitance $C(x)$ between rotor and stator can be expressed as [9,10]:

$$C(x) = \frac{2 \cdot n \cdot \varepsilon_0 \cdot h \cdot (x + x_0)}{g} \qquad \text{(Eq.4.8)}$$

and the change in capacitance $\Delta C(x)$ is given by:

$$\Delta C(x) = \frac{\partial C}{\partial x} \cdot x = \frac{2 \cdot n \cdot \varepsilon_0 \cdot h}{g} \cdot x \qquad \text{(Eq.4.9)}$$

With the number of comb-fingers n, dielectric constant ε_0, structure height h and gap distance g and initial overlap x_0.

At larger displacements the change in capacitance per change in displacement has to be detected from an increasing capacitance $C(x)$. In other words the ratio $\frac{\partial C}{\partial x}$ / $C(x) = 1/x$ (i.e. sensitivity) is decreasing for increasing displacement x. When two comb-sensors are read-out differentially with $C_1 = C + \Delta C(x)$ and $C_2 = C - \Delta C(x)$ we can measure $(C_1 - C_2)/(C_1 + C_2) = \Delta C(x)/C \propto x/x_0$ and the sensitivity has become constant. The total range of displacement is limited of course by the length of the comb-fingers. This is a drawback of the comb-drive actuator, not of the incremental capacitive sensor concept. With the combination of a comb-structure, functioning as a coarse position sensor, and the periodic capacitive position sensor presented in this paper, a high-accuracy, long-range incremental position measurement for microactuator systems may be obtained.

An alternative for the comb-drive actuators is the use of stepping micromotors reported by Tas [11] and Sarajlic [12]. The reported inchworm stepping motor [12] can be realized in a relatively easy three mask fabrication process using a single poly-silicon layer. In principle, stepping motors are able to generate much more force and displacement range than the conventional comb-drive. A combination of a capacitive incremental position sensor as presented in this thesis and a stepping motor maybe the most interesting option for position control and optimizing performance.

The given figures of measured resolution of capacitances and predicted simulated capacitance values also proof that measurement of the capacitance-changes of the periodic capacitive position sensor is feasible.

Thus, in chapter 6 we will present measurement results, for ICMM open-loop operation and CCMM closed-loop operation, and further assess and compare the measured results with the simulation results.

The results and conclusions after the comparison between ICMM and CCMM in terms of spatial frequency components, have further sustained the conclusions and expectations of the

analysis in chapter 3 for the CCMM concept. For CCMM a combination of a sine pattern on the slider and probe-like fingers on the sense-structure is expected to give a good approximation of a sine-shaped *Y(x)* function for the position of the sense-structure. The fingers should be longer than the amplitude of the sine for larger amplitudes of *Y(x)*.

A further optimization of geometry shape and ratio of feature dimensions to find an ideal sine-shaped or triangular-shaped capacitance function *C(x)* for ICMM or *Y(x)* for CCMM has not been undertaken yet. Also, the simulation algorithm for CCMM can be optimized with more advanced algorithms.

First, the realizability through micromachining and the measurability with the proposed methods has to be established and evaluated. This will be done in the successive chapters.

4.8 CONCLUSIONS

We have performed 2D-Finite-Element simulations for an in-plane periodical capacitive position sensor with micrometer dimensions. The basic idea is to have a periodic geometry or structure (slider) moving in relation to a fixed periodic sense-structure, giving a periodic capacitive read-out. Two concepts have been presented:

Open-loop Incremental Capacitance Measurement Mode (ICMM) is the measurement of capacitance-change vs. displacement (i.e. sense-structure is held at a fixed distance from the slider),

Closed-loop Constant Capacitance Measurement Mode (i.e. sense-structure is actuated to keep the capacitance between sense-structure and slider constant as the slider moves).

Simulation-results for the ICMM concept shows that the periodic change in capacitance is large enough to measure, providing an incremental position-measurement over ten's of μm range with potentially high accuracy.

The constant capacitance concept CCMM (closed-loop) may outperform the ICMM (open-loop) concept because for all positions of the slider the capacitance is held at a larger constant value, leading to a higher SNR.

The simulated displacement function *Y(x)* for CCMM approximates a perfect sine better than the capacitance *C(x)* for ICMM. The non-linearity due to higher order harmonics is a factor 4 - 5 less for CCMM and amounts to only 11% of the first order amplitude for a constant capacitance C_{set} = 300 aF/finger-pair.

However, the better performance of CCMM may be at the expense of more complicated closed-loop control electronics and more critical demands for the mechanical design and its dynamical performance.

References

[1] R.P.Feynman, R.B.Leighton, M.Sands, *The Feynman Lectures on Physics,* vol.2, 7-1/7-5, Addison-Wesley publishing company, 1977.

[2] M.Elwenspoek, R.J.Wiegerink, *Mechanical Microsensors,* Berlin Heidelberg New York, Springer-Verlag, 13-21, 2000.

[3] B.E.Boser, R.T.Howe, Surface micromachined accelerometers, *IEEE J.Solid-State Circuits*, **31**, 366-375, 1996.

[4] L.K.Baxter et al., *Capacitive Sensors: Design and Applications*, IEEE Press, New York, 1997.

[5] www.femlab.com, comsol, Sweden

[6] A.F.Zwijze, *Micro-machined high capacity siliconload cells,* Ph.D thesis, Enschede, University of Twente, 89-122, 2000.

[7] F.N.Toth, *A design methodology for low-cost, high performance capacitive sensors*, Ph.D.thesis, Enschede, University of Twente, 1997.

[8] J.T.Kung, H.S.Lee, An integrated Air-Gap-Capacitor Pressure sensor and digital readout with sub-100 attofarad resolution¸ *J. of Microelectromechanical systems*, **1**, no.3, 121-128, 1992.

[9] R.Legtenberg et al., Comb-drive actuators for large displacements, *J.Micromech. Microeng*., **6**, 320-329, 1996.

[10] R.Legtenberg, A.W.Groeneveld *et al*, Towards Position control of electrostatic comb drives, Proc. 6th Workshop on Micromachining Micromechanics and Microsystems (MME'95), Copenhagen, Denmark, 3-5 Sept.,1995.

[11] N.R.Tas, *Electrostatic Micro Walkers, Micro Electromechanics and Micro Tribology*, Ph.D. Thesis, University of Twente, Enschede 2000.

[12] E.Sarajlic, A low volume electrostatic inchworm microactuator with high-resolution and large force, *Proc. Eurosensors XVII*, 194-195, Portugal, Sept. 2003

5 Design and Fabrication

5.1 INTRODUCTION

This chapter gives the description of two fabrication processes for an electrostatic microactuator device with an integrated periodic capacitive position sensor.

The first process is a surface micromachining process (denoted as Poly-process) with poly silicon as the structural layer [1,2], the second is a newly developed bulk micromaching process (denoted as TWIN-process) with mono-crystalline Silicon of the substrate as the device layer [3,4].

The main objective has been to realize test-devices in order to do experiments and assess the feasibility, operation and performance of the concepts ICMM and CCMM as presented in chapter 3. Several designs have been made and realized and some details are given in this chapter and in the appendix a full design layout is given for both processes. The experimental results given in the next chapter are obtained with devices made with the Poly-process. Experiments with devices made with the TWIN process are anticipated in the near future.

The 2D-FE simulation results in the previous chapter show, the capacitances C(x) and capacitance changes ΔC(x) will be small for the presented concepts. The best way of measuring small capacitances is done when the device is enclosed with strong fixation inside a cage of Faraday (metal or conductive box), to shield the device under test from noise caused by the Electro Magnetic Interference (EMI) generated by external sources, and environmental disturbances e.g. change in humidity, temperature, pressure, vibrations etc. Ideally, only the capacitance that changes with displacements generated by the microactuator should change; all other capacitances (i.e. called parasitic) should be small and constant.

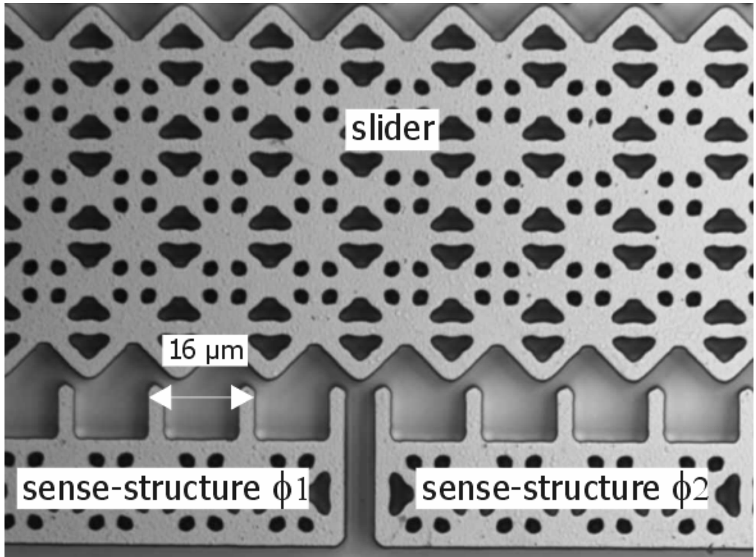

Fig. 1: Example of a micromachined device with integrated periodic capacitive position sensor.

With an increase in structure height the change in capacitance ΔC(x) is increased too, which means an increase in resolution and accuracy to detect and measure displacements.

The structure height for the Poly-process is limited to h = 5 μm. With the TWIN process structure heights can be increased by a factor 5 or more. This is also beneficial to a number of mechanical properties as will be explained in section 5.3.

5.2 TYPICAL FABRICATION STEPS IN POLY-PROCESS

The fabrication of the test devices with integrated incremental capacitive position sensor is relatively easy using a one-mask surface micromachining technology as described by Legtenberg [1, 2]. In this section the typical fabrication steps are given and discussed. A summary of the process outline is given in Table 1; the complete process-outline is given in Appendix 2.5

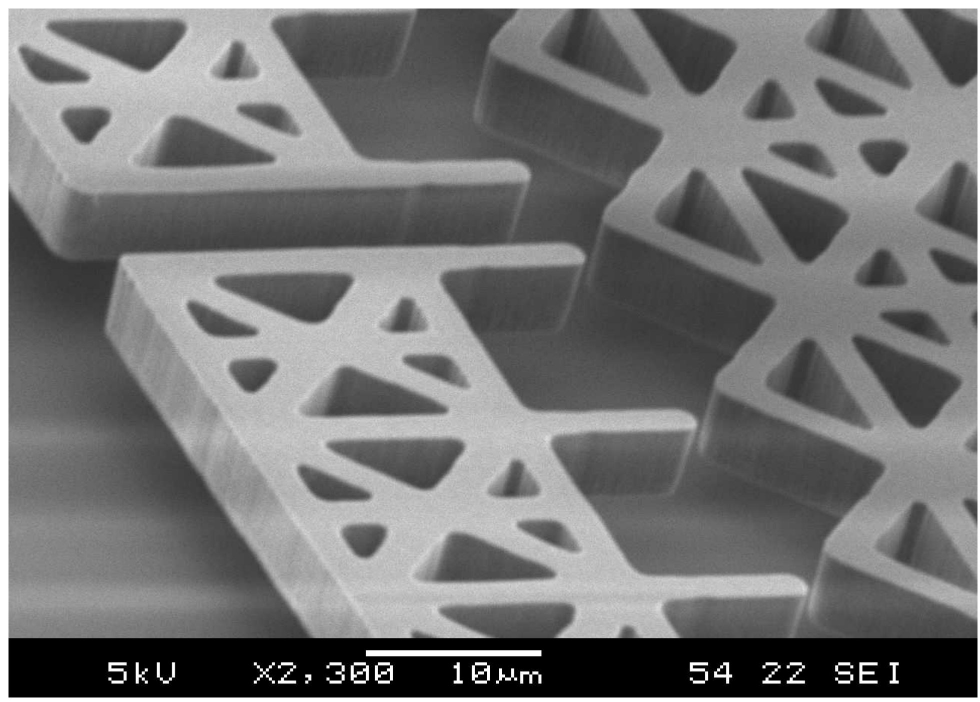

Fig. 2: SEM-photo of a surface-micromachined 5 μm-thick poly-Si device after wet release etching of the 3 μm-thick sacrificial oxide layer (SiO_2). The sense-structures have a rectangular, the slider a triangular periodic geometry with 16 μm period.

The basis of the surface-micromachined structures is a conducting Silicon (Si) wafer (4-inch – 100 mm) with a 3 μm thick sacrificial Silicon-Oxide layer and a 5 μm thick poly-Silicon (poly-Si) layer on top see Fig. 2 and Table 1. The poly-Si layer is made conductive by doping of the layer with Boron.

The first photolithography step is performed to develop Chrome / Platinum electrode pads for good electrical contact with the poly-silicon device.

After the second photolithography step, the structure is patterned by plasma-etching of the Poly-Si layer and finally this layer is released by wet-chemical etching of the sacrificial SiO_2 layer. The moveable parts of the device are suspended through flexure beams, which are at one end fixed to the substrate by anchor pads.

The SEM photo in Fig. 2 shows that all Poly-Si structure parts that should be fully suspended and moveable have an open structure. The (B)HF isotropically etches the SiO_2 underneath all Poly-Si parts. However, due to the open structure, the release time for all moveable parts is much shorter than for the parts that should remain fixed to the substrate

and therefore do not have this open structure. After release etching a freeze drying process is used to dry the released device and avoid stiction of the moving parts to other parts or to the substrate. The chip with the device is broken off from the wafer and ready to be connected, packaged and used for experiments. This summarizes the process outline given in Table 1.

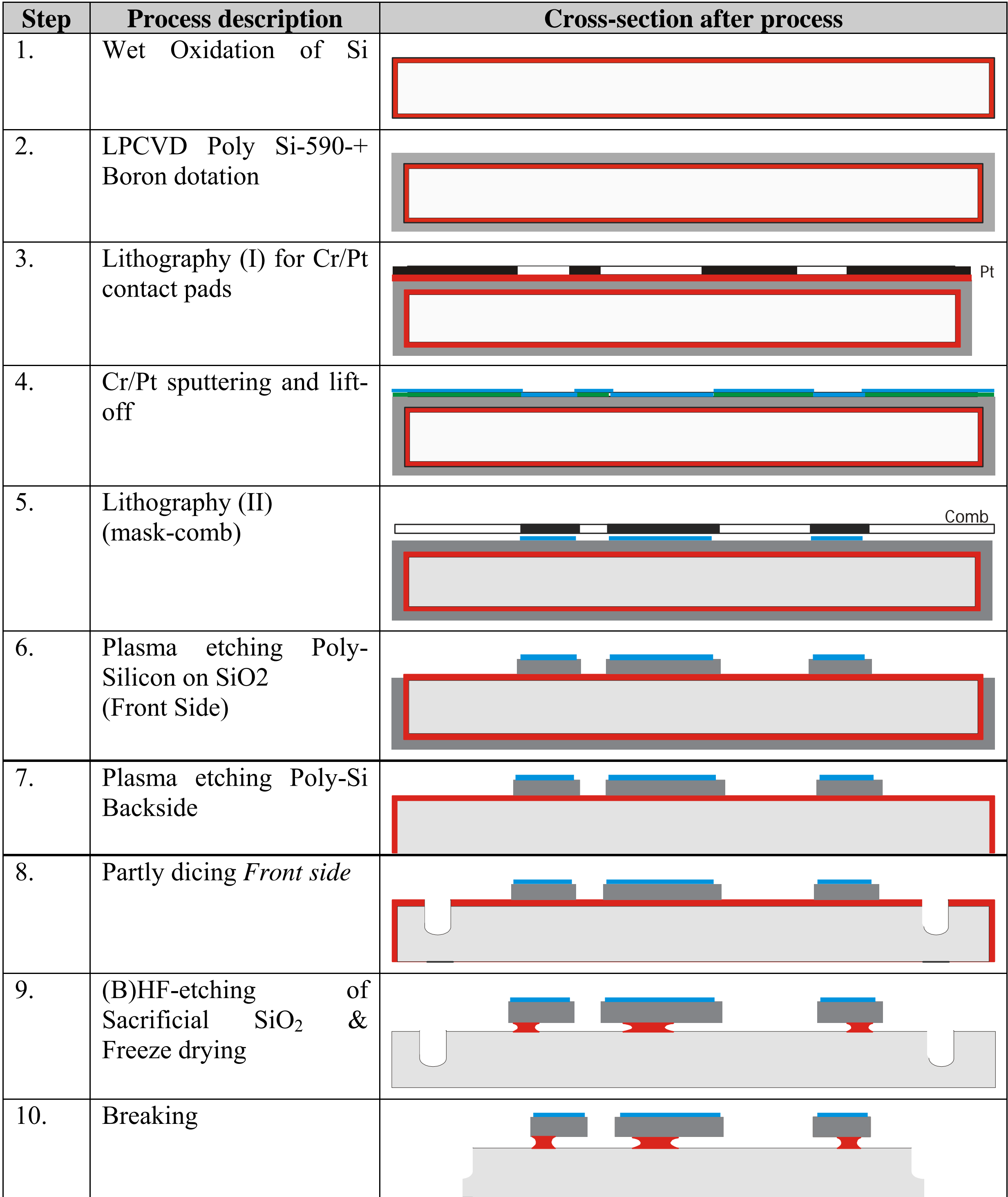

Step	Process description	Cross-section after process
1.	Wet Oxidation of Si	
2.	LPCVD Poly Si-590-+ Boron dotation	
3.	Lithography (I) for Cr/Pt contact pads	Pt
4.	Cr/Pt sputtering and lift-off	
5.	Lithography (II) (mask-comb)	Comb
6.	Plasma etching Poly-Silicon on SiO2 (Front Side)	
7.	Plasma etching Poly-Si Backside	
8.	Partly dicing *Front side*	
9.	(B)HF-etching of Sacrificial SiO_2 & Freeze drying	
10.	Breaking	

Table 1: A summary of the most important process steps

In the following part, each step in Table 1 is explained in more detail and supported with arguments.

Conduction of Substrate and structural layer

With the surface micromachining process presented and discussed in this section the aim has been to make a device with integrated periodic capacitive position sensor as in Fig. 1 and Fig. 2 which can be packaged and connected within a cage of Faraday. Further necessary requirements for measuring the small changes in capacitance versus displacement are to use a highly doped Silicon wafer and poly-silicon layer and glue the substrate on a grounded copper plate. This is necessary to have the in coupling of noise-sources (EMI) and induced currents and voltages as low as possible.

The Silicon wafer is highly Boron-doped such that it can function as an equi-potential plane. The resistivity of the wafers is specified as ρ_s = 0.001-0.002 Ωcm. Also the poly-Si layer is heavily Boron-doped. The resistance is measured and for Boron-doped poly-Si the resistivity is $\rho_s \sim$ 0.002 Ωcm. (Copper 16 nΩm)

Thickness of sacrificial oxide layer

Ideally, there wouldn't be any substrate underneath the sensor-capacitance unless if possible some form of guarding [5] could be used. The structure height would be at least 10x more than the gap-width of the sensor capacitances with the gap-width as small as possible. For this fabrication process and design however, a substrate and oxide layer are necessary as carrier of the device and for anchoring the suspended slider beam and sense-structures. The capacitances from contact- or electrode plates and sense-structures to the substrate should be as small as possible i.e. capacitance C_{10} in Fig. 3. The sensor-capacitances C_{12} should be as large as possible. If the input of the charge-amp, as explained in chapter 3, is connected to the slider beam it will become a virtual ground. If the substrate is proper grounded and highly conductive, there will be no voltage across capacitance C_{20} in Fig. 3 and thus C_{20} is effectively eliminated.

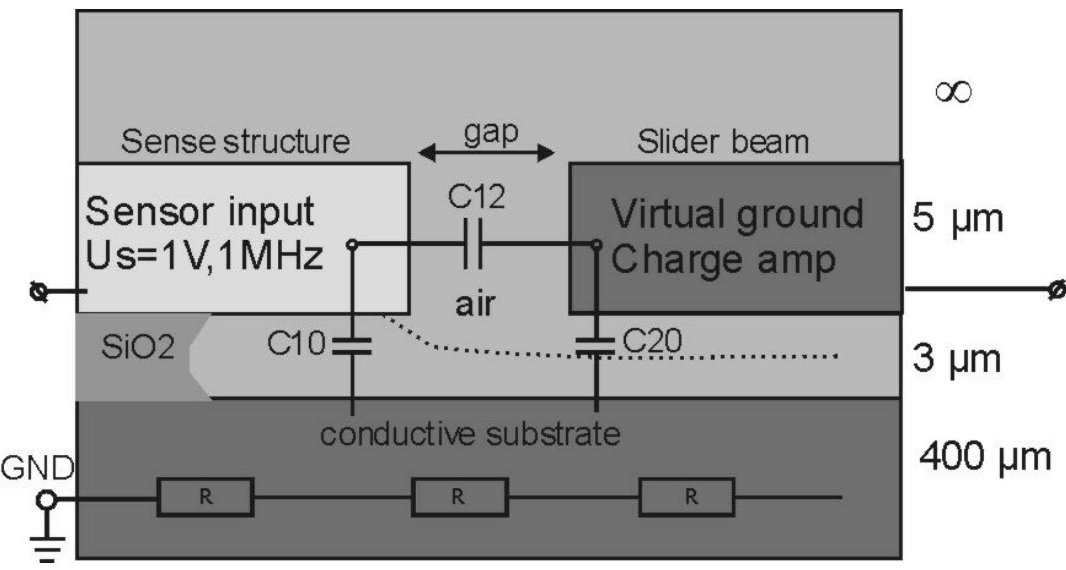

Fig. 3: A cross view of the gap between a sense-structure and slider beam and a lumped element model to depict the influence of structure height h, gap-size g, oxide-thickness d_{ox} and substrate resistivity R

A smaller thickness of the oxide layer means a larger capacitance C_{10} and an increase of the influence of the substrate on the electrostatic field and charge distribution between and on the two 'plates' formed by the slider and sense-structure.

Therefore, a smaller distance between structure and substrate will negatively affect the

sensor-capacitance C_{12}. Baxter [5] for example describes that the capacitance between two cylinders is reduced by the proximity of a ground plane.

This effect together with a limited or lower conductance of the substrate causes cross-talk and induced currents going directly through capacitance C_{10}, the substrate and C_{20}, are then picked up by the charge-amp.

However, a compromise is found within the current process where the height of the structure, the gap-width and the thickness of the oxide are limited between what is possible and what desirable. The thickness of d_{ox} = 3 μm is taken relatively large, larger than the minimum obtainable gap-size with standard lithography (i.e. 2 μm in MESA$^+$ clean room).

The advantage of growing this thick oxide layer by thermally oxidation in 30 hours at 1150°C is that this sacrificial layer is formed on both sides of the wafer. Any occurrence of stress or a stress-gradient in the layer is balanced on both sides of the wafer, and will have little effect on following processes. Alternative routes for the formation of oxide (PECVD) have been followed as well, but the combination of thermal oxidation and deposition and dotation of the 5 μm-thick poly-Silicon layer presented here gives the best result in terms of low stress and low stress gradient.

For the anchor points of the flexures of the moveable parts it would be possible to make holes in the oxide layer and have the poly-Silicon connected to the substrate. Thus avoiding any voltage differences between moveable parts and the substrate that form a risk of electrostatic pull-down and stiction of these parts Legtenberg [6]. To open these windows in the oxide layer would require another mask design. The step coverage of LPCVD poly is such, that the filling of the hole with poly will not cause any problems. However, this option has not been implemented in the process outline presented in this work. The process outline given here has the minimum required process steps for proven good operation of comb-drive devices.

Poly deposition + Boron doping of structural layer

The structural layer requires a low-stress, high conductive poly-layer, as thick as possible. With a low stress layer the structures will be perfectly in plane after releasing. A high conductance is desired for the same reasons as for the conductance of the substrate, no losses, less cross-talk. And an increase in thickness would give an increase in capacitance variations.

However, the thickness of the poly-silicon layer is limited to ca. 5 μm as a standard limit for the MESA$^+$ laboratory. The reason is that a uniform distribution of Boron through poly-layers without the built-up of stress (gradient) is problematic for layers thicker than 5μm. Therefore, the standard scheme for the deposition and doping of the poly-layer including the use of an oxide (SiO_2) capping layer has been followed. It had already been proven to result in working devices [1, 2, 7] and would therefore form less of a risk in the fabrication of working devices with integrated capacitive position sensors.

Photo-lithography (I): pattern transfer for Chrome/Platinum contact pads

In the first photolithography step the pattern for the Chrome/Platinum contact pads is transferred to the poly-SI layer. In IC-industry it is common practice to make electrical connection to heavily doped Poly-Silicon through a contact layer of aluminum. The use of aluminum is not possible in the current process-outline because the aluminum will dissolve in BHF during sacrificial etching. In this process scheme we built in the possibility to

develop a chrome / platinum (Cr / Pt) contact layer on top of the polysilicon contact pads for better electrical contact. A Cr / Pt pad also gives better wirebonding results (i.e. connecting every contact pad with an Aluminum-wire of 25 μm diameter) than on bare poly-Silicon pads and thus also for this reason a better electrical contact.

To this end, a second mask is used (photolithography (I)) in combination with a lift-off process. Thus, only on top of the poly-Si contact pads a small pad of Cr/Pt is sputtered on, the rest of the structure layout is completely without Cr/Pt.

The chrome layer of 20-50 nm is an intermediate adhesion layer because a platinum layer of 100 – 150 nm directly on top of the poly-Si contact pads would show poor adhesion. Both materials, Chrome and Platinum, are BHF resistant. The presence of a native oxide layer at the surface of the Poly-Si should be avoided to give better adhesion of the Chrome to the Boron-doped Poly-Si contacts and to give better conduction. Furthermore, if there are cracks and pinholes in the platinum and chrome layers, a possibly remaining layer of native oxide is etched by the BHF during sacrificial layer etching and the Chrome's adhesion to the Poly-Silicon pads is decreased and it may come off.

During dry-etching of the poly-silicon structures at a later stage in the processing, the chrome / platinum pads are covered by thick photoresist.

A Shottky-diode effect for the Cr / Pt to heavily Boron doped poly (p^{++}) or the aluminum wirebond connection to the Pt-layer is not studied. However in the appendix 2.6 a measurement result is given of the measured conduction (I-V curve) of two Cr / Pt pads on a highly-doped silicon wafer and it is concluded that a contact potential effect or a shottky-diode effect is negligible.

Photolithography (II): pattern transfer of structure layout

After deposition of the metal contact layers the second photolithography step is done to transfer the pattern for the structural layer. One important aspect of this second photolithography-step to the fabrication of the devices presented here is the minimum feature size of gaps, comb-fingers, flexure beams, etc. of the standard available photolithography in the MESA$^+$ laboratory. For the current lithography the smallest gap size and width of fingers is around 2 μm, see Fig. 5.

In the mask design (structure layout) the two periodic geometries on slider and sense structure respectively are displaced with a horizontal offset. The minimum gap-size can in this way still be smaller than 2 μm when the structures are facing each other at the tops. But, to implement a quadrature detection technique as explained in chapter 3, two sets of periodic geometries have to be employed to produce 2 measurement signals with a phase difference of 90 [deg.]. This is explained in Fig. 4. The smallest gap size that can be resolved in the photo lithography (with close to 100% yield) is indicated with distance c.

Taking distance a = $P_x/2$ in Fig. 4 (right) it follows that a/2 = $P_x/4$ in Fig. 4 (left). The gap-distance g_1 and g_2 are relatively free to choose but it also depends on the specific geometry combination. For a combination of 2 triangular patterns a minimum gap distance $g_{min} \sim 0.5$ μm was possible. For smaller g_{min} an initial actuation of the sense-actuators is required to pull the sense-structures away from the slider before the slider can move over larger distances. Still, a minimum gap of $g_{min} \sim 0.5$ μm is a significant increase of the change in capacitance ΔC by a factor more than 4, as concluded from the results in chapter 4.

However, this trick doesn't work as good for smaller period-sizes. The smallest finger width w = 2 μm for the finger-like pattern. The minimum period size for a pattern

combination as indicated in Fig. 5 (left) if quadrature detection is taken up in the design, is around P_x = 8 μm for a limited finger width of w=2 μm. Another aspect is that besides the limitation of the minimum width of the slider pattern to w = 2 μm also the maximum width is limited if the poly-process is used. Because, the aim is to release all moveable parts in approximately the same amount of time this slider pattern should also have a band of width ~ 2 μm. (The pattern in Fig. 5 (left) therefore would need some adjustment). Fig. 5 (right) shows a micromachined device with a Sine-Rectangular finger combination with a period size P_x = 16 μm.

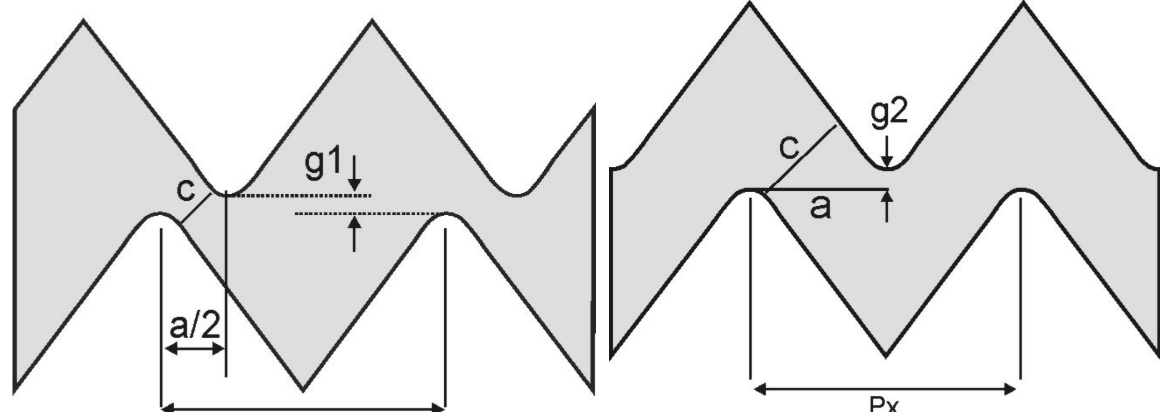

Fig. 4: For quadrature detection two sets of geometries are required. With a smart design the minimum gap-distance can be made smaller than the minimum resolvable gap of the Mesa$^+$ standard photo lithography.

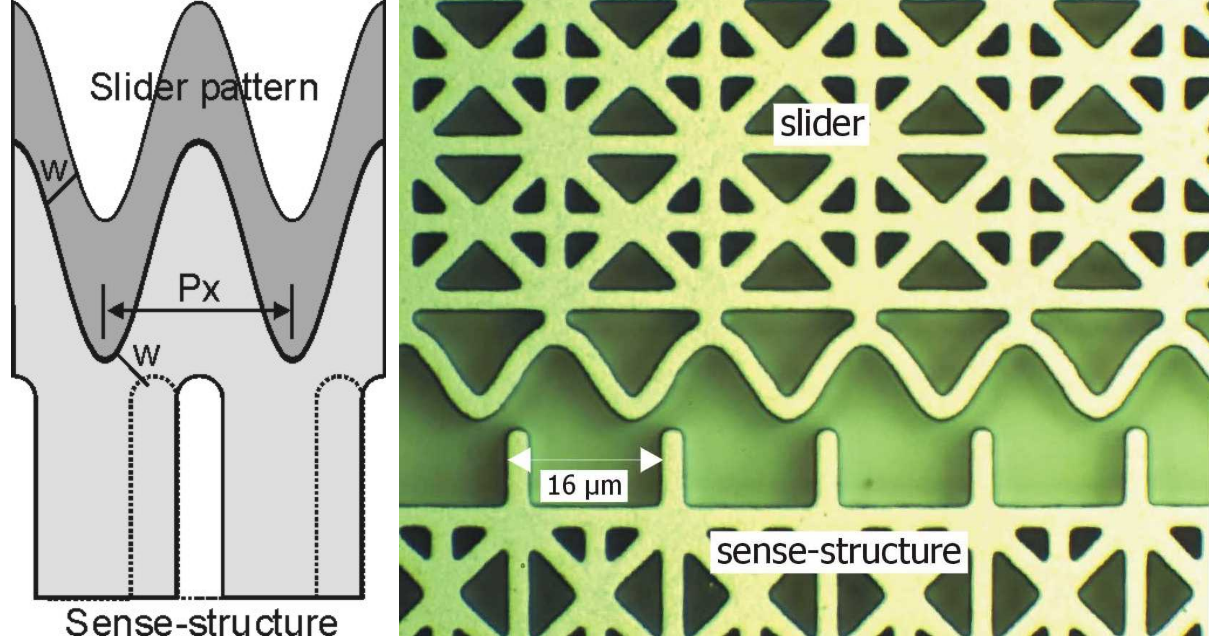

Fig. 5: (left) Illustration of limited period size for a limited resolvable gap-distance and feature size of w = 2 μm, especially if also quadrature detection is employed in the design. (Right) Picture of a realized device where the periodic geometry on the sense-structure has a horizontal offset with respect to the periodic geometry on the slider. The minimum gap distance between the geometries can be smaller than the design rule for the minimum allowable gap using the standard photolithography.

The aspect ratio for the plasma-etching of the poly-silicon structures is around 10-20. This means that for a height or layer thickness of 5 µm the smallest feature size is around 500 nm. Fig. 5 (right) also shows that rectangular fingers are rounded by the photo-lithography and the plasma etching.

The roughness of the structures depends on the settings of the Bosch plasma etching process. Each cycle in this process includes two steps: an etching step and a passivation step (to cover and protect the etched side-walls).The roughness will be around 50 – 100 nm.

These aspects play an important role that has to be considered in the fabrication and design of periodic geometries for which an ideal capacitance function versus displacement is expected e.g. a pure sine or triangular function see chapter 3 and 4.

If the plasma-etching process would be the limiting process for the minimum feature size of 500 nm for a thickness of 5 µm this would mean that the period size for the periodic geometries could be decreased by a factor 2 or more. This would in principal be beneficial to the measurement of position over long distances, because it would simply mean that more periods are counted for a certain displacement. However, the consequences for the change in capacitance within each period have to be considered too. The simulation results in chapter 4 predict that for a given ratio between period size and finger width the maximum variation in capacitance remains the same for a smaller finger width and period size.

A key aspect of the concept for the integrated periodic capacitive position sensor presented in this thesis is the possibility to move the sense-structures closer to the slider with additional actuators (e.g. comb-drives). This has been included in the design for the devices. Thus, a solution is found to get gap-sizes smaller than the minimum resolvable gap-size for the photolithography of ~2 µm. For the concept CCMM concept given in chapter 3, the controllable gap-size is crucial. Gap distances of around 200 nm can be expected for this concept.

Dicing

The mask used in the lithography-step (II) to transfer the mask-design to the poly-Si layer contains many cells of 5 x 5 mm^2. Each cell has 1 mm spacing with each neighboring cell to give enough room for dicing and breaking at the end. Before etching the SiO_2-layer and thus releasing the moveable parts of the poly-Si structure, the wafer is partly diced. With 1 mask and photolithography step the device structures and alignment markings for the dicing are transferred to the front side of the wafer. The right depth of dicing on the front side is empirically found. A height of around 280 µm including foil thickness will be left, indicated in Fig. 6. After dicing, the structures can be etched free and each cell is broken off from the wafer and packaged for further testing and measurements.

Fig. 6: Indication of dicing height.

Sacrificial SiO2 etching + Freeze drying

The releasing of the poly-Silicon structures through wet-etching of the sacrificial SiO_2-layer includes the cyclohexane freeze-drying process to prevent stiction and adhesive bonding of free structures to the substrate [2]. This process involves the sublimation of a solid (frozen cyclohexane) to a gas avoiding the melted fluidic phase. This prevents the capillary forces to pin the structures down to the substrate.

Reflection on an alternative option SOI

The use of so called Silicon-On-Insulator (SOI) wafers has also been considered. This option is interesting because a larger structure height is easily available and the structure layer is single-crystalline (instead of poly-crystalline) with better defined material properties. However, with the new developed TWIN process presented in the next section, the option of buying SOI wafers appears to be obsolete for the fabrication of our test devices with integrated incremental capacitive position sensors.

Results and redesign

Two generations of devices have been designed and realized with the fabrication process as explained in the previous chapter. The designs for generation (I) devices contain some design failures including sense-structures with a too high stiffness of the flexures and an error in the horizontal shift between periodic geometries to enable the quadrature concept. Controlling the gap-size between slider and sense-structures would require too high voltages for the sense-actuators. However, these devices contain various combinations of periodic geometries and the experimental results are given in the next chapter. A design lay out for one of the generation I devices is given in Appendix 2.1.

After a redesign a second generation of devices was realized. An example of a design layout is given in Appendix 2.2. The redesign made it possible to control the gap between sense-structures and slider and therefore perform measurements for CCMM concept. For these devices the extra steps in the process layout have been included to obtain Chrome – Platinum contact pads for better wirebonding results. Experiments with these devices for the concepts ICMM and CCMM are given in the next chapter.

We conclude this section with the presentation of some fabrication results of both generations. Appendix 2.5 gives the poly-process outline in more detail.

5.2.1 Examples of devices made with the poly-process

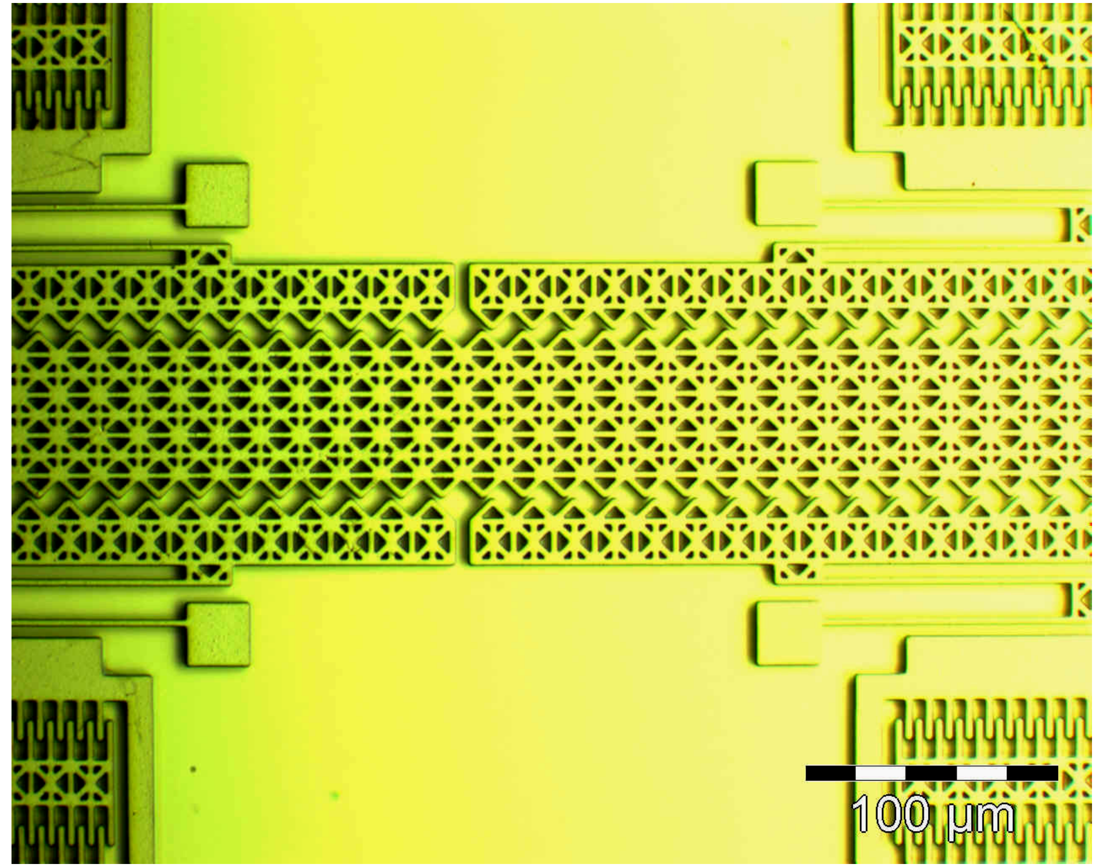

Fig. 7: Micromachined device with triangular patterns on both slider beam and sense-structures, (generation I).

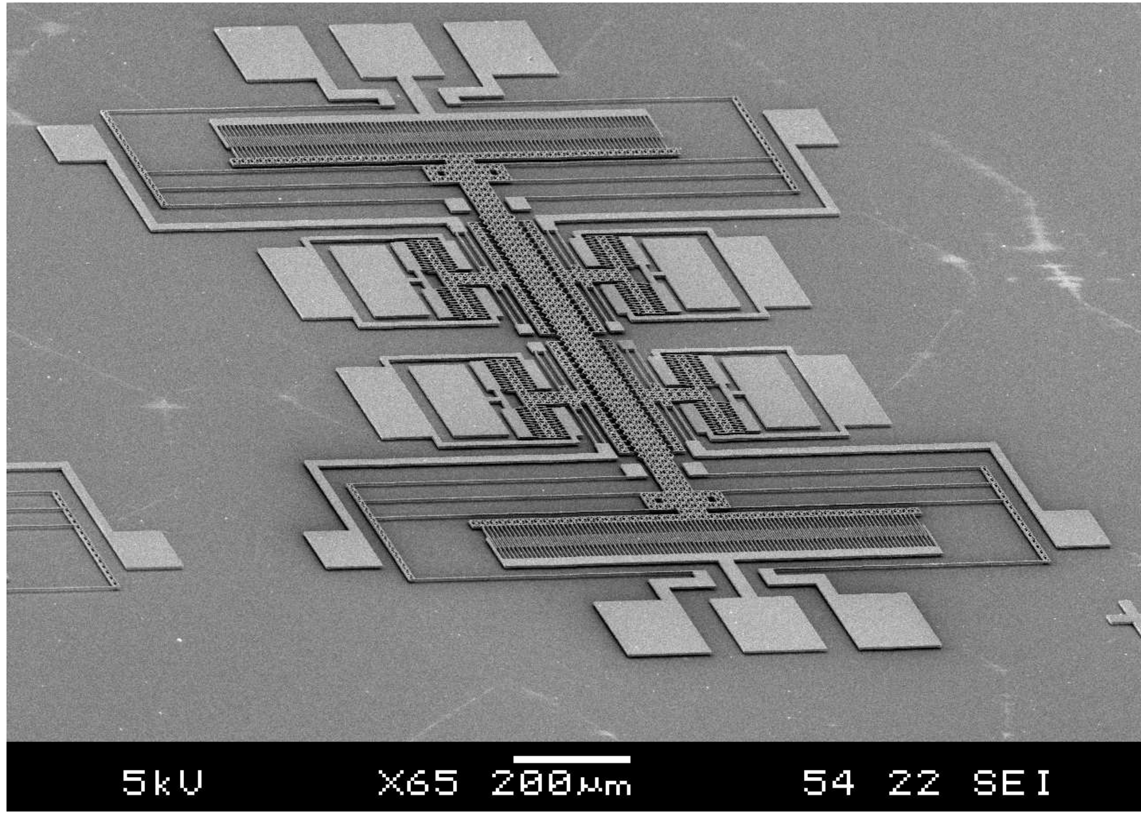

Fig. 8: SEM picture for a complete overview of a (test) device (generation I)

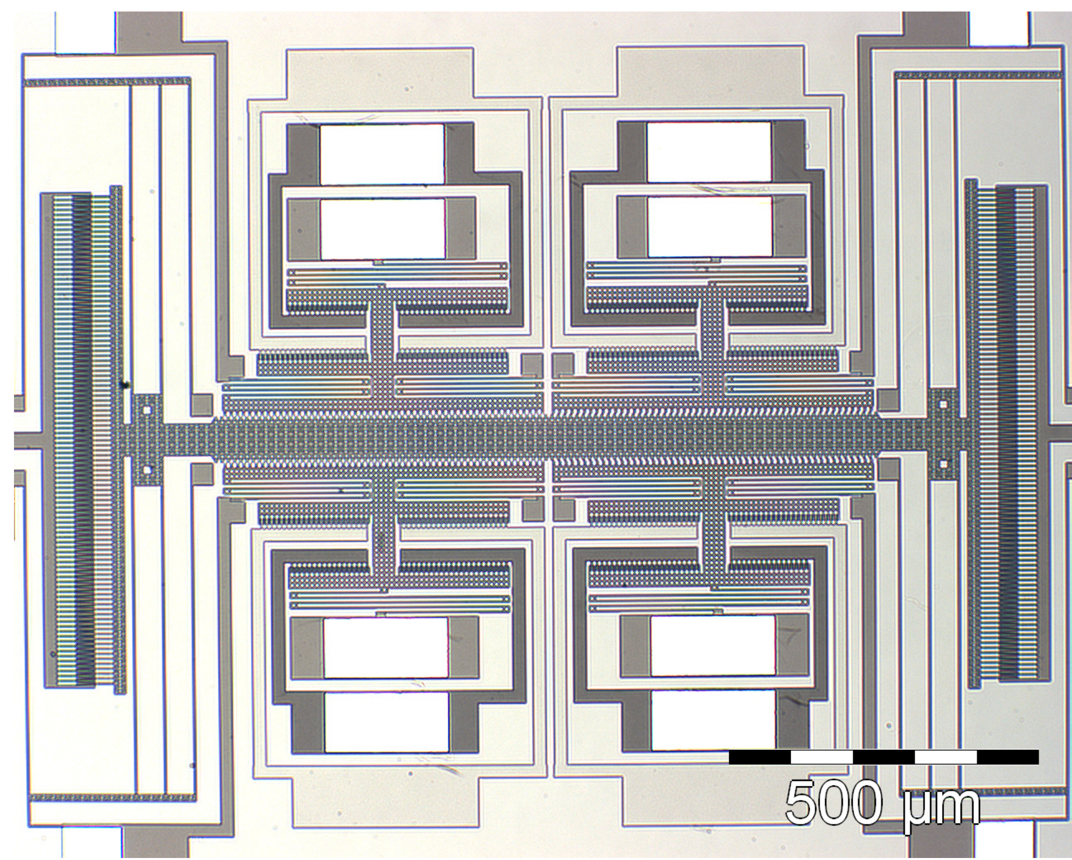

Fig. 9: Complete overview of device (generation II) made with poly-process.

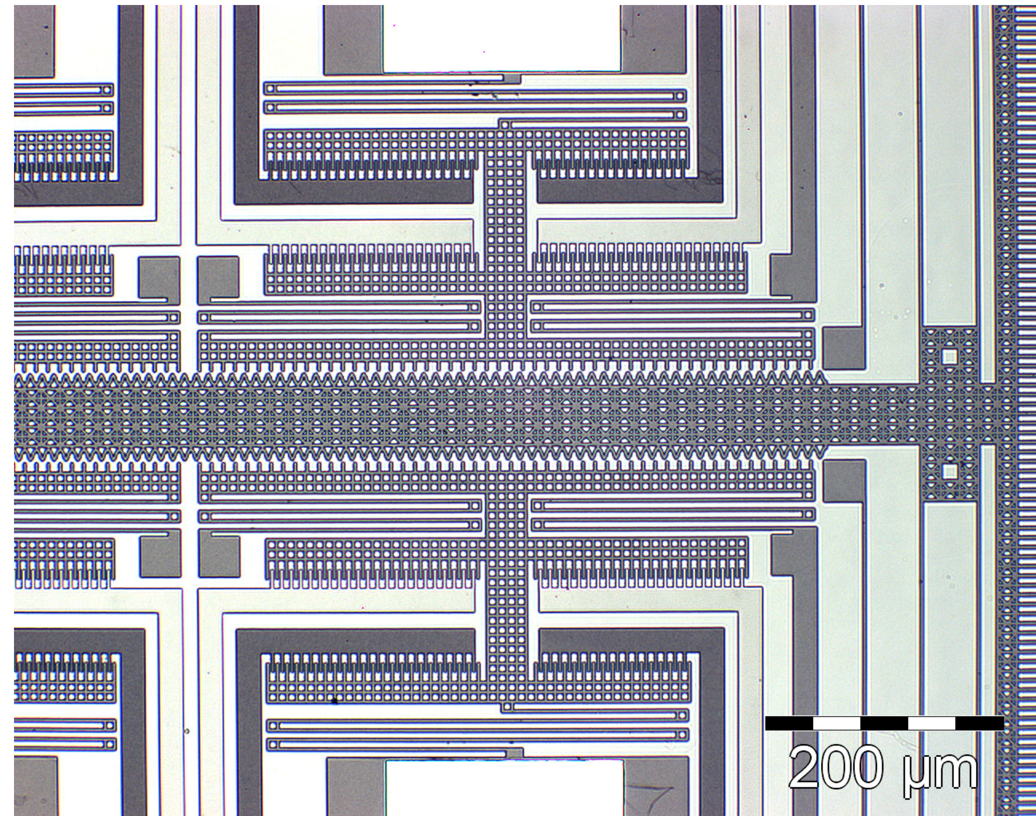

Fig. 10: Enlargement of Fig. 9 showing the sense-structures, sense-actuators at both sides of the slider beam.

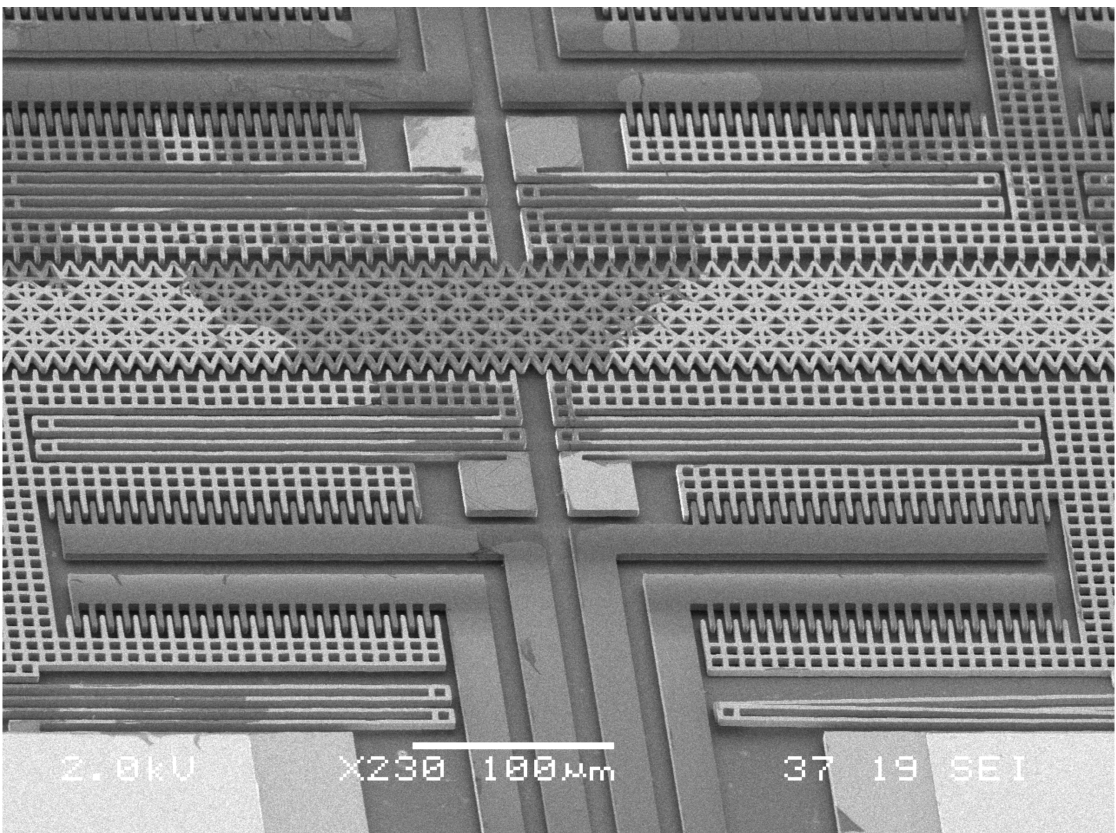

Fig. 11: SEM picture of device in Fig. 9

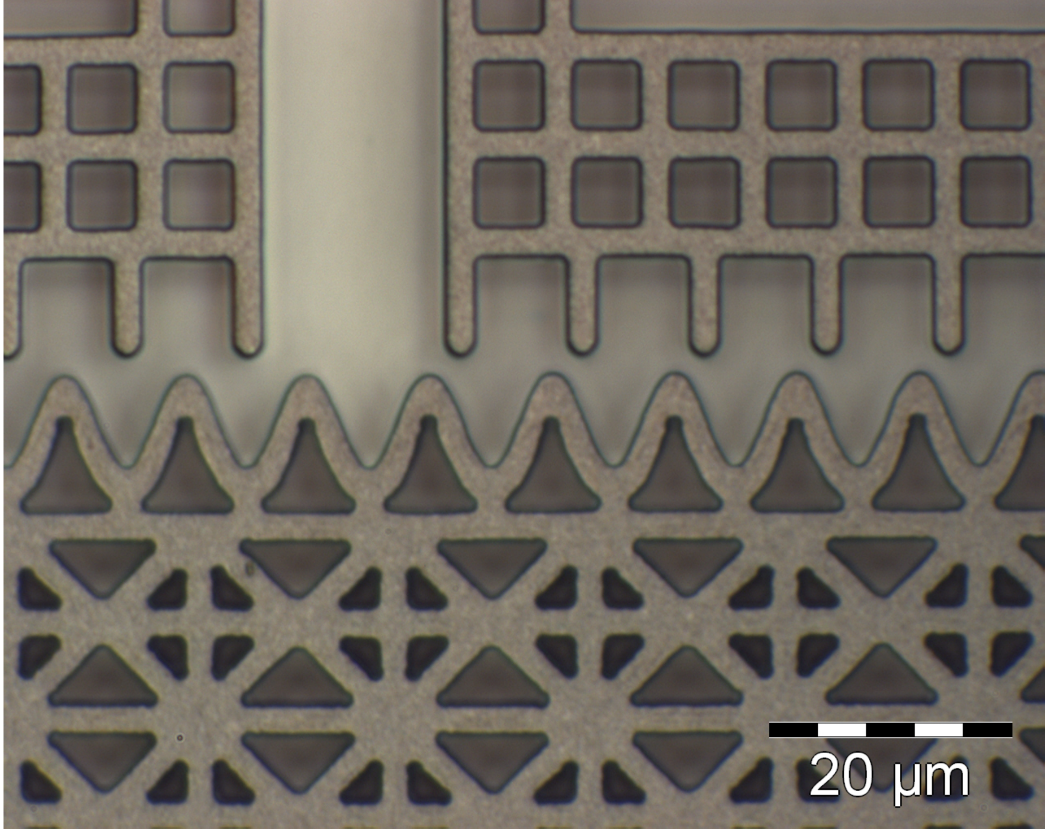

Fig. 12: Close-up showing (in) accuracies after the total process sequence of the shape of the sine-pattern and rectangular fingers with period P = 10 µm and the spatial offset of P/4 between the two sense-structures for quadrature detection.

5.3 FURTHER IMPROVEMENTS: TWIN PROCESS

In the previous section and in chapter 4 it is explained that a few items are very important for optimal performance of the incremental capacitive position sensing concepts presented in this thesis. First of all there is a direct relation between the changes in capacitance and the position sensing accuracy. Larger capacitance variations mean a higher resolution to detect displacements. Secondly, the ratio between a certain maximum change in capacitance ΔC with the always occurring parasitic capacitance C_p and (stochastic) changes in C_p determines the accuracy and signal to noise ratio by which ΔC can be measured.

Thus, an increase in capacitance variations ΔC means an increase in resolution. A decrease of parasitic capacitance C_p means an increase in the ratio of $\Delta C/C_p$ and thus an increase in the accuracy to detect and measure displacements.

For the capacitance variations predicted with the 2D-Finite Element simulations in the previous chapter for various periodic geometries a close to linear increase may be expected with an increase of electrode area (perpendicular to the substrate). Therefore, if the structure height of the devices, relative to those already realized with the Poly-process could be increased by a factor of 5 – 20x an equal increase in ΔC is expected. Like wise, if the distance from the sense-structures to the substrate underneath the sensing structures is increased with a factor of 5 or 10, the ratio of $\Delta C/C_p$ is expected to increase a factor of 25 to 200.

An extra benefit of an increase in structure height is the increase in stiffness in out-of-plane direction (z). For an N x higher structure a N^3 x higher stiffness in out-of-plane (z) direction versus an N x higher stiffness in the desired in-plane direction are obtained. Thus the sensitivity for and the amplitude of vibrations in the z-direction due to inertia effects and external moments and impulses are much reduced. The sensitivity to in-plane inertial effects remains the same as for the surface micromachined devices of the previous section, since both mass and in-plane stiffness scale linearly with structure height. Another benefit is expected due to a decrease in thermal mechanical noise because this scales with $1/\sqrt{\text{Mass}}$ as given by equation Eq.3.18 in chapter 3.

The new Twin process (Twin INovation) has been developed within the Transducers Science & Technology Group in collaboration with Adixen Micromachining Systems [3]. With this process it is possible to make high moveable structures from mono-crystalline Silicon, with all the benefits discussed in the previous paragraph. It even has the benefit of a larger distance between sense-structures and substrate.

The principle behind this process is given in Fig. 13. The technology basically is the etching of the structures down into the Silicon substrate succeeded with the refilling of trenches with a dielectric material (isolator) in our case with LPCVD of SiN. These isolation trenches filled with Silicon-Nitride (SiN) provide a mechanical connection between (fixed or moveable) parts without an electrical connection [4,8]. Next, the structure pattern is etched down into the substrate through an alternating cycle of DRIE etching, applying a passivation layer on the side-walls and removing the passivation layer at the bottom of the trench. Finally, the structure is plasma-released through isotropically RIE etching underneath the structure layer.

A vertical pull-in will be much easier to prevent because of the increased structure height and an increased distance between moveable parts and substrate which is no longer restricted by the oxide thickness as was the case with the Poly-process, see Fig. 3.

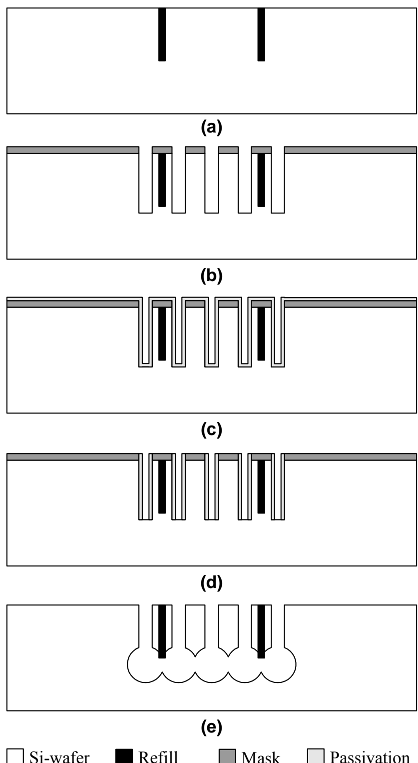

Fig. 13: Condensed fabrication sequence: (a) trench etching, refill and top layer removal (b) structure etching (c) side-walls passivation (d) bottom removal (e) plasma release

First the trenches are etched and filled with SiN. Then a critical step in this process is to determine the depth for the etching of the structures (i.e. height of the structures). The release process is an isotropic dry-etching process. Tests are included to be sure that the trenches of the release process *(25 microns)* are less deep etched than the depth of isolation trenches filled with nitride *(27.5 microns*). The maximum difference in depth between both trenches should be in the order of 3 *micron*. Then, the structures are released properly with electrical isolation in tact and sufficient structure height.

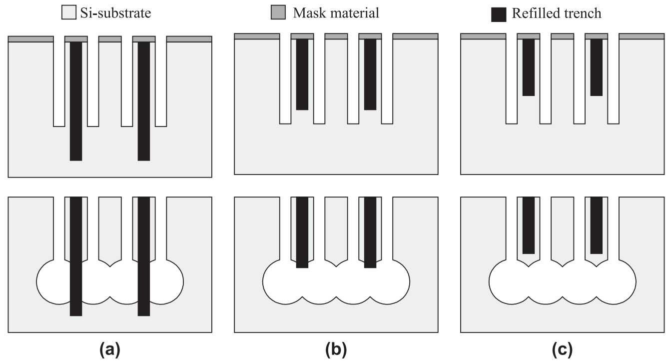

Fig. 14: Reliable isolation requires a careful control of design parameters: (a) high stiffness support (not ok) (b) movable structure with integrated isolation and PERFECT electrical isolation (c) electrical short cut (not ok)

The following critical aspects of the TWIN process are noted; The deeper the trenches the more difficult it becomes to etch narrow trenches of 2 μm width with straight side-walls

particularly if neighbouring trenches or areas need to be wider or more open. In other words, deep trenches with a width of 10 µm are etched faster than trenches with 2 µm width. This effect is called RIE-lag. The consequence is that in the mask design the RIE loading i.e. the alternation between exposed / open areas and closed has to be as uniform as possible. Otherwise, effects may occur as given in Fig. 14 (c) where the device may be released but with an unwanted electrical short cut between different parts.

For the current TWIN process an aspect ratio of ~ 20x has been established with very good trench profile even for trenches of 2 µm. A recent result given in Fig. 15 shows the RIE-lag can be practically eliminated.

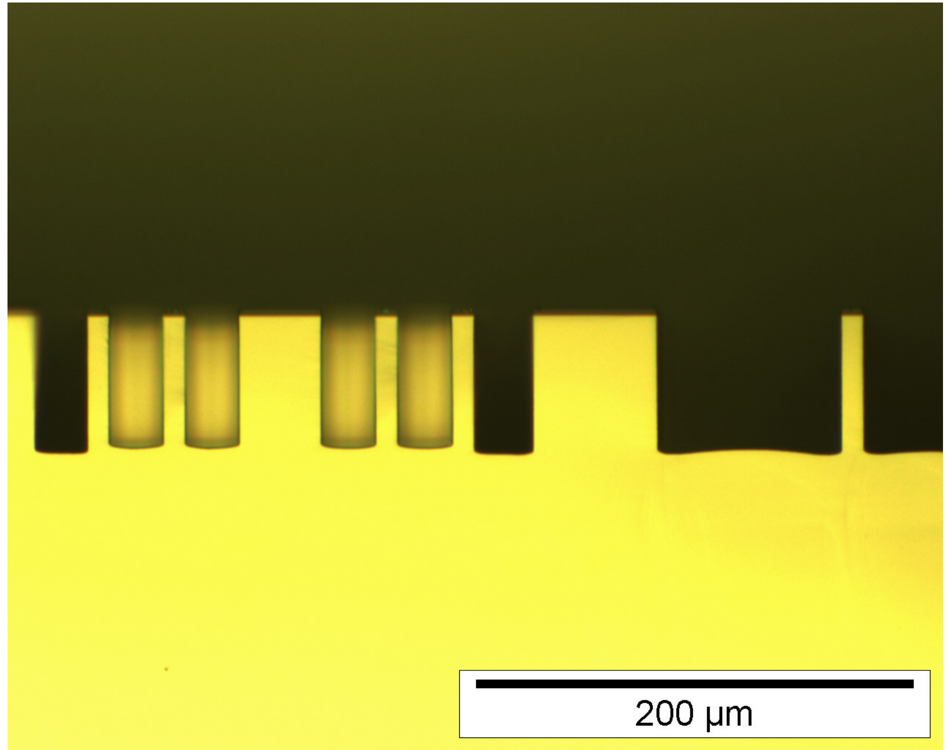

Fig. 15: Recent result with a modified Bosch plasma etching process show that the RIE-lag can be practically eliminated.

For the design given in appendix 2.3, the width between the comb-fingers of the comb-drives is taken 3 µm instead of 2 µm, which means we may need special voltage amplifiers or generators to produce the required higher actuation voltages. Also the minimum width between the sensor periodic geometries may not be limited by the minimum feature size of 2 µm for the standard available photolithography process, but by the etching performance of the deep-trench-etching process in the Twin Process.

Furthermore, the contact pads need to have open structures to have these pads electrically isolated from the bulk-potential with the help of SiN trenches. But wirebonding on these truss-like contact pads maybe a problem depending on the thickness of the device layer and if so, the only option of connecting these devices would be through probe needles which exclude the use of the preferred Faraday caging. No doubt, also here a solution can be found with extra Chrome / Platinum leads and pads as seen with the Poly-Silicon devices.

The next section and Appendix 2.3 give some examples of designs for this TWIN process. New experiments with devices made with this process are anticipated in the near future.

5.3.1 Examples of devices made with the TWIN bulk-process

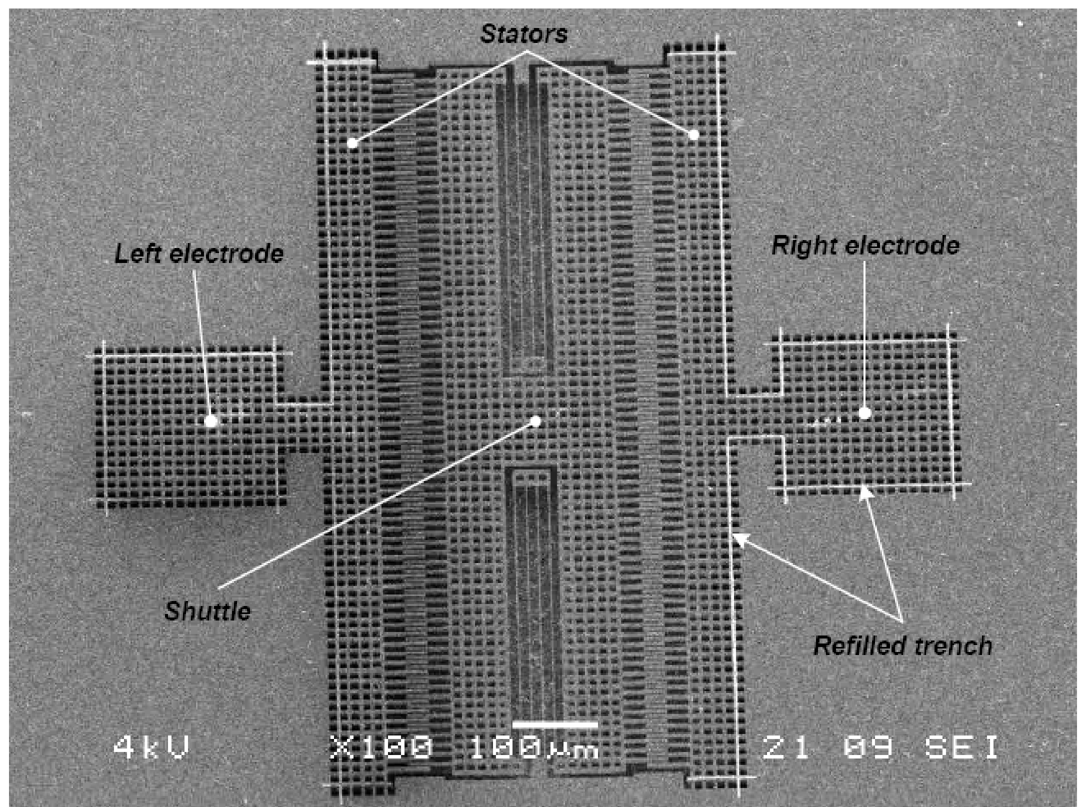

Fig. 16: Example of a comb-drive device designed by E.Sarajlic and fabricated with the TWIN process [3, 4]. The SiN trenches are specially marked in this photo.

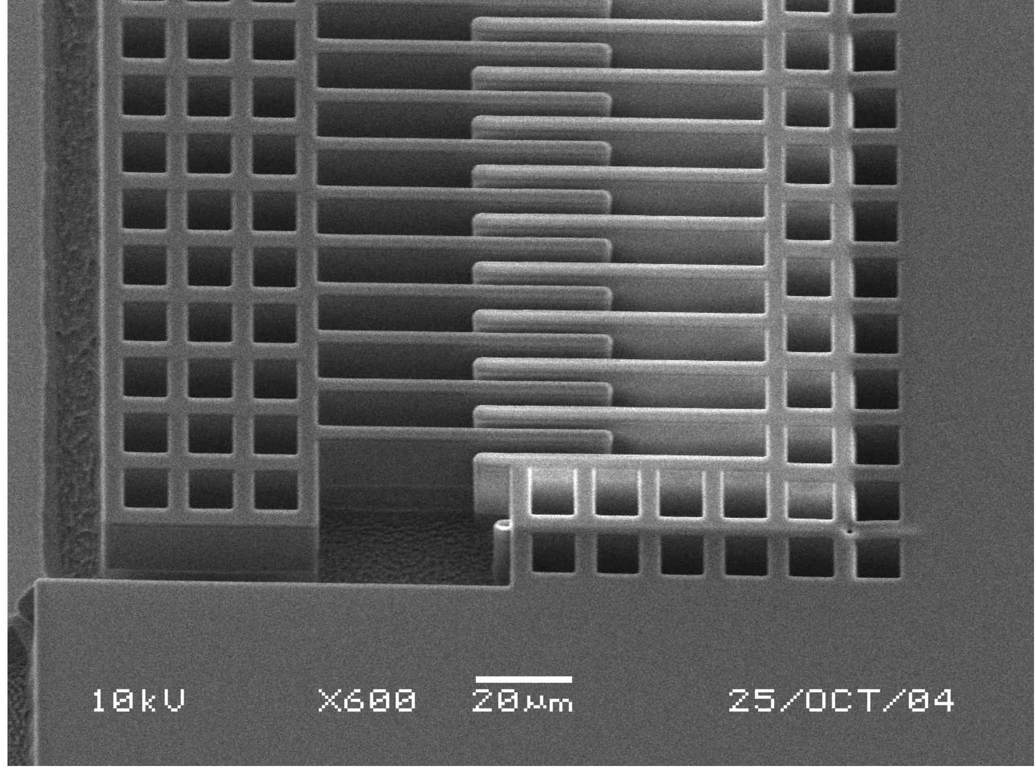

Fig. 17: Example of a comb-drive device fabricated for this project. The stator comb fingers get charged up due to the SEM. The resulting contrast difference shows the electrical isolation from the substrate and rotor parts.

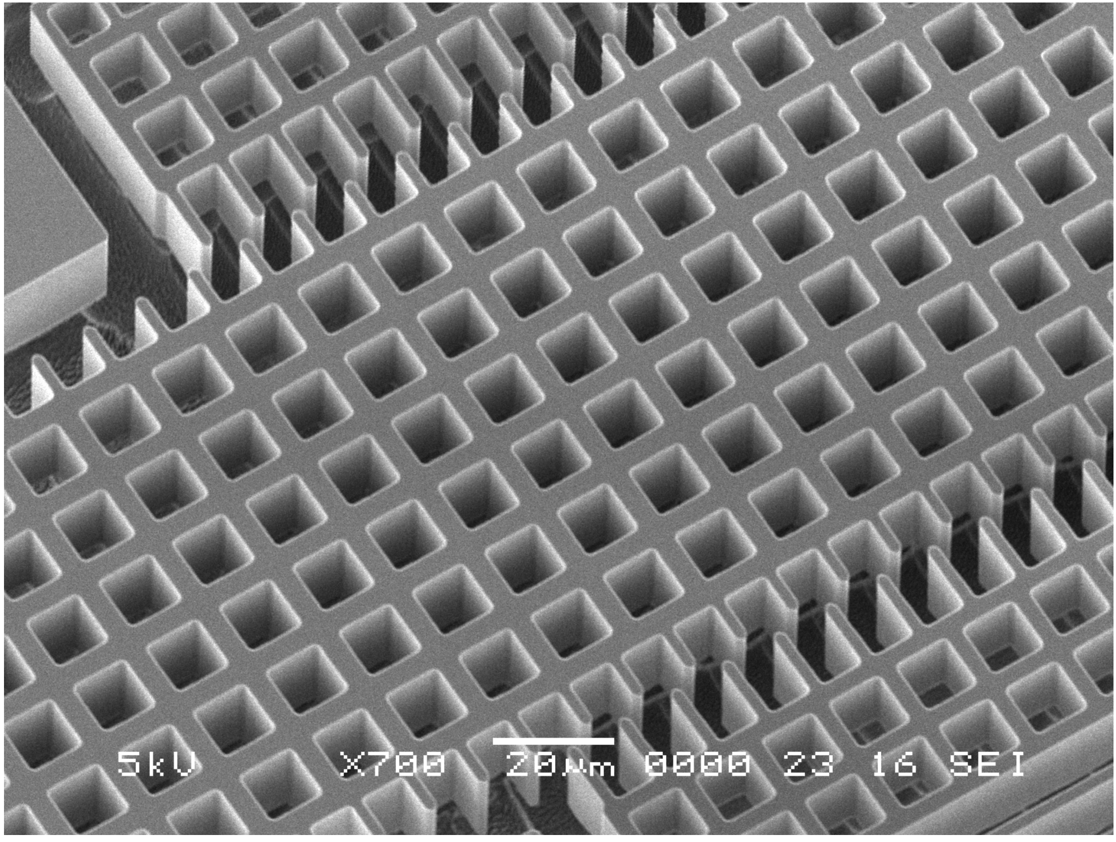

Fig. 18: A device with rectangular fingers on slider and sense-structures with period P= 10 µm

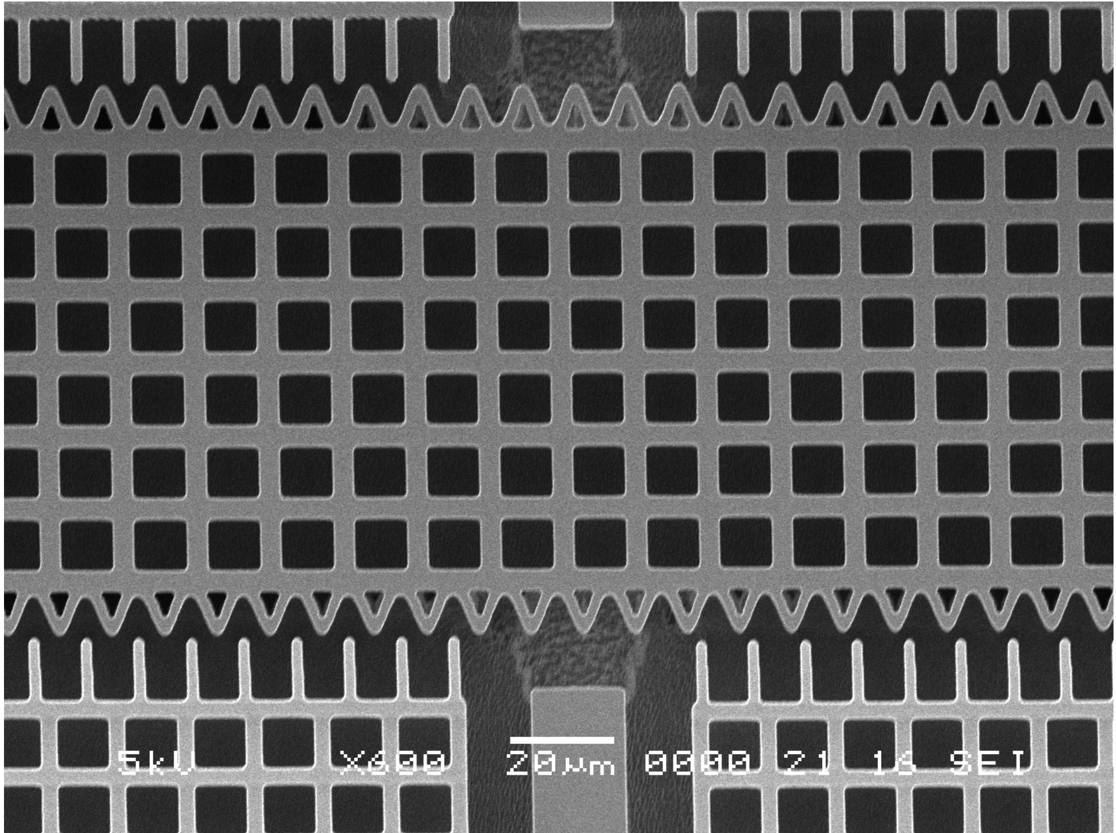

Fig. 19: Device with sine-rectangular geometry combination showing the design for quadrature position detection.

5.4 CONCLUSIONS

- Two processes have been developed and executed to obtain electrostatic microactuator devices with integrated capacitive incremental position sensors. i.e. a poly-Silicon surface-micromachining process (Poly) and a mono-crystalline bulk-micromachining process (TWIN)
- Several designs have been developed for a one-mask Poly process i.e. electrostatic microactuator and capacitive position sensors are fully integrated in the same layer. The designs are based on the periodic change in capacitance between a periodic geometry on a slider and a periodic geometry on a sense-structure as presented in chapters 3 and 4. Different periodic geometries for the incremental capacitive position sensor have been included.
- The direct objective with these devices is to perform experiments and measure the small changes in capacitance as a function of the displacement of the slider driven by two drive actuators (electrostatic comb-drive actuators).
- To this end, the process layout includes the possibility for packaging in a cage of Faraday in order to limit or eliminate external interference or noise during the measurement of the small changes in capacitance. The original process layout is extended with extra steps and a second mask to obtain Chrome-Platinum contact pads on top of the poly-Silicon connection pads for better wire bond connections.
- In terms of processing, the most critical processes are the formation of the thick (~3 µm) sacrificial oxide layer and the dotation of the 5 µm thick poly-Silicon structural layer with limited stress and limited stress gradient and the sacrificial layer etching containing the freeze drying step.
- The critical process-steps in terms of design aspects are the (standard) photo-lithography process and the plasma etching. The standard lithography-process limits the minimum gap-size and width of beams and fingers to around 2 µm. The aspect ratio of the plasma etching limits structure height relative to gap-size to a ratio of ~20 i.e. a gap size of 500 nm for a structure height of 5 µm.
- A key aspect in the current design for the periodic capacitive position sensors is the possibility to move the sense-structures with additional sense-actuators and obtain a gap between sense-structures and slider much smaller than is possible with standard available photolithography or with plasma etching with 5 µm high structures. This aspect is also crucial for the CCMM concept presented in chapter 3
- As an improvement a mono-crystalline Bulk-micromaching process has been developed called the TWIN process. With this process test devices with integrated incremental capacitive position sensors can be made out of the pure (doped) Silicon wafers with much larger structure height (~ 25 µm or more). This means an increase in accuracy and resolution of position detection can be expected of 5x or more. Measurements are anticipated in the near future.

References

[1] R.Legtenberg, Electrostatic Actuators Fabricated by Surface Micromachining Techniques, PhD Thesis, University of Twente, Enschede, 1996.

[2] R.Legtenberg, A.W. Groeneveld, M.Elwenspoek, Comb-drive actuators for large displacements, J.Micromech. Microeng., **6**, 320-329, 1996.

[3] E.Sarajlic, E.Berenschot, G.Krijnen, M.Elwenspoek, Versatile trench isolation technology for the fabrication of micro-actuators, Microelectronic Engineering, Vol.67-68, pp.430-437, June 2003.

[4] E.Sarajlic, M.J.deBoer, H.V.Jansen, N.Arnal, M.Puech, G.Krijnen, M.Elwenspoek, Integration of trench isolation technology and plasma release for advanced MEMS design on standard silicon wafers, 14th Micromechanics Europe Workshop (MME 2003), November 2003, Delft, the Netherlands.

[5] L.K.Baxter et al., *Capacitive Sensors: design and applications*, IEEE Press, New York, 1997.

[6] R.Legtenberg et al., Stiction of surface micromachined structures after rinsing and drying, Sensors and Actuators A, **43**, 198-201,1994

[7] N.R.Tas, Electrostatic Micro Walkers, Micro Electromechanics and Micro Tribology, Ph.D. Thesis, University of Twente, Enschede 2000.

[8] de Boer M J, Jansen H and Elwenspoek M 1995 A study of the fabricating of movable structures for MEMS Int. Conf. on Solid State Sensors and Actuators (Transducers 95) (Stockholm, Sweden) pp 565–8

6 Assessment of micromachined capacitive long-range position sensor

6.1 INTRODUCTION

In chapter 3 the concepts ICMM (open-loop) and CCMM (closed loop) are presented for a micromachined capacitive long-range position sensor that can be integrated into a MEMS device and enable nanometer-positioning over a long range of displacement (i.e. circa 100 μm). Both concepts are based on the measurement of small changes in capacitance between two periodic geometries as a function of their relative displacement. A combination of discrete measurement (i.e. counting the number of periods) and analog measurement keeps the demands for the dynamic sensing range modest. In chapter 4 for both concepts the periodic changes in capacitance for different combinations of periodic geometries are examined through 2D-Finite Element simulations. In chapter 5 the fabrication and design issues are given for a surface-micromachined device (test-vehicle) with integrated incremental capacitive displacement sensor. Both test-vehicle and position sensor are fabricated in a one mask process.

This chapter gives the assessment of the operation and performance of the two concepts as they are implemented in different devices for the periodic geometries presented in chapter 4. The experimental setup, the test-device, the measurement electronics and methods will be discussed in section 6.2. Two generations of devices have been realized with the poly-silicon fabrication process as explained in the previous chapter. The design for the first generation of devices contained sense-structures with flexures with a too high stiffness. Controlling the gap-size between slider and sense-structures would require too high voltages for the sense-actuators. Measurements for generation I devices included various combinations of geometries on respectively slider and sense-structures e.g. rectangular-rectangular, sine-rectangular. A comparison is made between the 2D-FE simulation results and the measurement results to explore the validity of 2D-FE modeling as a tool to predict the shape of the capacitance function versus slider displacement $\Delta C(x)$ and to determine the measured changes in capacitance ΔC_{max}.

After a redesign, experiments with the second generation of devices proved as expected to require much lower voltages for the sense-actuators to move the sense-structures closer to the slider. Experiments with Quasi-static and dynamic motion were carried out for one particular combination of geometries; Sine pattern on the slider – Rectangular fingers on the sense-structure with 10 μm period i.e. named SinP10.

In the quasi-static experiments the influence of a smaller gap between sense-structures and slider on the SNR is analyzed and of course it is interesting to evaluate the predictions for a better performance of the CCMM concept in terms of SNR and accuracy. In the dynamic experiments the assessment focuses on the performance of the ICMM concept at frequencies ranging from 500 mHz up to above the resonant frequency of the test-vehicle.

Finally, the assessment is given for experiments where one of the drive-actuators (comb-drive) of the test-vehicle is simultaneously operating as capacitive position sensor. This principle is called the comb-drive position sensor. It lacks the key aspect of the incremental capacitive position sensor, the periodicity. But the comb-drive may function as a course position sensor up to some unspecified distances. When the maximum traveling distance increases, the capacitance of the comb-drive will increase linearly. It will be increasingly difficult or impossible to measure a change in capacitance ΔC for a change in displacement dx = 1 nm i.e. the demands for the dynamic range may exceed a factor 10^5. Thus, the performance for this non-incremental sensor will be assessed.

In section 6.2 the measurement method, the setup and electronics and the device are introduced and explained in detail. The assessment for quasi-static operation of both concepts ICMM and CCMM is given in sections 6.3 and 6.4. The assessment for dynamic operation of the ICMM concept follows in section 6.5. The assessment of the performance of the comb-drive position sensor at higher frequencies is given in section 6.6.

6.2 Measurement method: Synchronous detection

This section presents and discusses the measurement method and electronics, the experimental setup including the test-device(s) and the approach or organization of the experiments to assess the operation and performance of the concepts ICMM and CCMM.

The measurement method is based on synchronous detection as introduced in chapter 3 using a so-called charge amplifier and a synchronous detector or demodulator, see Fig. 1.

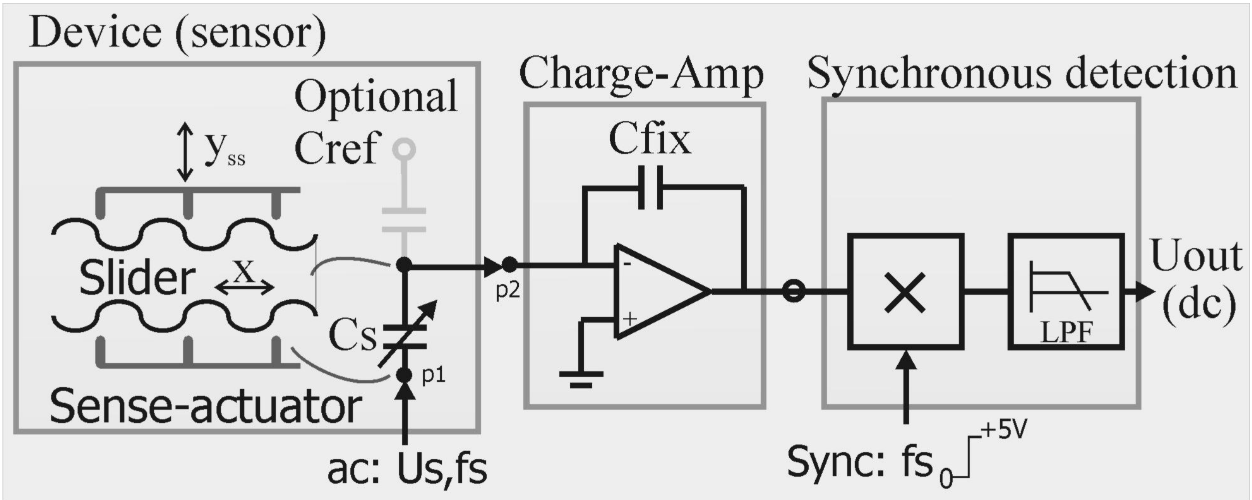

Fig. 1: Diagram of capacitance measurement using synchronous detection with a charge-amplifier and a synchronous detector

A signal (sine) with amplitude U_s and frequency f_s (e.g. 1 MHz) is applied at the sense-capacitance and the resulting current is converted to a voltage by the charge-amp. Mixing the output voltage of the charge-amp with the same frequency (Sync) and filtering the result with a low-pass-filter gives a dc-output voltage U_{out}, which is proportional to the sense capacitance C_{sens} and the change in capacitance ΔC_{sens} and therefore proportional to displacement (x) of the slider. This is illustrated by equation (Eq.6.1) under the assumption that both the capacitance and the slider displacement (x) are changing as a pure sine:

$$C(x(t)) = C_b + C_a \cdot sin(k_x \cdot x(t)) = C_b + C_a \cdot sin(k_x \cdot \hat{x} \cdot sin(\omega_{act} \cdot t)) \quad \text{(Eq.6 1)}$$

$$U_{out} = \alpha \cdot C(x(t)) + u_0 \quad \text{(Eq.6 2)}$$

As explained in chapter 3 with the use of a fixed reference capacitance C_{ref} and a second voltage source producing a voltage U_{s2} it is possible to eliminate the offset u_o in the output voltage U_{out} at position $x(t)$=0 due to static differences in capacitance between C_{sens} and C_{ref} Also parasitic changes in C_{sens} and C_{ref} due to changes in relative humidity, temperature and pressure can be eliminated. Voltage U_{s2} will have the same frequency but a 180° phase-shift and the amplitude U_{s2} is adjusted to null the output voltage U_{out} at initial position $x(t) = 0$. However, this possibility has not been implemented during the experiments performed in this work, because of the increase in complexity of the experimental setup. The first objective has been to demonstrate the feasibility of the two concepts ICMM and CCMM and assess the difference in performance by keeping the environmental conditions of the setup as constant as possible.

Fig. 2 depicts an example of a design for a microsystem with two electrostatic comb-drive actuators (comb-A & comb-B) connected by a sliderbeam. The connections st_A and st_B are used for the electrostatic actuation of the two drive actuators.

The change in capacitance between a periodic geometry on the slider and on the sense-structures is measured to give a measurement of the position of the slider. As discussed for Fig. 1 the sinusoidal signal *Us* (*fs* [Hz]) is applied to contacts SA0_a & SA0_b in parallel. The resulting current through the sense-capacitances C_{s1a} and C_{s1b} and the conducting flexure beams of comb-A (or comb-B) is picked-up by the charge-amp with the input connected to contactpad rt1_A (or rt2_A). Assuming the charge-amp has infinite gain, contactpad rt1_A becomes a virtual ground (i.e. p2 in Fig. 1). Because of the conducting flexure beams also the slider beam becomes a virtual ground. This prevents an electrostatic pull-down of the slider to the substrate because the voltage difference between slider and substrate is negligible with proper conduction of the flexure beams and high gain of the charge-amp.

The change in capacitances C_{s1a} and C_{s1b} for a displacement *(x)* of the slider as illustrated by Eq.6.1 will have the same phase. This design symmetry is deliberately chosen because these capacitances can also be seen as gap-closing transducers as explained earlier in chapter 3. Applying a signal voltage U_s to these capacitances will cause small electrostatic forces exerted on slider and sense-structures. The advantage of this design-symmetry is that the electrostatic forces exerted on the slider are balanced as much as possible. To this end the gap-sizes between the sense-structures and slider should be fairly equal even if the gaps are made smaller by the additional sense-actuators. However, as explained in the introduction, with the particular design given in Fig. 2 the required voltages for the sense-actuators to decrease the gap are too high.

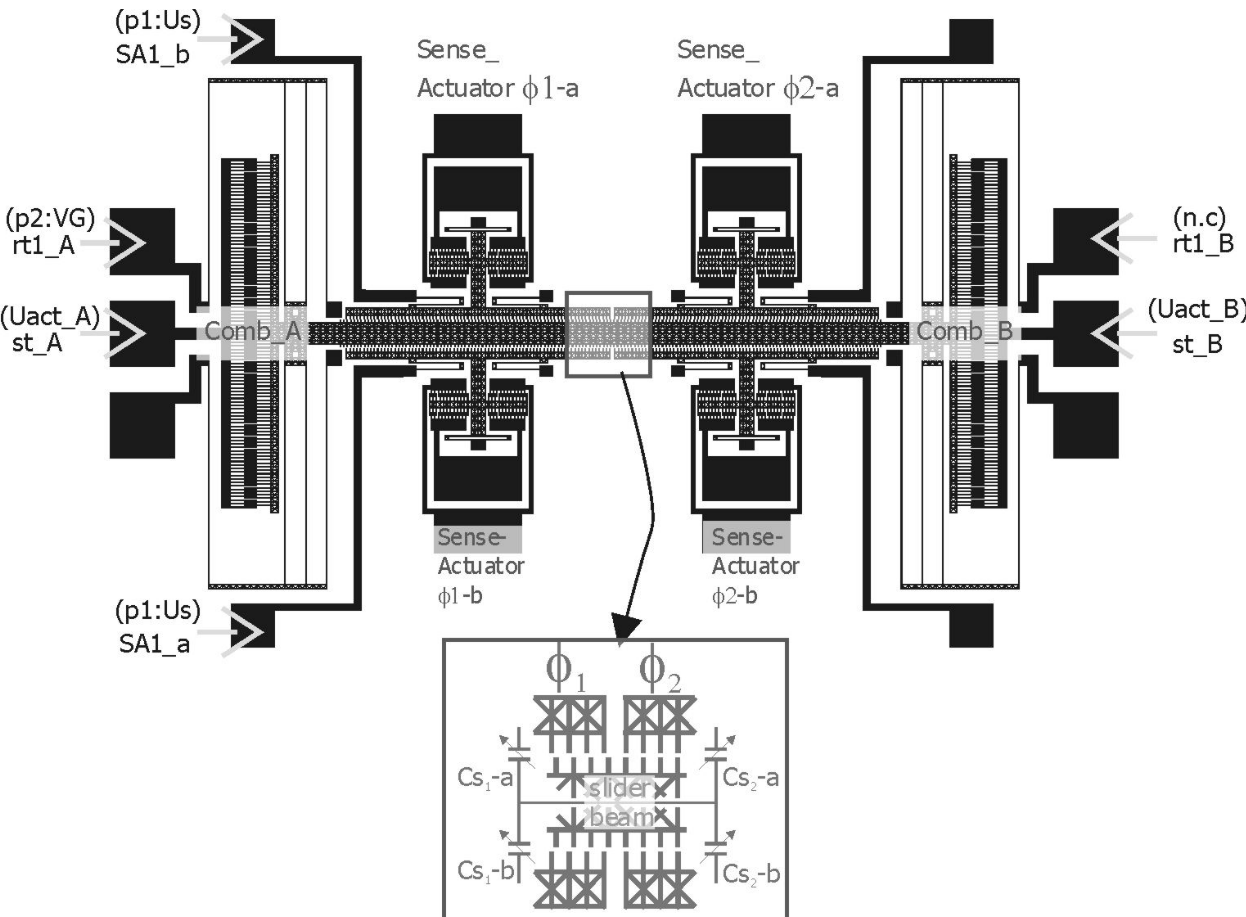

Fig. 2: A microsystem with 2 electrostatic drive-actuators (comb-drives A&B) and an integrated periodic capacitive position sensor with additional sense-actuators. Indicated are the names of the main parts, the connections and signals and a lumped model of the 4 sense-capacitances (inset).

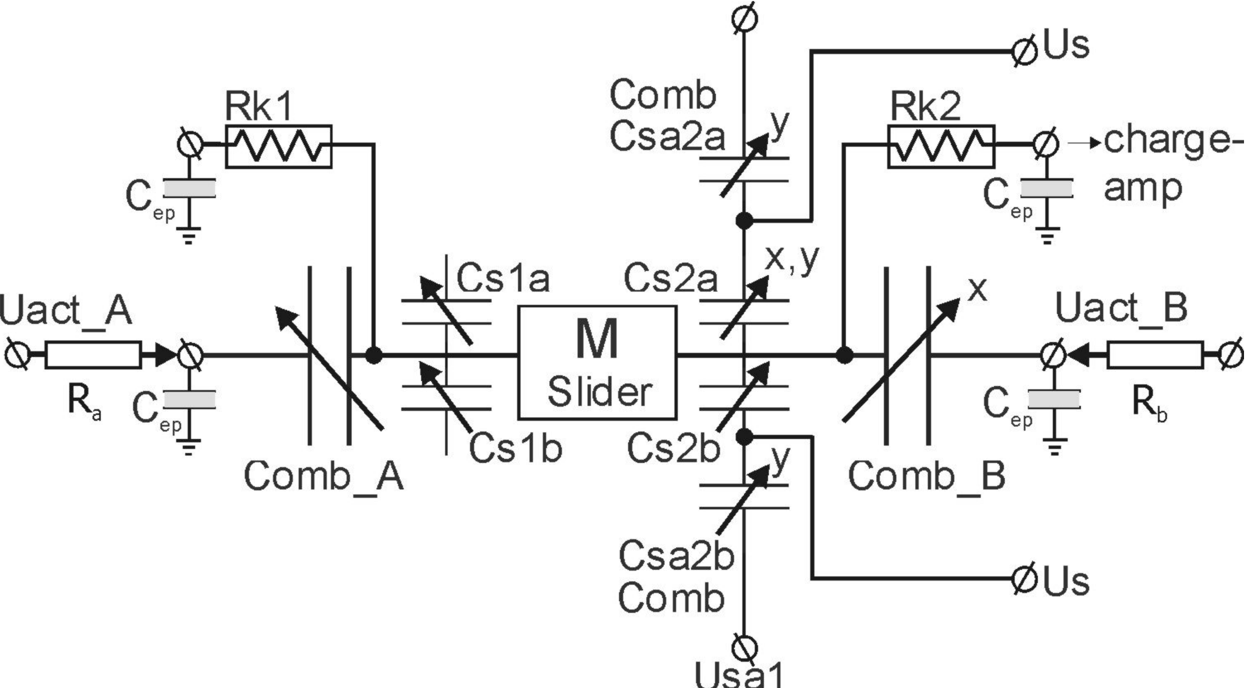

Fig. 3: Lumped model for the device in Fig. 2 with the actuator and sensor capacitances and the connections.

In Fig. 3 a lumped model is given with the main actuator and sensor capacitances for the microdevice given in Fig. 2. The two comb-structure capacitances Comb_A and Comb_B are the comb drive-actuators to displace the sliderbeam (x-direction). The two comb-structure capacitances *Csa1a & b* are the sense-actuators to move the sense-structures in y-direction closer to or away from the sliderbeam. The sensor capacitances *Cs1a* & *b* are a function of the slider position *(x)* and the y-position of the sense-structure. Only one pair of sense-structures is connected in parallel during the experiments presented here. But in principle the change in capacitances C_{s2a} and C_{s2b} will have a spatial phase-shift of 90° in respect with capacitances C_{s1a} and C_{s1b} to make an assessment of the quadrature position detection technique possible as discussed in chapter 3.

The two comb-drive actuators are connected as indicated in Fig. 3, through two 100 KΩ resistances R_a and R_b in series. Resistors R_a and R_b will limit the current in the case of side-pull-in of the comb-actuator or one of its fingers. The stiffness *k1* and *k2* of the folded flexures of each comb-drive, are also electrically conducting (Rk ~ 500Ω – 1KΩ). One of the flexures is connected with the input of the charge-amplifier.

As an alternative to synchronous detection with custom-made electronics, also an HP Impedance analyzer (HP4194A) was used to determine the change in impedance (i.e. change in capacitance) [1]. This method may in fact be more accurate than the measurement method presented in this chapter, because it uses 2 Kelvin probes and a 4 point/ terminal technique (2) and can in part compensate for additional unknown parasitic capacitances. However, only the capacitive impedance between one sense-structure and slider can be determined with 2 probes and proper connection with the impedance analyzer. Thus, the electrostatic force acting on sense-structure and slider due to the applied signal voltage U_s of the analyzer will not be symmetrically balanced by an equal force acting on the other side of the slider (see also section 3.5).

6.2.1 Implementation of the charge-amplifier

The current through the sensor-capacitances C_{s1a} and C_{s1b} is converted by the charge-amplifier to a voltage and applied to the synchronous detector. The higher the frequency, the lower the capacitive impedance as can be seen from the equation for a capacitive impedance

$$Z = \frac{1}{j \cdot 2\pi f C_{sens}} \qquad \text{(Eq.6 3)}$$

A lower capacitive impedance, gives a larger current through the capacitance and therefore it will give a higher signal-to-noise ratio (SNR). The upper limit for the frequency used is determined by the unit-Gain bandwidth of the OPAmp but in practice it is limited to the influence of cabling, grounding, shielding etc. to around 10 MHz. For the experiments presented in this work a frequency of f_s = 1 MHz was chosen.

The input of the charge-amp has to be as close as possible to the sensor-capacitances to prevent the influence of parasitic capacitances burdening the operation of the charge-amp. The charge-amplifier is custom made with a CLC425 ultra-low-noise wide

bandwidth OPAMP and a circuit design as given in Fig. 4 *(left)*. A custom designed and developed Printed Circuit Board (PCB) for Surface Mounted Devices (SMD) has resulted in a small PCB with a size of ca. 25 x 70 mm^2. The connection of the device has been through probe-needle micromanipulators as will be explained in the next section. Therefore, the PCB for the charge-amp is covered by aluminum foil for shielding and connected on a probe-needle micromanipulator, closely to the device under test.

Fig. 4 *(right)* shows a measured frequency response for a fixed capacitance C_s = 1 pF. At a frequency of f = 1 MHz the gain is reasonably flat and the phase is close to ϕ = -180° and stepping to + 180°.

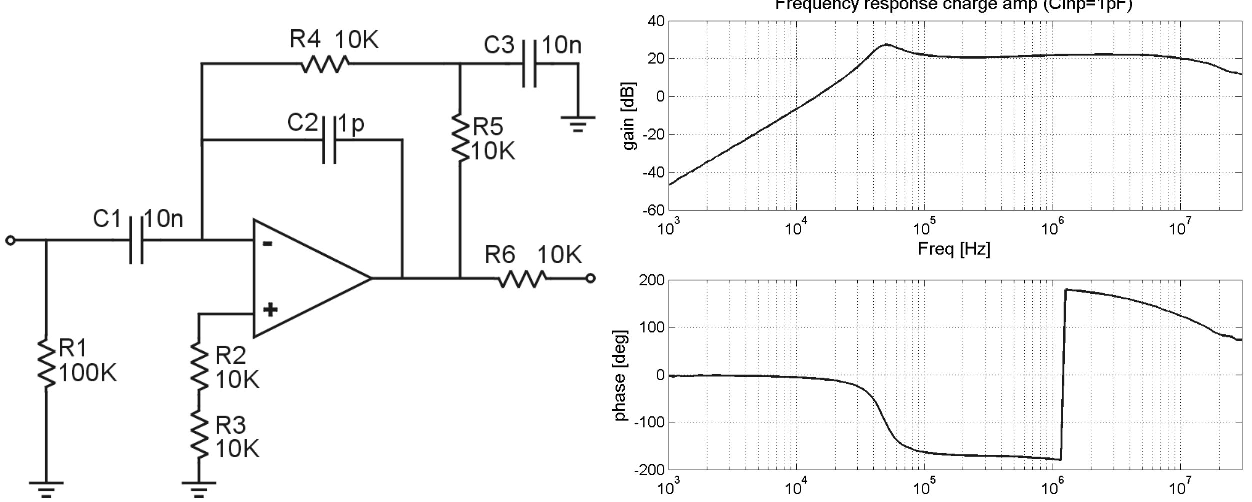

Fig. 4: (left) Circuit schematics of the charge-amplifier circuit. (right) the measured frequency response for an input capacitance of 1pF.

6.2.2 Implementation of the synchronous detector

The current implementation of the synchronous detector is done by synchronous switching and rectification of the input-signal as explained in Fig. 5. Switching with a frequency f_s will rectify the input signal. If the input signal contains frequency components other than with frequency f_s e.g. due to interference, will cause high frequency components at the input of the Low-Pass-Filter, due to the rectification process. These components will be filtered (averaged) by the Low-Pass-Filter.

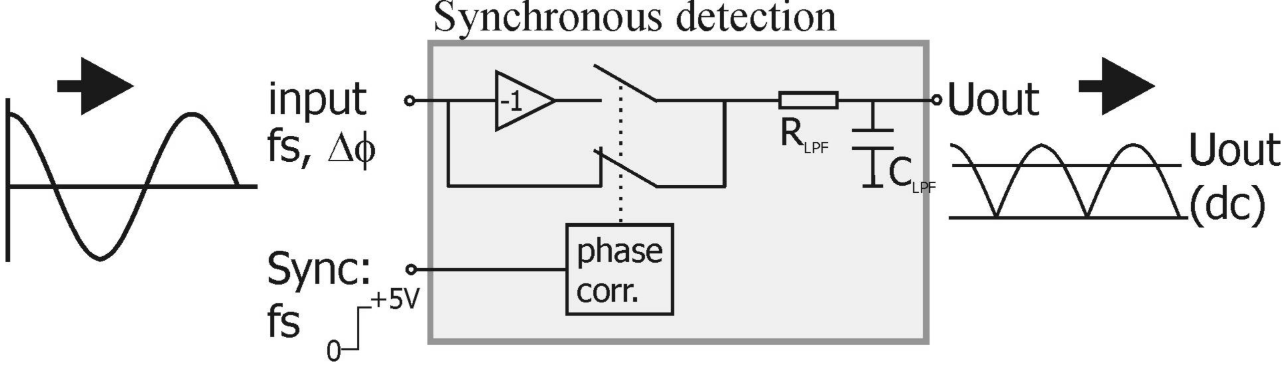

Fig. 5: Simplified schematics of the synchronous detection implemented with switches.

The input of the synchronous detector can have a phase shift $\Delta\phi$ with respect to the rectangular wave signal at the Sync-input. Ideally, switching should be done with 0° phase shift with respect to the input signal to maximize the dc-output voltage. The phase of the sync-input needs to be adjusted until the dc-output of the synchronous detector is maximal as illustrated by equation Eq.6.4.

$$U_{out} = \frac{1}{T}\int_0^T A\,cos(\omega t)\cdot\left(cos(\omega t + \phi)\right)dt = \frac{A}{2}cos(\phi) \quad \text{(Eq.6 4)}$$

The current implementation gives an undesired parasitic effect due to charge injection by the switches. The switches can pick-up small (residual) packets of charge, which is passed on when closing the switches. It is caused by small voltage-dependent parasitic capacitances from gate to source and drain electrode, and varies from 5 pC for discrete circuits to 5 -50 aC for small-geometry IC switches [3]. The current implementation through CMOS switches claims a charge injection of 8 pC [HCT4066].

Furthermore, any latency between the switching will also cause small glitches in the signal, which will be filtered to a small non-zero dc-voltage. The difference in phase between the sync and the input-signal of the synchronous detector can be corrected with additional custom-made electronics. Alternatively, an extra HP Arbitrary Waveform Generator (AWG) is used as shown in Fig. 6. It needs to be synchronously locked to the signal of the HP generator already used for injecting the signal with amplitude U_s and frequency f_s at the sense-capacitance C_s. The phase of the sync-signal of the second generator is shifted with respect to the output-signal of the first generator to maximize the output voltage of the synchronous detector.

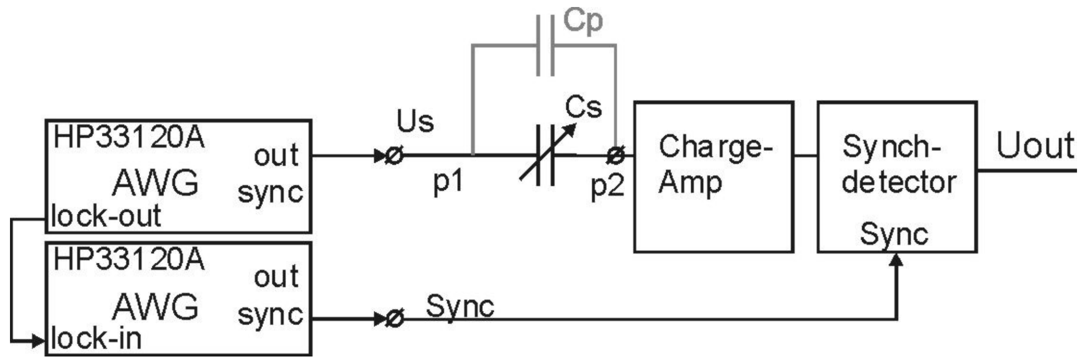

Fig. 6: the difference in phase between the input signal and the sync-signal of the synchronous detector can be corrected using two HP generators

Without second generator the sync-input of the synchronous detector is connected with the sync-output of the first generator and a possible phase difference between input-signal and sync-input is uncompensated but will give a dc-output voltage, which is proportional to the change in capacitance C_s.

The synchronous detector is made and developed on a custom made PCB-layout and covered by a metal Faraday-cage separated from the charge-amplifier. This is done because a good grounding scheme is to separate grounds for digital and analog circuitry.

A more complicated alternative is to develop a synchronous detector with an analog multiplier (AD834 / AD 835). This multiplier can operate at a higher frequency. Therefore, it is expected to give a larger SNR, and it will not suffer so much from the

parasitic charge injection. However, the measurements presented in this work have been performed using the synchronous switching technique to first determine and demonstrate the feasibility of the position sensing concepts.

6.2.3 Conversion of measured voltage to capacitance

The aim of the calibration given in this section is to quantify the size of the measured changes in capacitance relative to the measured output voltage U_{out} of the synchronous detector. The absolute capacitance values are not of much interest since the largest part will be taken by the parasitic capacitance and much effort has been done to keep it as constant as possible. It is the change in capacitance versus a change in displacement as detected by the charge-amp and synchronous detector that is really important.

For 2 SMD capacitor components of C_1 = 1 pF and C_2 = 2 pF soldered on a PCB the impedance is measured with the HP4194A impedance analyzer. Using the relation for a capacitive impedance (Eq.6.1) the capacitance C_s is calculated and related to the output voltage U_{out} measured with an HP34401A Multimeter as given in Fig. 7. The calibration measurements are performed without phase-correction of the sync-signal of the synchronous detector. As explained in the previous section, this is not ideal but it makes a comparison with the measurements with generation I devices possible, see section 6.2.5.

The capacitors are connected through probe-needles. The calibration is done with the same measurement set-up including the microscope, as we have used in the experiments with the micromachined devices, see section 6.2.4. The difference with the measurements with the micromachined devices is that the PCB (epoxy) is not conductive while the substrate of the devices is. Therefore, unlike the Silicon substrate, the PCB is not functioning as an equi-potential or grounding plane. Furthermore, for the connection of a device much more probes were neighboring the 2 probes needed to measure the capacitance C_s, thus much more chance of interference due to cross-talk and a different parasitic capacitance C_p. Finally, the impedance analyzer uses a 4-point terminal connection with so called Kelvin probes. With this facility the analyzer can in part compensate for additional unknown parasitic capacitances, which the method with the synchronous detector cannot.

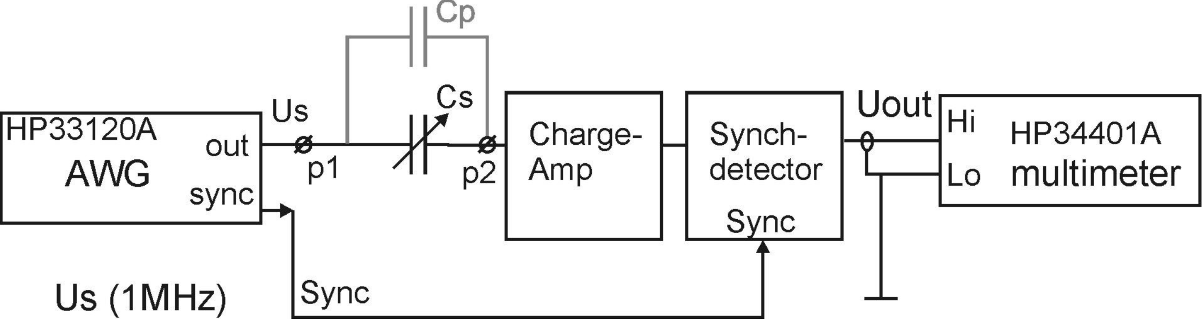

Fig. 7: Instrument connection scheme as used in the calibration measurements to relate the measured output voltage for the capacitive position sensor with a capacitance scale.

Because of the large capacitance values of C_1~1 pF and C_2~ 2pF only 2 signal levels of U_s were applied; U_s =100 mV and 200 mV. For higher U_s values the output voltage U_{out} of the synchronous detector would cross the limit of half the supply voltage (i.e.

supply voltage U_{sv} / 2 = 2.5 V) and become 'saturated'. The capacitance values for C_s of C_1 and C_2 are chosen large with the assumption that the parasitic capacitance parallel to C_s is then relatively smaller and therefore the relation between C_s and U_{out} more linear.

Table 1 gives the measured capacitance and measured output voltage for 2 signal levels of U_s, without phase-correction of the sync-signal of the synchronous detector. Fig. 8 gives the calculated linear relation between U_{out} and C_s based on the results in Table 1. Measurement settings are given in Appendix 3.2.

Capacitance with HP4194A	**Uout {Vdc} with Us1 = 100mV**	**Uout {Vdc} with Us2 = 200 mV**	**Ratio $U_i(U_{s2})/U_i(U_{s1})$**
C_1 = 1135 ± 26.73 fF	U_1 = -0.305108	U_1 = -0.617002	2.0222
C_2 = 2302 ± 29.79 fF	U2 = -0.659492	U2 = -1.31524	1.9943
C_2 / C_1 = 2.0282±0.074	U1(C2)/U1(C1) = 2.1615	U2(C2)/U2(C1) = 2.1317	

Table 1: Measured voltages with charge amplifier and synchronous detector for the capacitance values as measured by the HP4194A impedance analyzer. (No phase-correction of the sync-signal of the synchronous detector)

However, during the device experiments (section 6.3.1) a larger signal U_s was used, because the sensor-capacitance was much smaller and the unknown and unwanted parasitic capacitance appeared to be smaller too (i.e. U_s = 400mV and 1000 mV was used). To be able to convert the output voltage U_{out} from the device experiments to capacitance C_s, use is made of extrapolation of the linear relations in Fig. 8. The last column in Table 1 is added to show if the measured U_{out} is linear with U_s when $C_s = C_1$. This relation is used in the extrapolation for U_s = 1 V.

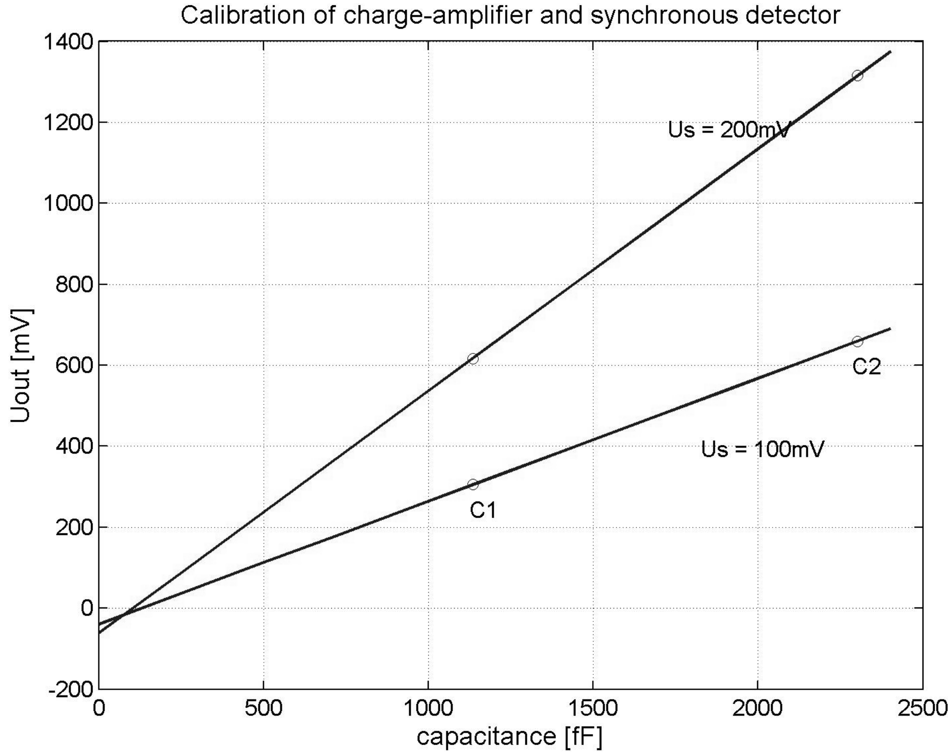

Fig. 8: Calibration of measured output voltage U_{out} with capacitance for different signal levels U_s (1MHz).

6.2.4 Connection of device under test

Two options of connecting the device with the actuation and measurement electronics were considered: connection by wirebonding and connection with probe-needles (Appendix 3.1).

Connecting the device with probe needles is easier to realize, because it does not need wirebonds and breaking of a sample from the wafer and it takes much less time to perform measurements and explore the feasibility of the concept. However, connection by probe-needles is expected to suffer more from a number of noise-sources i.e. (changing) Parasitic capacitances, temperature, humidity and pressure changes, EMI-noise.

With connection through wirebonding and packaging of a sample/device in a Faraday-cage the influence of these noise-sources will be significantly less. The wirebonding technique has been tested on a sample glued and packaged on a specially designed PCB, see Appendix 3.1. However, due to practical reasons it was not possible to perform useful measurements. To save time it was decided to first continue with the connection through probe-needles and further improve the measurement setup.

Besides wirebond connection and caging of device and electronics, further reduction of external disturbances can be acquired by using a reference capacitance (C_{ref} in Fig. 1) as explained in section 6.2. All the measurements presented here are done without reference capacitance because, the advantages of probe-needle connection were considered more significant than the disadvantages of a limited number of probe-needles and the larger influence of external disturbances. The environment conditions such as temperature and humidity (relative) have been kept as constant as possible. At a later stage of the experiments we have included an external temperature and humidity sensor and the data is logged on the PC together with the measured output voltage U_{out}, the actuation voltages and the time so that it is in principle possible to examine the correlation between environment changes and measured capacitance changes.

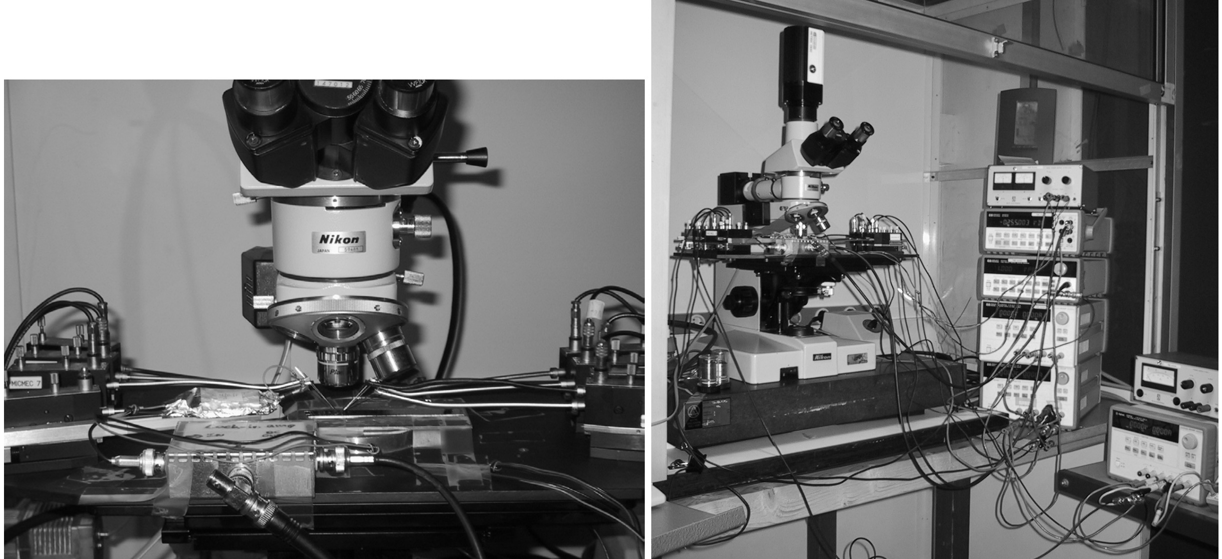

Fig. 9: photographs of the probe needle setup on the microscope table.

6.2.5 Actuation methods for quasi static and dynamic measurements

For the assessment of the feasibility, operation and performance of the two concepts ICMM and CCMM for an incremental capacitive position sensor, two basic approaches are followed for 2 generations of devices as explained in the introduction.

The first measurement approach has been the quasi-static measurement of the changes in capacitance. The displacement of a comb-drive actuator is proportional to the square of the applied voltage and illustrated in Fig. 10 *(left)* i.e. $x \propto U_{act}^2$. To measure the (periodic change in) capacitance as a function of equi-distant positions, a list of voltage increments has been computed conform a square root function illustrated with Fig. 10 *(right)*. First, the maximum actuation voltage is found empirically for the specific device under test at which side-pull in of one of the fingers of the comb-drive is encountered. To have N equi-distant positions up to $x_{max} = \{(U_{act})_{max}\}^2$ the voltage needs to be incremented conform Eq.6.5.

$$U_{act}[n] = \left[\sqrt{n \cdot \frac{\{(U_{act})_{max}\}^2}{N}} \right], \quad n = 0..N \qquad \text{(Eq.6 5)}$$

Fig. 10: Example of the applied actuation voltages to get a linear displacement function corresponding to a linear quadratic actuation voltage.

At each new voltage increment / position an HP34401A Multimeter is measuring the output voltage of the synchronous detector and thus the capacitance between sense-structures and slider (C_{s1a} // C_{s1b}) is measured as illustrated in Fig. 11. The DC voltage supplies (HP3631A) and the multimeter are fully PC controlled using interface and control software HPVee. The actuation profile as given in Fig. 10 has been successively applied to each comb-drive actuator by two different voltage supplies (HP3631A). When supply *Uact_A* is active, the slider is moving from zero-position maximally in one direction (left in Fig. 2 to X^{min}) and back to zero-position. Then supply *Uact_B (UA=0)* becomes active and the slider moves in the opposite direction and back to zero-position. This is 1 complete cycle of displacement. Thus, a complete range from X^{min} to X^{max} is covered in steps. The squared actuation voltage $Uact^2$ is used as the displacement-axis.

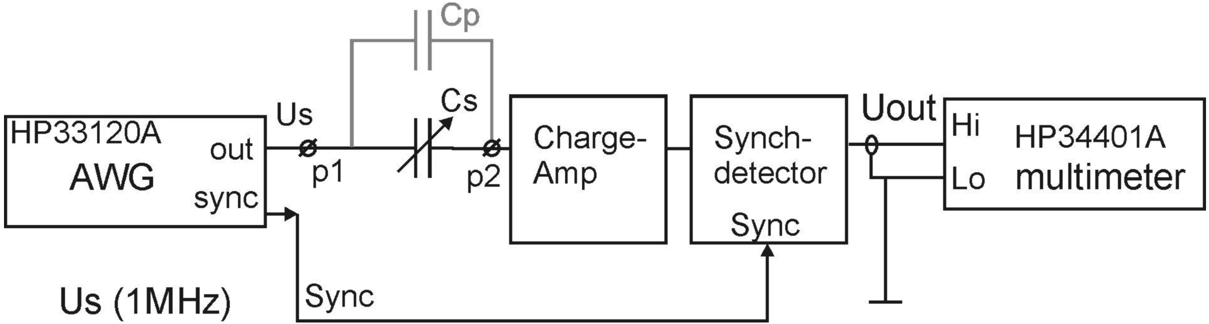

Fig. 11: Schematic for the connection of instruments and capacitive position sensor for the quasi-static measurements with a device as given in Fig. 2. As described in Table 3, only one AWG was used and no phase adjustment was applied.

The accuracy and resolution settings for the HP34401A multimeter have been as given in Table 2 for all quasi static measurements given in this thesis:

Setting	Ac-filter [Hz]	Resolution [digits]	Integration time [ms]
a)	3	Fast-6	(10 PLC) = 200 ms
b)	3	Slow-6	(100 PLC) = 2 s

Table 2: The accuracy settings for all quasi static measurements are performed with the HP34401A multimeter with setting a) or b).

For a resolution-setting called 'fast 6-digits' the multimeter uses 10 Power line cycles for averaging i.e. T_{meas} = 200msec or BW = 5 Hz, for slow 6-digits T_{meas} = 2 sec.

This quasi-static actuation and measurement approach has been followed for the ICMM (open-loop) concept and the CCMM (closed-loop) concept. The corner frequency of the LP-filter of the synchronous detector was set to f_c~ 50Hz and no phase adjustment for the sync-input signal of the detector was applied. This is summarized in Table 3.

For the dynamic actuation and measurement approach custom made actuation electronics are used to enable so-called pull-pull actuation (called pull-pull in [4]). This enables the assessment of the performance of the device under test at frequencies ranging from DC to ~10KHz

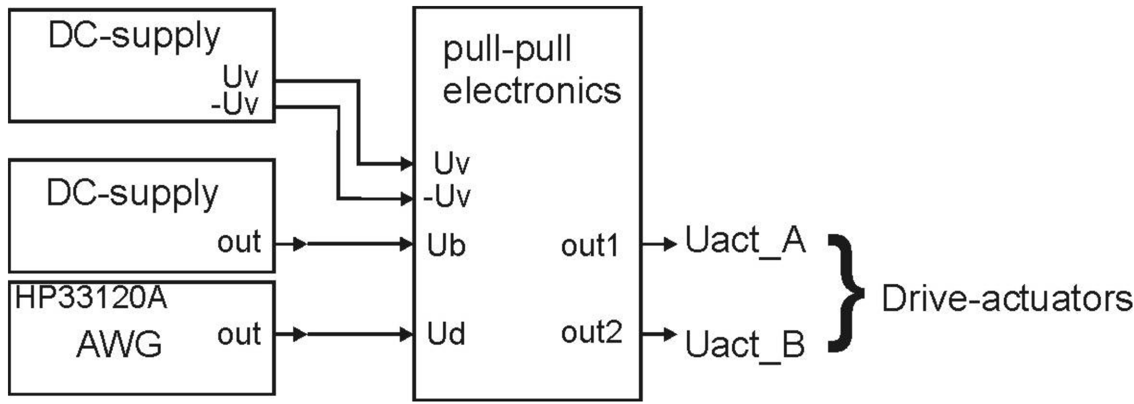

Fig. 12 Custom made pull-pull electronics enables the actuation of the device under test in pull-pull mode. i.e. the slider displacement becomes linear with signal *Ud*.

With pull-pull actuation a combination of a bias voltage U_{bias} and a differential voltage U_{diff} is applied to each drive actuator i.e.

$Uact_A = U_{bias} + U_{diff}$,

$Uact_B = U_{bias} – U_{diff}$.

The resulting force (F_R) and slider displacement (x) are proportional to:

$$x = \frac{F_R}{k_{eff}} \propto (U_{bias} + U_{dif})^2 - (U_{bias} - U_{dif})^2 = 4 \cdot U_{bias} \cdot U_{dif} \qquad \text{(Eq.6 6)}$$

The frequency of the motion of the device during these experiments ranges from DC to ~10 KHz. The RC-combination of the LP-filter of the synchronous detector is adjusted from 100 Hz to 100 KHz to decrease the phase-lag influence by the filter. The output of the synchronous detector is connected to either an oscilloscope or to the signal input of the gain-phase analyzer.

With the HP4194A gain-phase analyzer the mechanical dynamic frequency response of the device under test (DUT) is measured with small amplitudes around slider position x=0. The input U_d of the pull-pull electronics is then connected to the test signal of the analyzer.

For these dynamic experiments a second HP AWG was connected as in Fig. 6 to apply phase adjustment between sync and input signal for the synchronous detector.

In Table 3 a summary of the different measurement schemes and approaches is given.

	Quasi static experiments LPF=50Hz	**Dynamic experiments** LPF=100KHz	
	Multimeter	Oscilloscope	HP4194A
Incremental Capacitance Measurement Mode ICMM (open-loop)			
Generation I devices: Different geometries			
	No phase adjustment Section 6.3.1		
Generation II devices: Active gap-adjustment with additional sense-actuators			
SinP10	No phase adjustment Section 6.3.2	Phase adjustment Section 6.5	Idem oscilloscope
Constant Capacitance Measurement Mode CCMM (Closed-Loop)			
SinP10	No phase adjustment Section 6.4.3		

Table 3: Summary of different experiments, devices and implementations for the two concepts ICMM and CCMM.

6.3 QUASI-STATIC EXPERIMENTS FOR INCREMENTAL CAPACITANCE MEASUREMENT MODE

6.3.1 Measurements for different periodic geometries

In this section are presented the measurement results for different periodic geometries as given in Fig. 13. The first objective of these experiments is to prove that the concept of a periodically changing capacitance can be realized and to demonstrate the influence of different geometries on the shape of the output function in relation to the displacement of the slider. The measured curves for the different geometries are compared with the curves obtained through 2D-FE simulations as presented in chapter 4. In Fig. 13 the different geometries and their naming are given. And as an example a photograph is given of a realized device with a sine – rectangular geometry combination on slider and sense-structures with a period of 10 µm (SinP10). The photograph in Fig. 13 (right) shows, that the plasma-etching has a tendency to round fingers and other features, like a low-pass-filter effect.

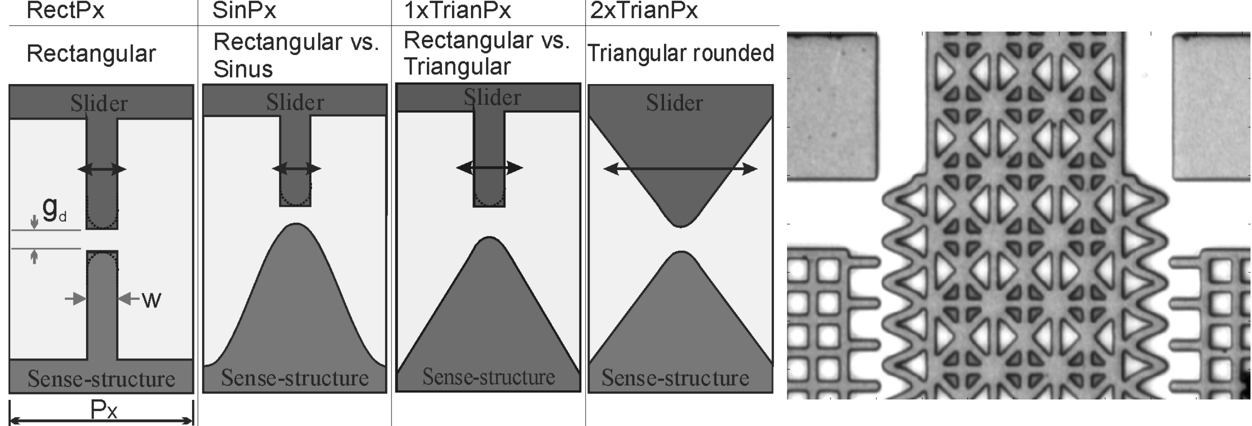

Fig. 13: (left) the naming of the different geometries used in the measurements, (right) an example of a realized device showing a sine vs. a rectangular geometry with a period of *Px* = 10µm i.e. SinP10.

Name	Period [µm]	Design gap distance	Number of periods
Rect-RectP8 (RectP8)	8	2	77
Rect-RectP12 (RectP12)	12	1.5	51
Sin-RectP10 (SinP10)	10	1.5	52
Sin-RectP16 (SinP16)	16	1	39
Trian-RectP16 (1xTrianP16)	16	1	31
Trian-TrianP16 (2xTrianP16)	16	0.5	33

Table 4: The different geometries included in the measurements and the design parameters.

The objective at this stage is not to compare each selected measured capacitance function for each geometry with a pure sine or triangular function and quantify the resemblance. The aim here is to demonstrate that each geometry produces a measurable

output function and has distinguishable shape characteristics. i.e. the SNR is sufficient to detect different shape and amplitude characteristics.

We like to explore and demonstrate if and how the position can be detected from any periodic output / capacitance function which in practice will always differ from a pure sine or triangular function, due to the finite resolution of the fabrication processes e.g. photo-lithography and the plasma-etching process.

The design gap-distance in Table 4 is an important parameter. It is the minimum gap-distance as it is drawn in the mask-design. The resolution of the available standard lithography is limited to roughly 2µm. In chapter 5 is explained that with a smart design smaller gap sizes can be made.

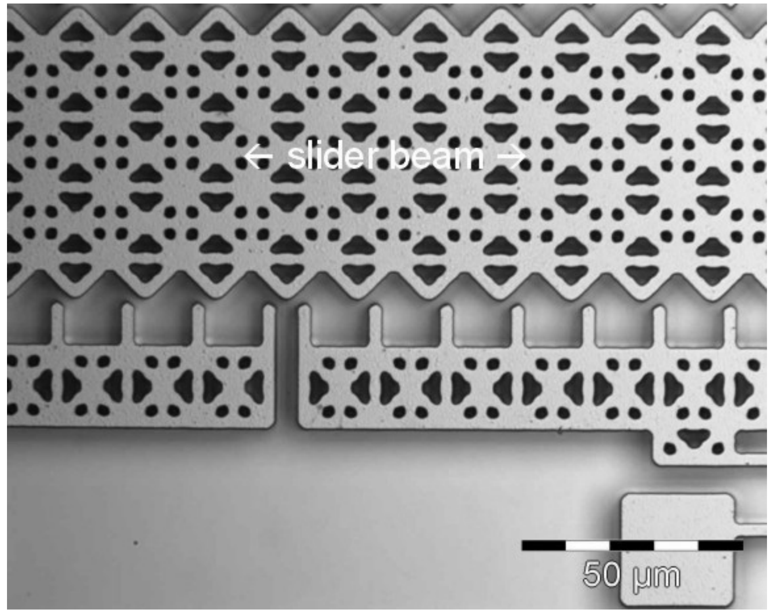

Fig. 14: Example of a micromachined device (generation I) with Triangular-Rectangular geometry with period size P_x = 16 µm.

The following experiments are performed with the actuation method explained in section 6.2.5. The slider moves over a range from X^{min} to X^{max} starting from $x = 0$. The squared actuation voltage $Uact^2$ is used as the displacement-axis.

As indicated in Table 3, the quasi-static experiments in this section are performed with generation I devices, without the possibility to electronically control the gap-size between sense-structures and slide. The connection schematic for the measurement instrumentation is given in 6.2.5. During these measurements the corner-frequency f_c of the LPF filter in the synchronous detector was set to f_c~50Hz. The phase correction for the synchronous detector is not implemented in this case.

At each position the output voltage of the synchronous detector is measured with the HP34401A Multimeter. After 10 cycles, the mean output voltage U_{out} and standard deviation are as given in Fig. 15.

The periodically changing capacitance between the two rectangular geometries on resp. slider and sense-structures is clearly visible. A maximum voltage U_{out} corresponds to a maximum capacitance and the period length of 12 µm can clearly be identified.

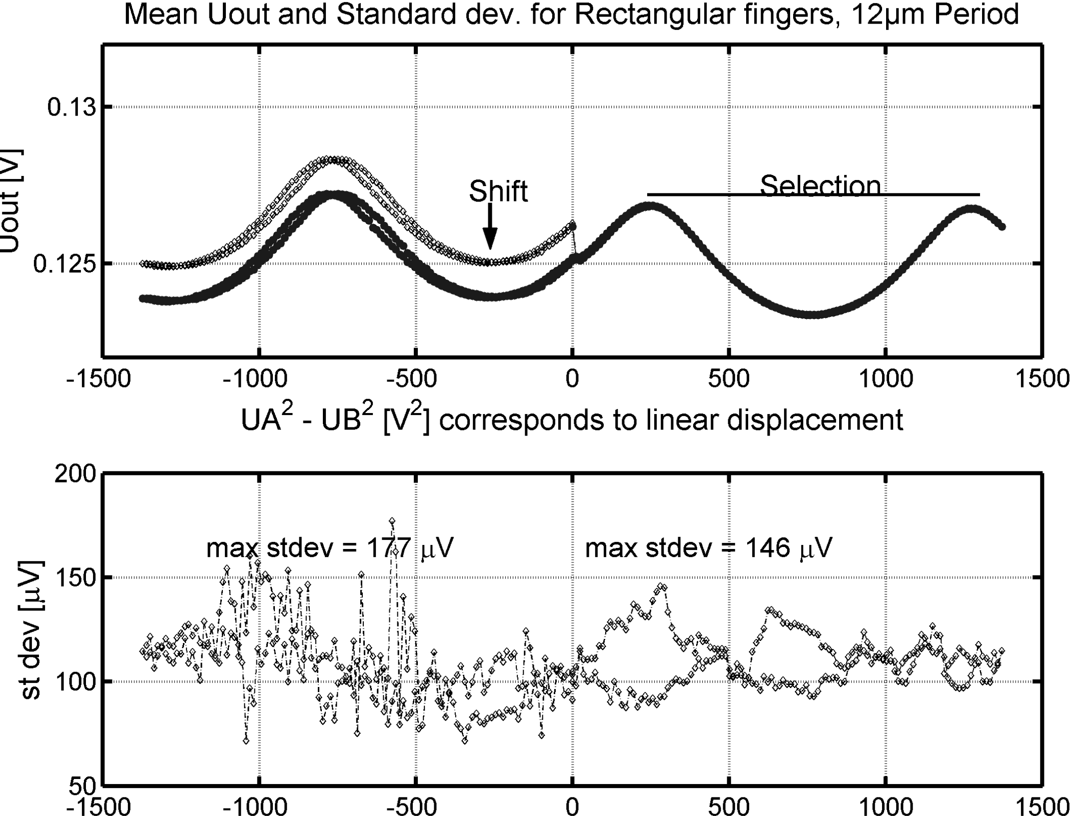

Fig. 15: Example of a measurement result for the geometry with rectangular fingers (RectP12). The mean output voltage (top) and standard deviation (bottom) are given after 10 cycles.

Whenever the slider is returning at the zero position and the voltage supply UB is becoming active and supply *UA* inactive (*UA*=0V) a sharp transition in output voltage is measured at the output of the synchronous detector. The effect is probably caused by a changing output impedance of the DC-supply and does not have anything to do with the device. The left part of the measured curve in Fig. 15 has been shifted downwards to make a better comparison with the results for other geometries.

For $UA^2 - UB^2 < 0$ the measured mean output curve also shows a considerable hysteresis effect. This effect is very probably due to small particles on the device and the substrate hampering the active comb-drive since the hysteresis in the curve for $UA^2 - UB^2 > 0$, where the other comb-drive is active, is visibly much less. Also, the maximum standard deviation is larger for this situation as Fig. 15 shows. Further measurements presented later will show that this hysteresis effect is not related to the measurement method or to the sensor concept, but only to the test-vehicle and perhaps the fabrication process. The same effect was reported in [1] with measurements performed with the impedance analyzer.

A segment of the curve, as indicated in Fig. 15 is selected and compared in Fig. 16 with other selections of the measured curves for the other geometries. In the Appendix 3.3 the measured curves for the other geometries are given. The periodicity of the measured output voltage U_{out} in Fig. 15 should correspond to the period size of P_x = 12 µm for the geometry with rectangular fingers on both slider and sense-structures. Therefore, the periodicity of U_{out} is used to relate the values for ($UA^2 - UB^2$) with the displacement (x) as used in Fig. 16.

The selected segments in Fig. 16 show that the bias or offset voltage, which is mainly caused by the parasitic capacitance *Cp* parallel to the sense-capacitance *Cs* in Fig. 11, is for each geometry roughly the same. The parasitic capacitance C_p changes with changes in the measurement conditions such as changes in the relative humidity, the temperature, the measurement set-up and the connection through probe-needles. Therefore, it is concluded that these measurement conditions are reasonably equal for all successive measurements.

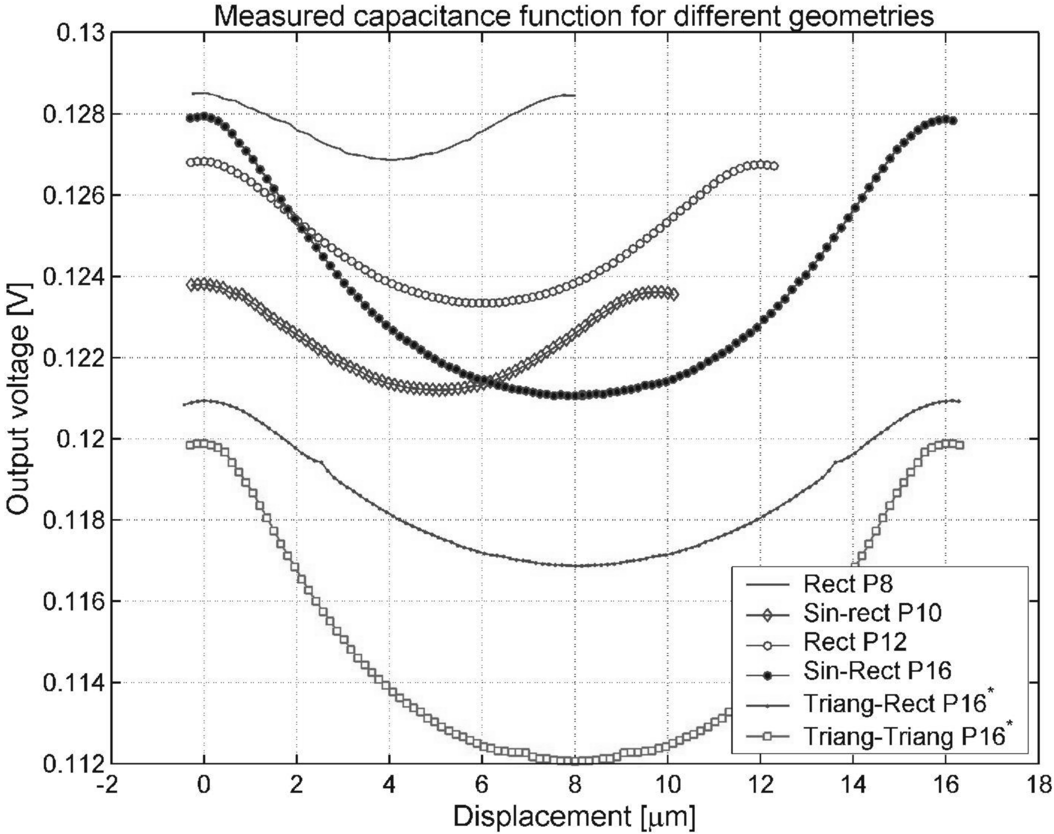

Fig. 16: Measured output voltage / capacitance function for different geometries. The curves indicated with * are mirrored around the x=P_x/2 –axis

Fig. 17 shows the measured difference or change in U_{out} (i.e. change in capacitance), for different geometries. For larger period sizes of the geometries the amplitude ΔU_{out} increases because of 2 effects:

1) the gap size between the structures can be designed smaller, without violating the rule for a minimum gap size (for x = 0) of 2 μm in the photo-lithography step as explained in chapter 5. (this is not the same gap as the design-gap g_d)
2) for a relative displacement of half a period $x = P_x/2$ the mutual distance between the peaks (fingers) of two opposing geometries is larger for a larger period. Therefore, the contribution of charge density on the side-walls to the effective capacitance C_s between the geometries is less for a larger period. The capacitance function will have a minimum which decreases for increasing period size. This effect corresponds very well with the earlier performed simulations in chapter 4

Because the gap-distance for the combination Triang-TriangP16 is g_d = 0.5μm as given in Table 4, this geometry is showing the largest maximum change in capacitance. Equally, because the gap-distance for the combination RectP8 is g_d = 2 μm in combination with the smallest period size, this geometry is showing the smallest maximum change in capacitance.

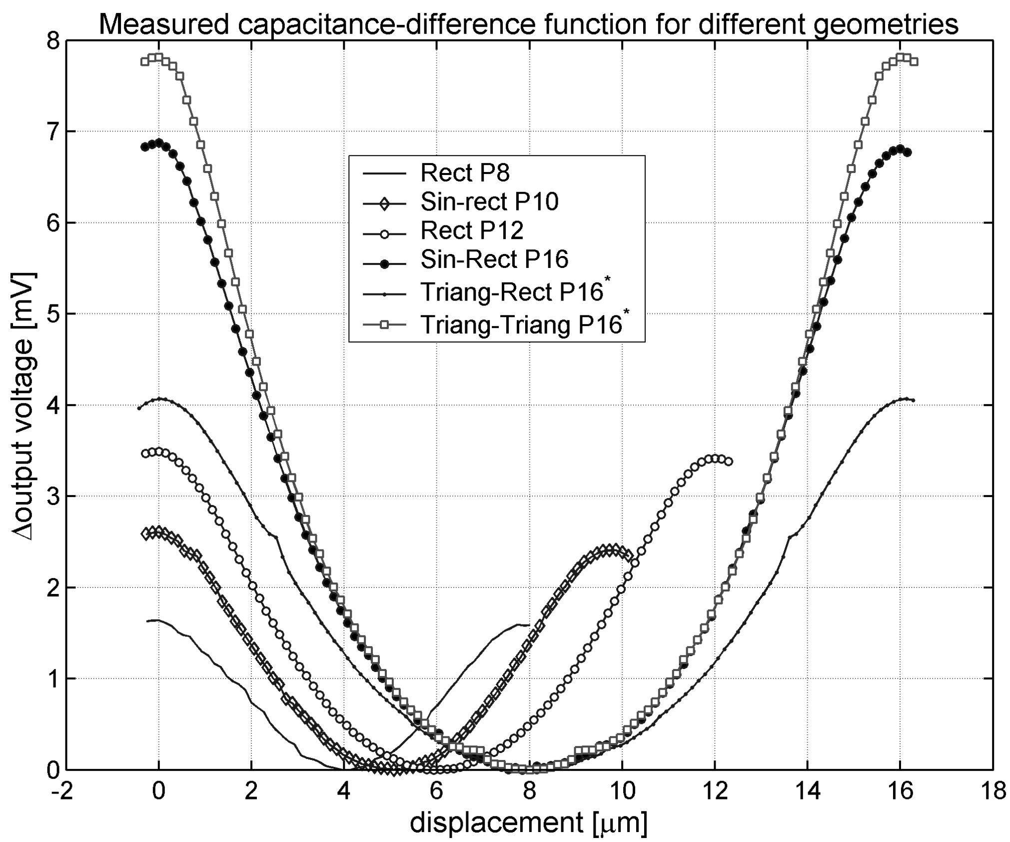

Fig. 17: The measured change in output voltage or capacitance function versus displacement up to one-period for each geometry. The curves indicated with * are mirrored around the $x=P_x/2$ **-axis.**

In Fig. 18 the capacitance functions for all geometry combinations are normalized in both output voltage and displacement i.e. $U_n = U_{out} - (U_{out})_{min} /(\Delta U)_{max}$ and $x_n = x/P_x$. This approach in theory makes it possible to compare between all available geometry combinations. If for example 2 sinusoids with amplitudes differing 10x are normalized and compared in this way, the difference between the two normalized curves will be zero because both shapes are purely sinusoid. It is in practice the SNR-ratio or the resolution and the dynamic range of the output voltage of the sensor, charge amplifier, synchronous detector and measurement unit that really determines the accuracy to detect an absolute position. However, Fig. 16 and Fig. 17 show that the measured values of the output curves are of the same order of magnitude and this makes a comparison as in Fig. 18 useful.

The measured curve for RectP8 is not as fluent as desired, because also with this device the motion was hampered by small particles as explained earlier. However, together with the curve for Sin-RectP10 they show the best but far from perfect correspondence with either a pure Sine or a pure Triangular curve. Therefore, these geometries are the favorite ones with some reservations.

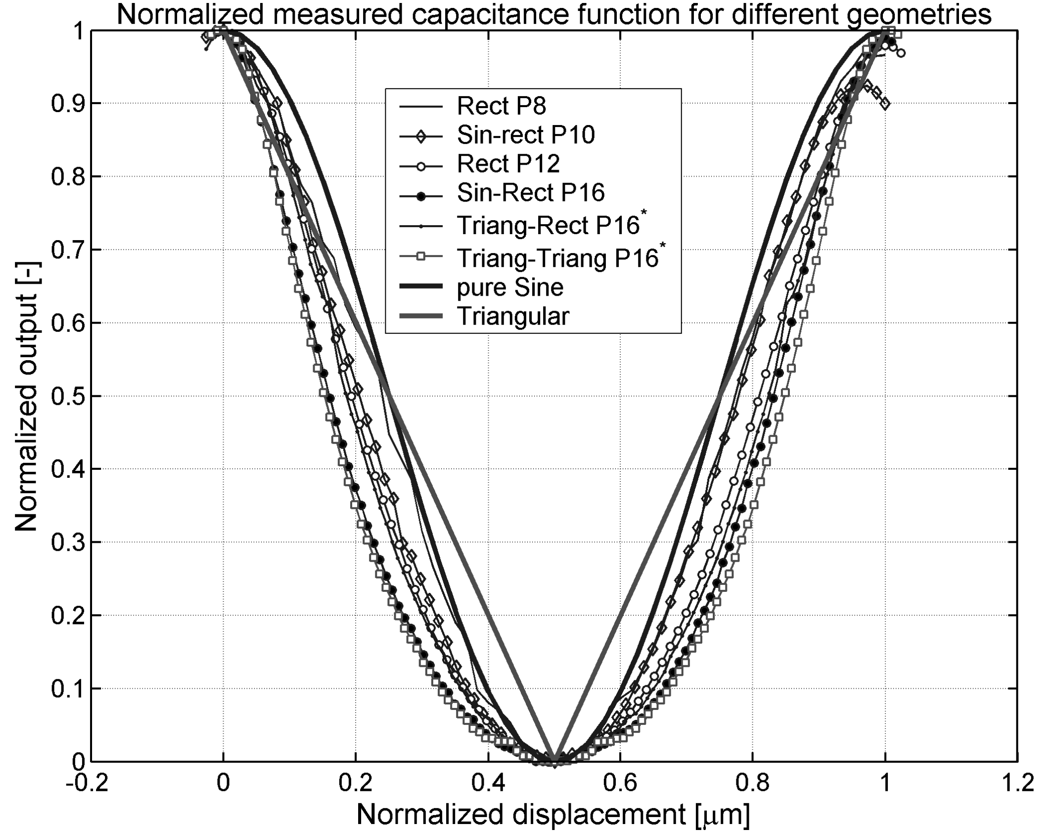

Fig. 18: Normalized output function versus normalized displacement

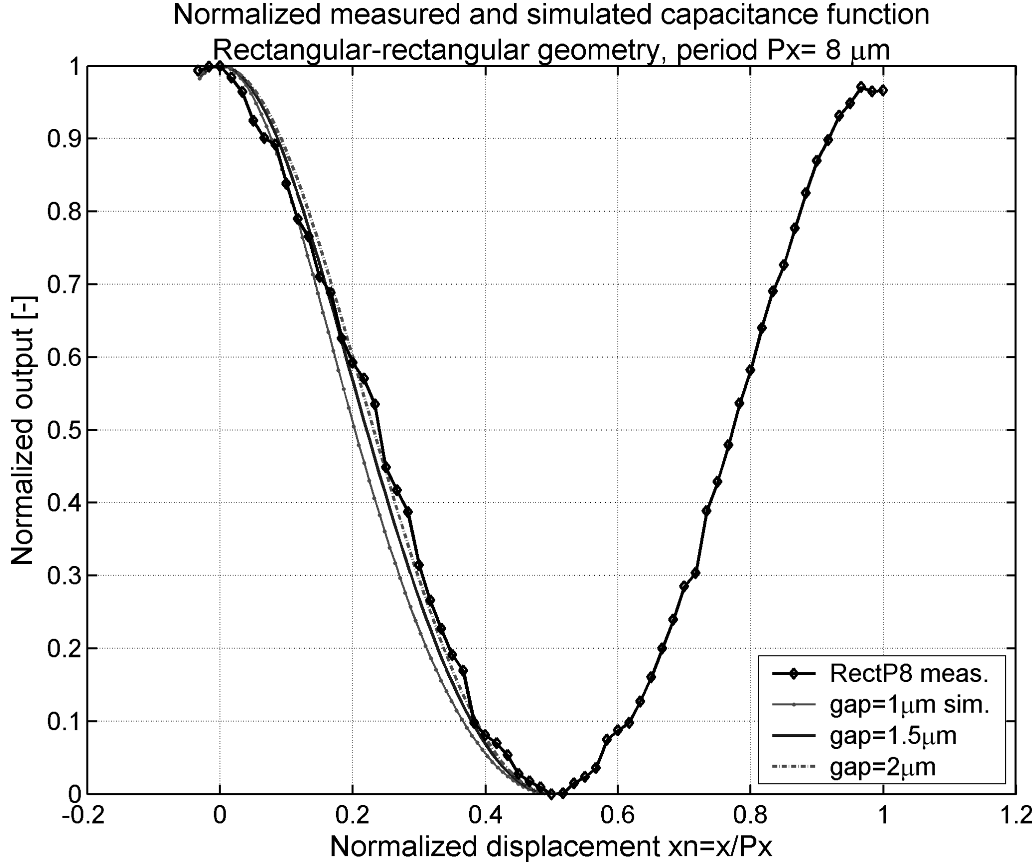

Fig. 19: Comparison between normalized measured curve and three simulated curves for the RectP8 combination with rounded instead of rectangular fingers.

In Fig. 19 a comparison is given between the normalized output curve for the RectP8 geometry combination and two normalized curves obtained through 2D-FE simulations. For the simulations the fingers were taken rounded as indicated in Fig. 13 to approach the real micromachined finger structure better. It is clear that the simulation results with a gap distance equal to the design gap distance of g_d = 2 µm or for a gap g = 1.5 µm, correspond reasonably well to the normalized measured curve. Simulation with a gap of g = 1 µm is clearly less good.

In Fig. 20 a comparison is given between the measured curve and three simulated curves for the geometry combination of rectangular fingers on the sense-structures and a sine pattern on the slider with period P_x = 10µm (Sin-RectP10). The simulated curves are for fingers with rounded edges as indicated in Fig. 13 and the minimum gap distance is g = 1 µm and g= g_d = 1.5 µm and g = 2 µm. It is clear from Fig. 20 that taking a gap distance in the simulations with rounded fingers close or equal to the design gap distance of g_d = 1.5 µm will give a simulation result corresponding very well to the normalized measured curve.

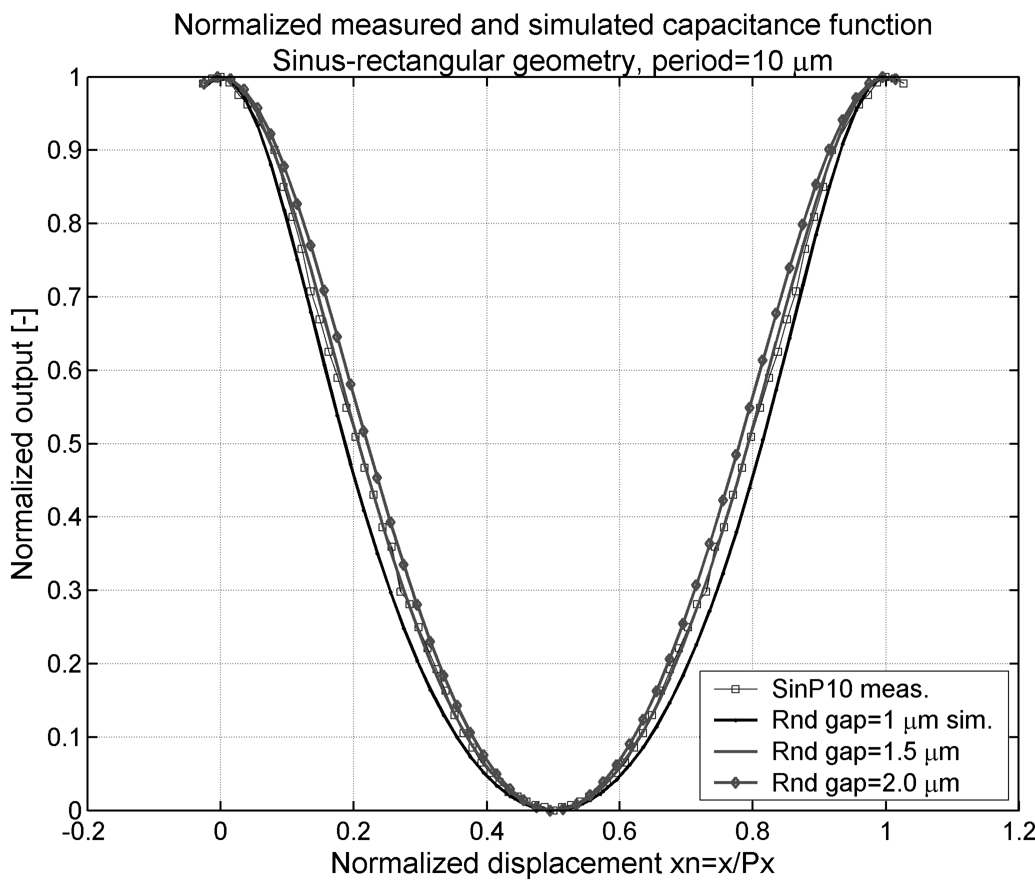

Fig. 20: The normalized measured curve and three simulated curves for the SinP10 combination. Simulations for rounded instead of rectangular fingers show a very good fit for a gap-distance g equal to the design gap-distance g_d .

Fig. 21 gives the normalized measured curve and three simulated curves for the RectP12 combination. A perfect fit is found for simulation with a gap g equal to the designed gap-distance g_d (g = g_d =1.5 µm).

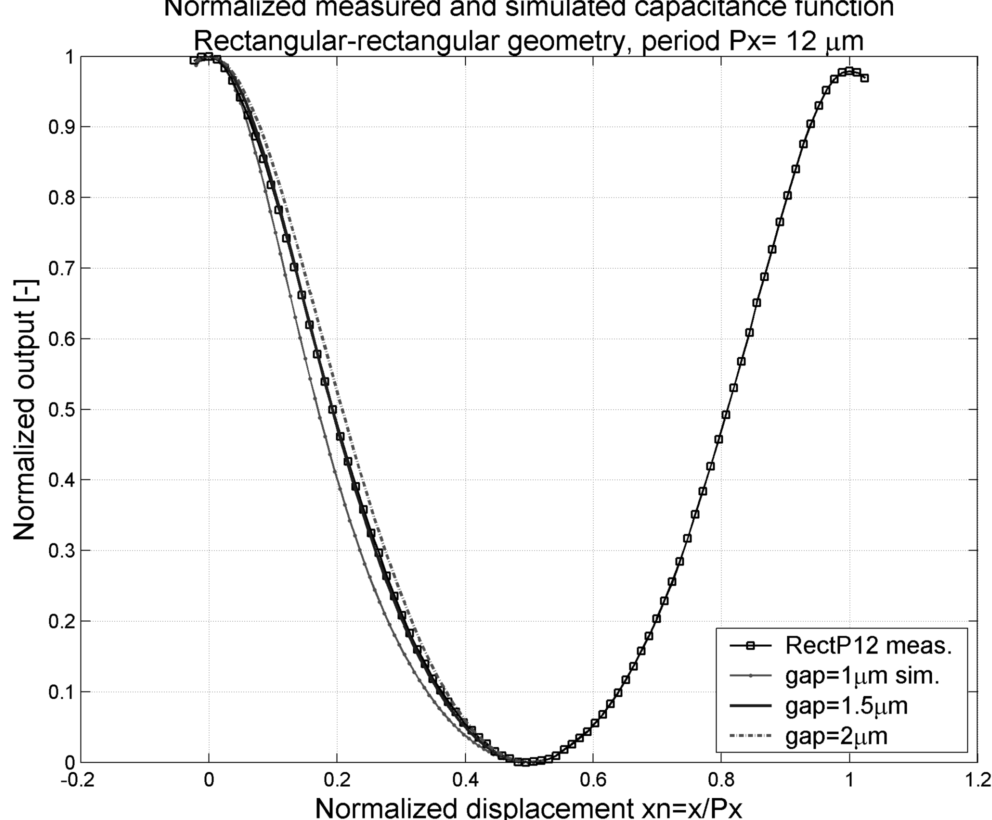

Fig. 21: The normalized measured curve and three simulated curves for the RectP12 combination. A perfect fit is found for simulation with a gap *g* = 1.5 µm

The conclusion is that, the simulation with 2D-Finite Elements with the assumption of infinitely high geometries as explained in chapter 4, is a useful tool to realistically predict the function of capacitance versus displacement for different combinations of opposing geometries. Only the absolute capacitance value may differ considerably from the value encountered in a realized micromachined sensor due to the unknown addition of parasitic capacitance. This is examined in the following part where the charge amplifier and synchronous detector are calibrated with the use of fixed discrete capacitor components.

With the acquired linear relations in section 6.2.3, Fig. 8, the measured relation between output voltage U_{out} and displacement (x) for the different micromachined geometries is compared in Fig. 22 with 2D-FE simulated curves. Naturally the 2D-FE simulations do not simulate the 3D effects of a ground-plane underneath the structure, or the additional parasitic capacitance C_p. However, under the assumption that the correspondence between measured and simulated capacitance functions will be best at maximum capacitance when the gap between the two geometries (S1 and S2) is minimal, the simulated graphs are vertically aligned by making the simulated maximum equal to the measured maximum value.

The comparison for three geometry combinations given in Fig. 22 shows that for the simulated curves with a gap smaller than designed as indicated in Table 4 the correspondence is better, although the maximum change $(\Delta C_{sim})_{max}$ is then predicted larger than measured. One obvious cause for this effect is the deviation between feature sizes of fingers and gaps in the mask design and the realized feature sizes after processing (i.e. Lithography and plasma etching). A deviation of 100-200 nm is not unrealistic.

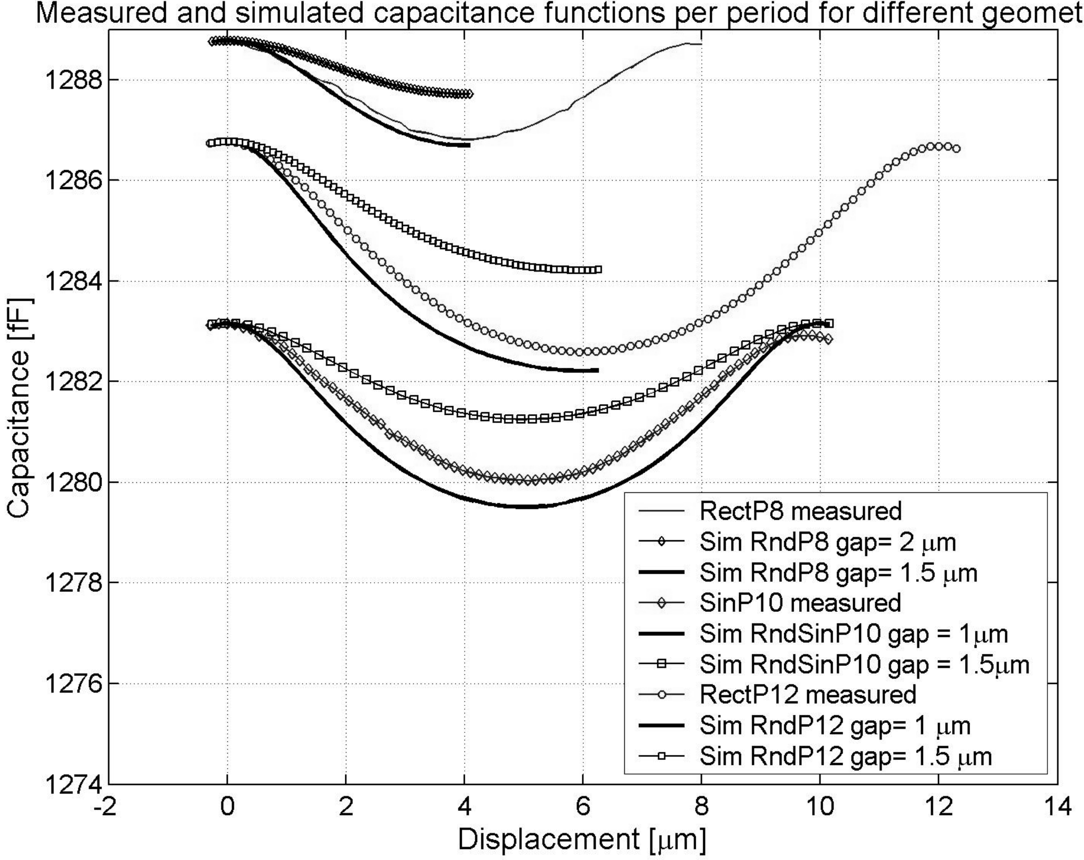

Fig. 22: The measured curves as given earlier in Fig. 16 and Fig. 17 are converted to capacitance-scale and compared with curves acquired through 2D-FE simulations.

Another cause for the fact that the measured change in capacitance is larger than predicted by the 2D simulations may be the 3D-effect of straying capacitance caused by the ground-plane underneath the structures. For a half-period displacement ($x = P_x/2$) when the distance between the geometries is largest the ground plane will have the most influence and the measured capacitance between the two geometries may be smaller than predicted by 2D-simulations. Field flux lines will originate on the charges on one geometry and go directly to the surface of the substrate. Therefore, if the number of field lines or the amount flux directly linking the two geometries will be less then, the capacitance can be less than without ground plane. (e.g. described by 3, 5).

6.3.2 Quasi-static experiments with active gap-adjustment

This section presents the results of measurements with a generation II device, with the possibility to move the sense-structures closer to the slider with additional sense-actuators (comb-drives). With this possibility an increase in capacitance variation and thus in output voltage is expected.

The following experiments are done with a device with a sine versus a rectangular geometry on respectively slider and sense-structure with a period size of P_x = 10μm (SinP10). The connection scheme is the same as in section 6.3.1. One pair of sense-structures on either side of the slider are connected in parallel (e.g. similar to *ϕ2-a&b* in Fig. 2)

In Fig. 23 the measured output voltage (i.e. corresponding to the capacitance function) of the synchronous detector is given for three sense-actuator voltages. The actuation or displacement method is the same as explained in 6.2.5. With 14Vdc_rev applied to the sense-actuators, which pull the sense-structures away from the slider (denoted as reverse) the capacitance decreases and the standard deviation increases. This is shown in Fig. 24 with the average of the measured output voltage U_{out} after 5 cycles and the standard deviation.

It is assumed that the standard deviation is related to noise. As a result of the smaller capacitance, the signal will decrease, the noise conform the *kT/C* – model (chapter 3) increases. Therefore, the SNR is decreased as depicted in Fig. 23 and Fig. 24. In return, with 14Vdc (forward) applied to the sense-actuators that pull the sense-structures towards the slider, the capacitance increases and the SNR too. For the three measurements the settings of the multimeter are given in Table 5 with reference to Table 2:

Curve in Fig. 23	Setting Table 2
a)	a) T_{int} = 0.2 sec
b)	b) T_{int} = 2 sec
c)	b)

Table 5: settings for HP34401A multimeter for the measurements in Fig. 23.

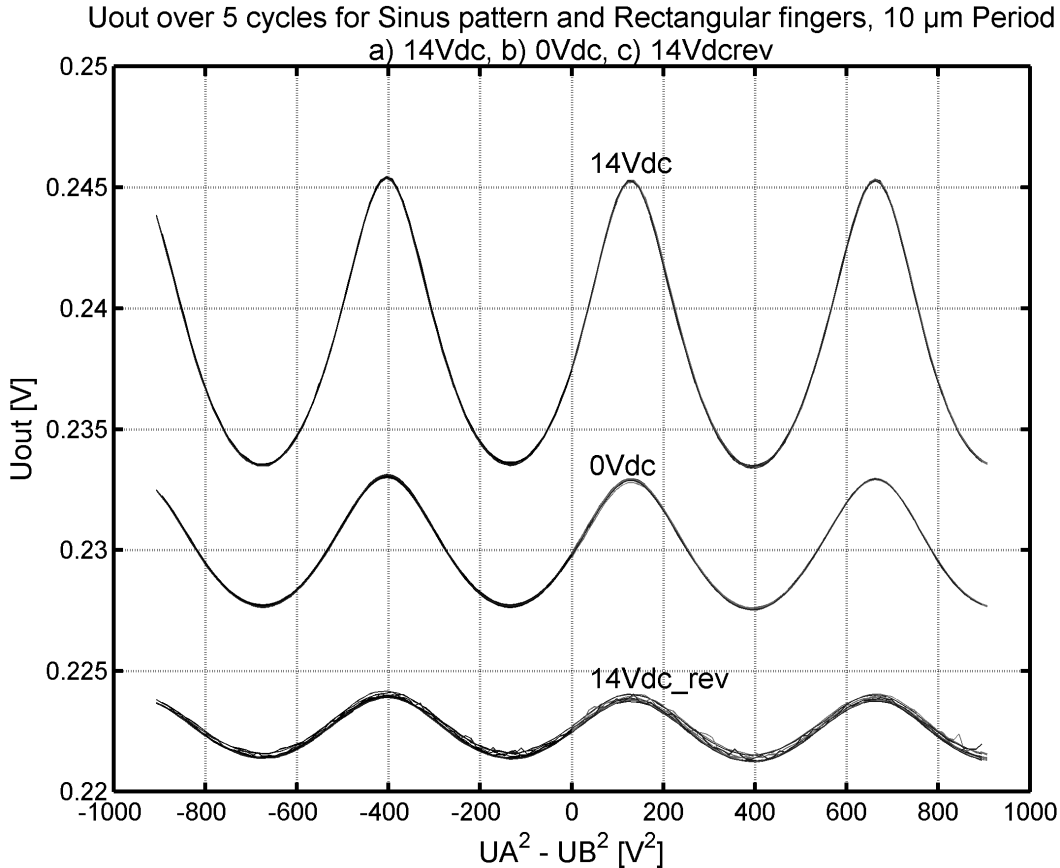

Fig. 23: The measured output voltage (capacitance) of five cycles for three different sense- actuator voltages i.e. gap-distances.

From Fig. 23 it is clear that decreasing the gap indeed increases the output U_{out} and thus the periodic capacitance increases. With 14 Vdc applied to the sense-actuators in forward (smaller gap) the maximum change in ΔU_{out} = 11.8 mV indicated in Fig. 25 over 5 µm (period size P_x = 10 µm) displacement corresponds with an average change of 2.4 µV per nanometer (nm) change in displacement. This figure is around a factor of 4.5x larger than the ΔU_{out} given in Fig. 17. The displacement axis can be calculated on the basis of the periodicity of the output voltage U_{out} and the period size of 10 µm for this geometry.

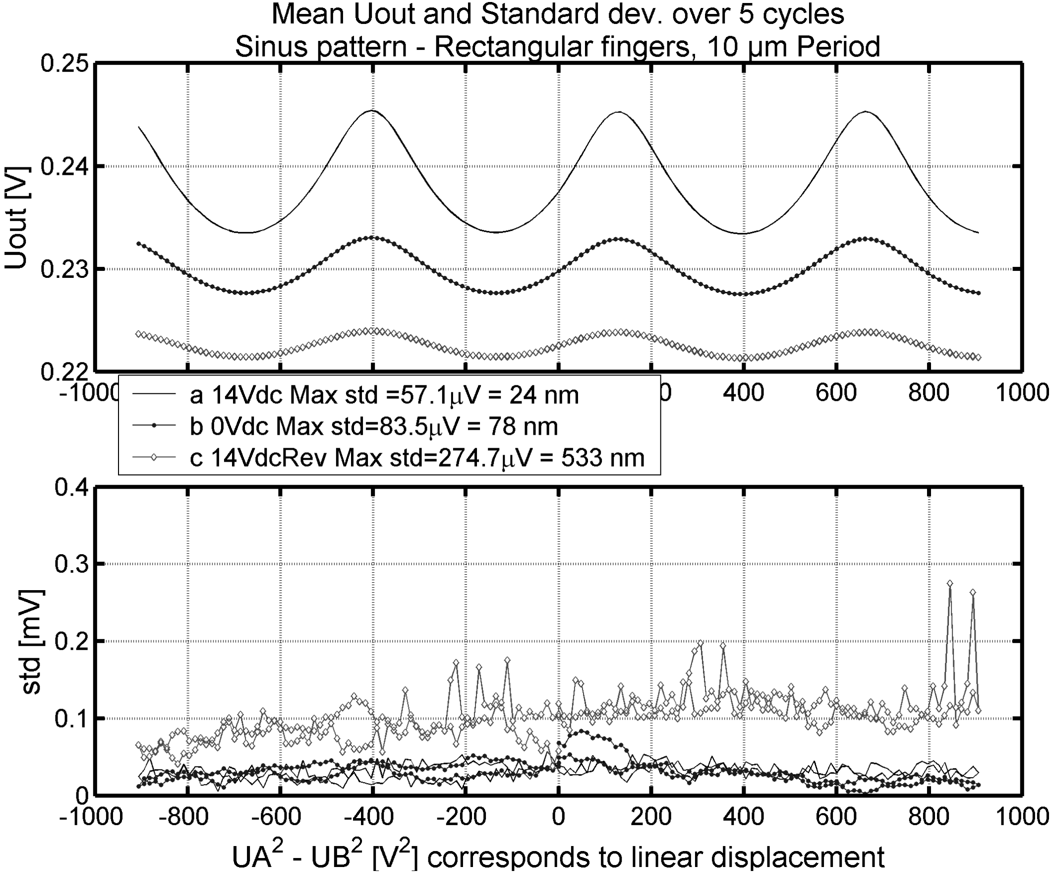

Fig. 24: The mean output voltage (top) and the standard deviation (bottom) of 5 cycles for 3 different sense-actuator voltages.

The standard deviation for curve a) in Fig. 24 of 57 µV can be seen as a position uncertainty. In ratio with the maximum change in output voltage ΔU_{out} per half-period the position uncertainty $|\Delta x|_{max}$ = 57 [µV] / (11.8 [mV] / 5 [µm]) = 24 nm and for curve b) $|\Delta x|_{max}$ = 79 nm. Fig. 24 and Fig. 25 indicate that the SNR does improve significantly when the gap between sense-structures and slider is decreased.

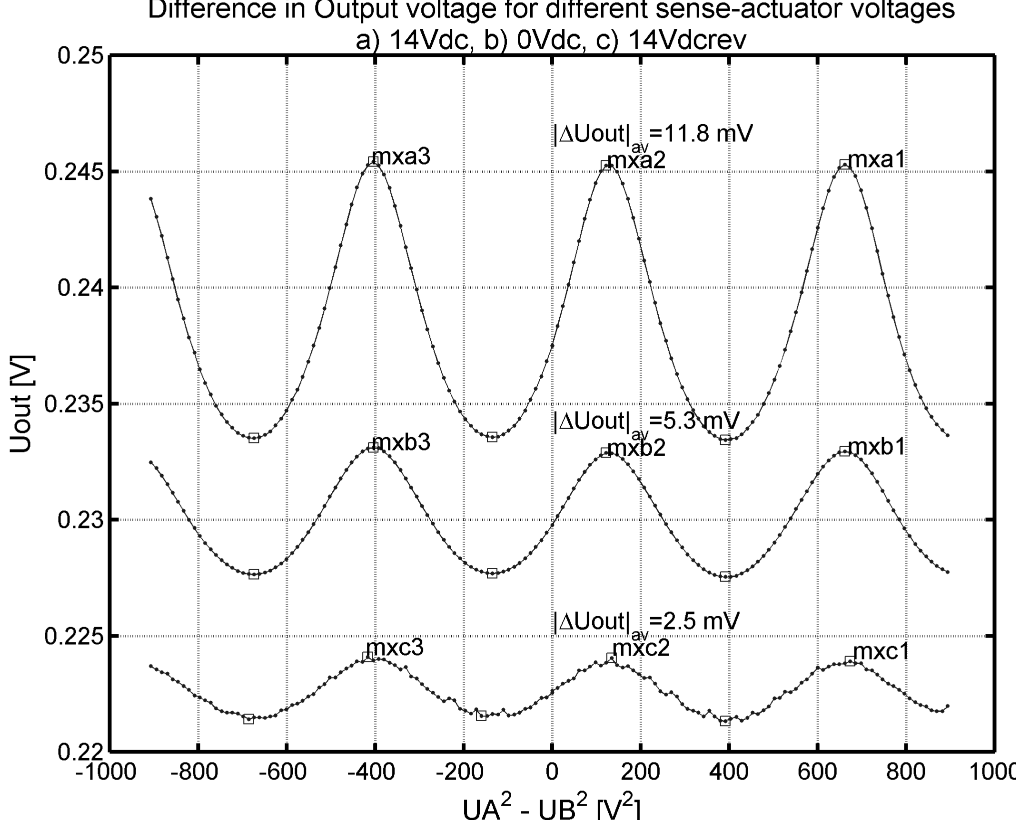

Fig. 25: The peak-peak output voltage (averaged over 2 periods) for 3 different sense-actuation voltages.

The previous calculation does not take into account the possibility for a difference (hysteresis) between the up-sweep and the down-sweep i.e. simply put, going from most left = X^{min} to most right = X^{max} instead of right to left. To clarify the naming of 'up-sweep and down-sweep the mean measured output voltage *$(U_{out})_{mean}$* after 5 cycles for up and down sweep has been shifted vertically in Fig. 26 *(Top)*. However, this curve is exactly the same as the curve a) with 14 Vdc forward in Fig. 24 and Fig. 25.

In Fig. 26 *(middle)* the difference *(E_{hyst})* in mean measured output voltage between up- and down sweep is given. In Fig. 26 *(bottom)* the standard deviation for 5 up-sweeps and 5 down sweeps is given.

The voltage difference *(E_{hyst})* between mean up- and mean down sweep is used to calculate the maximum, the average and the standard deviation of the position uncertainty (imprecision) due to hysteresis, drift and noise. Thus, the values for position imprecision can have a systematic component causing hysteresis and a stochastic component due to noise and drift caused by changes in temperature and relative humidity and general interference. In this respect, it is clear that a longer integration time for the multimeter also means a longer cycle time. This means that the probability increases that the difference *(E_{hyst})* between up- and down sweep increases due to drift. In other words, if the systematic component in E_{hyst} is not time-dependent, the difference E_{hyst} may increase with longer measurement time due to an increase of a stochastic component.

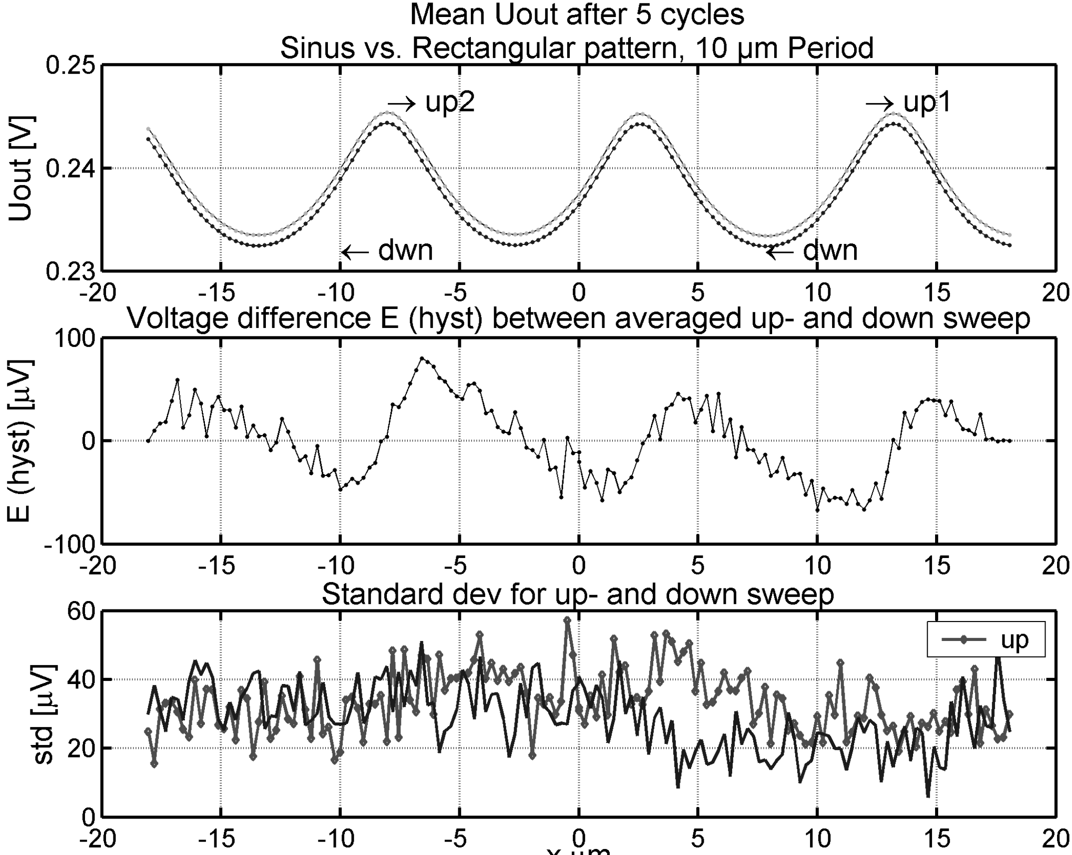

Fig. 26: The difference in voltage *Ehyst* between up- and down sweep averaged over 5 cycles. *(bottom): Std* for up-sweep and down-sweep.

The ratio of $|(E_{hyst})|$ and the maximum change in output voltage ΔU_{out} per half-period displacement is used to calculate the following error estimates:

$| E_{hyst} |_{max_h} = 79$ µV → $|\Delta x|_{max_h} = 34$ nm,
$| E_{hyst} |_{mean_h} = 29$ µV → $|\Delta x|_{mean_h} = 12$ nm,
$| E_{hyst} |_{std_h} = 19$ µV → $|\Delta x|_{std_h} = 8$ nm.

The difference E_{hyst} in Fig. 26 *(middle)* clearly exhibits a periodic hysteresis. This is very probably due to electrostatic forces between the two geometries on sense-structure and slider. Further study is necessary for this effect.

The standard deviation for the 5 up-sweeps and 5 down sweeps is given in Fig. 26 *(bottom)*. The average of the standard deviation for the up- and down-sweep is calculated and in the same way related to a position uncertainty:

$mean(U_{std_up}) = 33$ µV → $|\Delta x|_{std_up} = 14$ nm
$mean(U_{std_dwn}) = 29$ µV → $|\Delta x|_{std_dwn} = 12$ nm

A further study for the correlation of the standard deviation of U_{std_up} of the up-sweep with $(U_{out})_{mean}$ for the up-sweep could tell if the standard deviation is stochastic or influenced by a deterministic mechanism, such as the electrostatic forces between sense-structure and slider in combination with a periodic geometry.

We can conclude that as expected the possibility to decrease the gap between sense-structure and slider through extra sense-actuators is increasing the capacitance variation as function of displacement. A decrease in overall maximum standard deviation is demonstrated without discriminating between up- and down sweep and results in a maximum position uncertainty of $|\Delta x|_{max}$ = 24 nm.

An estimation of the position or displacement uncertainty has been obtained by discriminating between up- and down sweeps. The systematic difference is called hysteresis and amounts in average to $|\Delta x|_{mean_h}$ = 12 nm,

The average standard deviation of the measured output voltage U_{out} for the up- and the down sweep is respectively $|\Delta x|_{std_up}$ = 14 nm and $|\Delta x|_{std_dwn}$ = 12 nm.

For real accuracy determination a characterization facility or set up should be used for example a laser interferometer setup or image analysis setup [6,7,8]. However, nm accuracy appears to be feasible.

Estimation of Non-Linearity for experiments with gap-adjustment

For quadrature detection it is necessary to have either pure triangular or pure sine measurement signals, see chapter 3. Therefore, in the following a further assessment is done to determine how well the measured output signal of the synchronous detector U_{out} corresponds with a pure sine. The dominant harmonic in U_{out} is called $U_{out_\omega 0}$ and ω_0 = $2\pi/P$ is the spatial frequency of the periodic geometry. All higher order components of U_{out} define a residual signal U_{out_Rn}. For higher accuracy the ratio of the higher order components and the first order component $U_{out_\omega 0}$ should be as small as possible. In Fig. 27 the FFT spectrum is given of the measured U_{out} averaged over 5 up-sweeps.

$$U_{out}(x) = \frac{1}{N}\sum_{n=0}^{N} A_n \cdot \cos(n \cdot \omega_0 \cdot x) \quad \text{(Eq.6 7)}$$

And the amplitudes A_n are given by the FFT

$$A(n) = \sum_{n=0}^{N} X(k) \cdot exp(-i \cdot 2\pi \cdot n \cdot k / N), 0 \le n \le N \quad \text{(Eq.6 8)}$$

The first harmonic in space-domain $f_{\omega 0}(x) = U_{out_\omega 0} = A_1 \cdot cos(\omega_0 \cdot x)$

The residual spatial function of all higher order harmonics is defined by:

$$r_n(x) = \frac{1}{N}\sum_{n=2}^{N} A_n \cdot \cos(n \cdot \omega_0 \cdot x) \quad \text{(Eq.6 9)}$$

f(x) $_{(\omega 0=0.2\pi)}$ [mV]	**$f_{(2\omega 0)}/f_{(\omega 0)}$**	**$r(x_n)$ [mV]**	**$r(x_n)/ f(x)_{(\omega 0)}$**
5.6639	0.1727	1.4272	0.2520

Table 6: amplitudes and ratios for FFT components of Uout for situation a) 14 Vdc applied to sense-actuators

The amplitudes and ratios between the first order component $f(x)_{\omega 0\ =\ 0.1}$ and second

order component and the residual signal are given in Table 6. The amplitude of the residual signal is 25% of the first harmonic.

The inverse FFT of all higher order components defined as the residual signal $r_n(x)$ is given in Fig. 28.

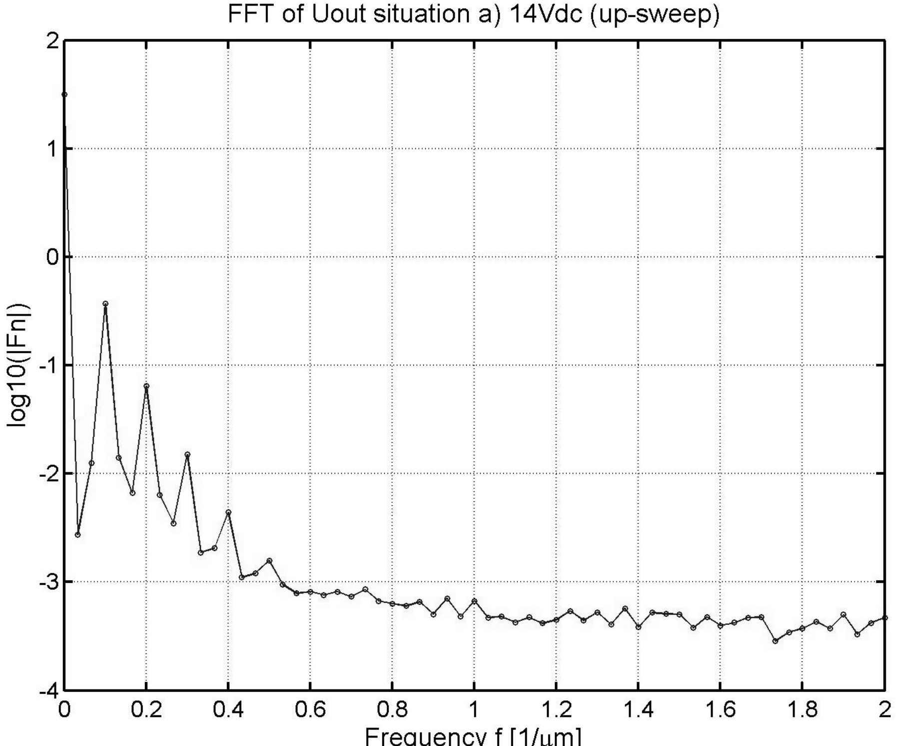

Fig. 27: FFT spectrum of the average of U_{out} for the up-sweep

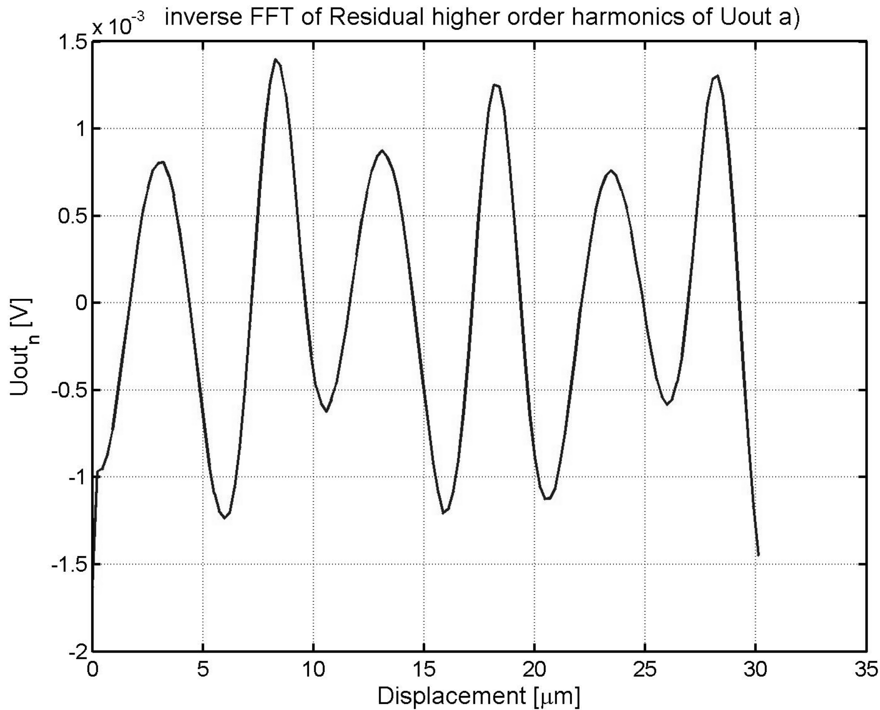

Fig. 28: The residual signal after the inverse FFT

It is concluded that the ratio of 25% of the residual signal versus the first order harmonics of the measured U_{out} is a concern for the implementation of quadrature detection and it will limit the obtainable accuracy. In the next section the same Fourier analysis will be done for the CCMM concept.

6.4 QUASI-STATIC EXPERIMENTS FOR CONSTANT CAPACITANCE MEASUREMENT MODE

6.4.1 Operation of constant capacitance measurement mode

In this section the assessment is given of the measurements with the closed-loop Constant Capacitance Measurement Mode (CCMM). As explained in chapter 3, the gap between slider and sense-structures is now continuously controlled by the additional sense-actuators (comb-drives) to keep the capacitance equal to a certain set-point value for all positions of the slider. The larger the set-point-value the more closely the sense-structures will be following the slider-pattern and thus a larger capacitance and signal to noise ratio (SNR) is expected. By measuring the periodic control voltage for the sense-actuators the slider-displacement can be measured with increased accuracy.

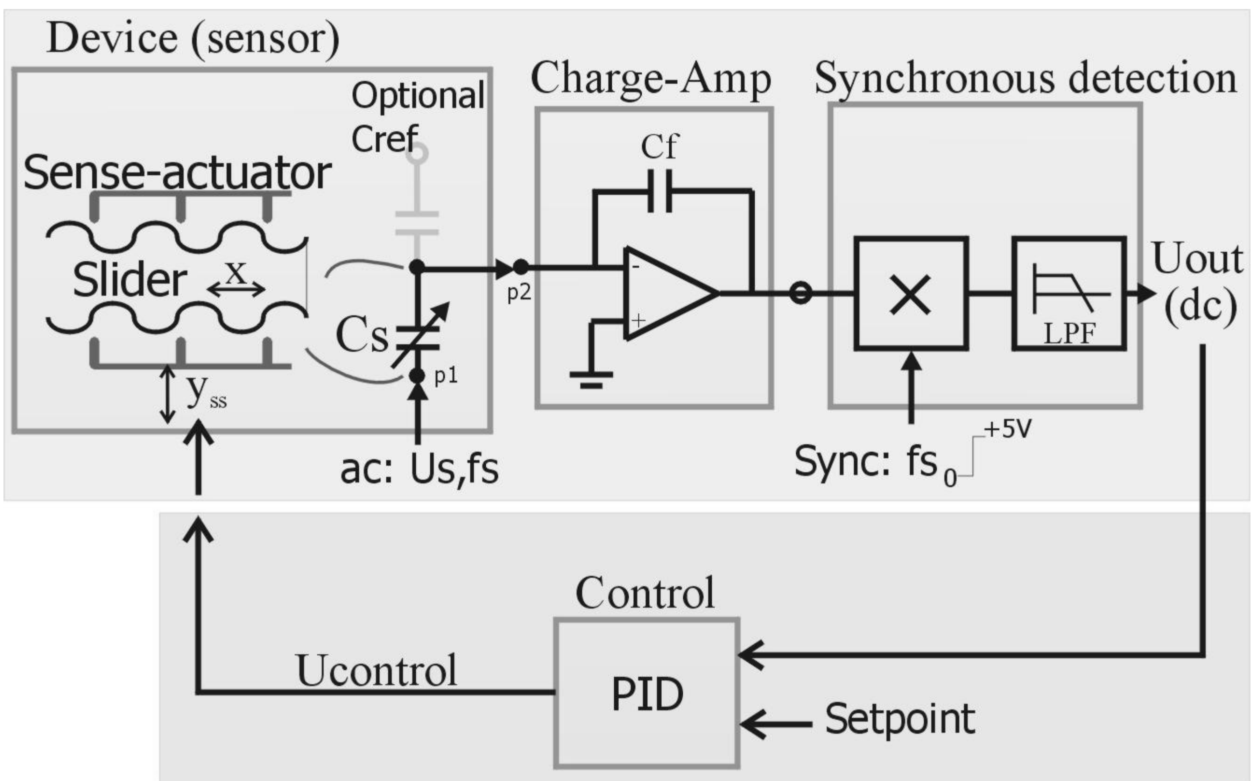

Fig. 29: Overview of the implementation for constant capacitance measurement mode

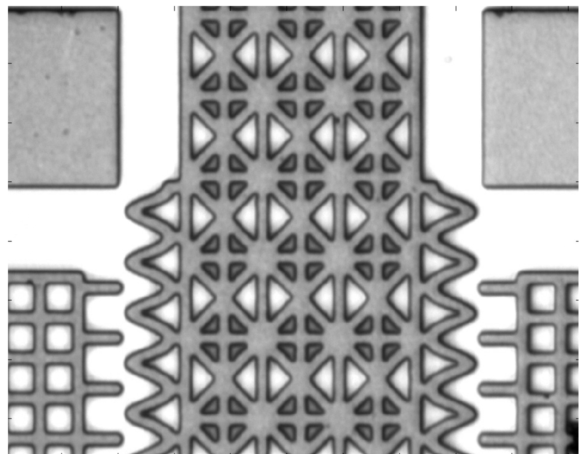

Fig. 30: Example of a micromachined device with sense-structures on both sides of the slider.

Based on the idea behind the CCMM concept and the analysis in chapter 3, the expectations for the experiments for CCMM are a better performance due to a higher SNR and a correspondence of the control voltage U_c to the slider pattern.

6.4.2 Implementation of constant capacitance measurement mode

The implementation of this concept to perform the measurements is the following; the drive actuators are actuated with the actuation method as discussed in section 6.2.5 i.e. the slider is linearly moving from position to position. At each position the value of the sense-capacitance between sense-structures and slider results in an output voltage U_{out}, measured by the HP 34401A multimeter with the same settings and set-up as in the previous section for the ICMM-concept. With a feedback control loop (closed-loop) an actuator voltage is calculated and supplied to the sense-actuators in order to minimize the difference/error between set-point U_{set} and measured value U_{out}.

As a first trial implementation the feedback control consists of a Proportional-Integrational-Differential (PID) control depicted in Fig. 31. It is implemented with PC-software (HPVee instrument driver).

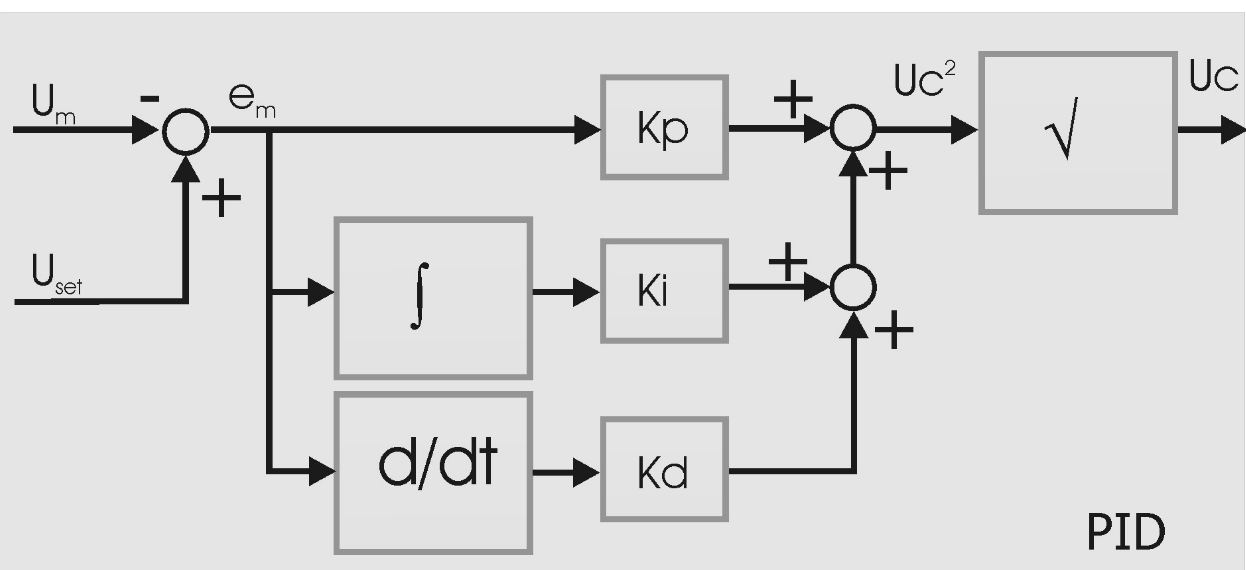

Fig. 31: Schematics of PID control with additional square root function

The error $e_m = U_m - U_{set}$ is used to calculate the control voltage for the sense-actuators, given with equation Eq.6.10.

$$U_c^2 = K_p \cdot (U_m - U_{set}) + K_i \cdot \left(\int U_m - U_{set}\right) + K_d \cdot d/dt\,(U_m - U_{set}) \qquad \text{(Eq.6 10)}$$

It is actually the y_{ss} position of the sense-structures (or the gap between sense-structures and slider) that is controlled. And because the sense-actuator is a comb-drive the y_{ss} position is proportional to the square of the applied voltage, as discussed in section 6.2.5. Therefore, the output of the PID controller is noted as U_c^2 and the result after taking the square-root is then send to the HP3631A DC-supply and applied to the sense-actuators in parallel.

The parameters for the PID-control were optimized empirically. Initially the values for K_i and K_d are taken zero, to prevent the controlled system to become unstable (i.e. $K_i = 0$, $K_d = 0$). For the implementation in HPVee the control criterion has been that a new slider position is taken only if the error $|e_m|$ has been below the error limit E_{limit} for four successive measurements:

$$X[i] \rightarrow X[i+1] \ \textbf{\textit{if}}\ |e[i]|, |e[i-1]|, |e[i-2]|, |e[i-3]| < E_{limit} \qquad \text{(Eq.6 11)}$$

Therefore, all measurements of $U_{out} = U_m[j]$ at slider position $X[i]$ are used by the PID control to calculate a new voltage $U_c[j]$. If the rule in (Eq.6.11) is accomplished, the last value U_c is recorded for position $X[i]$:

$$U_c[i] = U_c[j],\ j = 0,1,2,\ldots\ \ i = 0,1, ..N. \qquad \text{(Eq.6 12)}$$

The control voltage Uc has been limited to 28V. It was found that a higher voltage would cause side pull-in of one of the fingers of the comb-drive sense-actuators for the device at hand.

The slider is displaced over a range of ~32µm in N=150 steps, conform the actuation method in section 6.2.5. For this particular device a voltage larger than 30V would cause side-pull-in of one of the comb-fingers. Other devices (not included in the measurements presented in this thesis) would show this effect for a voltage of 37 V. This effect was calculated to occur at much higher voltages and displacements based on the derivations of Legtenberg [9].

6.4.3 Results of constant capacitance measurement mode

This section gives and evaluates the measurement results for the constant capacitance measurement mode.

The control voltage U_c versus the slider displacement is given in Fig. 32. This is for one complete cycle with a total displacement range of ~ 32 µm and a setpoint voltage of $U_{out} = 0.255$ V which is 10 mV more than for the measured maximum amplitude of U_{out} in Fig. 25 for ICMM with 14 Vdc forward (curve a) applied to the sense-actuators. Furthermore, the increase in U_{out} by 10mV is as much as the total change in output voltage $|\Delta U_{out}|^{pk\text{-}pk}$ for curve a) in Fig. 25. Clearly this should mean an improvement for

the SNR or the position uncertainty.

The absolute difference $|E_{Uc}|$ given in Fig. 33, is defined as the absolute difference in control voltage between up- and down sweep and between down and up2-sweep. It is calculated as $|E_{Uc}| = |U_{c_up}(x(i)) - U_{c_dwn}(x(i))|$ and given in Fig. 33.

Because the 2 drive actuators are successively actuated by 2 separate voltage supplies, see section 6.2.5, it is interesting to see if the averaged absolute difference $|E_{Uc}|_{mean}$ differs for the regions x < 0 and x > 0 as indicated in Fig. 33. Averaged over both regions the averaged absolute difference $|E_{Uc}|_{mean}$ = 15.4 mV and in ratio with the peak-peak control voltage of $|Uc|_{pk\text{-}pk}$ = 10.2V over 5 µm displacement, the absolute position uncertainty is calculated as $|\Delta x|_{mean}$ = 7.5 nm.

The whole measurement took ~5 hours for 1 cycle (up, down and up2 sweep).

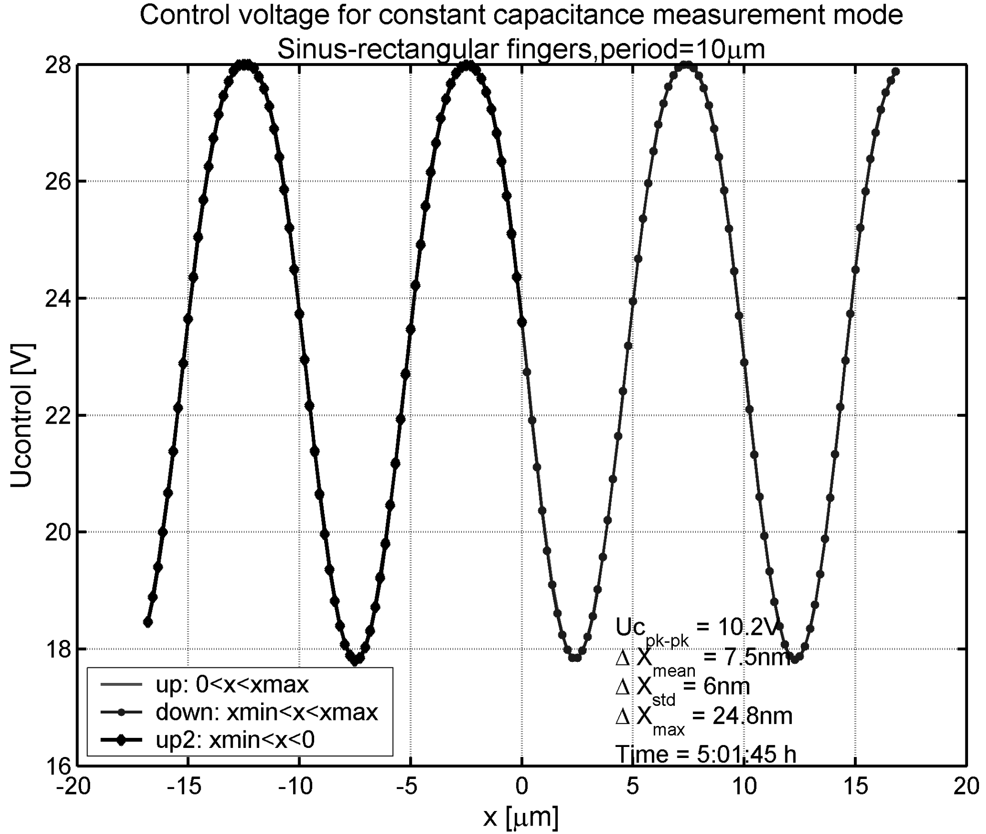

Fig. 32: The control-voltage of the sense-actuators for the closed-loop constant capacitance measurement mode. The mean displacement uncertainty is 7.5 nm over a total displacement range of ~32µm

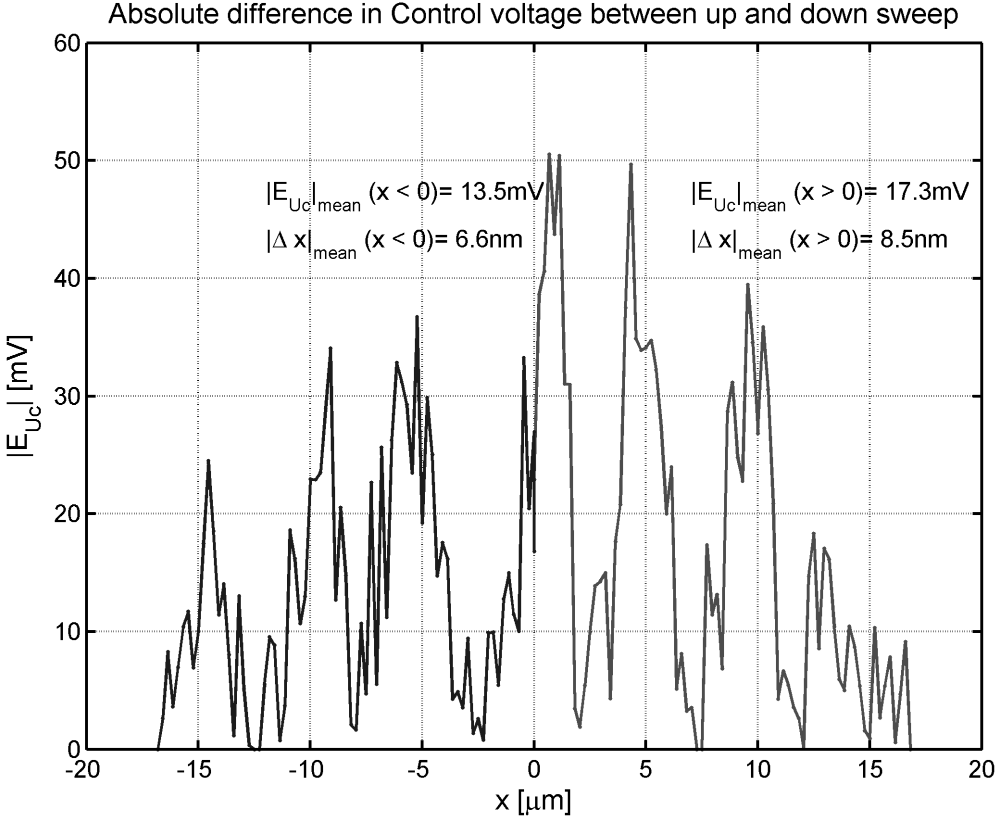

Fig. 33: The absolute difference $|E_{Uc}|$ in control voltage between up- and down sweep and the calculated position uncertainty for the sections x<0 and x>0.

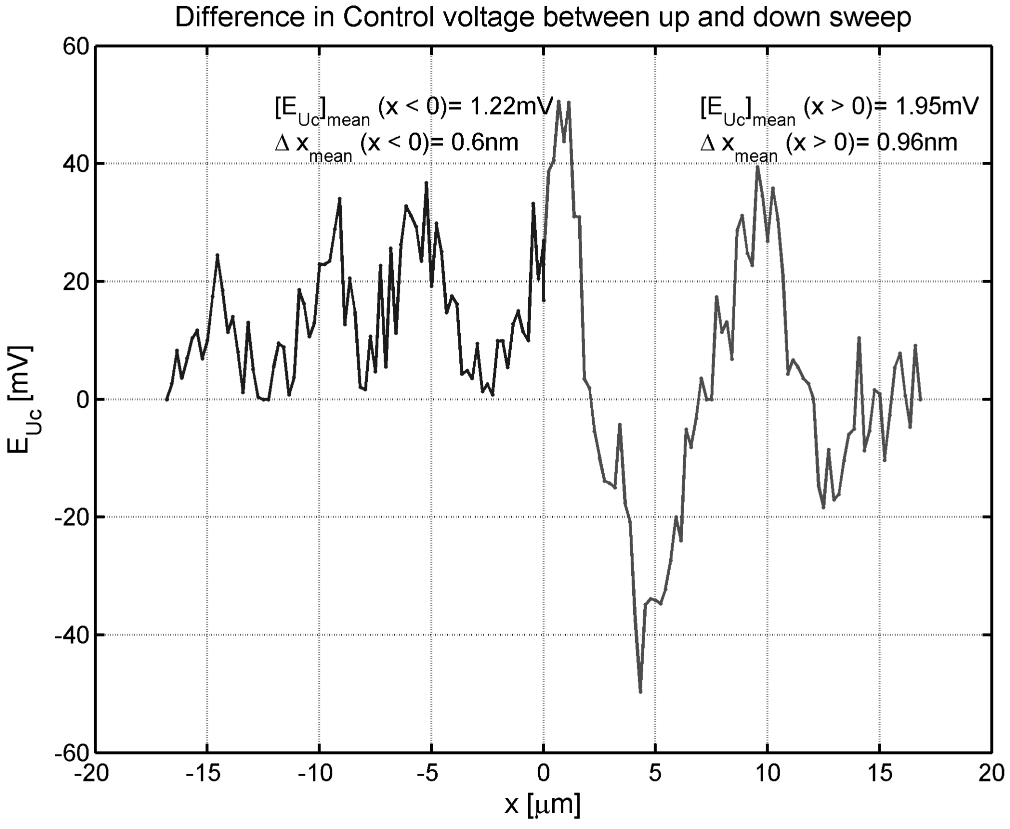

Fig. 34: The difference E_{Uc} in control voltage Uc between up and down sweep.

Fig. 33 and Fig. 34 show the (absolute) difference $|E_{Uc}|$ and E_{Uc} in control voltage $U_c(x)$ between up and down sweep. The difference $|E_{Uc}|$ and E_{Uc} shows different periodicity for x > 0 than for x < 0 and E_{Uc} is always larger than 0 for $x < 0$. This means that for all positions $X(i) < 0, U_{c_up} > U_{c_dwn}$.

Similar to the experiments for ICMM in the previous section, the difference in the control voltage between the up-sweep and the down sweep can be seen as a systematic error due to a hysteresis effect.

The absolute difference $(|E_{Uc}|)$ is in ratio with ΔU_c over 5 µm a position uncertainty of $|\Delta x|_{mean}$ = 6.6 nm for positions $X(i)$ < 0 and $|\Delta x|_{mean}$ = 8.5 nm for positions $X(i)$ > 0. Thus an average mean displacement uncertainty of $|\Delta x|_{mean}$ = 7.5 nm is achieved.

Similar to the given definition for the ICMM results this is a displacement uncertainty $|\Delta x|_{mean}$ with possibly a systematic component called hysteresis and a stochastic component due to drift and noise. However, after only 1 cycle it is not really possible to determine a systematic or stochastic nature.

For the normal difference (E_{Uc}) in Fig. 34 an position uncertainty of $(\Delta x)_{mean}$ = 0.6 nm for positions $X(i)$ < 0 and $(\Delta x)_{mean}$ = 0.96 nm for positions $X(i)$ > 0 is estimated.

The final remaining error between measured output voltage of the synchronous detector and the setpoint value, $e_m = U_{meas} - U_{setp}$ is given in Fig. 35 for all slider positions. For each position this is the 4th and last value below the error limit of E_{limit} = 50 µV after which a new position is taken by the slider as given by equation Eq.6.11 and Eq.6.12. At 3 positions the error e_m is larger than 50 µV because the control voltage U_c is limited to U_c = 28V although a higher voltage is needed to decrease the error e_m.

Further study is needed to derive a model or a relation between the error limit E_{limit} and the control voltage U_c or the position uncertainty $|\Delta x|$.

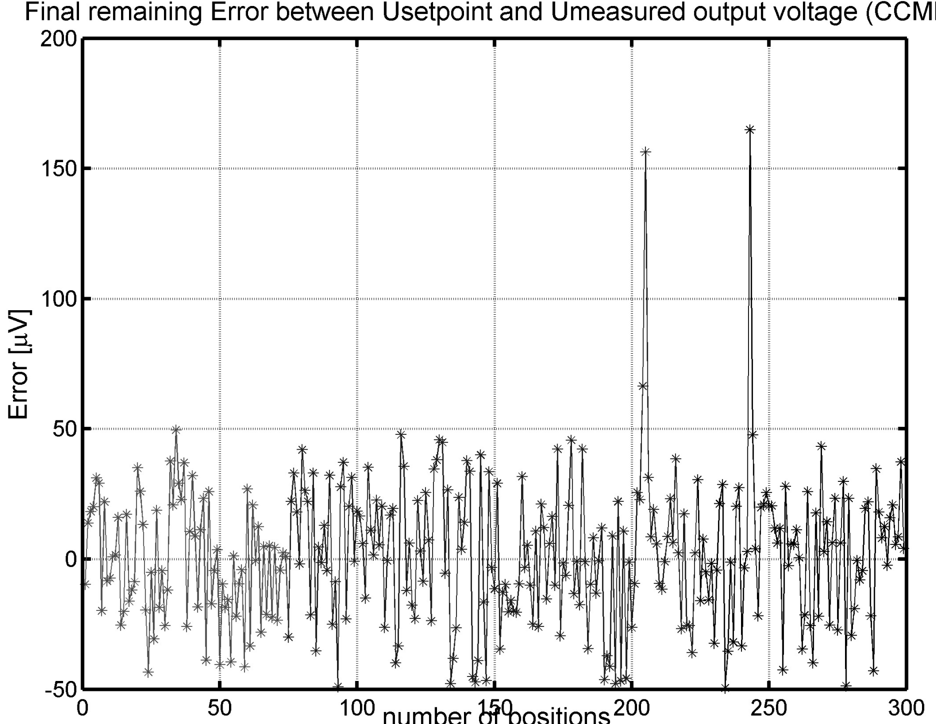

Fig. 35: For all slider positions the (remaining) error e_m (4th value) is below the error limit E_{limit} = 50µV.

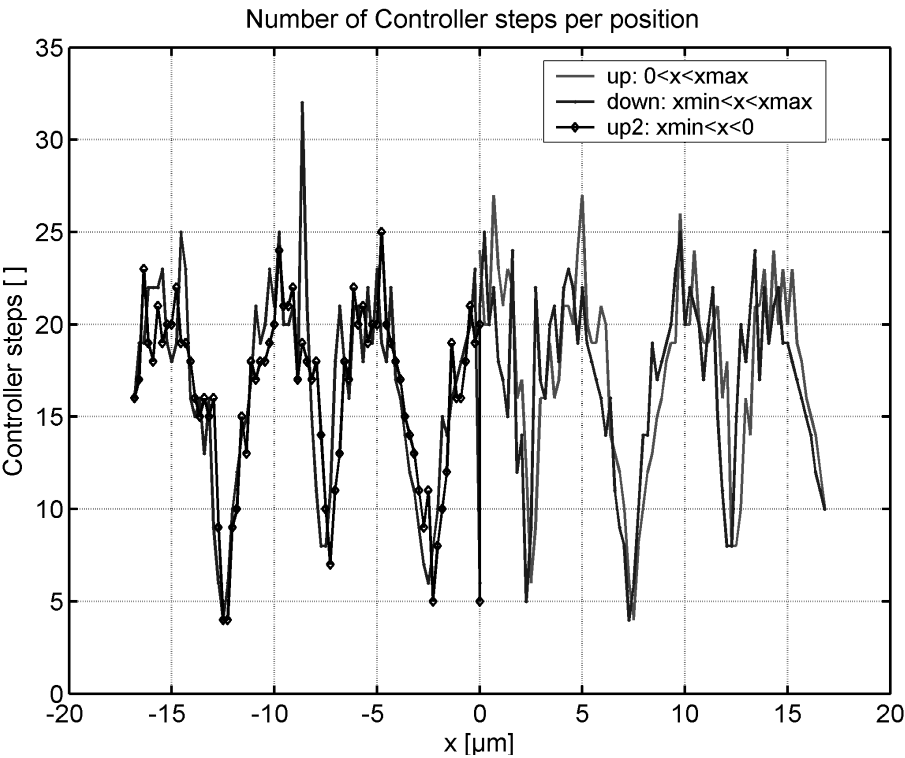

Fig. 36: The periodic geometry is reflected in the umber of controller steps per position *x(i)*.

The parameters K_p, K_i and K_d have been set to the following values K_p = 2, K_i = 0.1, K_d= 0. Increasing K_d the differential action (reacting to changes in the error e_m) would speed up the dynamic response time, but would also increase the risk of excessive overshoot and instability. Other experiments with $K_d \neq 0$ did not show any better result than presented in Fig. 32. Looking at the periodic curve in Fig. 36 it seems clear that the

specific shape of the periodic geometry is reflected in the number of controller steps. This gives some insight in the necessary model for the dynamic mechanical system and the controller including, if possible, a learning neural network.

Finally, a last aspect is evaluated, concerning the correspondence of the control voltage U_c with a pure sine. One of the conclusions of the closed-loop analysis in chapter 3 was that the y_{ss}-displacement of the sense-structures or the squared controller voltage U_c^2 for the sense-actuators would resemble the chosen periodic geometry on the slider more for a higher set point value. However, the 2D-FE simulations in chapter 4 showed that the chosen ratio of period size and finger width is not large enough, and the y_{ss}-displacement will have higher order spatial frequency components, besides the fundamental frequency corresponding with the period of the periodic geometry on the slider.

Therefore, following the same approach and arguments as for the experiments for ICMM with active gap-adjustment in the previous section, it is evaluated next if the ratio between higher order spatial frequency components in the control voltage U_c and the first order spatial frequency component $U_{out_\omega 0}$ is lower for CCMM.

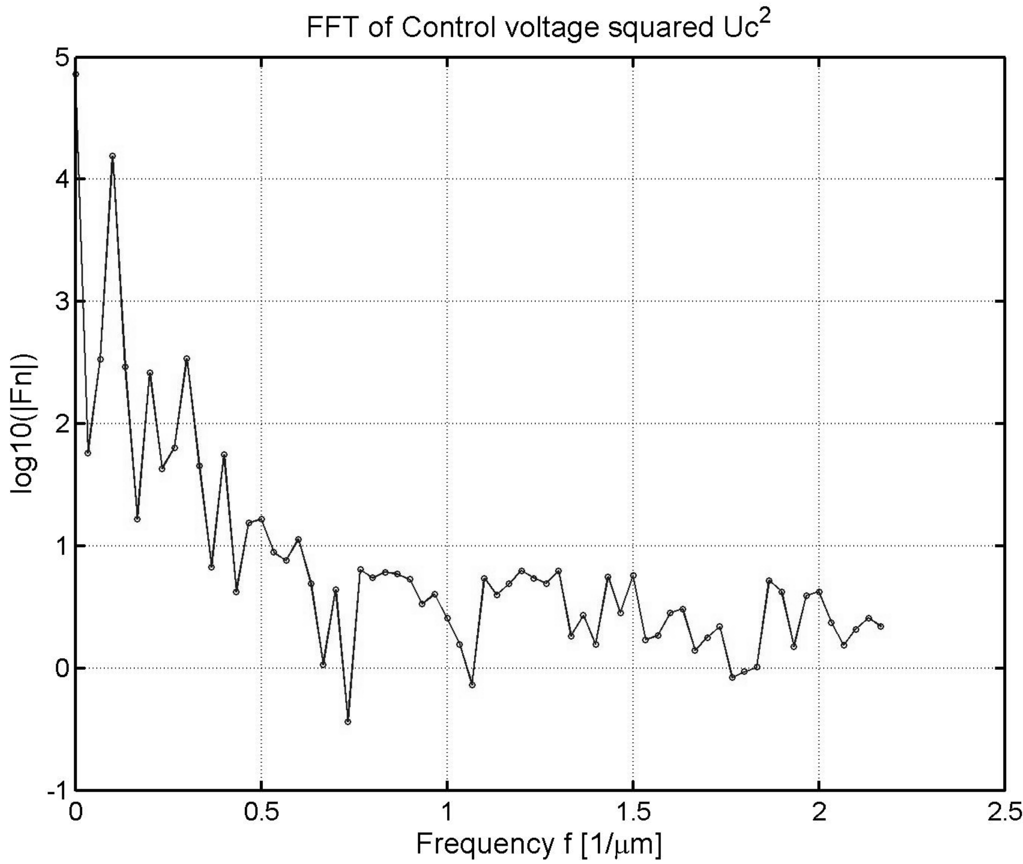

Fig. 37: FFT of squared control voltage Uc^2

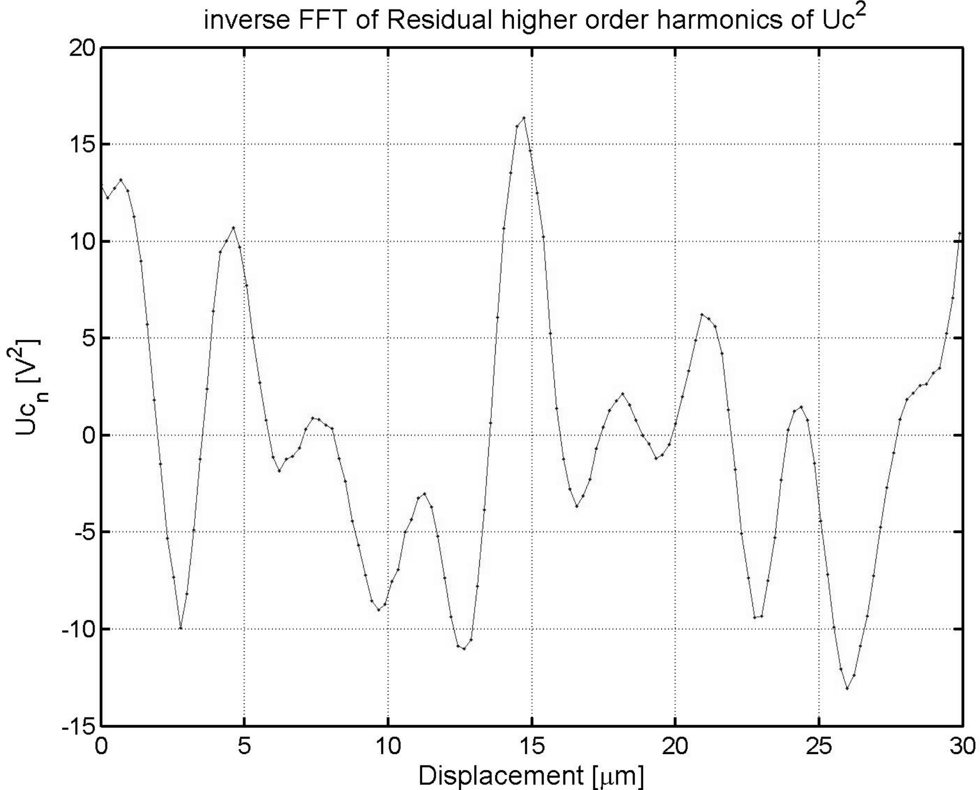

Fig. 38: Inverse FFT of all higher order harmonics of U_c^2 which define the residual signal U_{out_Rn}.

The first harmonic in space-domain $f_{\omega 0}(x) = U_{out_\omega 0} = A_1 \cdot cos(\omega_0 \cdot x)$

The residual spatial function of all higher order harmonics is defined by:

$$r_n(x) = \frac{1}{N}\sum_{n=2}^{N} A_n \cdot \cos(n \cdot \omega_0 \cdot x) \quad \text{(Eq.6 13)}$$

$f(x)$ $_{(\omega_0=0.2\pi)}$ $[V^2]$	$f_{(2\omega 0)}/f_{(\omega 0)}$	$f_{(3\omega 0)}/f_{(\omega 0)}$	$r_n(x)$ $[V^2]$	$r_n(x)/f(x)_{(\omega 0)}$
238.75	0.0167	0.0218	14.70	0.0616

Table 7: amplitudes and ratios for FFT components of squared control voltage (CCMM)

Thus, the amplitude of the residual signal $r_n(x)$ is 6% of the amplitude of the first harmonic in the function of U_c^2 i.e. the y_{ss}-displacement of the sense-structures. This is a 5x improvement over the result for ICMM.

The conclusion is that the CCMM concept can be a really significant improvement in position accuracy and repeatability to the ICMM concept. Further assessment will focus on real-time applications and actual nano-positioning.

The best-recorded result for CCMM shows a mean absolute position uncertainty of $|\Delta x|_{mean_h}$ = 7.5 nm with standard deviation of $|\Delta x|_{std_h}$ = 6 nm. These figures are better than recorded for the open-loop ICMM method i.e. $|\Delta x|_{mean_h}$ = 12 nm, $|\Delta x|_{std_h}$ = 8 nm.

This is due to an increase in SNR. However, one cycle (x_{pk-pk} = ~32µm, traveled length x_{tl} = 64µm) took ~ 5 hours and the capacitive sensing scheme was without compensation for changes in humidity or temperature. Actual absolute position detection using a quadrature position detection technique has not been implemented yet, but based on these results, both ICMM and CCMM have the potential to measure with nm-accuracy over unlimited length.

The earlier published results for CCMM [10] and taken up in Appendix 3.5 do show a slope in the curves for both concepts. A possible explanation for the slope could be that the slider and combs are moving also out of plane, maybe the z-displacement is more for displacements $x > 0$ than for $x < 0$ [11]. However, also here the position uncertainty for CCM is smaller than for ICMM. (For the results described in [10] no use was made of the square root function to create a constant loop-gain). A system with White Light Laser Interferometry could be used to determine both out-of-plane and in-plane motion [12]

6.5 DYNAMIC EXPERIMENTS FOR ICMM WITH ACTIVE GAP-ADJUSTMENT

As we have seen in the previous sections with the assessment for the quasi-static performance of ICMM and CCMM concepts, an active gap-adjustment increases the capacitance variation and therefore in principle the SNR and the accuracy of the detection of small displacements. However the experiments were far from real-time. A typical experiment for the ICCM concept with 5 cycles covering a displacement range of 32 µm per cycle took app. 2 hours, depending on the setting of the multimeter. For the CCMM concept one cycle alone took already 5 hours. In the following section we want to assess the operation and performance of the ICMM mode for higher frequencies and explore the limits of the current setup and the concept. The dynamic experiments for the CCMM concept oppose practical time consuming difficulties and therefore a start off with the ICMM concept was made with the same device as in the previous experiments for ICMM and CCMM in sections 6.3.2 and 6.4. The same device as in the previous sections was used. This device has a sine-rectangular geometry with 10 µm period (SinP10) and the possibility to control the gap between slider and sense-structures through additional sense-actuators.

In Fig. 39 the schematic is given of the connections to the capacitive position sensor for the measurements using an oscilloscope and an HP gain-phase analyzer as described in Table 3 and section 6.2.5. Two HP AWG's are used to apply the phase adjustment as described in section 6.2 between input signal and sync of the synchronous detector. The corner-frequency of the LPF filter of the synchronous detector is adjusted to 100 KHz and the output signal (*Uout*) is measured by a digital oscilloscope (HP) or an HP4194A gain-phase analyzer.

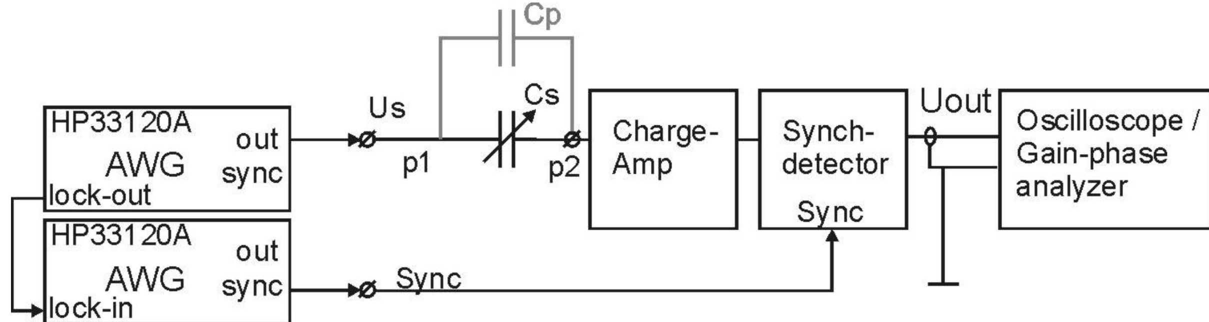

Fig. 39: For the measurements described in this section, an oscilloscope and a gain-phase analyzer are used to measure and display the output voltage Uout which corresponds linearly with the sensor capacitance Cs.

The 2 drive-actuators (comb-drives) of the test device are connected in pull-pull with custom made electronics as discussed in section 6.2.5.

The resulting force (F_R) and slider displacement (x) are proportional to :

$$x = \frac{F_R}{k_{eff}} \propto (U_{bias} + U_{dif})^2 - (U_{bias} - U_{dif})^2 = 4 \cdot U_{bias} \cdot U_{dif} \qquad \text{(Eq.6 14)}$$

The two outputs of the pull-pull electronics are connected to the comb-drive actuators as indicated in Fig. 3.

In Fig. 40 the dynamic frequency response is measured around slider-position x=0 with the HP gain-phase analyzer using the periodic capacitive position sensor (C_{s2} a&b). This means test signal of the HP analyzer is connected with U_d input of the pull-pull electronics in Fig. 12. Two oscillation (actuation) levels U_d = 0.5 V and U_d = 1.2 V respectively have been applied to the comb-drive drive-actuators with the pull-pull electronics. Thus, $U_{diff} = U_d \cdot cos(\omega_a \cdot t)$, the bias-voltage U_{bias} = 12 V, the sensor input signal U_s = 1 V, f_s = 1 MHz. For an actuation level of U_d = 0.5 V a displacement amplitude of $\Delta x^{pk} \sim 0.5$ µm is expected.

For the frequency response in Fig. 40 with U_d = 0.5 V, Averaging = 16x and T_{int} = medium, the maximum gain is found at f = 1.7 KHz with the phase ϕ = -94 [deg].

For the frequency response with U_d = 1.2 V, Averaging = 128x and T_{int} = medium, the peak is flattened, due to a non-linear changing capacitance and non-linear damping. For both actuation voltages and frequencies higher than ~ 6 KHz a strong increase in gain and phase is seen, due to cross-talk from the sensor input electrodes (SA0_a & b in Fig. 2) directly to the charge-amp input-pad (rt1_A). The higher amplitude of 1.2V and an increase in averaging do not decrease this effect, therefore it is not ordinary white noise which would decrease with a stronger signal and more averaging.

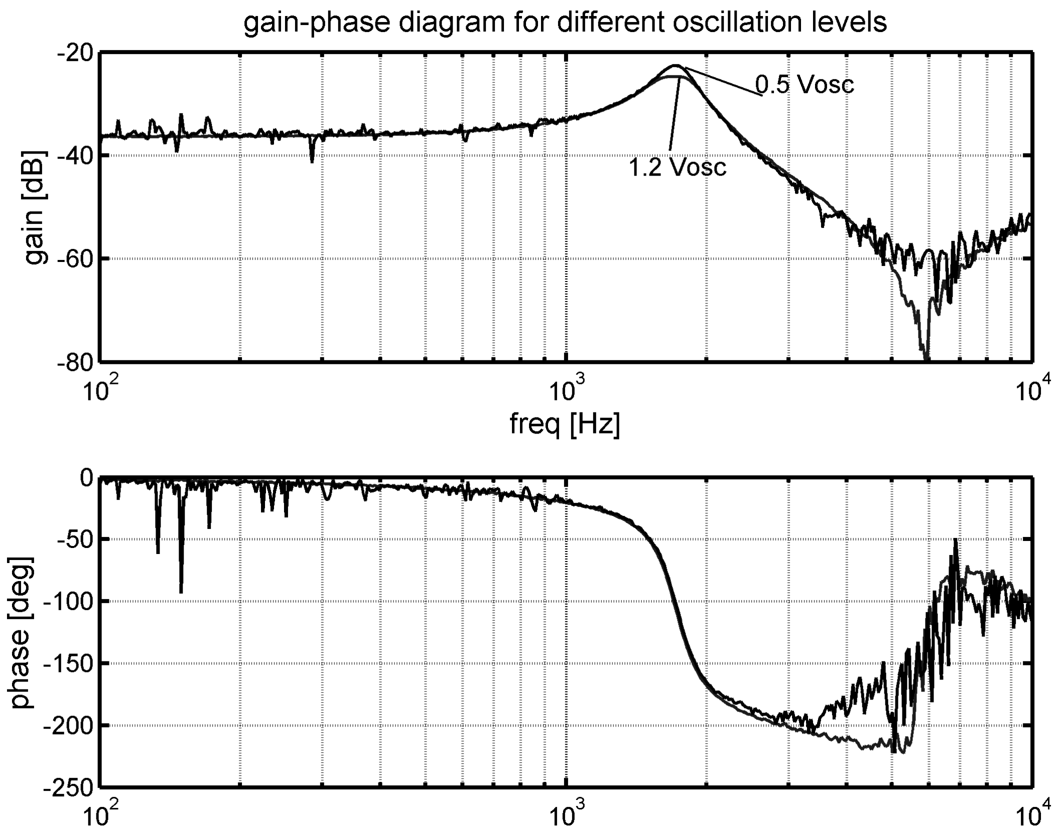

Fig. 40: With the periodic capacitive position sensor the dynamic response around position x=0 is measured using the HP gain-phase analyzer for 2 actuation levels.

In Fig. 41 the measured output voltage U_{out} of the synchronous detector is given for the SinP10 geometry combination. The actuation voltage U_{act} is a triangular function with frequency f_{act}=500 mHz , U_{bias} =15V, U_{diff} = 14V_{pk} .

The sense-structures are brought closer to the slider by applying U_{senact} = 14 Vdc to the sense-actuators at both sides of the slider (in parallel). By counting the peaks / periods in Fig. 41 the total range of displacement is estimated to $X^{pk\text{-}pk}$ ~ 32µm. The peak-peak output voltage of $U_{out}^{pk\text{-}pk}$ = 17 mV per 5 µm (3.4 mV/µm). The signal U_{out} has been averaged 16x by the oscilloscope. Also here a small slope in the measured curve is noticeable as is seen with the quasi-static experiments in section 6.3.1 for different geometries. A possible explanation for the slope could be that the slider and combs are moving also out of plane and more so for x>0 than for x<0 [11].

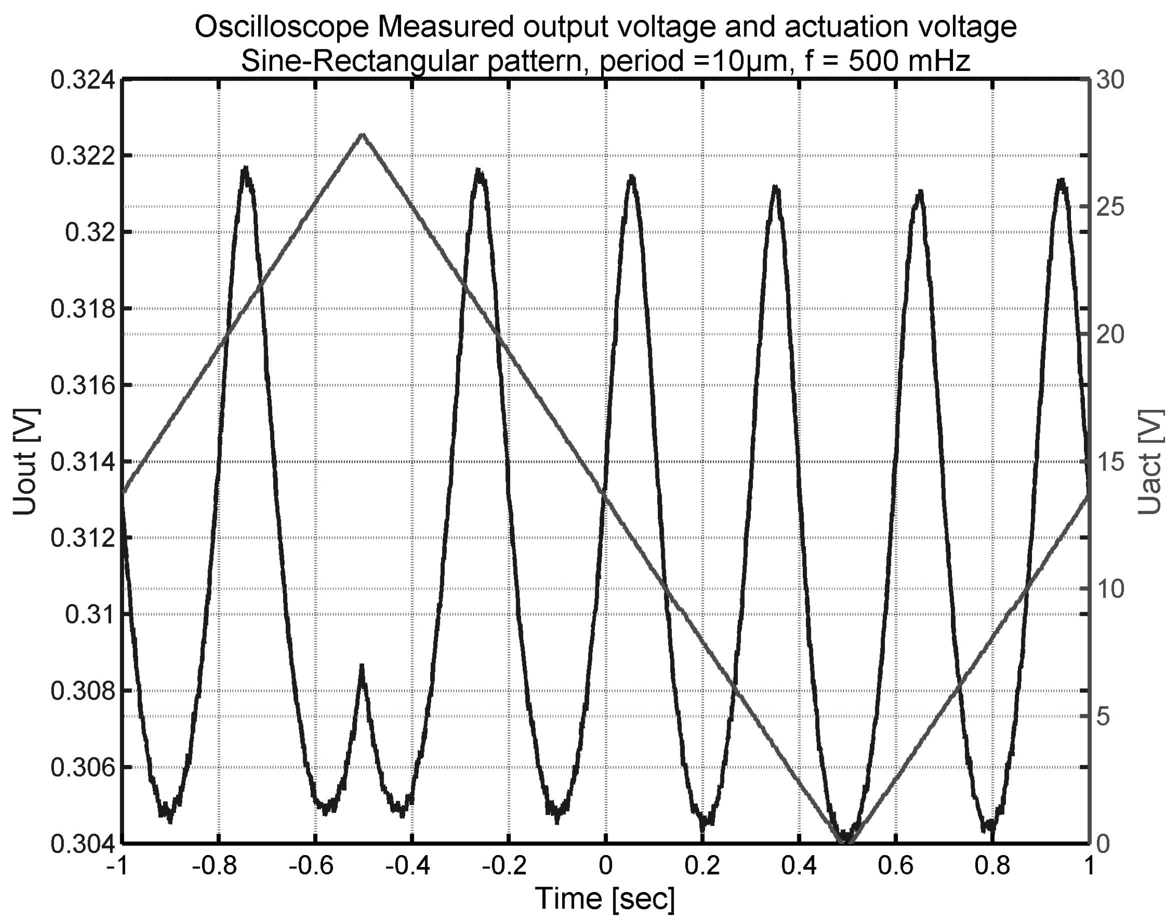

Fig. 41: The output voltage with a triangular actuation function. The actuation frequency is 500mHz. The range of displacement is in the order of ~32 µm.

In Fig. 42 is shown that a much higher actuation frequency of f_{act} = 1.4 KHz with U_{diff} = 10V_{pk}(Sine) and U_{bias} = 12 V still gives a well detectable output signal U_{out}. However, the signal plotted in Fig. 42 has been averaged 256x.

As discussed for the frequency response in Fig. 40, the resonant frequency could be determined to be f_{res} ~ 1.7 KHz and a Q-factor ~ 5, for the part of the device containing the slider and two drive actuators. Therefore, the displacement at 1.4 KHz as estimated from the measured output signal Uout in Fig. 42 (by counting the periods/peaks) is $X^{pk\text{-}pk}$ ~ 45 µm, much more than the $X^{pk\text{-}pk}$ ~ 32µm at low frequency. The phase shift between

actuation voltage U_{act} (or U_{diff}) and output voltage U_{out} is circa $\Delta\Phi \sim -33$ [deg] (U_{out} lags) due to the dynamic mechanical behavior of the two drive-actuators and the sliderbeam.

The maximum velocity of the device for the measurement in Fig. 42 can be calculated to be $v_{max} \sim (X^{pk\text{-}pk}/2)\cdot\omega \sim 20$ cm/sec.

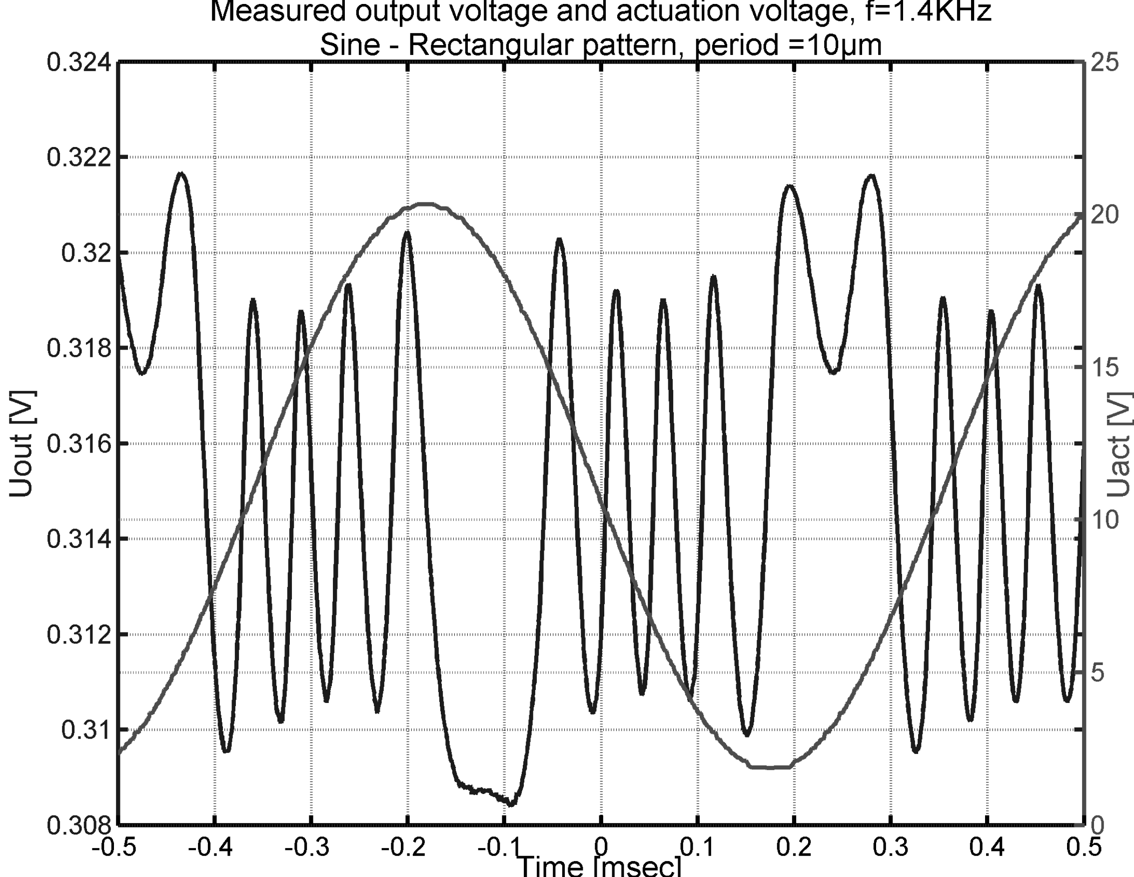

Fig. 42: The actuation frequency f_{act} = 1.4 KHz close to resonance f_{res} ~ 1.7 KHz. The total range of displacement is ~45µm.

Such a measurement result is still a far way from actual real-time (absolute) position detection and positioning. A characterization set-up is needed to characterize the measured output voltage / capacitance with the displacement measured with another sensing technique with known accuracy or precision e.g. Image analysis, laser interferometry, etc. However, also for these characterization systems to determine the position accuracy with these velocities will be far from straight forward. This aspect will be taken up again in more detail in the discussion in chapter 7.

Conclusions dynamic experiments with ICMM concept

The ICMM concept can operate at frequencies even higher than the resonant frequency of the test-vehicle. A resonant frequency f_r = 1.7 KHz and a Q-factor of 5 have been determined for small displacements around x = 0. The bandwidth was limited to around 6 KHz, due to cross-talk.

Operation at f = 1.4 KHz with a travel range of ~ 45 µm has been demonstrated. An extension of the means for characterization is needed to assess the real-time operation and accurate positioning at these frequencies.

6.6 DYNAMIC EXPERIMENTS USING A COMB-DRIVE ACTUATOR AS POSITION SENSOR

In this section the change in capacitance of one of the two comb-drive drive-actuators is measured while simultaneously both drive-actuators are actuated in pull-pull-mode. As explained in the introduction, a comb-drive is a non-incremental position sensor. It will eventually fail in measuring with nm-accuracy over very large displacements (e.g. >100 μm) because the dynamic sensing range will be limited. To illustrate this we will derive the change in capacitance per nm-change in displacement for the comb-drive drive-actuator as used in all previous experiments.

The comb-capacitance of a comb-drive actuator can be written as:

$$C(x) = \frac{2n \cdot \varepsilon_0 \cdot h}{d} \cdot (x_0 + x) \qquad \text{(Eq.6 15)},$$

With the number of fingers n on the moving comb, dielectric constant ε_0, structure height h and gap distance d. With the initial overlap x_0 for x=0 equation Eq.6.10 can be written as a constant capacitance C_0 and a linear changing Capacitance:

$$C(x) = C_0 + dC_x \cdot x \qquad \text{(Eq.6 16)}$$

For a comb-structure with n = 100 (moving) comb fingers, a height h = 5 μm, a gap distance d = 2 μm, initial overlap x_0 = 30 μm and dielectric constant $\varepsilon_0 = 8.854$ pF/m, the initial capacitance $C_0 \sim 132.81$ fF. For a maximum displacement of x = 30 μm (otherwise the fingers will no longer overlap) the capacitance has increased to C_{max} = 265.62 fF.

A change in displacement of 1 nm comes down to a change in capacitance $\Delta C \sim 4.4$ aF with 100 comb-fingers. The ratio or the dynamic range is then $C_{max} / \Delta C = 6 \times 10^4$ or simply $2 \cdot x_0 / dx$.

With two differentially operated comb-drives working simultaneously as actuator and as sensor, the changes in capacitance can be measured differentially and then using a charge amp and synchronous detector, the output voltage is linear with the change in capacitance, see section 3.4:

$$U_{ca} = \left(\frac{2\Delta C}{C_f} \right) \cdot U_1 \qquad \text{(Eq.6 17)}$$

In terms of position control this sensing principle has the advantage of a linearly changing measurement signal whereas the incremental principle is offering the advantage of large dynamic range at the expense of more complicated electronics and position control.

In the following the assessment is given of experiments with one drive-actuator simultaneously working as comb-sensor to explore the practical limitations for dynamic operation and the possibility to use the comb-sensor as a course position sensor in addition to the incremental capacitive position sensor.

The same device, the same measurement method and electronics were used as in the

previous sections with dynamic experiments. Only one comb-sensor was connected because of practical limitations of the probe set-up. The sensor input signal U_s is applied to one of the comb-drive structures through a capacitance C_{sin} given in Fig. 43 in order to separate both voltage supplies in the frequency domain through filtering.

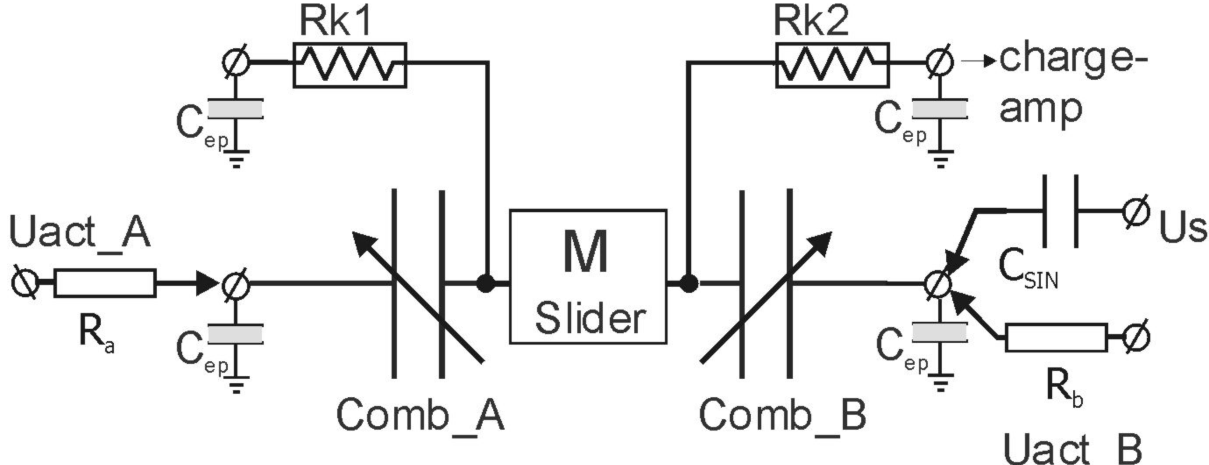

Fig. 43: Lumped model showing different mechanical and electrical elements and the connections to measure the change in comb-capacitance (comb_B) while driving the device in pull-pull mode.

The capacitance C_{sin} has been chosen with some care. For the signal generator the connection of the device through capacitance C_{sin} forms a high-pass network given in Fig. 44 (right). With C_{sin} ~100pF the voltage-drop over C_{sin} will be zero at f_s = 1MHz (C_b~ 1pF, Rb = 100KΩ). For the actuation voltage supply the resistor R_b and capacitance C_{sin} form a low-pass filter given in Fig. 44 (left), with corner frequency of f_k ~ 15 KHz. The stiffness *Rk1* and *Rk2* are electrically conducting and have a resistance in the order of ~ 1 KΩ. Stiffness *Rk2* is connected with the input of the charge-amp, which forms a virtual ground (0V). The electrical contact pads are anchored through the remaining SiO_2 to the substrate and are therefore modeled as capacitances C_{ep}.

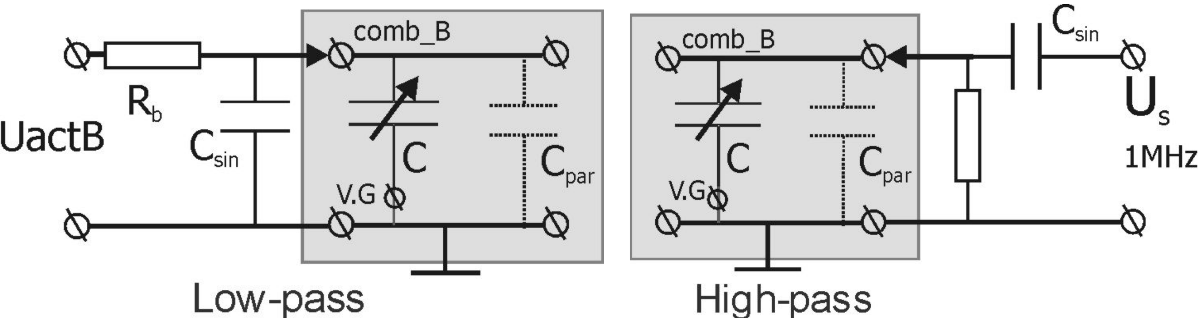

Fig. 44:(left) connection of actuation voltage supply to the comb-drive is modelled as a low-pass network. (right) connection of the signal generator to the device forms a high-pass network.

In Fig. 45 a measurement with the HP4194A gain-phase analyzer is given for the device actuated in pull-pull mode and with one of its 2 comb-drive actuators connected as capacitive position sensor as well. The oscillation signal V_{osc} of the analyzer is added to a bias voltage U_{bias} = 12 V with the pull-pull electronics i.e. U_d = V_{osc} in Fig. 12. The response in Fig. 45 is the dynamic response around slider position x=0.

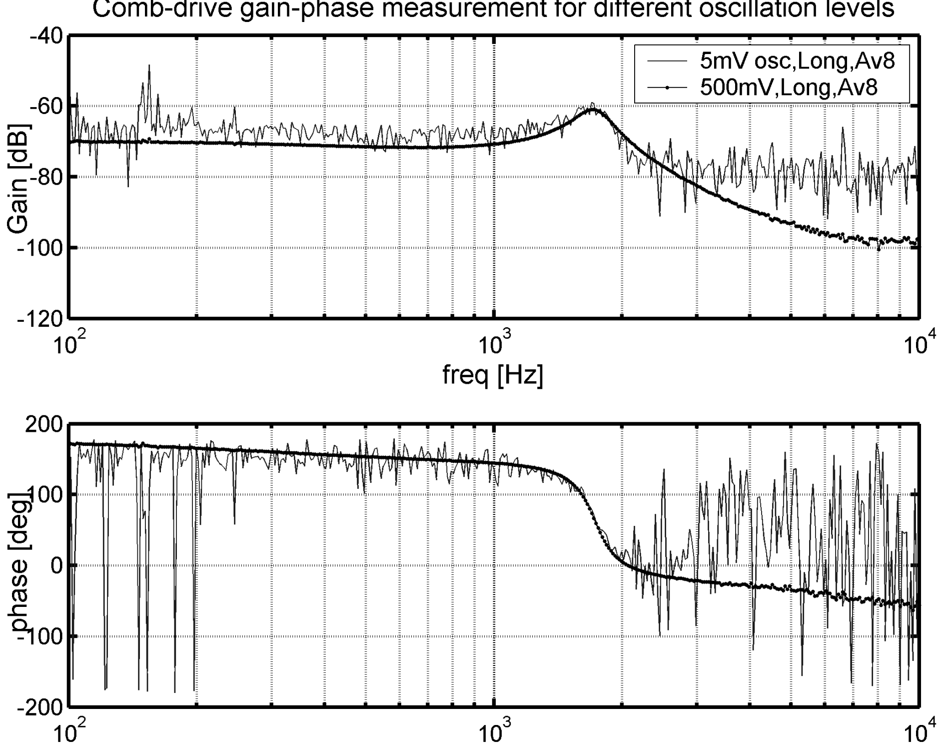

Fig. 45: Gain-Phase measurement with a micromachined device actuated in pull-pull mode and one of the comb-drive-actuators simultaneously used as capacitive position sensor.

For the measurement in Fig. 45, maximum gain is found at the resonant frequency of $f \sim$ 1.72 KHz. The signal or oscillation level of U_{gp} =500 mV of the gain-phase analyzer is measured with the oscilloscope and turns out to be 322 $mV^{pk\text{-}pk}$. With this signal level generated by the HP-AWG (see Fig. 12) at a frequency of f = 1.7 KHz, the displacement amplitude around slider-position x = 0 is $\Delta x^{pk\text{-}pk} \sim 1 - 1.5$ [µm]. For frequencies up to 1 KHz the displacement-amplitude is 10dB lower i.e. $\Delta x^{pk\text{-}pk} \sim 300$ [nm]. For the signal level of 5 mV for the gain-phase analyzer, the displacement-amplitude is 100x smaller, i.e. $\Delta x^{pk\text{-}pk}$~3 [nm]. The noise-band or floor around the measured Gain for V_{osc} = 5mV and for frequencies up to $f \sim$ 1KHz is circa 3 dB which corresponds to an estimated resolution of $\Delta x_n^{pk\text{-}pk} \sim 1.5 - 2$ [nm] for the current measurement setup, electronics and device characteristics. Considering the 4.4 aF / nm for the comb-drive with 100 fingers, this amounts to ~6 aF as smallest detectable change in capacitance. The integration time of the gain-phase analyzer was set to 'Long' (T_{int} = 300 ms) and the number of averaging was 8x. This corresponds according to the HP4194 manual to a total measurement time of T = 1 s and a bandwidth of BW = 1 Hz.

With a response of the device $R(\omega, V_{osc})$ as function of frequency ω and signal voltage V_{osc}, and the measurement noise u_n, the gain can be seen as the ratio given in Eq.6.18:

$$Gain = \left(\frac{R(\omega, Vosc) + \overline{u_n}}{Vosc} \right) \qquad \text{(Eq.6 18)}$$

A decreasing signal voltage V_{osc} will eventually lead to negligible amplitude of $R(\omega, V_{osc})$ and an increasing Gain if a constant level of noise u_n is assumed with a setting

of ‘Long’ integration time and 8x averaging.

An alternative calculation to estimate the resolution is the following: For a signal voltage of V_{osc} = 5mV at a frequency of f = 1.7 KHz would give a slider displacement of $\Delta x^{pk\text{-}pk}$ = 10 - 15 nm. For higher frequencies, the response $R(\omega, Vosc)$ in (Eq.6.13) of the device in Fig. 45 drowns in the noise-floor u_n which is 20 dB lower than the gain at f = 1.7 KHz with V_{osc} = 5 mV. Therefore, the resolution for the current measurement settings, setup and device is determined to a slider displacement of Δx_n ~ 1.5 nm. For a change of 4.4 aF/ nm, this amounts to ~ 6 aF as smallest detectable change in capacitance

Fig. 46 gives the ouput voltage U_{out} of the synchronous detector (Fig. 39) and an actuation voltage *Uact_B*, as measured with the digital oscilloscope. The bias voltage U_b = 12 Vdc, the differential voltage U_d = 10 V^{pk} and the actuation frequency f_{act} =800 Hz. The oscilloscope was set to 8x averaging.

The displacement (x) of the slider should be proportional to the actuation voltage in Fig. 46 according to equation (Eq.6.14), with a possible phase-shift of 180 [deg]. However, the measured change in capacitance (U_{out}) predicts a much more complicated motion.

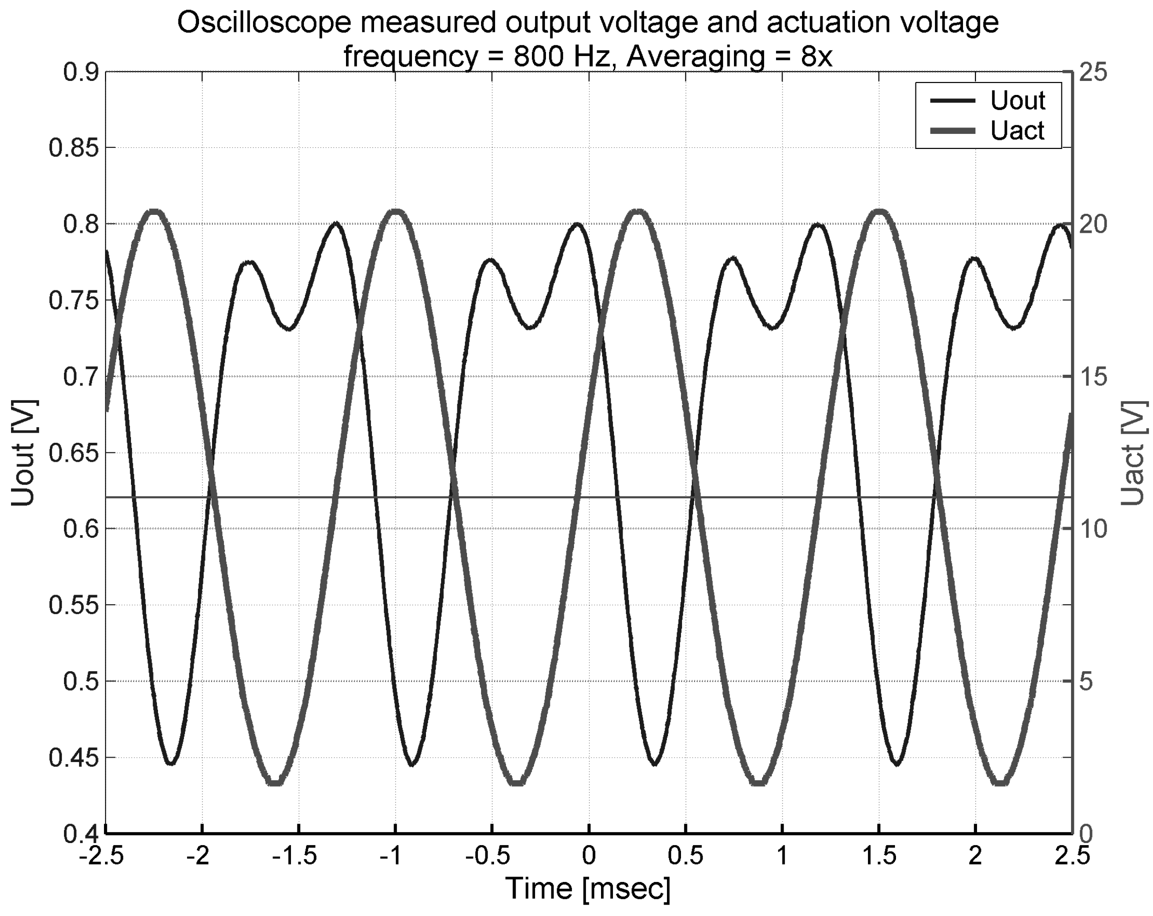

Fig. 46: Measured change in comb-capacitance for a device with two comb-drives actuated in pull-pull mode. One comb-drive is used also as position sensor.

For frequencies around 200 Hz the change in capacitance corresponds to the expected change in displacement much better. Closer examination through FFT-analysis reveals that the output-signal U_{out} includes a 1-omega *(1-ω)* as well as a *2-ω* term. The magnitude of the *2-ω*-component is changing with frequency and has a maximum when the *2-ω* component is around the resonant frequency of the device, as given in Fig. 47.

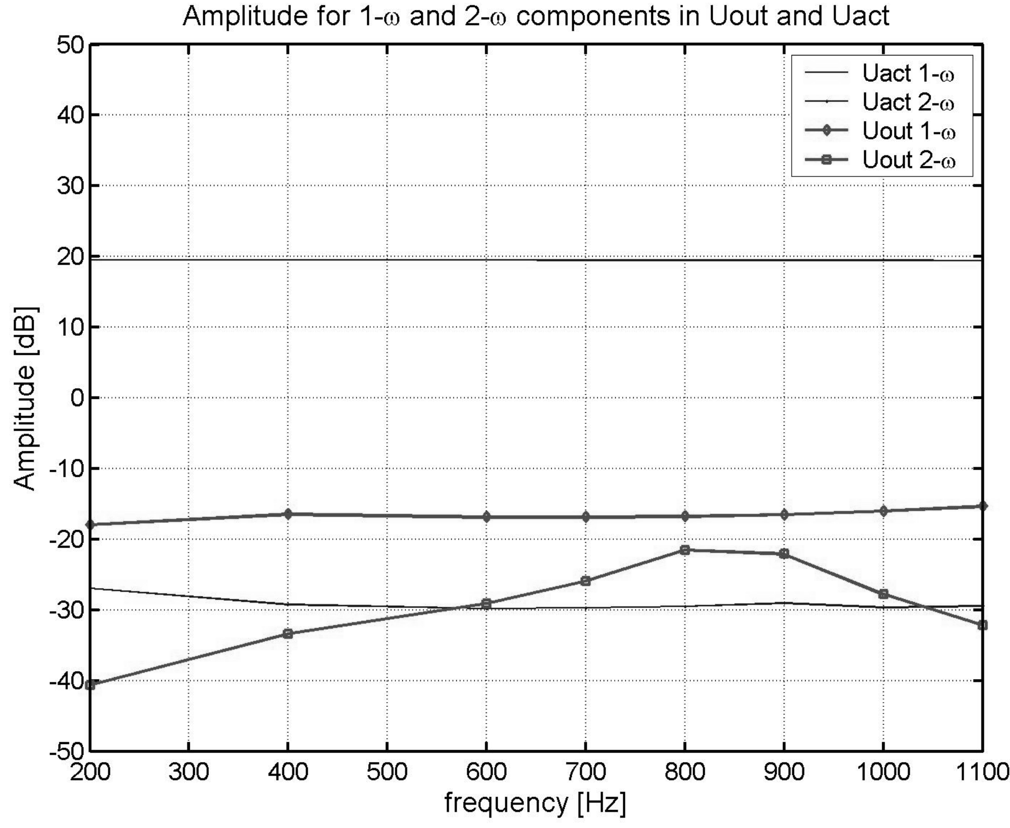

Fig. 47: Through FFT analysis the 1-ω and 2-ω components in the measured signals Uout and Uact_A are determined.

From Fig. 47 it is clear that already in the actuation signal Uact_A (i.e. one of the two output signals of the pull-pull electronics in Fig. 12) a *2ω* component is present, but its magnitude is 50 dB lower corresponding to 32 mV and thus its effect can be neglected. However, the *1-ω* and *2-ω* components in U_{out} do show the same behaviour as the measured mechanical dynamic response in Fig. 45, and the *2-ω* component for f = 800 Hz (i.e. $2f \sim f_{res}$) has an amplitude close to the amplitude of the *1-ω* component.

There are four possible reasons, which could cause this effect.

1. A possible mismatch in the capacitances of the comb-drives
2. The influence of the resonance mode in out-of plane direction (z-direction)
3. A difference in actuation voltages due to a mismatch in the amplifier gains of the pull-pull electronics (Fig. 12)
4. A difference in actuation voltages for the 2 comb-drives due to capacitance C_{sin}

For a comb-drive the electrostatic force and the resulting displacement (x) are proportional to the applied actuation voltage squared and the differential change in capacitance versus displacement $\partial C/\partial x$. For two comb-drives in pull-pull mode, a

difference in $\partial C/\partial x$ for both comb-drives results in a $2\text{-}\omega$ component in both force F_R and displacement (x):

$$UactA = U_{bias} + U_{diff};$$

$$UactB = U_{bias} - U_{diff}:$$

$$x = \frac{F_R}{k_{eff}} \propto \frac{\partial C}{\partial x}(U_{bias} + U_{dif})^2 - \alpha \cdot \frac{\partial C}{\partial x}(U_{bias} - U_{dif})^2 =$$

$$\propto U_{bias}{}^2 \cdot (1-\alpha) + 2 \cdot U_{bias} \cdot U_{dif} \cdot (1+\alpha) + U_{dif}{}^2 \cdot (1-\alpha) \quad \text{(Eq.6 19)}$$

With $U_{dif} = U_d \cdot \cos(\omega_a \cdot t)$, $U_{dif}^2 = 1/2U_d^2 \cdot (1 - \cos(2 \cdot \omega_a \cdot t))$ a mismatch in the differential change in comb-capacitance with $\alpha \neq 1$, causes a dc, $1\text{-}\omega$ and a $2\text{-}\omega$ component in the resulting force and displacement.

Another mechanical effect that is important to consider, is the resonant frequency in z-direction. In the Appendix 2.4 a calculation is given of the theoretical stiffness and mass. The stiffness in x-direction is given by:

$$k_x = \frac{4Ehw^3}{l_{fb}{}^3}, k_z = \frac{4Ewh^3}{l_{fb}{}^3} \quad \text{(Eq.6 20)}$$

Therefore the resonant frequency in z-direction $f_{R_z} = \frac{h}{w} \cdot f_{R_x}$, with height h, width w and length l_{fb} of the flexure beams and the Young's Modulus E.

For the surface-micromachined device the height of the polysilicon layer is 5µm and the width of the flexure beams is w = 2µm. Thus, the resonant frequency in z-direction is 2.5x the resonant frequency in x-direction.

By applying the actuation voltages *Uact_A* and *Uact_B* to the two comb-drives a force in z-direction (out-of-plane) is generated by each drive actuator respectively [11]:

$$F_A_z \propto Uact_A^2, \qquad F_B_z \propto Uact_B^2$$

So at both ends of the slider beam connecting the two drive-actuators a force in z-direction is generated with a dc, 1-ω and a 2-ω component. Therefore, with an actuation frequency close to the resonant frequency in x-direction ($\omega \sim \omega_{R_x}$) the 2-ω component for the actuation force in z-direction is close to the mechanical resonant frequency in z-direction. This could also have an effect in the measured change in capacitance depending on the damping forces in z-direction.

Damping effects are caused by the surrounding air (or fluid) and can in general for conventional machines be ignored but for micro mechanical devices these effects play an important role, since they determine the dynamic performance of the devices.

There are two basic different air damping mechanisms possible: Squeeze-film air damping and Slide film damping [4].

For the out-of-plane motion of slider beam the Squeezed film damping mechanism is important. It is the damping caused by the air which flows in and out of the gap between two plates when the gap is changing.

By definition the damping force $F = -D \cdot \dot{z}$. The coefficient of damping force D is for a rectangular plate with length L much larger than width B derived as [4]:

$$D = \frac{\mu \cdot B^3 \cdot L}{h^3} \qquad \text{(Eq.6 21)}$$

For a slider beam width B = 50 μm, length L = 1 mm, and distance between slider and substrate $d = d_{ox}$ = 3 μm and viscosity coefficient μ = 1.8 $\cdot 10^5$ [Pa ·sec] the damping coefficient is $D = 8.33 \cdot 10^{-5}$ N/(m/sec). The damping ratio ζ of the system is defined as:

$$\zeta = \frac{D}{2m\omega_0} \qquad \text{(Eq.6 22)}$$

And for small damping the relation between the quality factor Q and the damping ratio is

$$Q = \frac{1}{2\zeta} \qquad \text{(Eq.6 23)}$$

With the mass M ~ 1 μg calculated in Appendix 2.4 and a resonant frequency f_z = 4.2 KHz (i.e. $f_z = 2.5 \cdot f_x$ and f_x ~ 1.7 KHz) the quality factor Q ~0.32.

In Appendix 2.4 is calculated that although the moveable structures of the test device have a truss like structure with holes and looks like a perforated plate, the surface of the device with holes is 75 % of the completely closed surface of a solid mass. In other words, the holes in the sliderbeam make up for only 25% of the area and volume of a solid mass.

As a first order approximation it is decided that the damping forces in z-direction will be considerably large, therefore the Q_z factor will be small, and the amplitude of the displacement in z-direction will be negligible. Therefore, the effect in Fig. 46 is not likely to be explained by a resonant frequency for a motion in z-direction.

The third possible explanation for the effect seen in Fig. 46 is a difference in the applied actuation voltages of both amplitude and phase due to a mismatch in the amplifier gains for the outputs of the pull-pull electronics. This again can cause a $2\text{-}\omega$ component in the resulting force. In the Appendix 3.6 the measured gain and phase of the pull-pull electronics is given. The difference in amplitude and phase between the two generated output voltages is less than 0.1dB and 0.5 [deg]. It is clear that the difference in gain and phase is minimal and it is unlikely that this could solely cause the $2\text{-}\omega$ component with the dynamic response as present in the results of Fig. 47

More important appears to be the resistor R_b and the decoupling capacitance C_{sin} which form a Low-Pass Filter as seen from the actuator voltage supply for $Uact_B$. This can cause a difference in amplitude and phase between the voltages applied to the two actuators.

To examine this possibility more closely, a model is made including the components R_b and C_{sin} and the 2nd-order dynamic system characteristics for a mass-damper-spring model. The different elements are shown in Fig. 48.

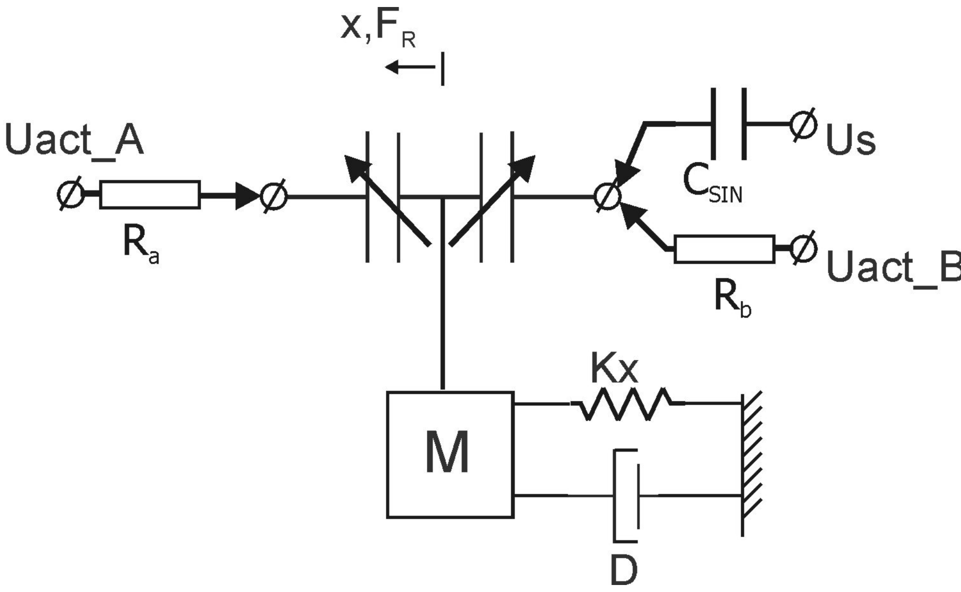

Fig. 48: Simplified lumped 2nd-order dynamic model of the device with two comb-drive actuators coupled by a slider beam and one comb-drive operating simultaneously as position sensor.

The generated actuation voltage *UactB* by the pull-pull electronics is changed in amplitude and phase by the LP-filter formed by C_{sin} (= C) and R_b (= R):

$$UactA = U_{bias} - U_d \cdot cos(\omega_a \cdot t)$$

$$UactB2 = U_{bias} + U_d \cdot |G_1| \cdot cos(\omega_a \cdot t + \phi_1)$$

With,

$$G_1 = \frac{1}{|1 + j\omega RC|}, \phi_1 = -arctan(\omega RC) \qquad \text{(Eq.6 24)}$$

The displacement according to the static model for $\omega << \omega_r$ is the resulting force divided by the stiffness k_x: This can be seen as quasi static displacement or as the displacement for a system with resonant frequency $f_r >> 800$ Hz:

$$X_s = \frac{F_r}{k_x} = \frac{\partial C}{k_x \cdot \partial x}(UactA^2 - \alpha \cdot UactB2^2) \qquad \text{(Eq.6 25)}$$

with differential capacitance change

$$\frac{\partial C}{\partial x} = \frac{n \cdot h \cdot \varepsilon_0}{d},$$

where n is the number of rotorfingers, h is the height of the structure, dielectric constant ε_0 and gap distance d.

The dynamic behavior of the mass-spring-damper system can be analyzed by

considering the differential equation Eq.6.26:

$$M\frac{d^2x}{dt^2}+D\frac{dx}{dt}+K\cdot x=F_r=F_A-F_B \qquad \text{(Eq.6 26)}$$

The frequency transfer function of dynamic displacement versus quasi-static displacement is given by:

$$G_2=\frac{X_d}{X_s}=\frac{k_x}{M}\frac{1}{(j\omega)^2+(j\omega)\cdot\frac{\omega_r}{Q}+\omega_r^2}=\frac{k_x}{M}\frac{1}{(\omega_r^2-\omega^2)+(j\omega)\cdot\frac{\omega_r}{Q}} \qquad \text{(Eq.6 27)}$$

$$|G_2|=\frac{k_x}{M}\frac{1}{|(\omega_r^2-\omega^2)+(j\omega)\cdot\frac{\omega_r}{Q}|},\phi_2=-arctan(\frac{\omega\cdot\frac{\omega_r}{Q}}{(\omega_r^2-\omega^2)}) \qquad \text{(Eq.6 28)}$$

With the resonant frequency f_R ~ 1.72 KHz determined from Fig. 45, the stiffness k_x can be calculated, and the mass M is estimated from the mask design, material properties and processing details, see Appendix 2.4.

$$\omega_r=\sqrt{\frac{k_x}{M}} \qquad \text{(Eq.6 29)}$$

Also the Q-factor is determined from the measurement in Fig. 45, with [4]

$$\mathrm{Q}=\frac{\mathrm{f_r}}{(\mathrm{f_2}-\mathrm{f_1})}, \qquad \text{(Eq.6 30)}$$

Where f_2 and f_1 are the frequencies for which the gain in Fig. 45 is –3dB lower than the (maximum) gain at resonance.

The 1-ω and 2-ω terms in Eq.6.19 are adjusted by the modulus and phase of transfer function G2, leading to Eq.6.31 for an actuation frequency ω_a:

$$X_d=\frac{\partial C}{k_x\cdot\partial x}\bullet$$
$$\left[\begin{array}{c}U_b^2\cdot(1-\alpha)+\frac{U_d^2}{2}\cdot|G_1(\omega_a)|^2\cdot|G_2(2\omega_a)|(1-\alpha)+\\ 2U_bU_d\cdot|G_2(\omega_a)|\cdot\left[|G_1(\omega_a)|\cdot(cos(\omega_a\cdot t+\phi_1(\omega_a)+\phi_2(\omega_a))+\alpha\cdot cos(\omega_a\cdot t+\phi_2(\omega_a))\right]+\\ \frac{U_d^2}{2}\cdot|G_2(2\omega_a)|\cdot\left[|G_1(\omega_a)|^2\cdot cos(2\omega_a\cdot t+2\phi_1(\omega_a)+\phi_2(2\omega_a))-\alpha\cdot cos(2\omega_a\cdot t+\phi_2(2\omega_a))\right]\end{array}\right]$$

(Eq.6 31)

For a frequency of f_a = 800 Hz, a bias voltage U_b=12 V, U_d =10 V^{pk}, R=100KΩ, C_{sin} = 1000pF (10x larger than used in the experiment) the calculated 'static' displacement (Eq.6.19) and the displacement according to (Eq.6.31) is as given in Fig. 49. The device parameters are:

$k_x \sim 0.139\ Nm^{-1}$, $M = 1.19 \cdot 10^{-9}$ Kg, $Q = 5.2$,
$n = 100$, $\varepsilon_0 = 8.85e\text{-}12\ Fm^{-1}$, $h = 5\ \mu m$, $d = 2\mu m$.

The comb-structures are assumed to be fully symmetric, so $\partial C/\partial x$ is the same for both drive actuators i.e. α=1.

The calculated displacement with a capacitance C_{sin} = 1000 pF (10x larger than used in the experiment), clearly shows a fair comparison result in Fig. 46. For a 10x smaller C_{sin} this effect is not present, only a significant change in amplitude and phase is noticeable.

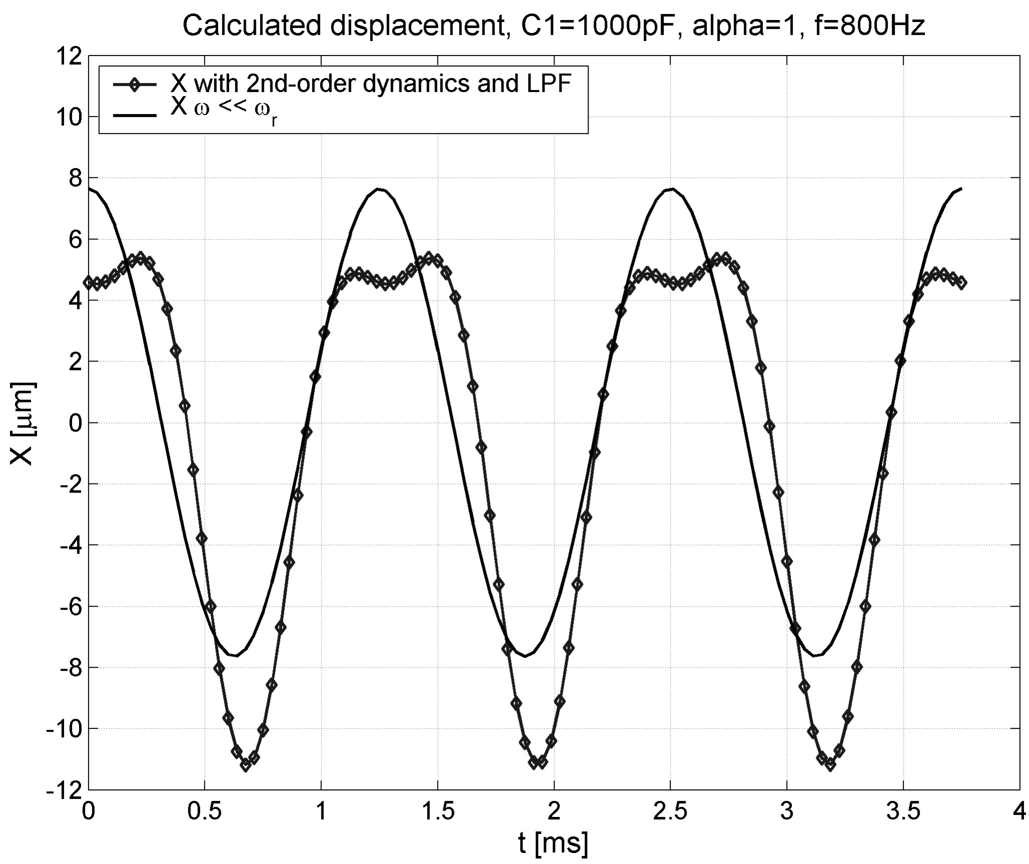

Fig. 49: Calculated displacement response for the model in Fig. 48 of the device under test with 2nd-order dynamics, and a LP-filter for the actuation voltage.

From the calculated response in Fig. 49 it appears that the capacitance C_{sin} may have been 10x larger, unintentionally, or more probably the amount of parasitic capacitance and cable capacitance standing parallel to the comb-capacitance is much more than expected.

The easiest solution with this setup would be to preserve symmetry and connect both comb-drive actuators differentially. Another voltage generator is needed for the sensor

input signal with opposite phase connected in the same way, using a capacitor of C_{sin} = 100pF. But the influence of cable capacitances may still be significant and limiting the performance of the device under test.

A minor improvement is the connection as given in Fig. 50. The influence of the cable capacitances is much less, however the practical connection with resistor R_b and capacitance C_{sin} between coax-cable and probe needle manipulator may not be straightforward. The parasitic capacitance remains unknown and its presence should be avoided or decreased as much as possible.

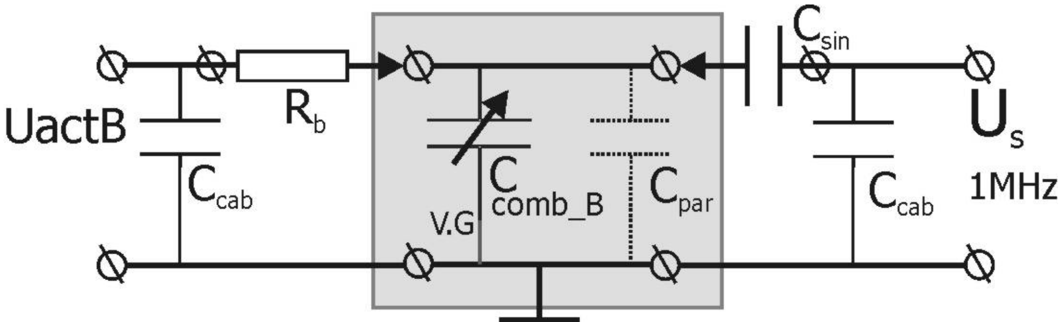

Fig. 50: The alternative lumped model when the components R_b and C_{sin} are connected at the end of the coax-cables as close as possible to the device's sensor is a small improvement to the connection used in the experiment. Ideally, the resistors R_a and R_b are replaced with fast current limiters and the cable capacitances eliminated through active electronics.

The connection as depicted in and Fig. 50 is far from ideal however, only the gain of the frequency response given in Fig. 45 will change when the device is connected ideally.

In the worst case the voltage applied to comb-structure B (Fig. 43) may have been only $UactB2 = U_{bias}$.

Then the forces on the slider mass M would have been with (Eq.6.19):

$$F_r = \frac{\partial C}{\partial x} \cdot (UactA^2 - UactB2^2) = \\ = \frac{\partial C}{\partial x} \cdot (U_{bias}^2 + 2U_{bias} \cdot U_d \cos(\omega_a \cdot t) + U_d^2 \cos^2(\omega_a \cdot t) - U_{bias}^2) \qquad \text{(Eq.6 32)}$$

This would have resulted in a slider displacement (x) having a static offset, a 1-ω and 2-ω component.

The gain-phase measurement in Fig. 45 would remain the same because the analyzer also uses a synchronous detection or mixing technique with a 1-ω signal. A possible 2-ω component in the response of the device under test is filtered out.

The change in stiffness due to the static offset in displacement x is negligible, so the resonant frequency f_r and the Q-factor remain the same when $UactB2 = U_{bias}$ and $UactA = U_{bias} - U_{diff}$. Therefore, only the gain will increase with 6 dB when $UactB2 = UactB = U_{bias} + U_{diff}$, because the total range of displacement has doubled, as given by equation Eq.6.19 with the possible addition of 2nd-order dynamics given in equation Eq.6.27.

Ideally, the performance of both actuators and sensors should not be influenced or burdened by the connections through cables or the actuation and measurement electronics. In Fig. 51 a lumped model is given for the ideal case where the cable capacitances are electronically eliminated by keeping the outer core of the cables to the same potential as the inner core, using active electronics. With fast current limiting electronics the resistors R_a and R_b can also be omitted.

With these electronics it would be possible to apply both actuation and sensing signals to both comb-drives differentially as depicted in Fig. 51 for the ideal case. If both comb-structures A & B are connected differentially as explained earlier another 6dB would be added to the mechanical frequency response similar to Fig. 45. This would require a second 1 MHz source with a phase shift of 180 [deg] and an amplitude *Us'* adjusted in such a way to make the output voltage of the synchronous detector U_{out} = 0 for x = 0.

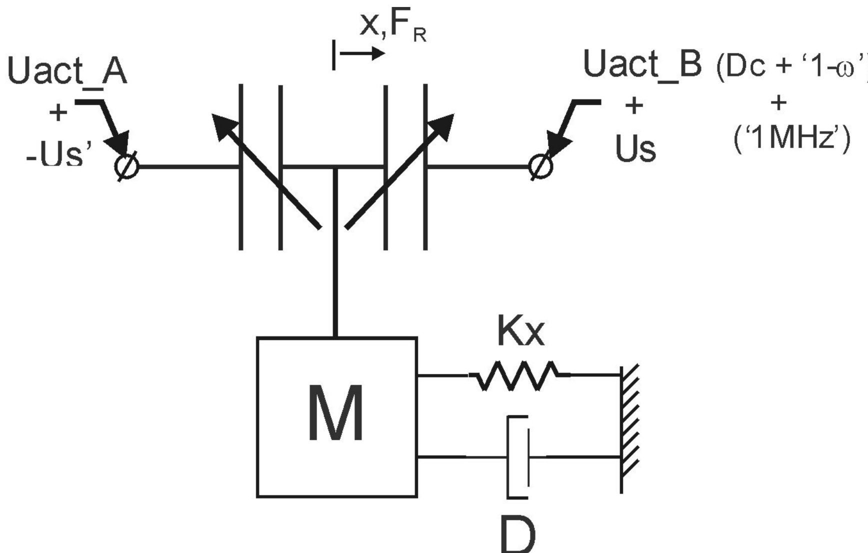

Fig. 51: Ideally both comb-drives are connected as both actuator and sensor differentially with electronically eliminated cable-capacitances and fast current limiter.

Implementation of closed-loop control with a sensor output voltage which is linear with displacement, without an offset voltage, is easier to implement than with a sensor voltage that is periodic with displacement. But ultimately, with the desired nanometer-accuracy over a range of 100 µm or more, the aim for nano-position control will be very hard or impossible to establish without the intrinsic benefits of a periodic position sensor, namely, the periodicity.

Conclusions on experiments with comb-drive sensor in pull-pull mode

Two comb-drives have been actuated in pull-pull mode with one comb-drive simultaneously operating as position sensor.

The displacement resolution has been estimated to be Δx_n ~ 1.5 nm for small displacements around x =0. This amounts to ~6 aF as smallest detectable change in capacitance in the presence of noise of the current measurement set-up.

The chosen connection method causes an unbalance between the two differential pull-pull actuation voltages. The resulting displacement of the device contains a 1-ω and a 2-ω component which amplitudes and phases follow a 2nd-order mass-spring-damper model with parameters corresponding to the device under test. The measurement results were

correctly measured.

For ideal connection of the device, the addition of cable capacitances and current limiting resistors should be eliminated. To this end, new investments should be done to purchase or build the high quality electronics needed.

Two differentially operating comb-structures can operate as both actuators and non-incremental coarse position sensors with less complicated position control. These sensors lack however the benefits of an incremental position sensor: A decoupled range and resolution.

References

[1] A.A.Kuijpers et al., Micromachined capacitive long-range displacement sensor, *Proc. Eurosensors XVII,* Guimarães, Sept. 21-24, 2003, 560-563.

[2] K.Okada, T.Sekino, Agilent Technologies, The impedance measurement handbook, dec 2003, http://cp.literature.agilent.com/litweb/pdf/5950-3000.pdf.

[3] L.K.Baxter et al., *Capacitive Sensors: design and applications*, IEEE Press, New York, 1997

[4] M.H.Bao, S.Middelhoek et al, *Handbook of Sensors and Actuators*, **8**, Elsevier Science, Amsterdam, 2000.

[5] D.K.Cheng, Field and Wave Electromagnetics, Addison-Wesley 1989

[6] M.R. Hart, R.A.Conant, K.Y. Lau, R.S. Muller, Stroboscopic Interferometer System for Dynamic MEMS Characterization, J. of MEMS, 9, no. 4, dec 2000

[7] C.Rembe, R.S. Muller, Measurement System for Full Three-Dimensional Motion Characterization of MEMS, J. MEMS,(11),no. 5, OCT 2002

[8] F.M. Dickey, S.C. Holswade, L.A. Hornak, K.S. Brown, Optical methods for micromachine monitoring and feedback, Sensors and Actuators 78 1999 220–235

[9] R.Legtenberg et al., Comb-drive actuators for large displacements, J.Micromech. Microeng., **6**, 320-329, 1996.

[10] A.A. Kuijpers, R.J. Wiegerink, G.J.M. Krijnen, T.S.J. Lammerink and M. Elwenspoek, *Capacitive long-range position sensor for microactuators*, Proc. Of MEMS2004, Maastricht, Netherlands, pg 544, January 2004.

[11] W.C.Tang, M.G.Lim, Howe R.T., Electrostatic Comb Drive Levitation and Control Method, J.MEMS, 170-178, dec 1992,

[12] www.polytec.com

7 Conclusions and Discussion

7.1 CAPACITIVE INCREMENTAL POSITION SENSING

This thesis presents an integrated capacitive incremental position sensor for long-range nano-positioning of MEMS devices. The aim of the work within this thesis has been to implement concepts and demonstrate the possibilities through analysis, simulation and assessment of the performance by experiments and preferably characterization.

Capacitive sensing offers relative easy integration of a capacitive sensor with an electrostatic microactuator through micromachining technology. Integration with conventional comb-drive microactuators in a two-mask micromachining process has been demonstrated. Furthermore, this sensing principle offers possibilities for monolithic CMOS compatible integration and a wide range of electronic interfacing possibilities [1,2].

The target-specification for the sensor is to measure with nanometer-accuracy (nm) over a long-displacement range of X^{max} = 100 micrometers (µm) or more. This requires a dynamic sensing range of 10^5. Incremental sensing in combination with quadrature detection gives a periodicity of $P_x/4$. Hence, the dynamic range requirement is reduced to $4\ X^{max}/P_x$ i.e. 50x reduction for $P_x = 8$ µm. In combination with a translation velocity of $v = 50$ mm/s this would require a bandwidth BW $\geq v / P_x = 6.25$ KHz.

Two related concepts for a novel capacitive incremental position sensor are devised and presented:

- Incremental Capacitance Measurement Mode ICMM (Open-Loop)
- Constant Capacitance Measurement Mode CCMM (Closed-Loop)

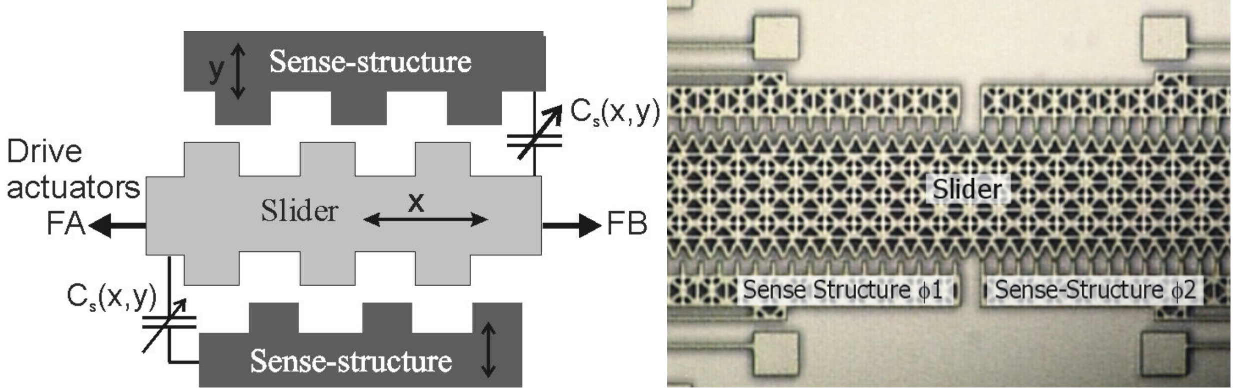

Fig. 1: the capacitive long-range incremental position sensor is based on the change in capacitance for a displacement between 2 periodic geometries.

ICMM: In the Incremental Capacitance Measurement Mode concept the slider displacement is detected by measuring the periodic change in capacitance for a relative displacement between two opposing periodic geometries Fig. 1

CCMM: In the concept Constant Capacitance Measurement Mode, the sense-structures are continuously adjusted in y-direction by additional sense-actuators to keep the capacitance between the two periodic geometries constant as the slider moves in x-

direction. The control voltage U_c for the sense-actuators becomes a measure for the slider displacement.

In chapter 3 is shown that the ratio between the SNR for CCMM and ICMM can increase by a factor of 320 for a controlled gap-size of 250 nm between a sine-pattern on the slider and a finger pattern on the sense-structures. For quadrature detection either a triangular sensor signal or a sinusoid signal is needed for fine position measurement. Analysis predicts that the larger the ratio between period size and finger width, the better the y_{ss}-displacement of the sense-structure will approximate a sine. This is confirmed with 2D-FE simulations and with quasi-static measurements.

The implementation of both incremental sensing concepts offers several advantages. A primary advantage over a non-incremental capacitive sensing concept is the reduction of the demands for dynamic sensing range and the intrinsic possibility to characterize a certain displacement by calibrating the periodic sensor read-out with the periodic geometry. Furthermore, the innovative design offers a possibility to increase the signal to noise ratio by reducing the gap-size. The electrostatic forces are parallel to the substrate (i.e. in-plane) and on both sides of the slider opposite to each other. The symmetry of the design therefore balances the electrostatic forces between slider and sense-structures. Thermal electrical and mechanical noise sources will not be an immediate obstacle in order to reach nm-accuracy. However, the generated electrostatic forces between slider and sense-structure due to a sensor input voltage can result in a systematic displacement error of $x_e \sim 2 - 8$ nm depending on the stiffness of the (test) vehicle.

Two micromachining fabrication processes are described (chapter 4) which enable a complete integration of the capacitive incremental position sensing concept with an electrostatic microactuator device.

The Poly-process is a standard surface-micromachining process described by Legtenberg [3,4]. The Poly-silicon structural layer with limited height of 5 μm is deposited on top of a sacrificial Silicon-oxide (SiO_2) layer with thickness limited to 3 μm. The TWIN process is a novel bulk micromachining process [5,6]. In contrast with the 'wet' chemical sacrificial release etching of the Poly-process, the plasma release etching prevents the effects of stiction due to capillary forces.

For the TWIN process an increase in ratio of capacitance variation $\Delta C(x)$ over parasitic capacitance C_p is predicted of a factor 25 – 200 compared to the Poly-process. This is due to an increase in structure height and a larger distance between structure layer and substrate. An extra benefit by the increased structure height is the reduction in sensitivity to vibrations in the z-direction due to inertial effects and a reduction of the thermomechanical noise.

With the currently standard available photo-lithography in the Mesa+ laboratory gap-distance and finger width are limited to $w = 2$ μm. A solution was found in a smart design, which results in gap-sizes as small as around 0.5 μm. Furthermore, within the design concept for both ICMM and especially for CCMM a crucial option is included to reduce the gap-distance between sense-structure and slider pattern through additional sense-actuators. The resulting gap-distances can be as small as ~200nm depending on the side-wall roughness of the patterns on slider and sense-structures.

The second dominant process limitation is the RIE plasma etching process. For the Poly-process the aspect-ratio is circa 10. Thus, for a height of 5 µm the minimum width of fingers and gaps is circa 500 nm. The TWIN process has an aspect ratio of circa 20x. Therefore, a height of 40 µm defines the minimum finger width and gap-width to circa 2 µm and the minimum period size to about 8 µm. With the implementation of quadrature detection a periodic measurement read-out with periodicity ≥ 4 µm can be achieved. For the Poly-process the periodicity may be as small as 2µm. Experiments with TWIN devices are anticipated in the near future.

7.2 CONCLUSIONS EXPERIMENTAL RESULTS

In chapter 5 the assessment is given for both concepts ICMM and CCMM by experiments with surface micromachined devices (Poly-process).

Various designs were made with different periodic geometry combinations on slider and sense-structures respectively. All the designs use two electrostatic comb-drive microactuators in pull-pull configuration [7] to drive the slider beam.

Experiments are divided in quasi-static and dynamic experiments. All experiments use a charge amplifier (based on a CLC425 OPAMP) and a synchronous detector implemented with CMOS switches and a Low-Pass RC-Filter. The change in low-frequency-output voltage U_{out} is a linear measure for the change in capacitance C_s on the input of the charge amp.

Results of quasi-static experiments without gap-adjustment (ICMM):

For various periodic geometry combinations the periodic change in capacitance versus displacement of the slider has been demonstrated. The smallest maximum change in output voltage U_{out} ~ 2mV per 4 µm is measured. After calibration this amounts to ΔC_{max} ~ 2 fF per 4 µm.

A comparison between 2D-FE simulation and these quasi-static measurement results showed that both the shape of $\Delta C(x)$ as the values for maximum change ΔC_{max} are quite well predicted. 2D-FE simulations are a useful tool to predict the shape and the variations in capacitance.

Results of quasi-static experiments with gap-adjustment (ICMM):

Measurements with a redesigned device with a sine – rectangular geometry with 10 µm period size show a 4.5 x increase in output voltage to a maximum change of $(\Delta U_{out})_{max}$ ~12 mV per 5 µm displacement due to an active reduction of the gap-distance. A decrease in the standard deviation is demonstrated by reducing the gap with the sense-actuators. A systematic position uncertainty due to hysteresis is estimated to be $/\Delta x/_{mean_h}$ = 12 nm, In addition a repeatability position uncertainty is estimated to $/\Delta x/_{std}$ = 13 nm.

Results of quasi-static experiments Constant capacitance mode (CCMM):

A mean absolute position uncertainty is calculated as $/\Delta x/_{mean}$ = 7.5 nm over the total displacement range of 32 µm. The standard deviation of the estimated position uncertainty Δx_{std} = 6 nm. The bandwidth BW << 1 Hz due to a slow PC interface. An improvement is expected from implementation of CCMM with improved electronics.

The measured squared control voltage U_c^2 i.e. $Y(x)$ for CCMM approximates a perfect sine better than ICMM. The non-linearity due to higher order harmonics is a factor 4 - 5

less for CCMM and amounts to only 6% of the first order amplitude. This corresponds with both analysis and 2D-FE simulations and therefore, clearly demonstrates the high potential of CCMM in terms of obtainable position accuracy for both concepts.

Dynamic measurements for ICMM with active gap-adjustment

A frequency response is measured using a HP4194A gain-phase / Impedance analyzer for small amplitudes of ~1 µm around position $x = 0$. A resonant frequency of $f_r = 1.7$ KHz and and Q-factor ~ 5 of the test-vehicle are measured with the capacitive incremental position sensor. For frequencies above 6 KHz too much cross talk prevented a useful measurement. An improvement of the experimental setup is expected to reduce or eliminate this effect significantly.

With the same device and actuation electronics for large displacement amplitudes at $f_{act} = 1.4$ KHz, a total displacement range of $|\Delta x|^{pk\text{-}pk}$ of ~45 µm is measured with 256x averaging. This corresponds to a maximum slider velocity of v_{max} ~ 20 cm/s.

Dynamic measurements for with comb-drive as displacement sensor

With 2 comb-drives actuated in pull-pull and one comb-drive simultaneously operating as displacement sensor we were able to determine a sensitivity of Δx_n ~ 1.5 nm. This amounts to ~ 6 aF as smallest detectable change in capacitance in the presence of noise of the current measurement set-up.

With both comb-drives operating simultaneously as drive-actuator and sensor a course position sensor can be added to a comb-drive system which simplifies the implementation of closed-loop position control [8,9,10]. However, this type of sensing is non-incremental and therefore offers no inherent calibration possibility. It will eventually fail over very large distances and is directly limited by the actuation-displacement range.

All experiments are performed without an extensive electric shielding in a cage of Faraday and without the implementation of a reference capacitance to reduce or eliminate parasitic effects due to changes in relative humidity and temperature. Proper grounding and maintaining the environmental conditions minimizes the unwanted parasitic capacity changes. The measurement results may improve by a factor of 10 using the possibilities for compensation described in chapter 3.

The next challenges are to implement quadrature detection and actual nano-positioning control and to build a characterization setup to assess the accuracy over a bandwidth of about 1 KHz. Both concepts have demonstrated a high potential to obtain nm-accuracy over infinite range.

7.3 DISCUSSION ON EXPERIMENTAL RESULTS

The presented results were obtained without reference capacitance and compensation of changes in charge-amplifier gain and without the use of a cage of Faraday. However, we have kept the environmental conditions as constant as possible. We have demonstrated a considerable improvement compared to previous reported results [11.

The quasi-static experimental result for CCMM showed a mean absolute position uncertainty of $/\Delta x/_{mean}$ = 7.5 nm with standard deviation of position uncertainty Δx_{std} = 6 nm. The complete measurement for one complete displacement cycle over ~ 32 μm took ~ 5 hours.

This can be defined as an expectation of the detection accuracy. The interpretation is that all positions in the measured displacement range of ~ 32 μm will have a mean detection error of 7.5 nm ± 3 nm

Other characterization techniques are necessary to determine precision and accuracy and sensitivity of position measurement and position control. Furthermore, implementation of the sensor concept with a prototype x/y-stage for a probe recording memory array or for an AFM based device for in-situ characterization of surface properties and nano-lithography (see chapter 1) is anticipated [12]

The challenge for the characterization techniques is to detect in-plane motions rather than out-of-plane motions. A laser interferometry technique could be used. However, it would most likely require the assembling of a mirror on top of the slider beam. For the poly-devices the assembling of a micromirror on top of the slider is not possible. For the devices made with the TWIN process it maybe possible.

In the following section we reflect on reported measurement and characterization results found in literature.

Chu et al [13] report on a micromachined 2D positioner with electrothermal actuation and sub-nanometer capacitive sensing. With a (SOI) device thickness of 63 μm and a lever, or displacement amplifier, the displacement range on the output side is amplified by a factor of ~3.37 and measured with comb-sensors. Chu claims the measured sensitivity is 333.0 ± 10 fF μm^{-1} or 333.0 ± 10 aF nm^{-1} and a reliable measurement of 0.1 fF which corresponds to a displacement accuracy of 0.3 nm at the input side of the lever. However, Chu uses calibrated imaging technique for displacement measurements with an accuracy of ~ 500nm. For small displacements the uncertainties are significant.

Horsley et al [9] demonstrated closed-loop control up to a bandwidth of ~ 2.5 KHz of a micro fabricated actuator with a gap-closing parallel plate capacitive sensor. They implemented a switched capacitive sensing scheme based on correlated double sampling to remove amplifier offset, *1/f* noise, switch-charge injection, and *kT/C* sampling noise.

With a 1.6 mg ceramic slider assembled on top of an actuator optical position measurements were possible using a laser Doppler vibrometer. This technique allows measurement of both actuator position and velocity with a bandwidth of more than 50 KHz, and a position resolution of 2 nm.

Another technique to detect in-plane motions is described by Rembe and Muller for a

stroboscopic microscope interferometer system [14,15]. They use stroboscopic imaging, interferometry and image analysis. This technique is computational very intensive. The SMIS can extract data at time intervals as short as 100 nanoseconds and measures full 3-D displacements with resolutions within 5 nm in surface dimensions and 0.7 nm for displacements perpendicular to the surface.

An overview of other optical methods is given by Dickey et al [16].

We have implemented image analysis methods. Preliminary results show an obtainable resolution in the order of 1-10 nm. Measurements with this technique were performed with 0.5Hz motion. The design of the slider structure has to be designed with a 1D-repetitive pattern to improve the accuracy of the image analysis. The image analysis technique selects a repetitive pattern on a moving part of the device. Through cross-correlation techniques the displacement of this selected area in sub sequent image frames can be determined. For better characterization the repetitive pattern of the slider should be 1D with known dimensions.

A considerable improvement of the results is expected at much higher bandwidth if the compensation techniques for parasitic changes in relative humidity ΔH_r, given in chapter 3 are implemented. The implementation of closed-loop control for constant capacitance with improved electronics is expected to increase the bandwidth enormously. Also the use of a new probe station recently obtained promises better and extended connection possibilities. The implementation of actual nano-positioning with similar control-methods as reported by Pantazi is another interesting future topic to investigate [17].

The TWIN process offers an increased structure height and increased distance between structural layer and substrate compared with the poly-silicon devices. Therefore, an increase in ratio of capacitance variation $\Delta C(x)$ over parasitic capacitance C_p is predicted of a factor 25 – 200 and consequently an equal increase in obtainable accuracy is expected, especially with the compensation for ΔH_r and ΔT and improved shielding and grounding as explained in chapter 3 and by Baxter [2].

The TWIN process also offers the possibility to electrically isolate parts in a moving slider beam or table [5]. This also makes it interesting to again consider implementation of the multiple parallel plate principle and implement phase detection [2,18,19]. Also for the implementation of this design-concept the electrostatic forces on the electrode plates are directed in-plane and can be balanced on both sides of the moving translator. The gap between the plates may be reduced once by additional actuators, as demonstrated for the ICMM concept in this thesis. Implementation of CCMM will not be possible. CCMM can in principle produce both sinusoidal and triangular measurement signals. With the implementation of multiple rectangular plates in the TWIN process only triangular ouput signals can be produced. A multiple parallel plate principle with electrode plates underneath the structure layer is not possible with TWIN. With SOI wafers this principle was demonstrated by Hu for an accelerometer [20].

Limitations of surface roughness, processing uncertainties on the achievable accuracy needs to be further assessed.

For the designs presented in this thesis for both Poly-process and TWIN process comb-drives are used as driving actuators. The advantage is that fabrication requires only one mask and one structural layer. Furthermore, the actuation and displacement are

continuous, whereas the microwalkers demonstrated by Tas [21] provide discontinuous motion and more complicated fabrication.

However, stepping micromotors reported by Sarajlic [22] can be realized in a relatively easy three mask fabrication process using a single Poly-Silicon layer. For the reported inch-worm motor the maximum stroke of 11 μm and force of 0.55 mN were limited by physical constraints. In principle however, stepping motors are able to generate much more force and displacement range than the conventional comb-drive. A combination of a capacitive incremental position sensor as presented in this thesis and a stepping motor maybe the most interesting option for position control and optimizing performance.

For a comb-drive the maximum displacement is limited by side pull-in of either the whole suspended structure as described by Legtenberg [23] or side pull-in of only one comb-finger. This last effect we have encountered regularly. The maximum allowable actuation voltage was 30 V for the device used in all experiments except the experiments described in section 5.3.3 for different periodic geometries. Other devices would show side pull-in of one of the comb-fingers at 37 V. For the sense-actuator comb-drives the individual side pull-in voltage was 28 V. The fingers would not permanently stick to each other and the input resistances reported in section 5.2 to prevent permanent damage after electrical short cut worked well. In an improved design the side pull-in of an individual finger can be avoided following the analysis given by Tas [21]. Furthermore, with improved actuation electronics active fast shortcut current limiters the cable capacitances and the resistors can be eliminated.

A further improvement when comb-drive actuators are used may be to implement the flexure as reported by Grade [24] with tilted folded flexures to extend travel ranges to as much as 150 μm in less than 1 ms. A similar approach is reported by Zhou [25]. The maximum stable displacement of a comb-drive with conventional folded flexure was extended with the tilted folded flexure from 33 μm to 40 μm.

The comb-drives need to be designed such that each comb-drive can be actuated with a differential voltage supply. This ensures that moving parts are really zero voltage and not average zero voltage.

References

[1] M.Elwenspoek, R.J.Wiegerink, *Mechanical Microsensors,* Berlin Heidelberg New York, Springer-Verlag, 2000

[2] L.K.Baxter et al., Capacitive Sensors: Design and Applications, IEEE Press, New York, 1997.

[3] R.Legtenberg, Electrostatic Actuators Fabricated by Surface Micromachining Techniques, PhD Thesis, University of Twente, Enschede, 1996.

[4] R.Legtenberg et al., Comb-drive actuators for large displacements, J.Micromech. Microeng., 6, 320-329, 1996.

[5] E Sarajlic, M J de Boer, H V Jansen, N Arnal, M Puech, G Krijnen, M Elwenspoek, Advanced plasma processing combined with trench isolation technology for fabrication and fast prototyping of high aspect ratio MEMS in standard silicon wafers, J. Micromech. Microeng. (14), S70–S75, 2004

[6] E.Sarajlic, M.J.deBoer, H.V.Jansen, N.Arnal, M.Puech, G.Krijnen, M.Elwenspoek, Integration of trench isolation technology and plasma release for advanced MEMS design

on standard silicon wafers, 14th Micromechanics Europe Workshop (MME 2003), November 2003, Delft, the Netherlands.
[7] M.H.Bao, S.Middelhoek et al, *Handbook of Sensors and Actuators*, **8**, Elsevier Science, Amsterdam, 2000.
[8] R.Legtenberg, A.W.Groeneveld, Towards Position control of electrostatic comb drives, *Proc. Micromech. Microeng. (MME'95)*, Copenhagen, 3-5 Sept., 1995.
[9] D.A.Horsley, N.Wongkomet, R.Horowitz, A.P.Pisano, Precision positioning using a microfabricated electrostatic actuator, IEEE Trans. On Magnetics, (35), 2, march 1999
[10] P.B.Chu, K.P.B. Pister, Analysis of closed-loop control of parallel-plate electrostatic microgrippers, IEEE Int. conf. on Robotics and automation, 820-825, 1994.
[11] A.A.Kuijpers et al., Micromachined capacitive long-range displacement sensor, *Proc. Eurosensors XVII,* Guimarães, Sept. 21-24, 2003, 560-563.
[12] S. Deladi, J.W. Berenschot, M.J. de Boer, G.J.M. Krijnen and M.C. Elwenspoek, An AFM-based device for in-situ characterization of nano-wear, Proc. Of MEMS2004, Maastricht, Netherlands, pg 181, January 2004.
[13] L.L.Chu, Y.B.Gianchandani, A micromachined 2D positioner with electrothermal actuation and sub-nanometer capacitive sensing, J.Micromech. Microeng., (13), 279-285, (2003)
[14] M.R. Hart, R.A.Conant, K.Y. Lau, R.S. Muller, Stroboscopic Interferometer System for Dynamic MEMS Characterization, J. of MEMS, 9, no. 4, dec 2000
[15] C.Rembe, R.S. Muller, Measurement System for Full Three-Dimensional Motion Characterization of MEMS, J. MEMS,(11),no. 5, OCT 2002
[16] F.M. Dickey, S.C. Holswade, L.A. Hornak, K.S. Brown, Optical methods for micromachine monitoring and feedback, Sensors and Actuators 78 1999 220–235
[17] A Pantazi,MA Lantz, G Cherubini, H Pozidis and E Eleftheriou, A servomechanism for a micro-electromechanical-system-based scanning-probe data storage device, Nanotechnology, (15), S612–S621, 2004
[18] P.B.Kosel, G.S.Munro, R.Vaughan, Capacitive Transducer for Accurate Displacement Control, IEEE Trans. On Instrumentation and Measurement, (IM-30),2,114, June 1981
[19] K.B.Klaassen, J.C.L.van Peppen, Linear capacitive microdisplacement transduction using phase read-out, Sensors And actuators, 3, 1982/83, 209-220
[20] H.H.Hu, W.Fang, A novel (111) Single Crystal-Silicon Accelerometer using parallel connected parallel plate capacitance, Proc. Of MEMS2004, Maastricht, Netherlands, pg 597, January 2004.
[21] N.R.Tas, Electrostatic Micro Walkers, Micro Electromechanics and Micro Tribology, Ph.D. Thesis, University of Twente, Enschede 2000.
[22] E.Sarajlic, A low volume electrostatic inchworm microactuator with high-resolution and large force, Proc. Eurosensors XVII, 194-195, Portugal, Sept. 2003
[23] R.Legtenberg et al., Comb-drive actuators for large displacements, J.Micromech. Microeng., **6**, 320-329, 1996.
[24] J.D.Grade, H.Jerman, T.W.Kenny, Design of large deflection electrostatic actuators, J.of MEMS, (12), 3, Jun 2003
[25] G.Zhou, P.Dowd, Tilted folded-beam suspension for extending the stable travel range of comb-drive actuators, J.Micromech. Microeng., (13) 2003, 178-183

Appendix 1 Examples 2D-FE simulation results

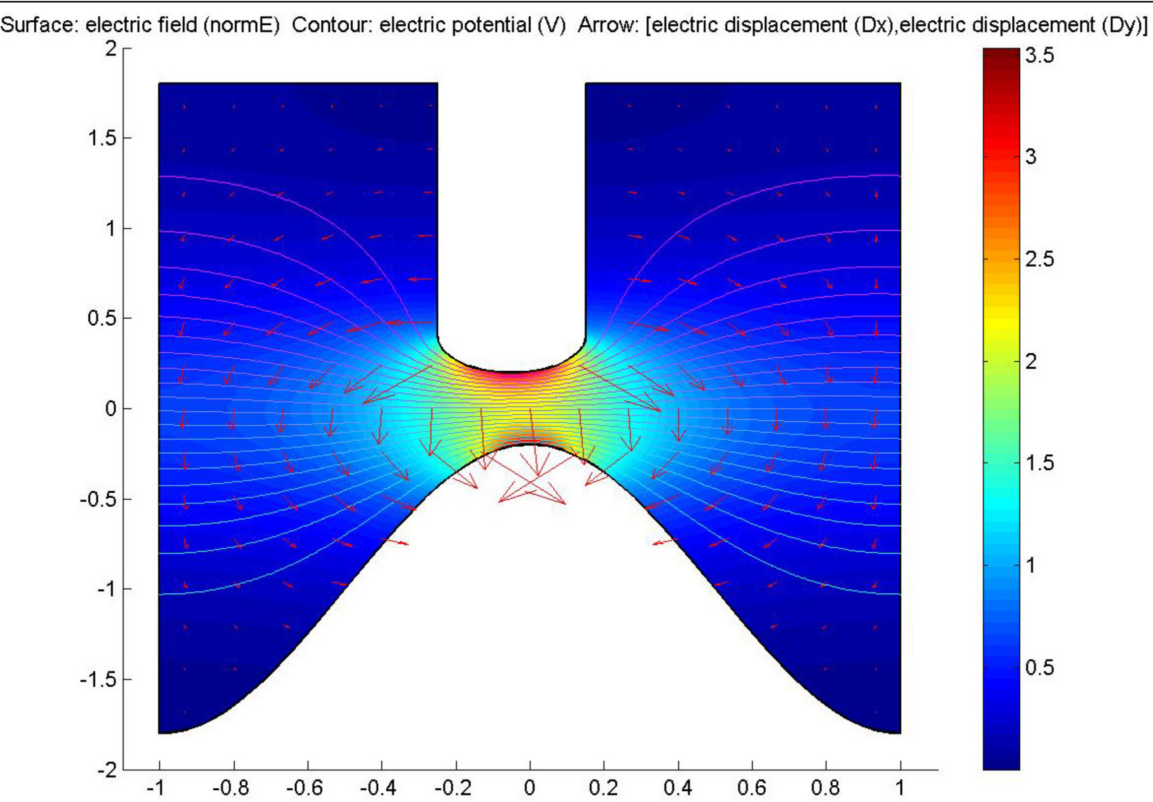

Fig.A1- 1: 2D-FE Simulation result for sine-rounded finger combination, 1 µm = 0.2 unit

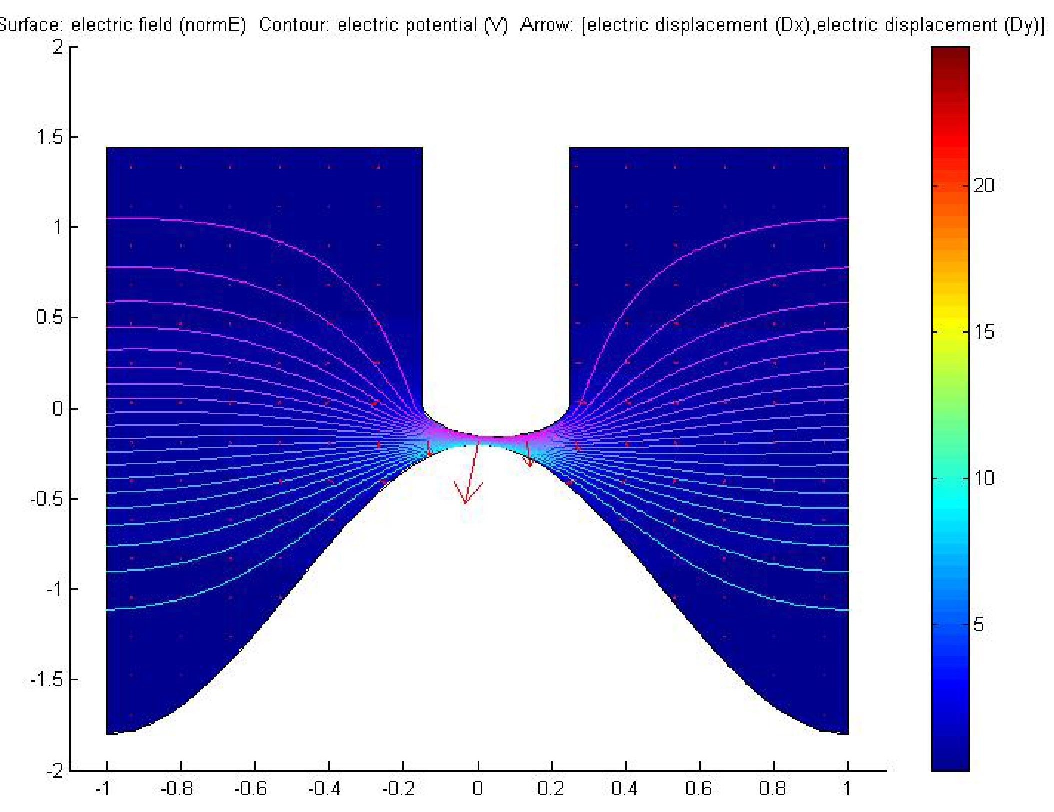

Fig.A1- 2: Position for which $C(x,y) = C_{set}$ = 300 aF / finger pair

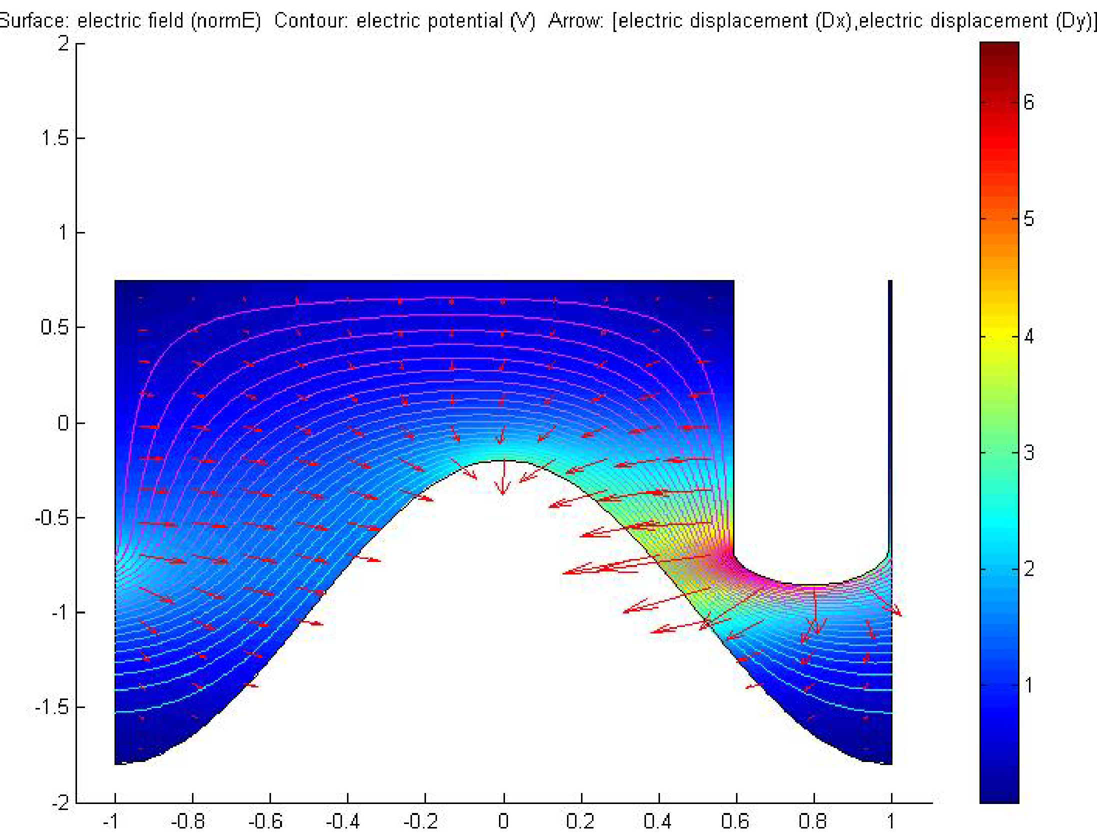

Fig.A1- 3: result shows the consequences of the periodic boundary conditions. On the left side another finger is almost entering the segment.

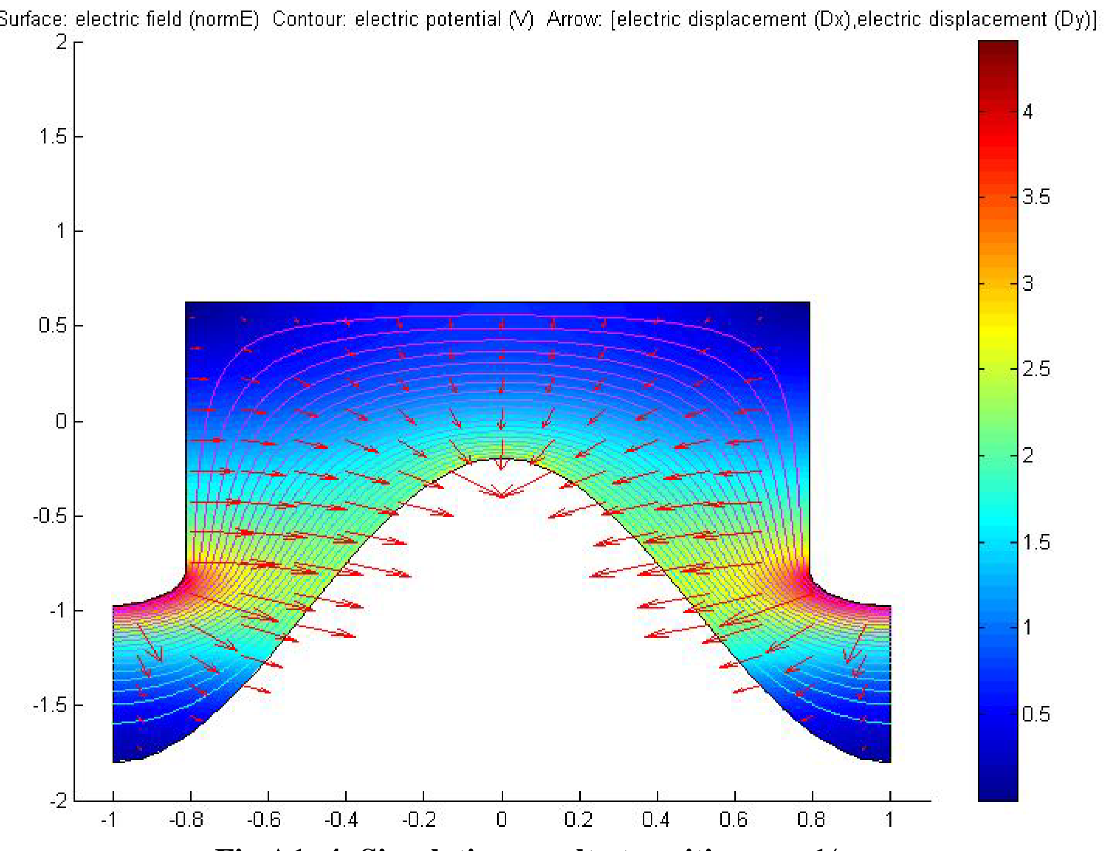

Fig.A1- 4: Simulation result at position $x_n = ½$

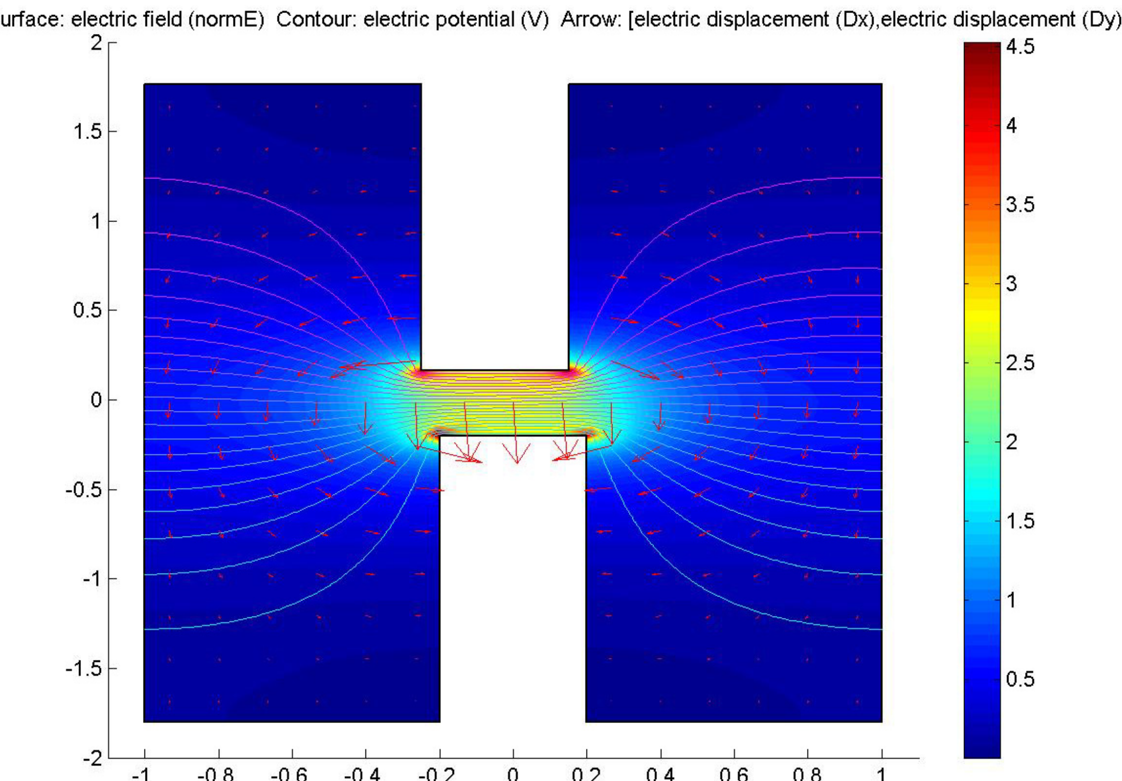

Fig.A1- 5: Example simulation result for rectangular-rectangular combination, period P = 10 µm

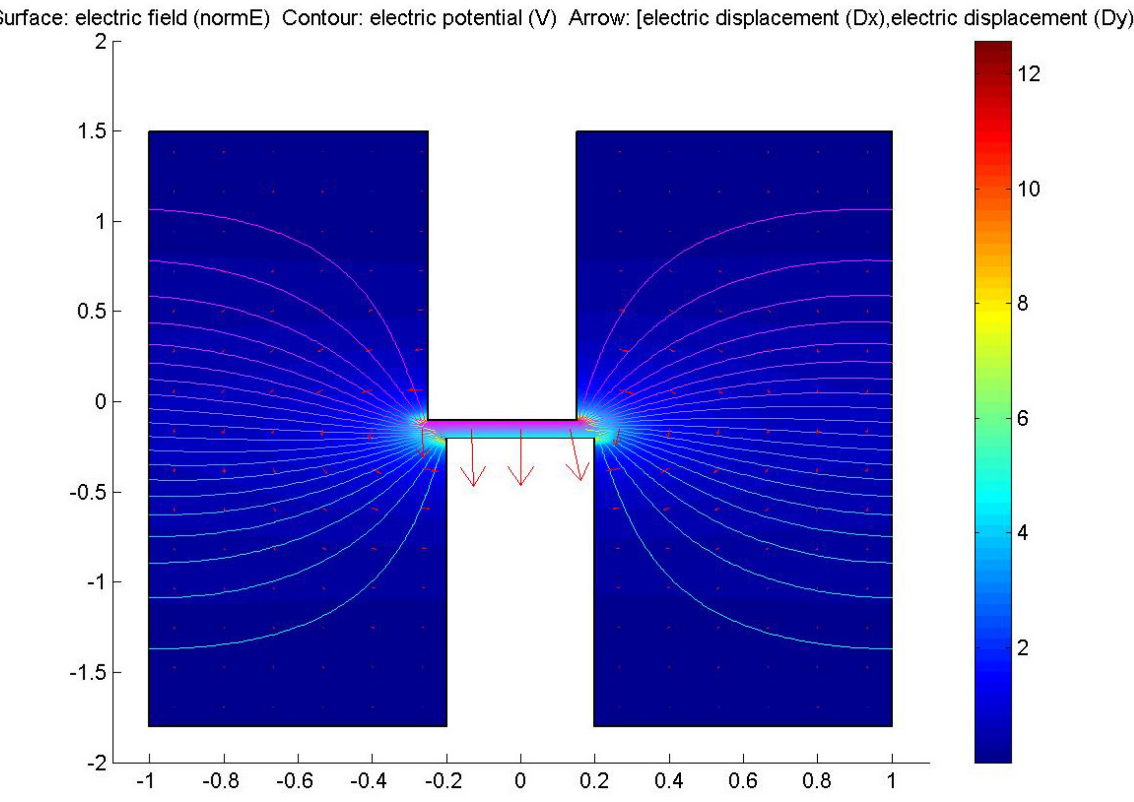

Fig.A1- 6: Situation for which $C(x,y) = C_{set} = 300$ aF

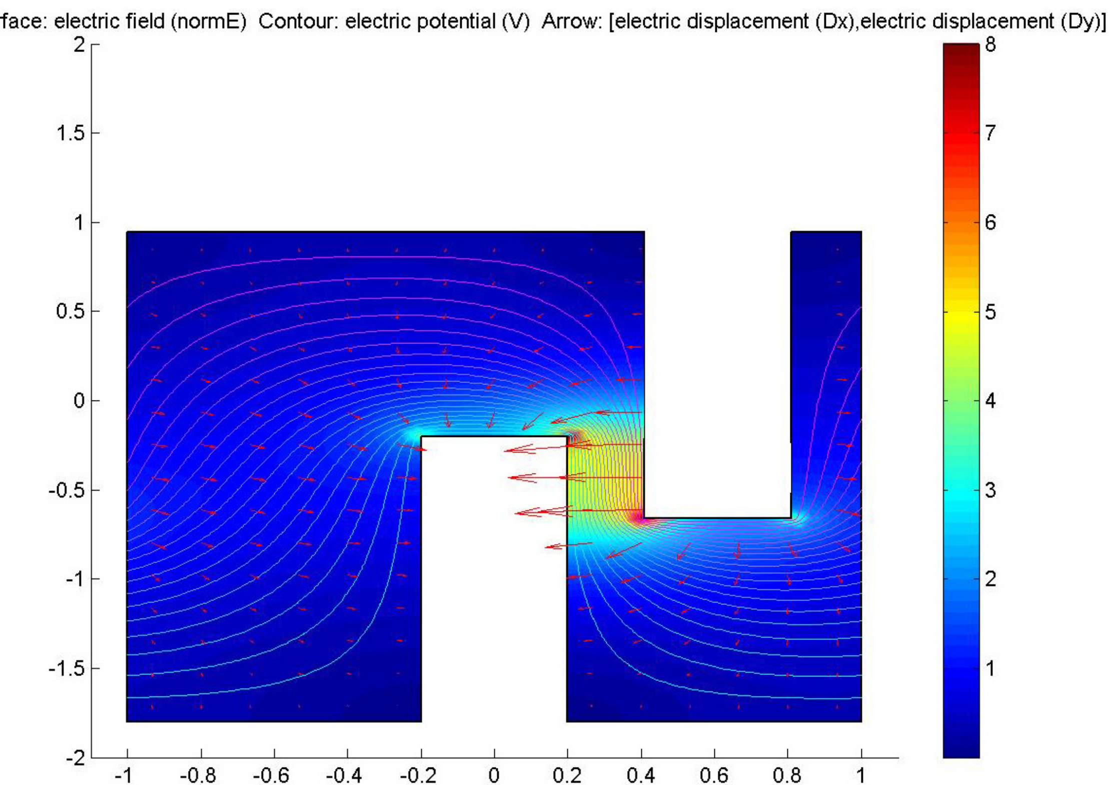

Fig.A1- 7: result shows the consequences of the periodic boundary conditions. On the left side the influence of a finger on the point of entering the segment.

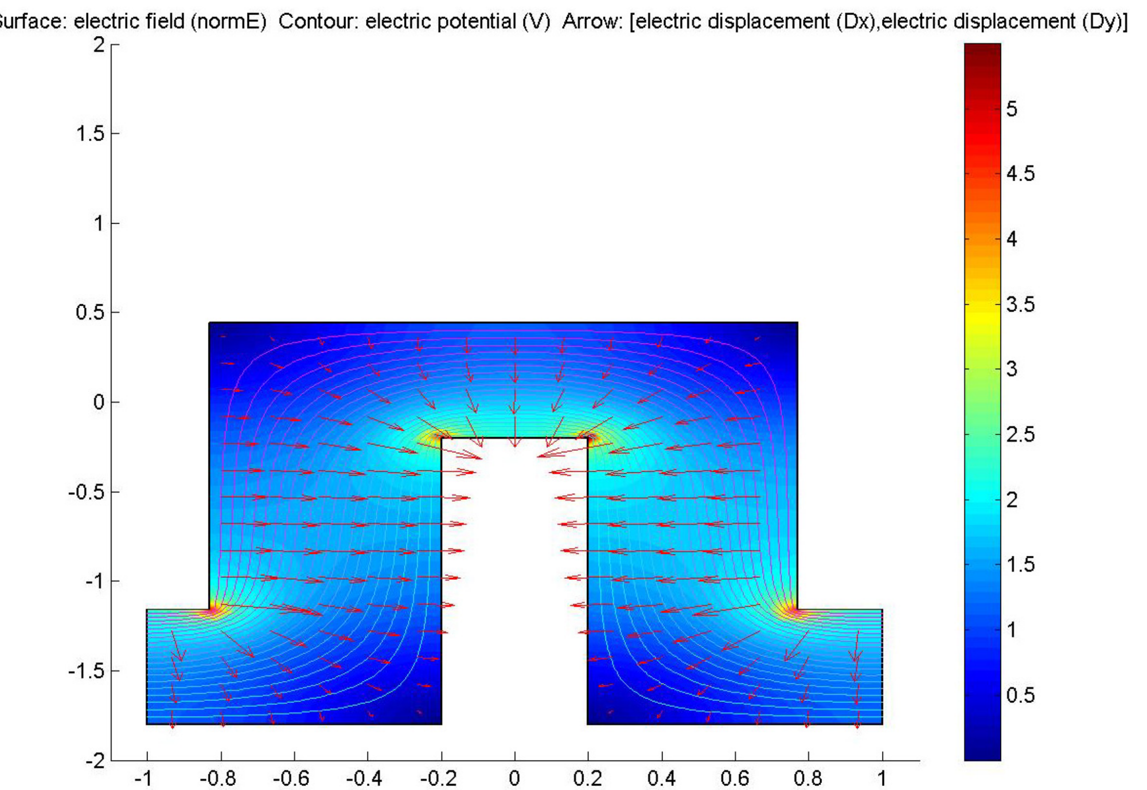

Fig.A1- 8: situation for displacement x_n = 1/2 (half period P) for which C(x,y) = C_{set}

Appendix 2 Design and Fabrication

2.1 Poly-process: Design RectP12 (generation 1)

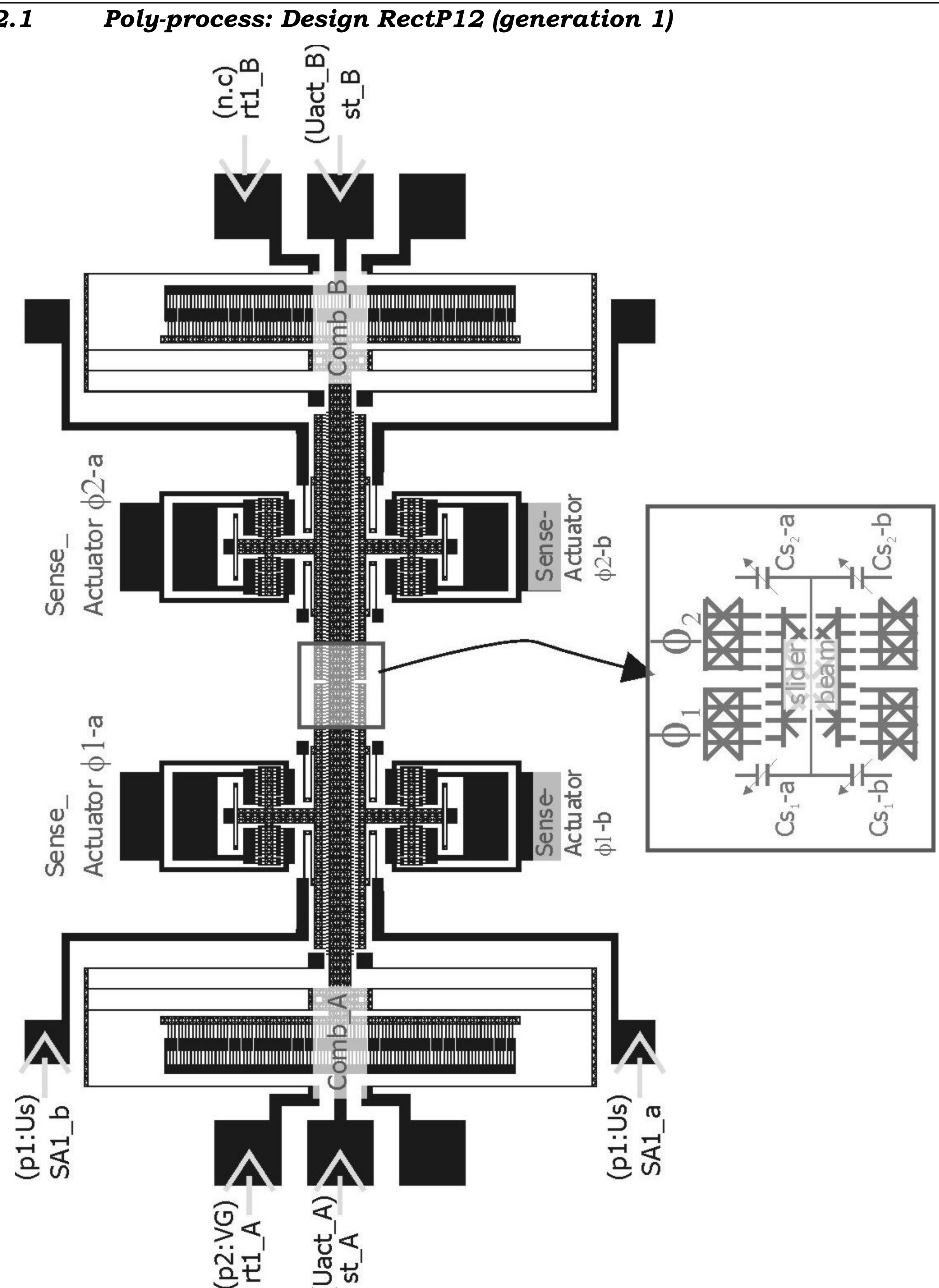

Fig. A2 - 1: Design of device with Sine-rectangular period P = 10 µm (generation I).
Indicated are two comb-drive actuators driving the slider beam and 2 pairs of sense-actuators and the typical connection in the experiments. The inset shows the periodic capacitances.

2.2 Poly process: redesign SinP10 generation II

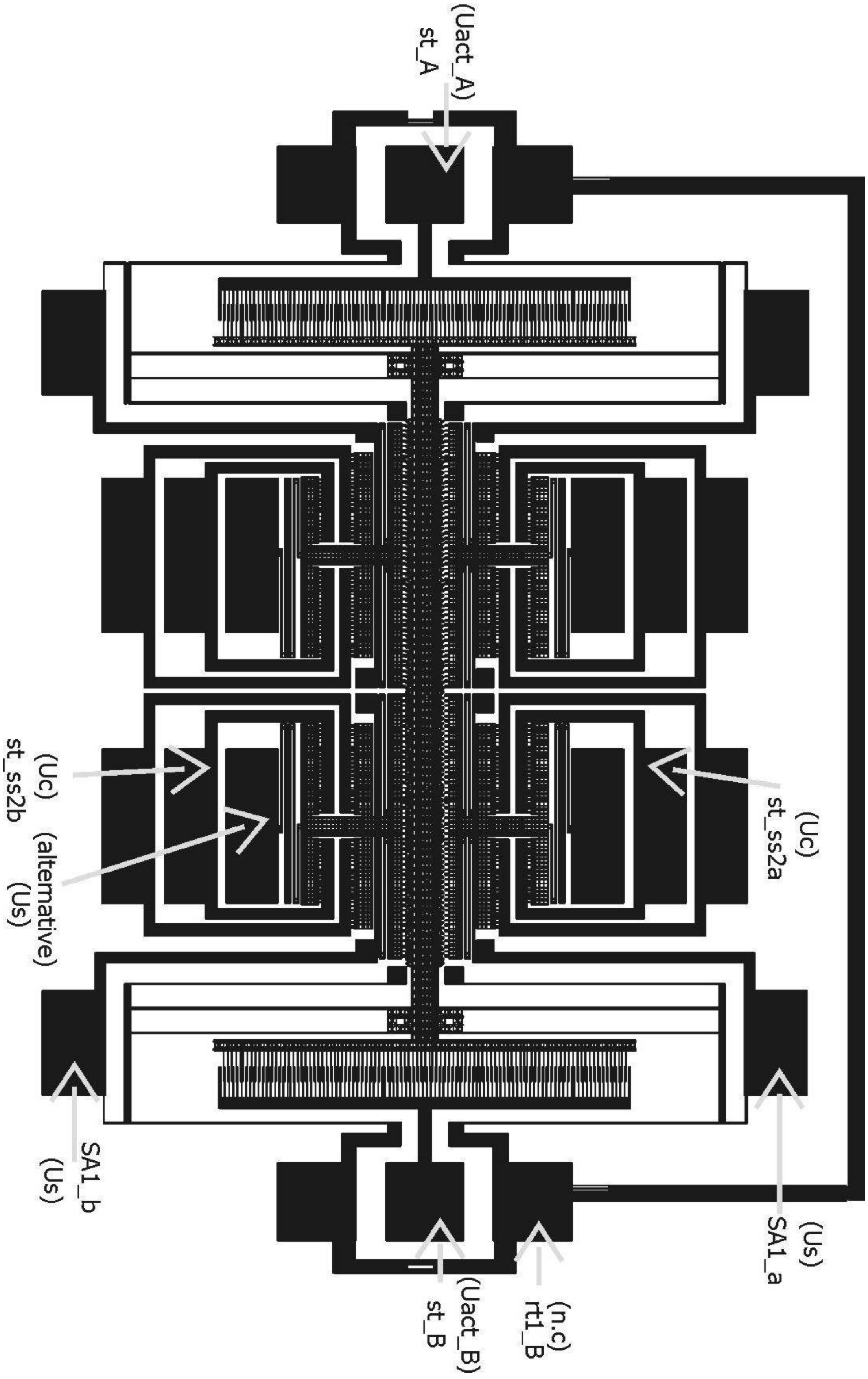

Fig. A2 - 2: Design of a poly-device with Sine-rectangular period P = 10 after a redesign. (Generation II).

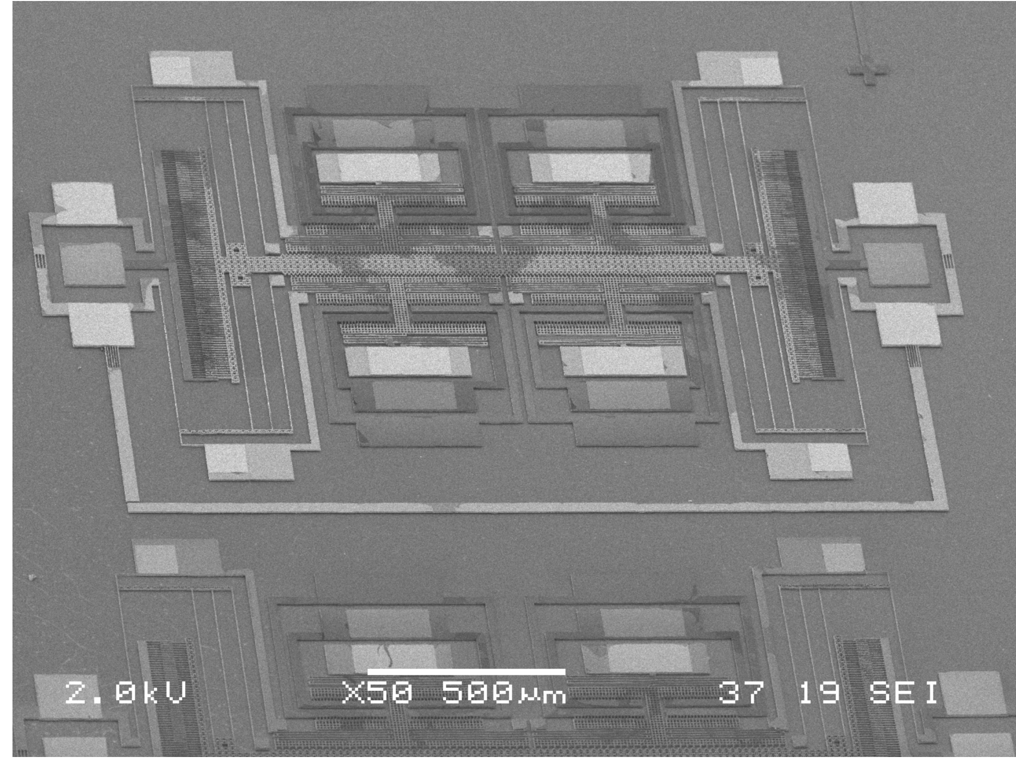

Fig. A2 - 3: SEM picture giving an overview of the device given in Fig. A2 - 2

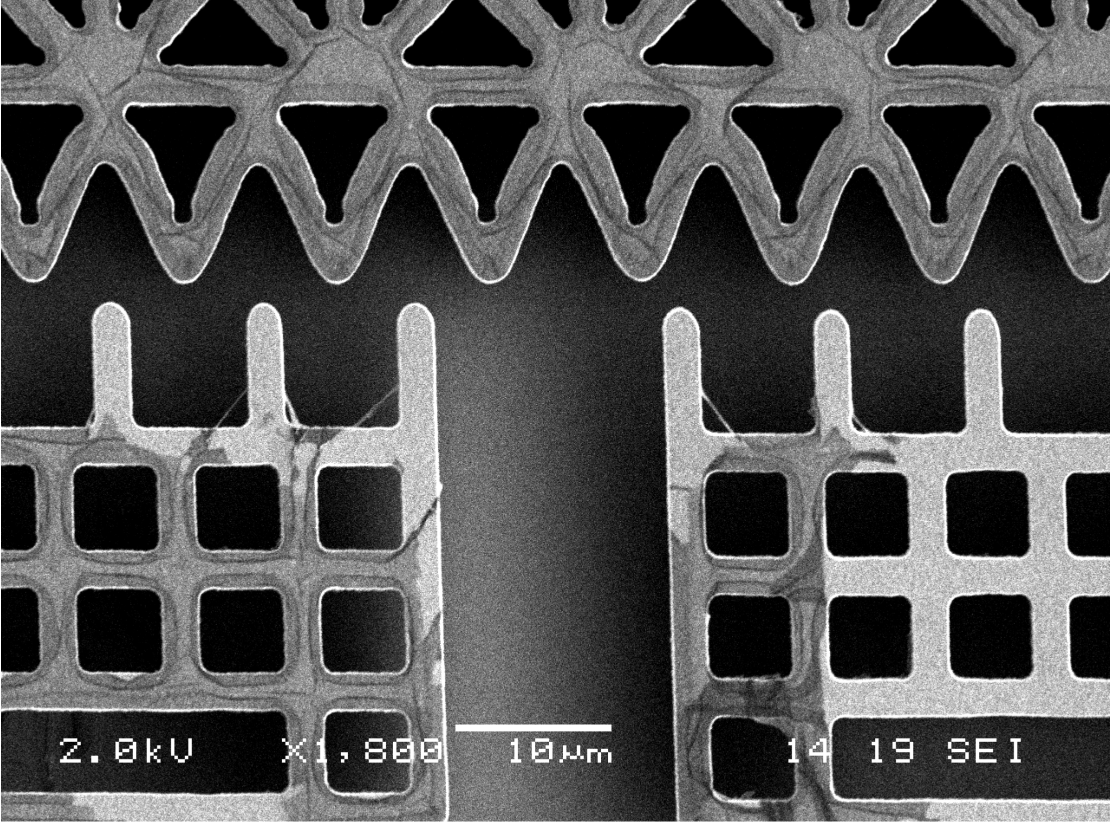

Fig. A2 - 4: SEM picture of the poly device given in Fig. A2 - 3, shows the (in) accuracy sine-slider pattern and the fingers on the sense-structure. The accuracy of the geometry functions is determined by the complete processing sequence, mask design, litho, plasma etching. Also important is the spatial offset between the sense-structures which should be P/4. A small process residue is noticeable, maybe photo resist, but not of importance here.

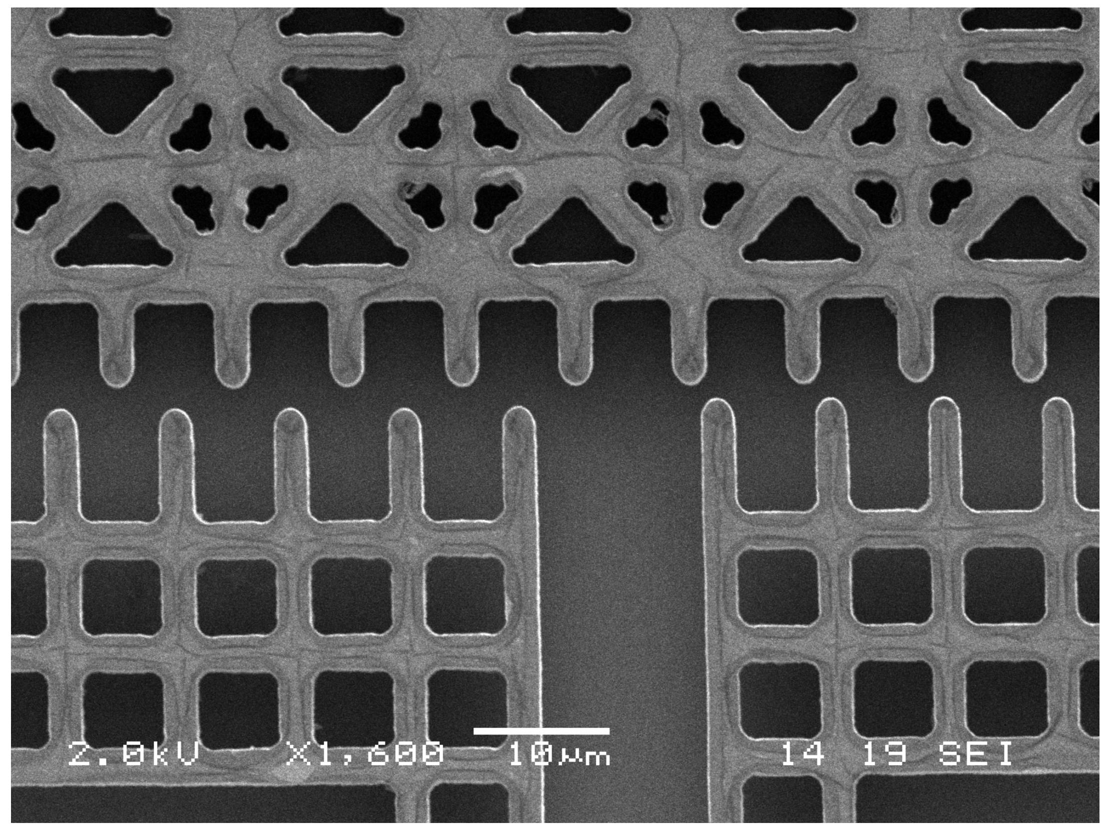

Fig. A2 - 5: SEM picture of poly-device showing the rectangular-rectangular geometry combination with period P = 8 µm. The spatial offset should be P/4 for accurate quadrature position detection. More analysis and measurements will determine the actual offset and its influence on the position measurement accuracy.

2.3 TWIN process: design SinP10

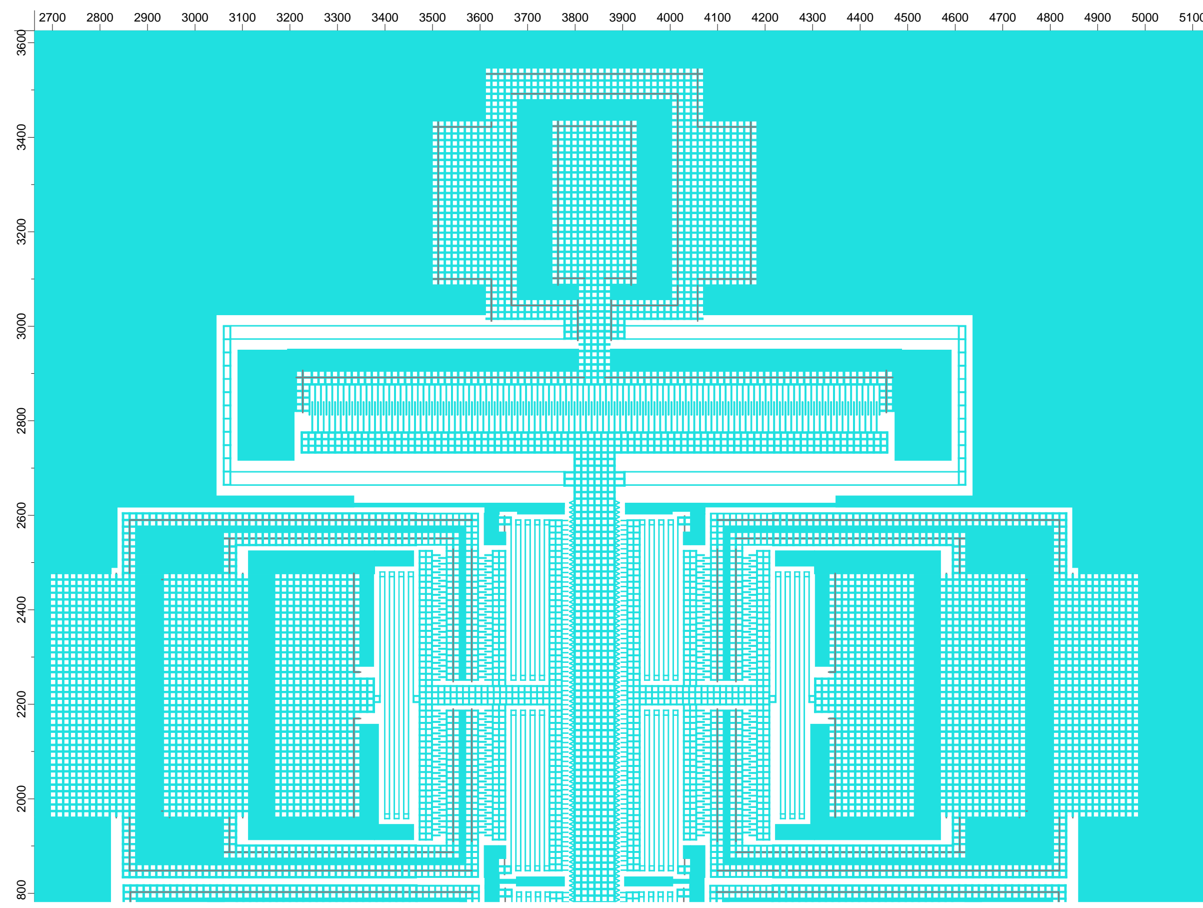

Fig. A2 - 6: Mask lay-out for a device made with the TWIN process

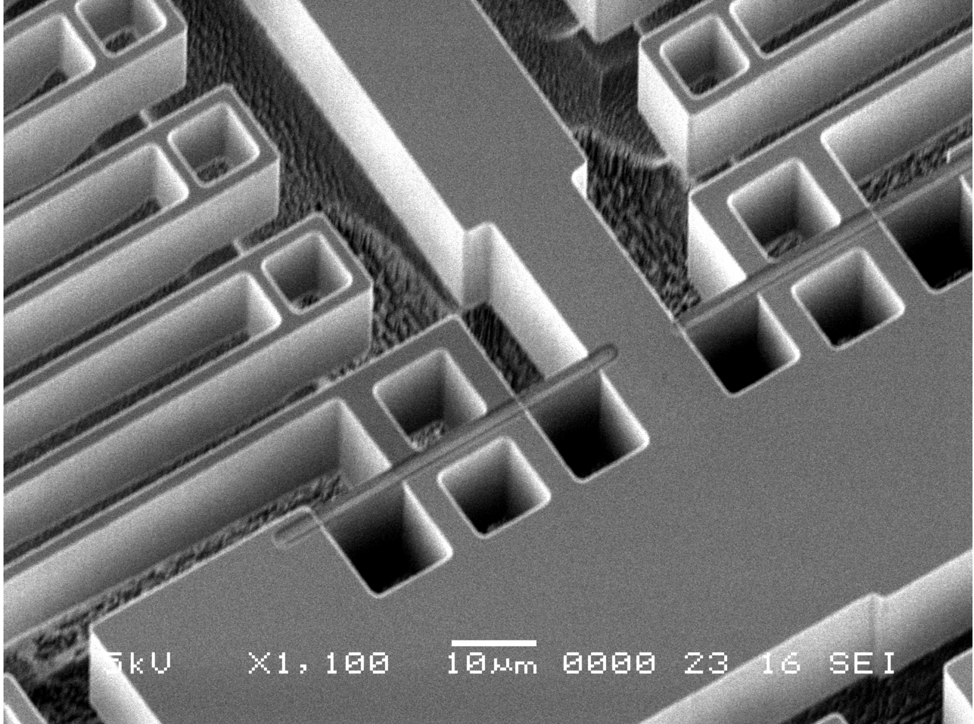

Fig. A2 - 7: SEM picture showing the SiN trench isolation which electrically isolates the moving parts of the sense-actuators from the parts connected to the substrate (foreground).

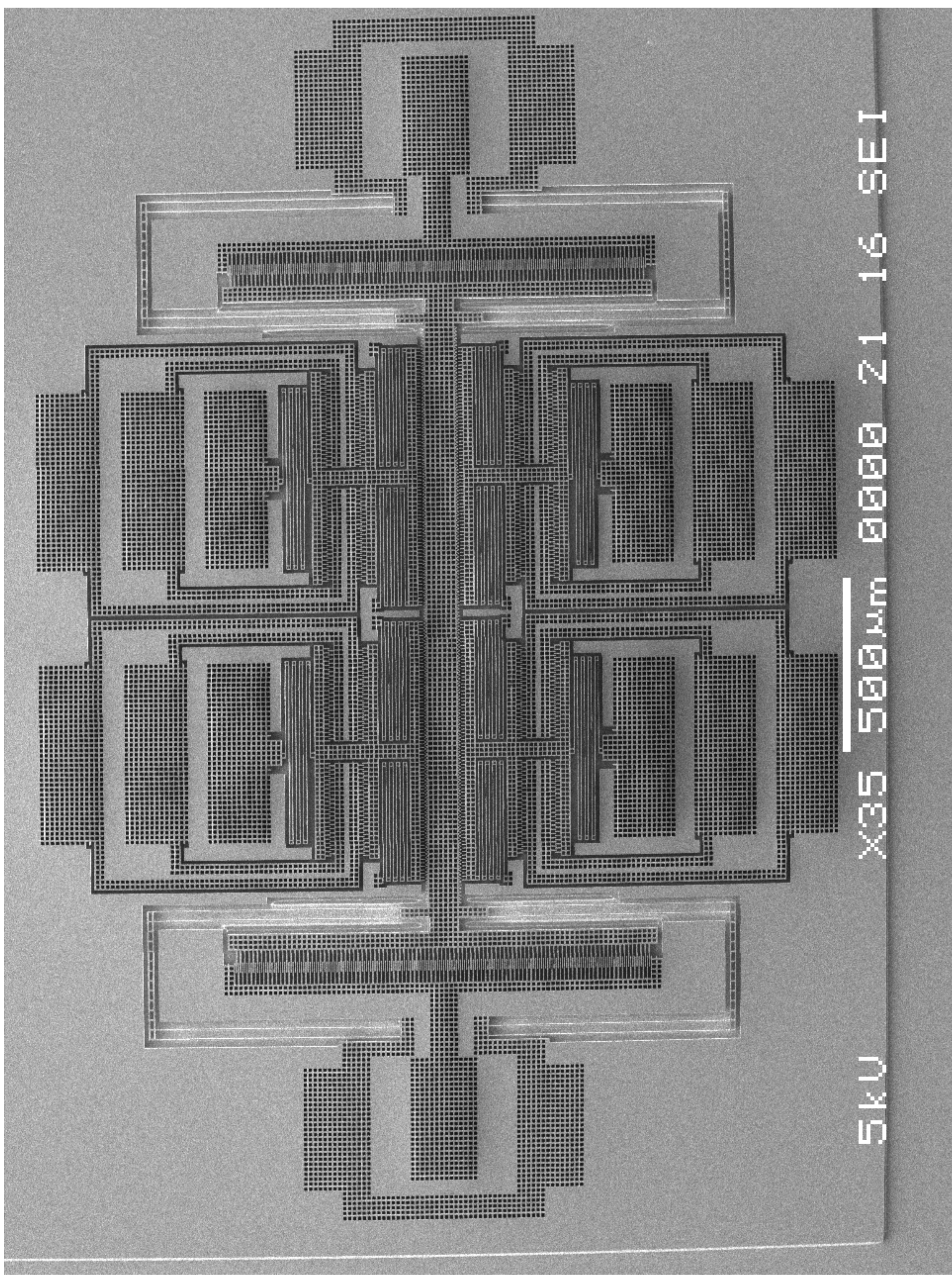

Fig. A2 - 8: SEM picture of a TWIN-process device

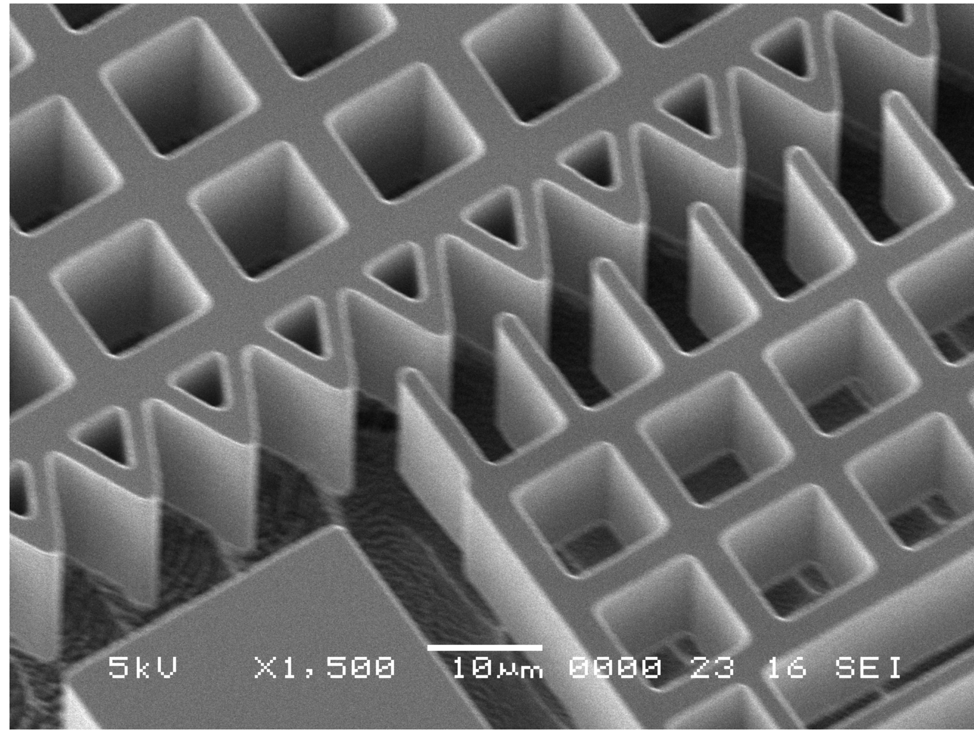

Fig. A2 - 9: TWIN process Triangular slider pattern with period P = 10 µm

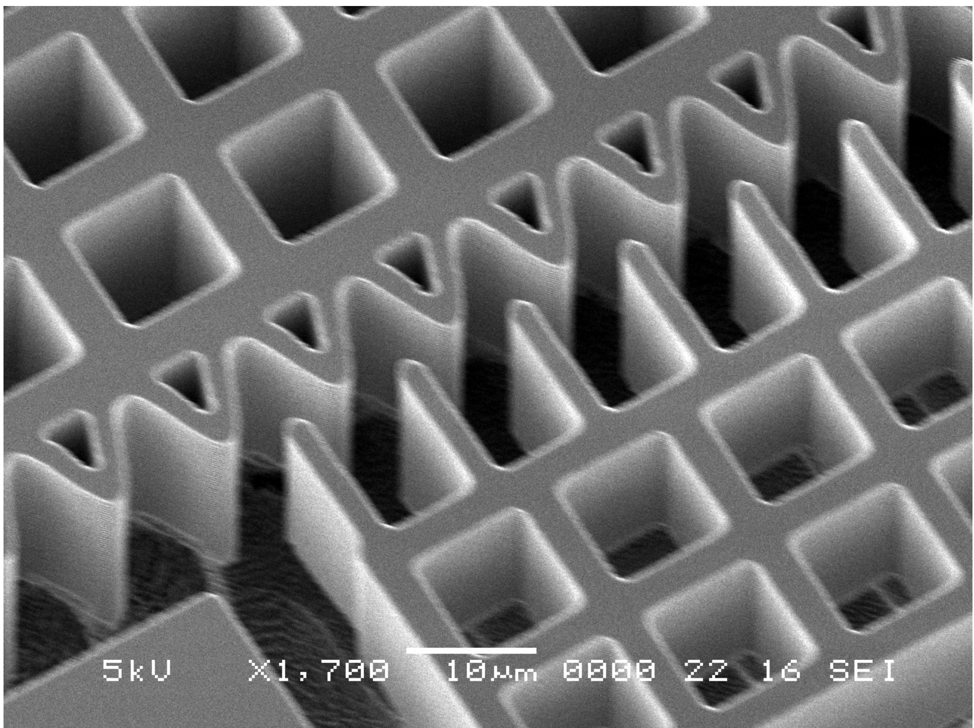

Fig. A2 - 10: Twin process Sinusoidal slider pattern with period P = 10 µm

2.4 *Design calculations*

a) Clamped beam b) Clamped - Guided beam c) Single Folded beam d) clamped-clamped beam

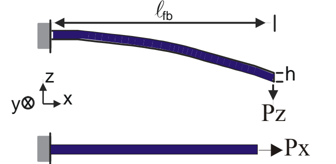

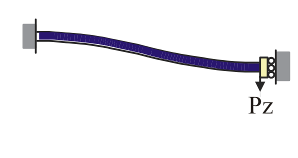

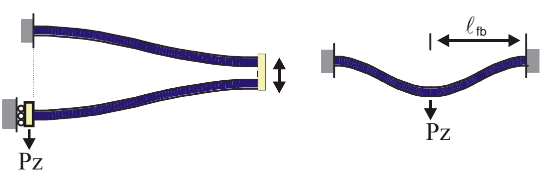

Moment of inertia: $Iy = \frac{wh^3}{12}$ $Iz = \frac{hw^3}{12}$

$$k_{x,single} = \frac{E\,w\,h}{lfb} \qquad k_{x,double} = k_{x,single} \qquad k_{x,\ single\ folded} = \tfrac{1}{2}\,k_{x,double} \qquad k_{x,clamp\text{-}clamp} = 2\,k_{x,double}$$

$$k_{y,single} = \frac{3\,E\,Iz}{lfb^3} = \frac{E\,h\,w^3}{4 \cdot lfb^3} \qquad k_{y,double} = 4\,k_{y,single} = \frac{12\,E\,Iz}{lfb^3} \qquad k_{y,\ single\ folded} = \tfrac{1}{2}\,k_{y,double} \qquad k_{y,clamp\text{-}clamp} = 2\,k_{y,double}$$

$$k_{z,single} = \frac{3\,E\,Iy}{lfb^3} = \frac{E\,w\,h^3}{4 \cdot lfb^3} \qquad k_{z,double} = 4\,k_{z,single} = \frac{12\,E\,Iy}{lfb^3} \qquad k_{z,\ single\ folded} = \tfrac{1}{2}\,k_{z,double} \qquad k_{z,clamp\text{-}clamp} = 2\,k_{z,double}$$

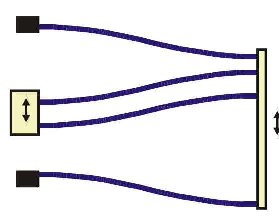

=

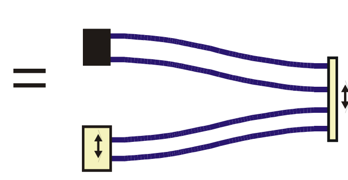

$$k_x = 2\,k_{x,single\ folded}$$

$$k_y = 2\,k_{y,single\ folded}$$

$$k_z = 2\,k_{z,single\ folded}$$

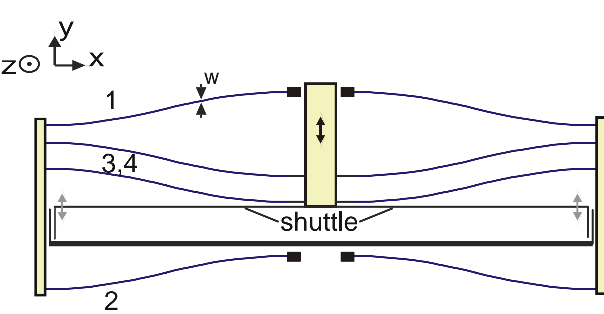

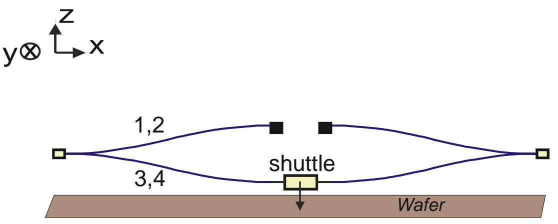

$$k_{x,\ folded\ flexure} = 4\,k_{x,single\ folded\ beam} = 2\,k_{x,single} = \frac{E\,h\,w^3}{2 \cdot lfb^3}$$

$$k_{y,\ folded\ flexure} = 4\,k_{y,single\ folded\ beam} = 8\,k_{y,single} = \frac{2 \cdot E\,hw^3}{lfb^3}$$

$$k_{z,\ folded\ flexure} = 4\,k_{z,single\ folded\ beam} = 8\,k_{z,single} = \frac{2 \cdot Ewh^3}{lfb^3}$$

Some formulas for stiffness calculations for a folded flexure design.

Calculation of Energy, Force and capacitance for a comb-drive structure with folded flexure

Co-energy

$$WL := (x, u) \rightarrow -\frac{1}{2}\,\mathrm{C}(x)\,u^2 + \frac{1}{2}\,ky\,x^2$$

External Force for equilibrium:

$$Fxt_scd := -\frac{1}{2}\left(\frac{\partial}{\partial y}\,\mathrm{C}(y)\right)u^2 + ky\,y$$

Comb-Capacitance with number of rotor fingers n, dielectric constant e_0, initial overlap l_o, gap d, height h,

$$C := y \rightarrow 2\,\frac{n\,e_0\,h\,(y + lo)}{d}$$

Displacement of comb-drive

$$Y := \frac{n\,e_0\,h\,u^2}{d\,ky}$$

Voor n= 100, e0 =8.854e-12, d=2 μm, $k_y = 2 \cdot k_{y,\text{folded flex}}$,E = 170 e9, l_{fb} = 500 μm, w = 2 μm
For two comb-drives in pull-pull $K_{[u]} = 2 * k_{[u],\text{ single folded}}$ e.g. $K_y = 2\,k_{y,\text{ single folded}}$

$$K_dcd := \left[4\,\frac{E\,w\,h}{lfb},\ 4\,\frac{E\,h\,w^3}{lfb^3},\ 4\,\frac{E\,w\,h^3}{lfb^3}\right]$$

$$[\,12800.00000,\ .2048000000,\ 1.280000000\,] \quad \text{N/m}$$

Displacement as function of u^2

$$Y2 := .1017233456\ 10^{-7}\,u^2$$

Voor u =37 V

$$y_37V := 24.06400014 \quad \mu\text{m}$$

Mass calculation

Sliderbeam element

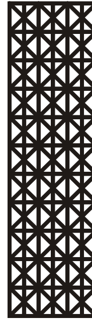

Single truss element $\ell_{tbe}=16$

2, 16, 16, 2

k^{th} kolumn element rotorbeam

2x ($\ell_{tbe}=16$) + 2x (ℓ_{tbe}-2=14) + 2x ($\sqrt{2}$ x ℓ_{tbe} -2=19.8)

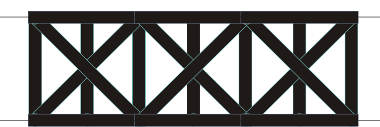

n^{th} row element shuttlebeam

7x (ℓ_{tbe}-2=14) + 6x ($\sqrt{2}$ x ℓ_{tbe} -2=19.8) + 50

```
> rho_Si:=2.33*10^3;
```

$$rho_Si := 2330.00$$

Rotorbeam van single comb-drive

```
> Mrotorbeam:=subs(h=5,51*Mste);
```

$$Mrotorbeam := .1183451736\ 10^{-9}$$

```
> Mrotorfingers:=subs(h=5,98*(62*2)*h*1e-18);
```

$$Mrotorfingers := .60760\ 10^{-13}$$

```
> Mrotorfingers/Mrotorbeam;Mrotor:=Mrotorbeam+Mrotorfingers;
```

$$.0005134134173$$

$$Mrotor := .1184059336\ 10^{-9}$$

```
> A_n:=1*(50*2) + 7 * (14 * 2) + 6 * (1.414 * 15 * 2):
```

Lengte of slider from rotor to rotor beam / height of each row = n°. of rows

```
> Lslider:=1552:Wslider:=50:
```

For the connections of flexurebeams ot the slider, adds another 8 rows:

```
> n_row:=8+Lslider/16;
```

$$n_row := 105$$

```
> vol_n:=A_n*n_row*h*1e-18;
```

$$vol_n := .57804600\ 10^{-13}\ h$$

```
> Mslider:=subs(h=5,rho_Si*vol_n);#[Kg]
```

$$Mslider := .6734235900\ 10^{-9}$$

```
> Msolslider:=subs(h=5,rho_Si*h*(Lslider)*Wslider*1e-8);
> ratio of mass =Mslider/Msolslider;
```

$$Msolslider := .9040400000\ 10^{-9}$$

$$Verhouding = .7449046392$$, so 75 %

```
> Mrotor/Mslider;# mass 1 rotor scd
```

$$.1758268278$$

```
> Mdcd:=2*Mrotor + Mslider;
```

$$Mdcd := .9102354572\ 10^{-9}$$

Resonance frequencies for n= 100, e0 =8.854e-12, d=2 µm, $k_y = 2 \cdot k_{y,\text{folded flex}}$,E = 170 e9, l_{fb} = 500 µm, w = 2 µm :

$$fres := \left[.3183098861 \sqrt{\frac{E\,w\,h}{lfb\,M}}, .3183098861 \sqrt{\frac{E\,h\,w^3}{lfb^3\,M}}, .3183098861 \sqrt{\frac{E\,w\,h^3}{lfb^3\,M}} \right]$$

$$fres1 := [596826.6970, 2387.306789, 5968.266970]$$ [Hz]

And for w=1.9 µm

$$fres1 := [581714.7074, 2210.515889, 5817.147074]$$

Side pull-in voltage and displacement taken from Legtenberg:
Square voltage u_{si}^2 for single comb-drive U_{si_scd}:

$$usi := \frac{\left(-\frac{1}{2}\, y0\, ky + \frac{1}{2}\sqrt{y0^2\, ky^2 + 2\, kx\, ky\, d^2}\right) d}{h\, e_0\, n}$$

side-pull-in displacement :

$$ysi_rob := -\frac{1}{2}\, y0 + \frac{1}{2}\, d \sqrt{\frac{y0^2}{d^2} + \frac{2\, kx}{ky}}$$

For double comb-drive in pull-pull $U_{si} = (\sqrt{2})\cdot U_{si_dcd}$:

$$Usi_dcd := 2\, \frac{E\, w^3\, d^2 \left(-\frac{y0}{d} + \sqrt{\frac{y0^2}{d^2} + \frac{2\, lfb^2}{w^2}}\right)}{lfb^3\, e_0\, n}$$

$$Usi_dcd := 177.0690677$$

$$Usi_scd := 125.2067386$$

$$ysi_dcd := -\frac{1}{2}\, y0 + \frac{1}{2}\, d \sqrt{\frac{y0^2}{d^2} + \frac{2\, lfb^2}{w^2}}$$

With $y_0 = 30$ μm, $d = 2$ μm, $l_{fb} = 500$ μm, $w = 2$ μm:

$$ysi_r1 := 338.8714456$$

The current k_x is only valid for $y = 0$, so zero displacement. One should compensate k_x with the formula given by Legtenberg:
The stiffness in x-direction decreases for increasing y-displacement:

$$Kx = \frac{300 \cdot E \cdot I}{3 \cdot L \cdot \delta y^2}$$

The total spring constant in x-direction is a series connection $K_x(y=0)$ and k_x ($y \neq 0$), but u_{si} becomes implicit function, not straightforward to solve.

2.5 Process outline surface-micromachined integrated capacitive position sensor for microactuators

Step	Process		Comment
1	Substrate selection - Silicon <100> OSP (low resist.) (#subs008)	CR112B / Wafer Storage Cupboard Supplier: Orientation: <100> Diameter: 100mm Thickness: 475µm Polished: Single side Resistivity: 0.0015-0.019Ωcm Type: p	Process data for fabrication process with Cr-Pt contact pads
2	Cleaning Standard (#clean003)	CR112B / Wet-Bench 3-2 HNO_3 (100%) Selectipur: MERCK 100453 HNO_3 (69%) VLSI: MERCK 116445 • Beaker 1: fumic HNO_3 (100%), 5min • Beaker 2: fumic HNO_3 (100%), 5min • Quick Dump Rinse <0.1µS • Beaker 3: boiling (95°C) HNO_3 (69%), 10min • Quick Dump Rinse <0.1µS • Spin drying	
3	Wet Oxidation (WOX) at 1150°C of Silicon (#depo014)	CR112B / Furnace B2 Standby temperature: 800°C Check water level of bubbler • Program: WOX-1150 • Temp.: 1150°C • Gas: $H_2O + N_2$ (Bubbler)	3.2 micron, 30 hr
4	Micro Balance Measurement (#char006)	CR125C / Satortius Micro Balance	(G1) 8.50820 gram
5	Cleaning Standard (#clean003)	CR112B / Wet-Bench 3-2 HNO_3 (100%) Selectipur: MERCK 100453 HNO_3 (69%) VLSI: MERCK 116445 • Beaker 1: fumic HNO_3 (100%), 5min • Beaker 2: fumic HNO_3 (100%), 5min • Quick Dump Rinse <0.1µS • Beaker 3: boiling (95°C) HNO_3 (69%), 10min • Quick Dump Rinse <0.1µS • Spin drying	
6	Etching HF (1%) Native Oxide (#etch027)	CR112B / Wet-Bench 3-3 HF (1%) VLSI: MERCK 112629.500 • Etch time: >1min • Quick Dump Rinse <0.1µS • Spin drying	

Step	Process		Comment
7	LPCVD Poly Si – 590°C (#depo005)	CR125C / Tempress LPCVD/HC Tube: G1 SiH_4 flow: 50sccm temperature: 590°C pressure: 250mTorr • program: Poly590C deposition rate: 5.6-6.1 nm/min	Thickness 5 μm Time 16 hr
Step	**Process**		**Comment**
8	Micro Balance Measurement (#char006)	CR125C / Satotius Micro Balance	G2: 8.63029 gram, Thickness: 4.7 micron Poly-Si-layer 4.55 nm/min
9	Cleaning Standard (#clean003)	CR112B / Wet-Bench 3-2 HNO_3 (100%) Selectipur: MERCK 100453 HNO_3 (69%) VLSI: MERCK 116445 • Beaker 1: fumic HNO_3 (100%), 5min • Beaker 2: fumic HNO_3 (100%), 5min • Quick Dump Rinse <0.1μS • Beaker 3: boiling (95°C) HNO_3 (69%), 10min • Quick Dump Rinse <0.1μS • Spin drying	
10	Etching HF (1%) Native Oxide (#etch027)	CR112B / Wet-Bench 3-3 HF (1%) VLSI: MERCK 112629.500 • Etch time: >1min • Quick Dump Rinse <0.1μS • Spin drying	
11	Solid Source Diffusion (SSD) of Boron at 1050°C (#dopi004)	CR112B / Furnace B1 Standby temperature: 700°C • Program: SSD-1050 • Temp.: 1050°C • Gas N_2: 3.80 SLM • Gas O_2: 0.20 SLM • Time:	3hr soak
12	Etching BHF (1:7) B_2O_5 (#etch026)	CR112B / Wet-Bench 3-3 NH_4F/HF (1:7) VLSI: MERCK 101171.2500 • Etch time: 5min • Quick Dump Rinse <0.1μS • Spin drying	10 min, wafer should be white, and no color rings should be present.
13	Dry Oxidation (DOX) at 800°C of Silicon (#depo026)	CR112B / Furnace B3 Standby temperature: 800°C • Program: DOX-800 • Temp.: 800°C • Gas: O_2 • Flow: 4l/min	30 min

Step	Process		Comment
14	Etching BHF (1:7) SiO_2 (#etch024)	CR112B / Wet-Bench 3-3 NH_4F/HF (1:7) VLSI: MERCK 101171.2500 • Quick Dump Rinse <0.1µS • Spin drying Etchrate thermal SiO_2 = 60-80nm/min Etchrate PECVD SiO_2 = 125/nm/min Etchrate TEOS SiO_2 = 180/nm/min	Time 15 min, or till Hydrophobic surface is observed and the color of the poly-silicon surface should be white
15	Sheet Resistance measurement (#char009)	CR118B / Resistance Measurement Equipment	Value should be in the order of 1.024 10=3 ohm.cm
Step	**Process**		Comment
16	Cleaning Standard (#clean003)	CR112B / Wet-Bench 3-2 HNO_3 (100%) Selectipur: MERCK 100453 HNO_3 (69%) VLSI: MERCK 116445 • Beaker 1: fumic HNO_3 (100%), 5min • Beaker 2: fumic HNO_3 (100%), 5min • Quick Dump Rinse <0.1µS • Beaker 3: boiling (95°C) HNO_3 (69%), 10min • Quick Dump Rinse <0.1µS • Spin drying	
17	PECVD of SiO_2 (#depo009)	CR102A / Elektrotech PF310/340 • Electrode temp.: 300°C • SiH_4/N_2 flow: 200sccm • N_2O flow: 710sccm • pressure: 650mTorr • power: 60W LF Etchrate = 30nm/min	Capping for out diffusion of boron Thickness 1µm Time = 40 min
18	Cleaning Short (#clean002)	CR112B / Wet-Bench 3-2 HNO_3 (100%) Selectipur: MERCK 100453 • Beaker 1: HNO_3 (100%) 5min • Beaker 2: HNO_3 (100%) 5min • Quick Dump Rinse <0.1µS • Spin drying	
19	Annealing at 1100°C with N_2 for diffusion of B or P and annealing for Silicon-Silicon bonding (#anne006)	CR112B / Furnace B3 Standby temperature: 700°C • Program: ANN-1100-N2 • Temp.: 1100°C • Gas: N_2 • Flow: 1l/min • Ramp: 20°C/min	Tim 3hr To achieve uniform distribution of boron, load the wafers in afternoon and anneal during the night, a long anneal at 800 degrees is now also included

Step	Process		Comment
20	Etching BHF (1:7) SiO_2 (#etch024)	CR112B / Wet-Bench 3-3 NH_4F/HF (1:7) VLSI: MERCK 101171.2500 • Quick Dump Rinse <0.1µS • Spin drying Etchrate PECVD SiO_2 = 125/nm/min	Time 44 min Removal of capping layer, wafer surface was hydrophobic and showed a light color
21	Sheet Resistance measurement (#char009)	CR118B / Resistance Measurement Equipment	5.4 ohm/□, n=4
22	Cleaning Standard (#clean003)	CR112B / Wet-Bench 3-2 HNO_3 (100%) Selectipur: MERCK 100453 HNO_3 (69%) VLSI: MERCK 116445 • Beaker 1: fumic HNO_3 (100%), 5min • Beaker 2: fumic HNO_3 (100%), 5min • Quick Dump Rinse <0.1µS • Beaker 3: boiling (95°C) HNO_3 (69%), 10min • Quick Dump Rinse <0.1µS • Spin drying	
Step	**Process**		**Comment**
23	Lithography - Priming (liquid) (#lith001)	CR112B / Headway Spinner HexaMethylDiSilazane (HMDS) • Dehydration bake (120°C): 5min • Spinning speed: 4000rpm • Spinning time: 20s	
24	Lithography - Coating Olin907-17 (Headway) (#lith005)	CR112B / Headway Spinner Olin 907-17 • Spinning speed: 4000rpm • Spinning time: 20s • Prebake (95°C): 90s	
25	Lithography - Alignment & Exposure Olin 907-17 (Karl Süss) (#lith018)	CR117B / Karl Süss Mask aligner MA55 Karl Süss MA55 • Exposure Time: x sec Hotplate 120°C (CR112B or CR117B)) • After Exposure Bake (120°C): 60sec	Use mask with bond pads Time 6.0 sec
26	Lithography - Development Olin Resist (#lith011)	CR112B / Wet-Bench 11 Developer: OPD4262 Hotplate 120°C (CR112B or CR117B)) • After Exposure Bake (120°C): 60sec Development: • Time: 30sec in Beaker 1 • Time: 15-30sec in Beaker 2 • Quick Dump Rinse <0.1µS • Spin drying	65 sec
27	Optical microcopic inspection-lithography (#char001)	CR112B / Nikon Microscope	

Step	Process		Comment
28	Etching HF (1%) Native Oxide (#etch027)	CR112B / Wet-Bench 3-3 HF (1%) VLSI: MERCK 112629.500 • Etch time: >1min • Quick Dump Rinse <0.1µS • Spin drying	
29	Sputtering of Cr (#depo017)	CR106A / Sputterke Cr Target • Electrode temp.: water cooled electrode • Ar flow: 45% = 90sccm • Base pressure: 6.7.10-6 mbar • Sputter pressure: 5.0e-3mbar • power: 200W Deposition rate = 10nm/min	10 nm
30	Sputtering of Pt (#depo018)	CR106A / Sputterke Pt Target • Electrode temp.: water cooled electrode • Ar flow: 45% = 90sccm • Base pressure: 6.7 e-6mbar • Sputter pressure: 5.0e-3mbar • power: 200W Deposition rate = 10nm/min	100 nm

Step	**Process**		**Comment**
31	Lift-off Olin-PR in Acetone (#etch042)	CR116B / Wet-Bench 2 Acetone VLSI: MERCK 100038 Isopropanol VLSI: MERCK 107038 • Acetone Beaker 1: >20min • Quick Dump Rinse, single run • Acetone Beaker 2: >5min • Isopropanol Beaker 3 • Spin drying Optionally use ultrasonic bath to enhance lift-off	
32	Optical microscopic inspection-Lithography (#char001)	CR112B / Nikon Microscope	When the lift-off is not yet completed, continue again with the lift-off process.
33	Lithography - Priming (liquid) (#lith001)	CR112B / Headway Spinner HexaMethylDiSilazane (HMDS) • Dehydration bake (120°C): 5min • Spinning speed: 4000rpm • Spinning time: 20s	
34	Lithography - Coating Olin907-17 (Headway) (#lith005)	CR112B / Headway Spinner Olin 907-17 • Spinning speed: 4000rpm • Spinning time: 20s • Prebake (95°C): 90s	

35	Lithography - Alignment & Exposure Olin 907-17 (Karl Süss) (#lith018)	CR117B / Karl Süss Mask aligner MA55 Karl Süss MA55 • Exposure Time: 5.7 sec Hotplate 120°C (CR112B or CR117B)) • After Exposure Bake (120°C): 60sec	Use mask combdrive new design date 12th of June
36	Lithography - Development Olin Resist (#lith011)	CR112B / Wet-Bench 11 Developer: OPD4262 Hotplate 120°C (CR112B or CR117B)) • After Exposure Bake (120°C): 60sec Development: • Time: 30sec in Beaker 1 • Time: 15-30sec in Beaker 2 • Quick Dump Rinse <0.1µS • Spin drying	65 sec
37	Optical microscopic inspection - Lithography (#char001)	CR112B / Nikon Microscope	
38	Lithography - Postbake standard (#lith009)	CR112B / Hotplate 120°C • Time: 30min	

Step	**Process**		**Comment**
39	Plasma etching of Silicon - Bosch standard (Plasma Therm) (#etch018)	CR102A / Plasma Therm SLR 770 Parameters are valid for 100mm wafer Etchrate/cycle are guidelines and depend on loading area	Apply a test run first, Guideline for 5 micron polysilicon, 50 cycles are needed Strip poly-silicon also at the backside of the wafer

Parameters	Deposition step	Removal step	Etch step
C_4F_8 [sccm]	70	2	2
SF_6 [sccm]	2	50	50
Ar [sccm]	80	80	80
t [s]	2	2	6
ICP [W]	950	950	950
CCP [W]	1.0	14.0	1.5
V_{DC} [V]	16	70	2.1
p [mTorr]	12	12	13
Temp. Chiller [°C]	25	25	25
Temp. LN_2 [°C]	20	20	20

Material	Etch [nm/cycle]
Resist Olin907	5-6
Poly-Silicon 590°C (undoped)	150
Poly-Silicon 590°C (SSD Boron doped)	80-110

Step	Process		Comment
40	Plasma etching of Quartz - SF_6 (Plasma Therm) (#etch019)	CR102A / Plasma Therm SLR 770 Parameters are valid for 100mm wafer Use quartz cover plates for long runs (>>30min) to avoid resputtering of ALOx particles	Strip THOX on backside of wafer, Time :3.2 micron/0.2 = 16 min

Parameters	Value
SF_6 [sccm]	30
Ar [sccm]	60
He-backside cooling [sccm]	9
He-backside cooling [Torr]	6
ICP [W]	1200
CCP [W]	18
V_{DC} [V]	114
p [mTorr]	5
Temp. Chiller [°C]	25
Temp. LN_2 [°C]	20
Material	Etch [nm/min]
Fused silica (use Cr or Ni as mask material)	200

Step	Process		Comment
41	Optical microcopic inspection (#char002)	CR112B / Nikon Microscope CR117B / Olympus Microscope CR102B / Olympus Microscope	
42	Stripping of polymers in HNO_3 user made (#lith014)	CR116B / Wet-Bench 2 HNO_3 (100%) Selectipur: MERCK 100453 • Beaker 1: HNO_3 (100%) 20min • Quick Dump Rinse <0.1µS • Spin drying	Removal of PR
43	Etching HF (1%) Native Oxide (#etch027)	CR112B / Wet-Bench 3-3 HF (1%) VLSI: MERCK 112629.500 • Etch time: >1min • Quick Dump Rinse <0.1µS • Spin drying	
44	Sputtering of Cr (#depo017)	CR106A / Sputterke Cr Target • Electrode temp.: water cooled electrode • Ar flow: 45% = 90sccm • Base pressure: 6.7.10-6 mbar • Sputter pressure: 5.0e-3mbar • power: 200W Depositionrate = 10nm/min	Backside 10 nm Time 12 sec

45	Sputtering of Pt (#depo018)	CR106A / Sputterke Pt Target • Electrode temp.: water cooled electrode • Ar flow: 45% = 90sccm • Base pressure: 6.7.10-6 mbar • Sputter pressure: 5.0e-3mbar • power: 200W Deposition rate = 10nm/min	Backside 100 nm, Time 10 min
46	Lithography - Priming (liquid) (#lith001)	CR112B / Headway Spinner HexaMethylDiSilazane (HMDS) • Dehydration bake (120°C): 5min • Spinning speed: 4000rpm • Spinning time: 20s	Front side (device)
47	Lithography - Coating Olin908-35) (#lith006)	CR112B / Headway Spinner Olin 908-35 • Spinning speed: 4000rpm • Spinning time: 20s • Prebake (95°C): 120s	4000 rpm, 40 sec
48	Lithography - Postbake standard (#lith009)	CR112B / Hotplate 120°C • Time: 30min	20 min
49	Dicing of a Silicon wafer (#back001)	CR128C / Disco DAD dicing saw	front-side dicing depth 200 micron

Step	**Process**		**Comment**
50	Stripping of polymers in HNO_3 user made (#lith014)	CR116B / Wet-Bench 2 HNO_3 (100%) Selectipur: MERCK 100453 • Beaker 1: HNO_3 (100%) 20min • Quick Dump Rinse <0.1µS • Spin drying	Time 20 min
51	Optical microcopic inspection - Lithography (#char001)	CR112B / Nikon Microscope	If wafer is not clean repeat HNO3 step !
52	Freeze drying (#etch001)	CR112B / Etching HF HF (50%): MERCK 100373.2500 IPA VLSI: MERCK 107038 NH_4F/HF: MERCK 101171.2500 Cyclohexan: MERCK 109666.1000 Parameters are valid for 4-inch wafers or smaller samples • 200 ml HF-50 % or NHF_4/HF 1:7 (choice of etchant is defined by design) • Rinse with 6 liters of DI-water, time 30 min • Dilute DI with 800 ml IPA, time 15 min • Transport sample in 200 ml IPA, time 30 min	BHF 1:7 time 70-75 min

		• Dilute IPA with 600 ml cyclo hexane, time 15 min • Transport sample in 100 % cylcohexane I, 200 ml, time 15 min • Transport sample in 100% cylcohexane II 200 ml, time 15 min • Freeze drying: 0.5 Bar dry nitrogen, electrode temperatures of –5°C • Total process time: 135 min, SLE time not included See related file:	
53	Optical microcopic inspection (#char002)	CR112B / Nikon Microscope CR117B / Olympus Microscope CR102B / Olympus Microscope	

2.6 Conduction measurement Chrome Platinum pads

With a Keithley Source Measurement Unit a voltage is applied to two different Cr-Platinum pads deposited on a highly doped Si-substrate and the current is measured. The maximum current is limited to ~100mA.

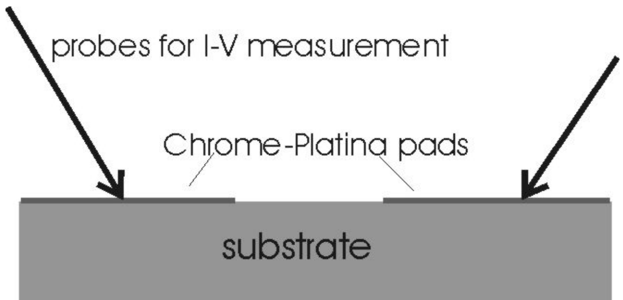

Fig. 20: I-V measurement of conduction of Cr-Pt pads and substrate.

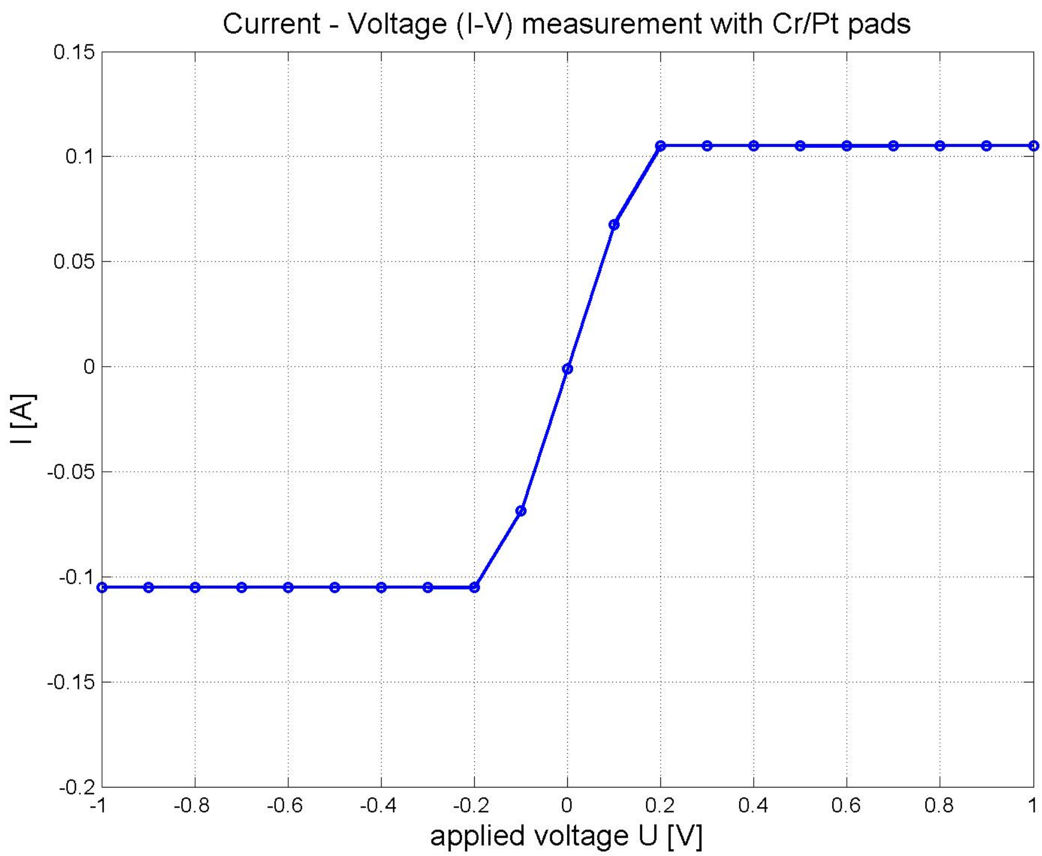

Fig. 21: Current – Voltage Measurement of Chrome – Platina pads on Si-wafer. The current is limited to ~ 100mA.

The conductance does not show any hysteresis and a resistance of about R ~ 1 Ω. Therefore, it is decided to neglect the possibility of a shottky diode effect. Combination of a metal contact and a semiconductor can give ohmic contact or a rectifying diode contact, depending on dotation of the semiconductor. More information can be found in literature, e.g. S.M. Sze, Semiconductor Devices: Physics and Technology, 2nd Edition, Publisher: Wiley; 2nd edition, ISBN: 0471333727

Appendix 3 Experiments and setup data

3.1 *Measurement setup and electronics*

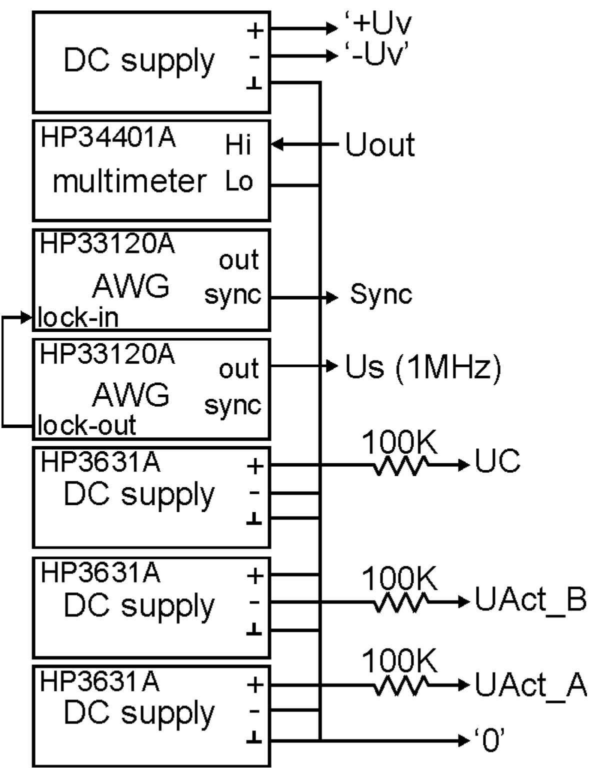

Fig.A3 - 1 : Equipment and interconnections used during the experiments for both open-loop DCM and closed-loop CCM modes

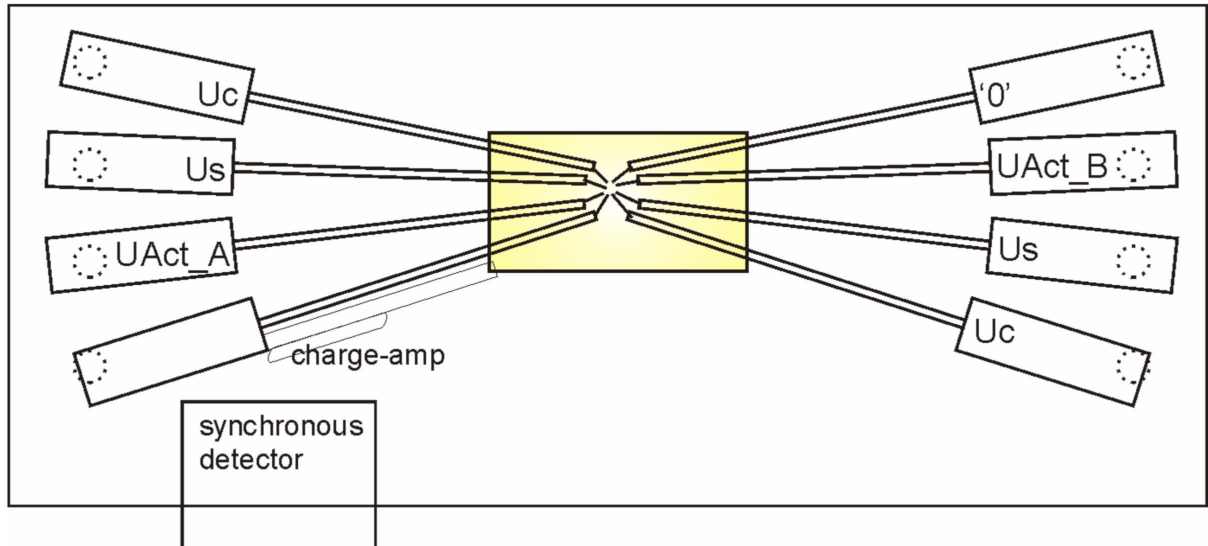

Fig.A3 - 2 :Top view schematic of microscope 'probe' table. The number of probe manipulators is limited to 8. The synchronous detector is positioned and fixed with tape as close as possible to the PCB for the charge-amp which is covered in aluminum-foil.

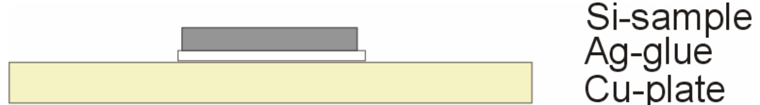

Fig.A3 - 3 : Cross-view of cupper-plate with Silicon sample glued on top with Silver-glue

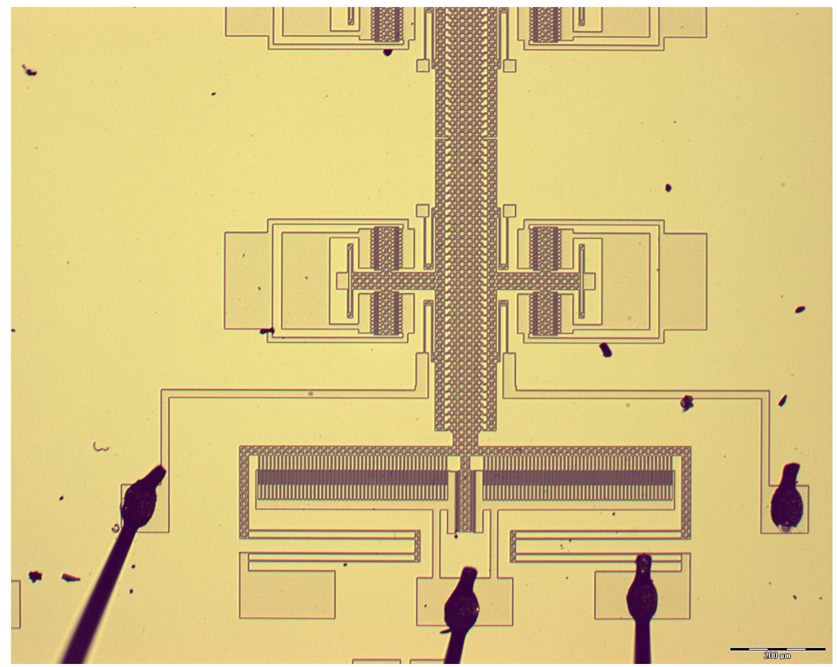

Fig.A3 - 4 : Example of wirebonded devices

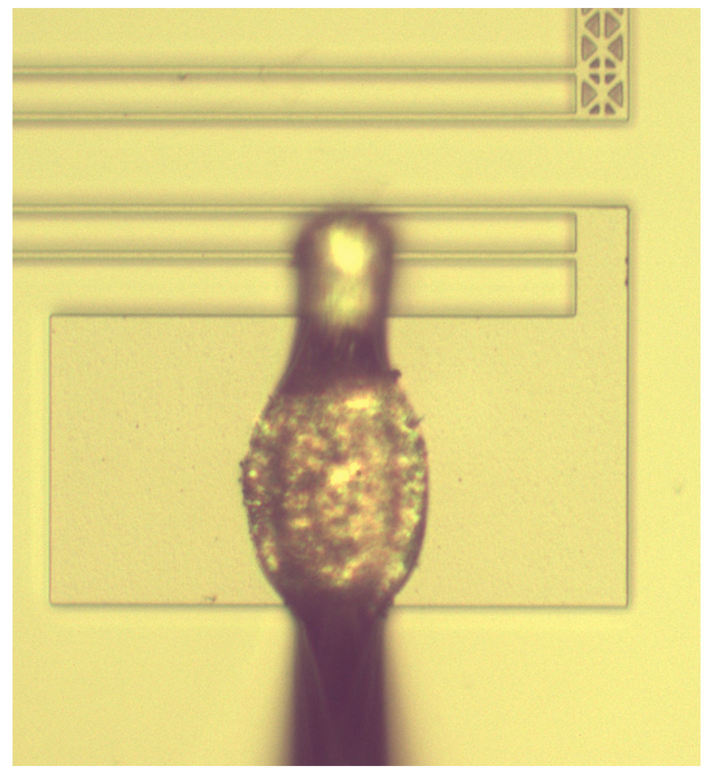

Fig.A3 - 5 :Close-up of wirebond on contact pad. The pads are a bit to small, area = 100 x 200 µm

The pads are taken small to minimize their capacitance : $C_{ep} = \varepsilon_0 \cdot \varepsilon_r \cdot A/d_{ox} = 5\varepsilon_o \cdot 100 \text{ x } 200\ \mu m^2 / 3\ \mu m \sim 300$ fF

3.2 measurement data Calibration

Measurement settings HP4194A analyzer :

f_{center} = 1 MHz + 10 Hz, SPAN = 10 Hz, 400 frequency points, Averaging 16x, Integration time = 'Medium' i.e. T_{int} = 20 msec, T_{BW} = 16 x T_{int} =320 msec.
Formula by HP from instrument manual for impedance measurement accuracy :
$|Z_1|$,mean = 140.284 KΩ, $Z_{std_1} = std(|Z_1|)$ = 6.61 Ω
$|Z_2|$,mean = 69.1469 KΩ, $Z_{std_2} = std(|Z_2|)$ = 1.79 Ω

Calculated for C1 and C2:

$C + \Delta C_{std}/2 = 1/(2\pi f\cdot|Z| - Z_{std}/2)$, $C - \Delta C_{std}/2 = 1/(2\pi f\cdot|Z| + Z_{std}/2)$
$C_1 + \Delta C_{std_1}/2$ = 1134.55 fF $C_1 - \Delta C_{std_1}/2$ = 1134.49 fF $\Delta C_{std_1}/2$ = 26.73 fF
$C_2 + \Delta C_{std_2}/2$ = 2301.72 fF $C_2 - \Delta C_{std_2}/2$ = 2301.66 fF $\Delta C_{std_2}/2$ = 29.79 fF

Settings HP34401A multimeter:
Fast-6 digits, averaging with 10 Power Line Cycles corresponds with T_{int} = 200 msec and an AC-filter was set to 3 Hz.
Formula HP34401A accuracy

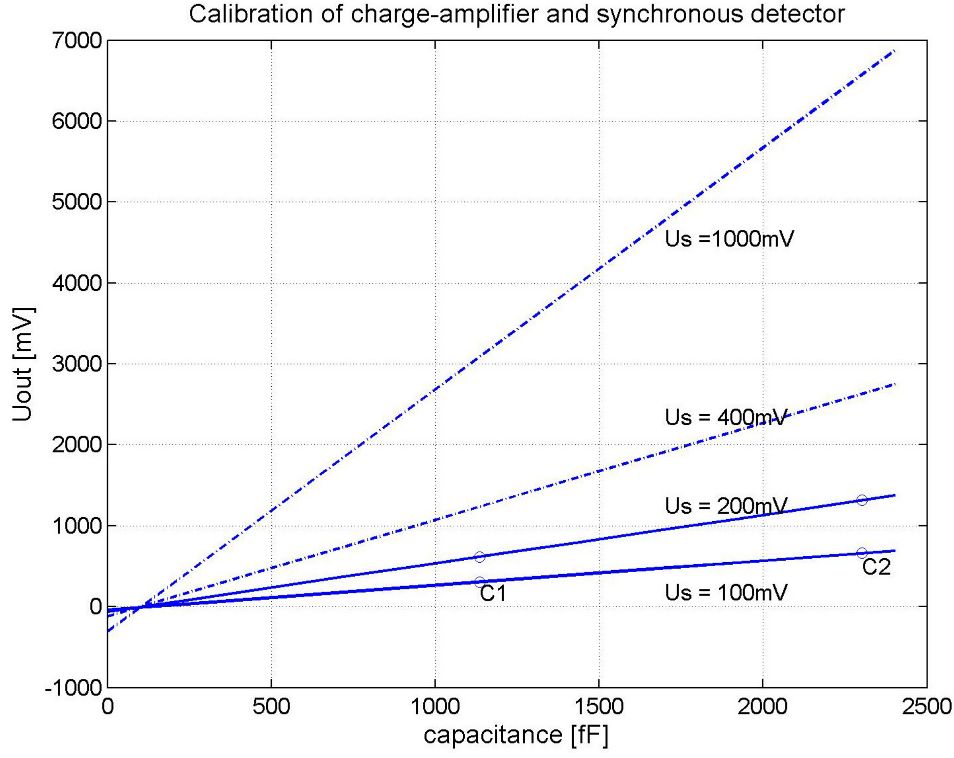

Fig.A3 - 6 : Calibration of measured output voltage Uout with capacitance for different signal levels U_s (1MHz). The dotted lines are extrapolated from the line with U_s =200mV.

3.3 Additional measurement results for ICMM

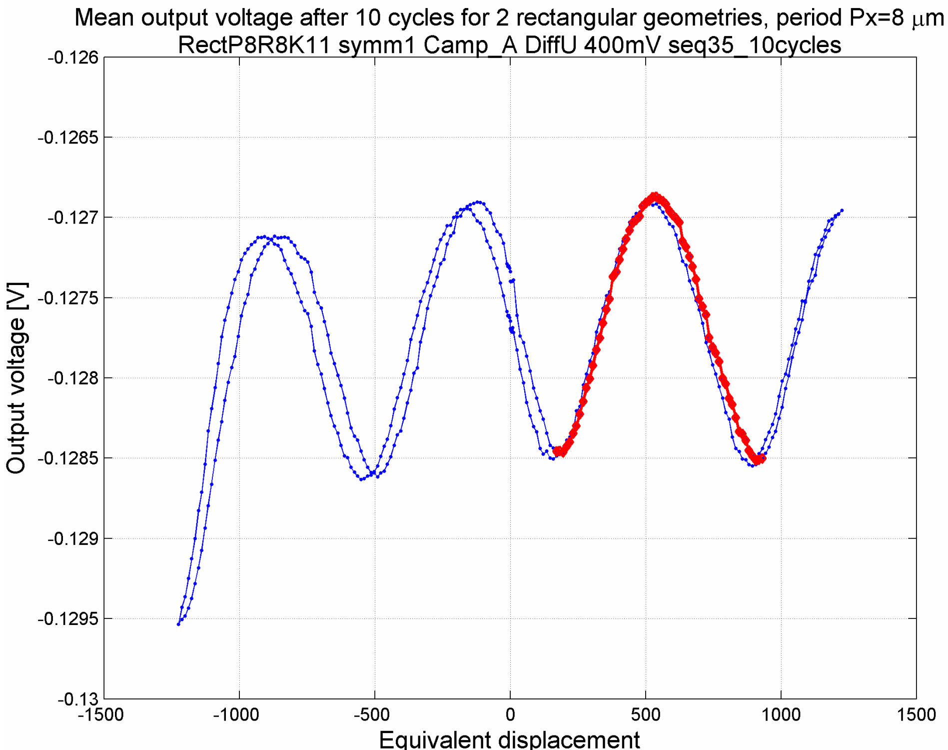

Fig.A3 - 7 : Result for Rectangular- Rectangular P8 geometry Poly-genration I)

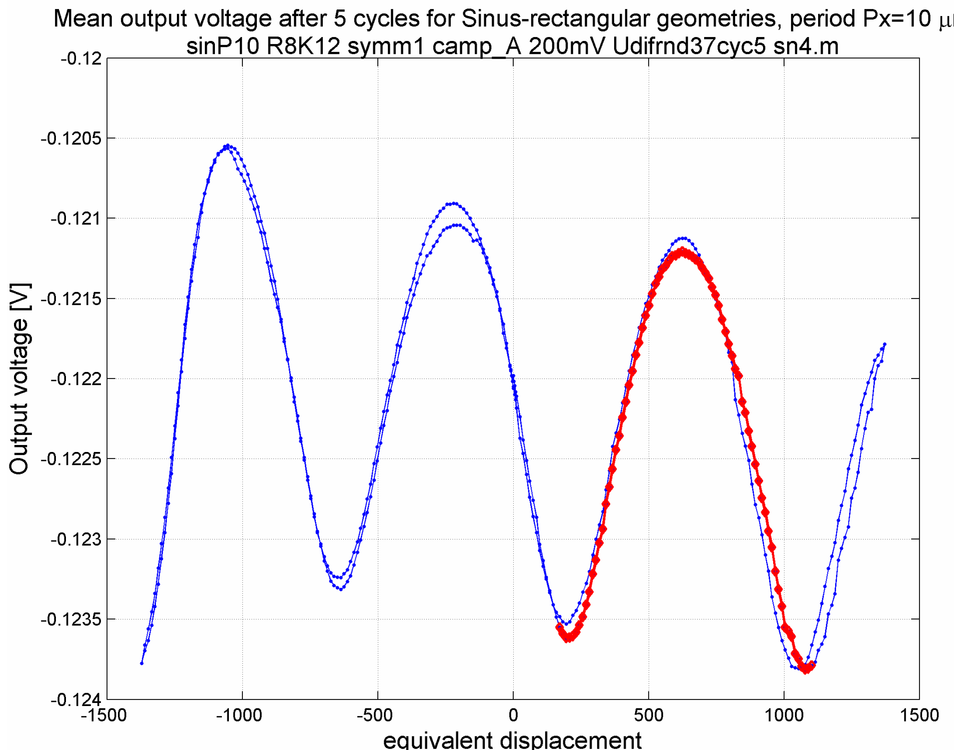

Fig.A3 - 8 : Out put voltage Uout for the SinP10 geometry with carrier voltage Us = 200 mV and pull-pull or differential actuation. For comparison, the Uout of SinP10 is multiplied by a factor 2x.

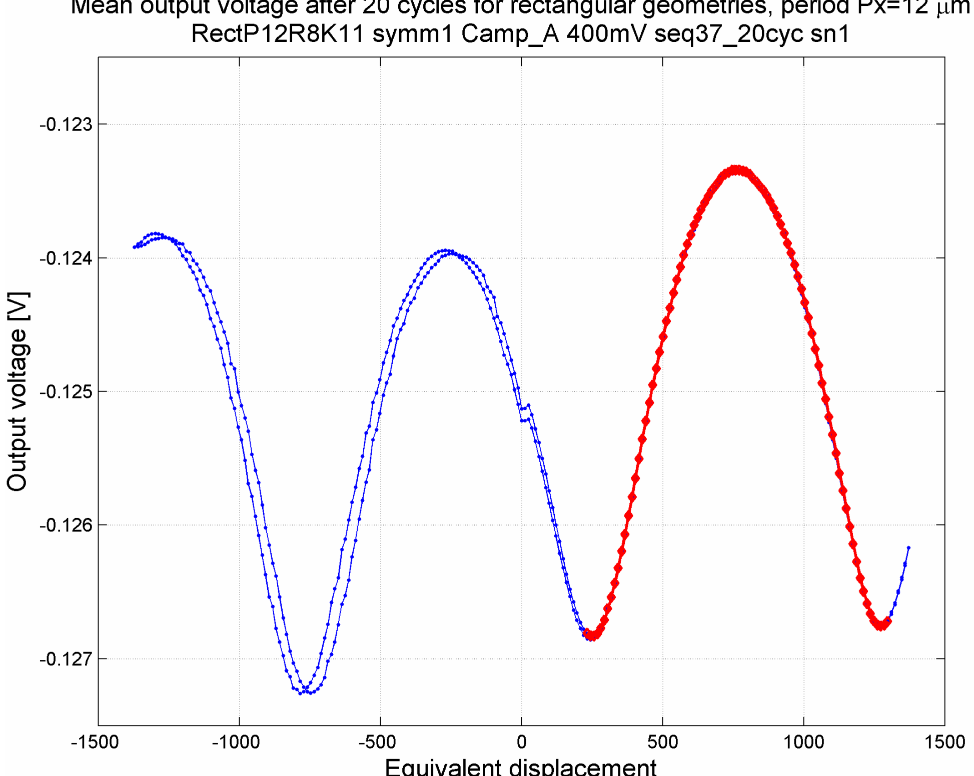

Fig.A3 - 9 : Uout for the RectP12 geometry

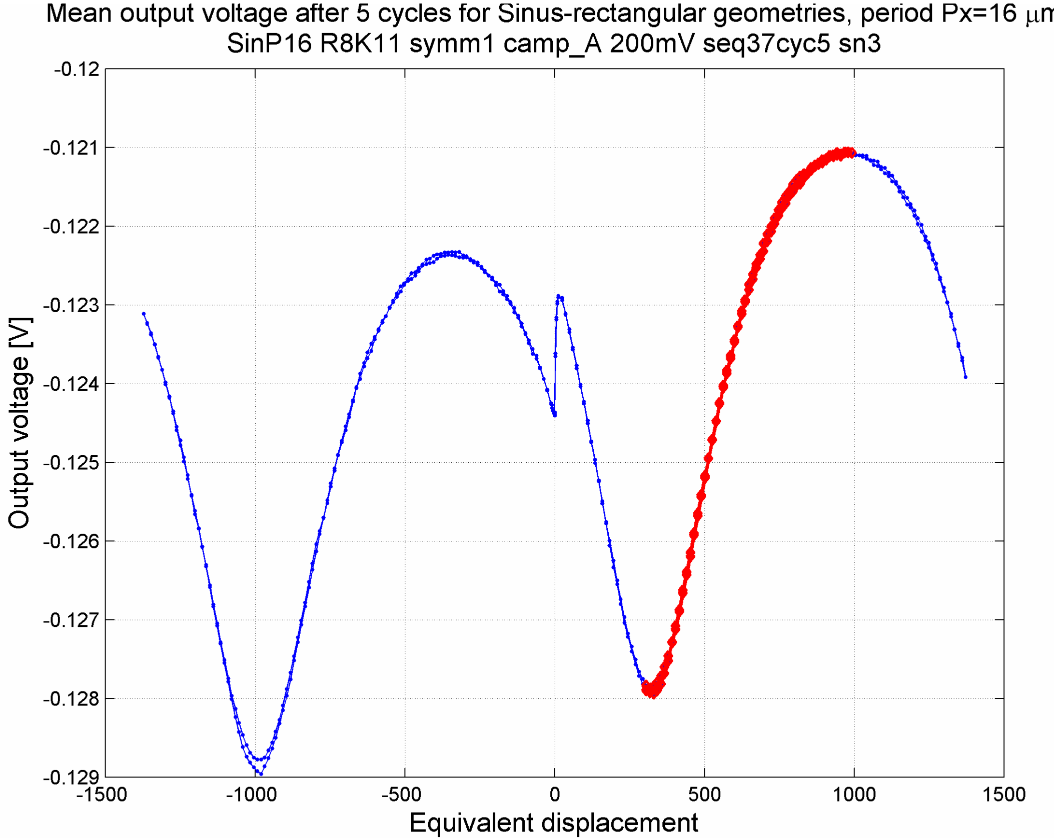

Fig.A3 - 10 : Uout for the SinP16 geometry

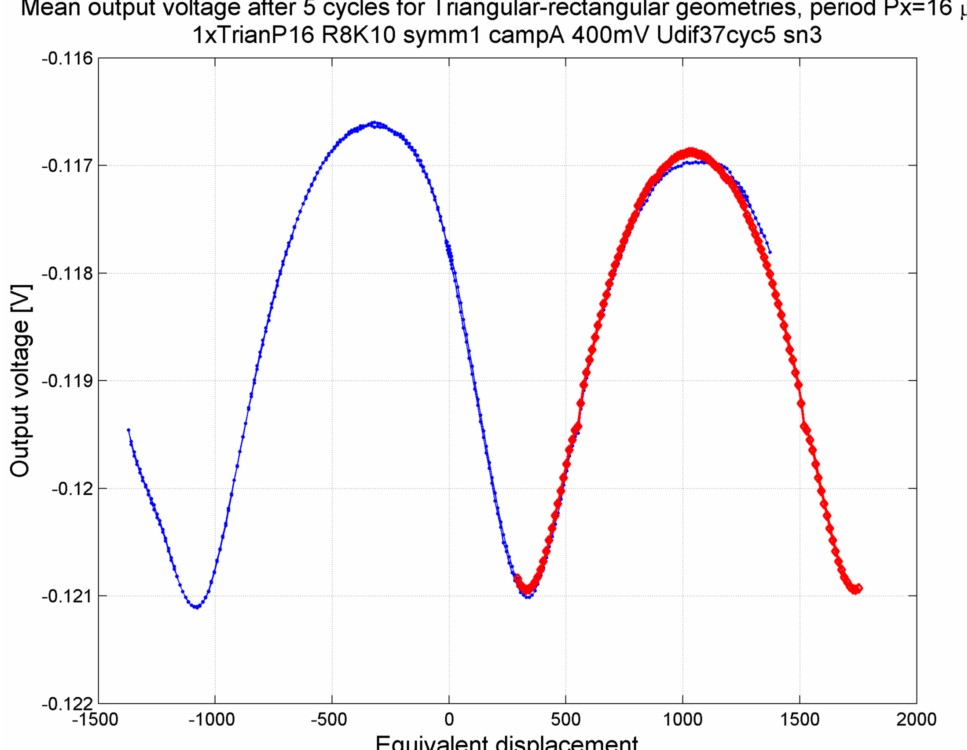

Fig.A3 - 11 : Uout for the Triangular-Rectangular P16 geometry

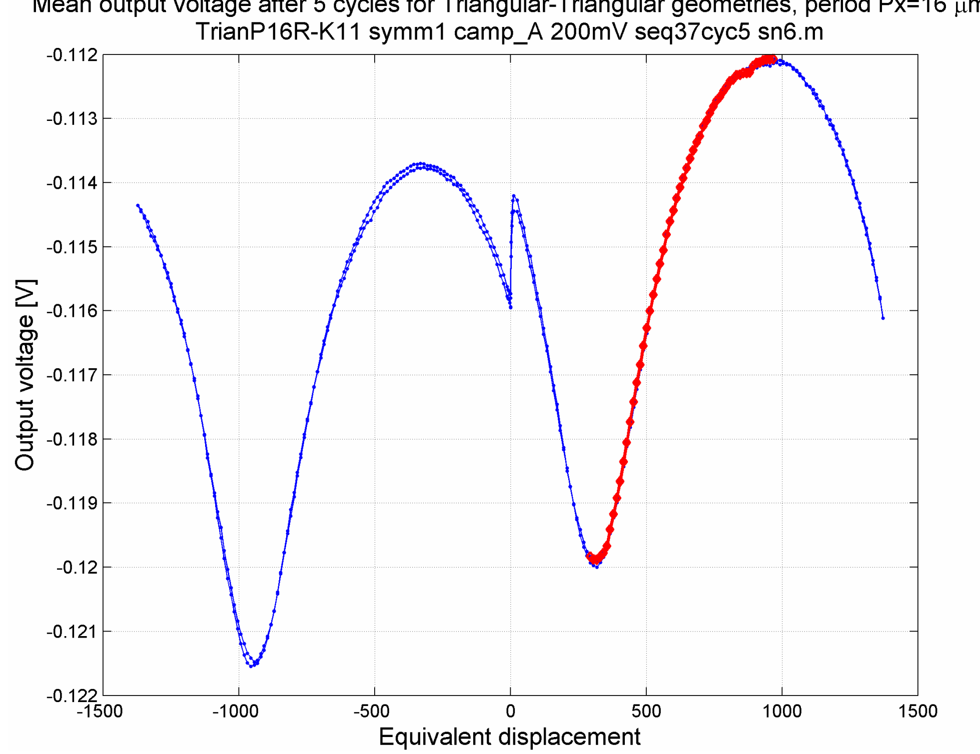

Fig.A3 - 12 : Uout for the Triangular-Triangular P16 geometry

3.4 Additional results comparison simulations and measurements

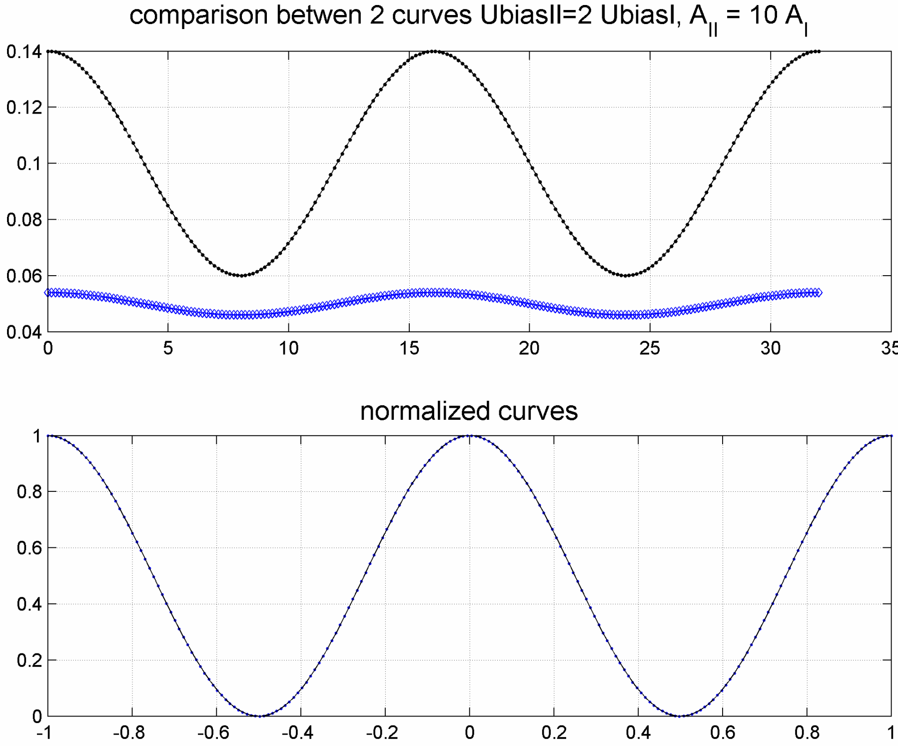

Fig.A3 - 13 : Two signals give the same normalized curve although signal II is favorable due to a 10x larger amplitude. But by normalization only the shape of the function is compared and any sinusoidal has the shape of a sine whatever its amplitude.

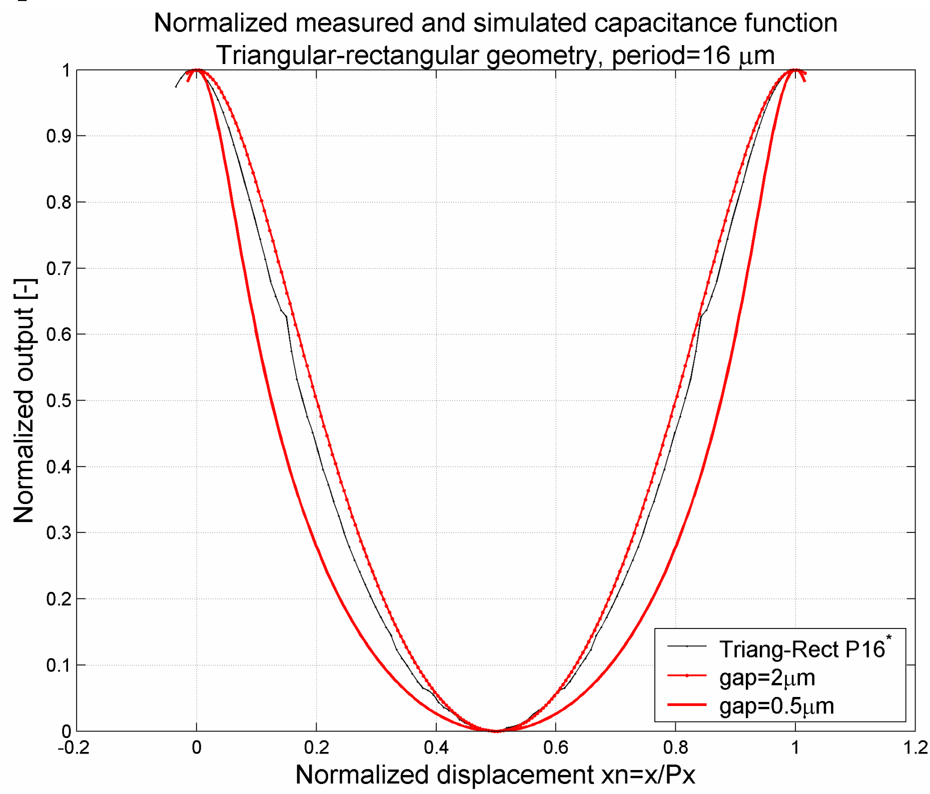

Fig.A3 - 14: Comparison between measurement and simulation

3.5 Additional results for CCMM

A typical result is given in Fig.A3 - 15 for two setpoint values as reported earlier in [10]. Setpoint 2 (SP2= -0.554V, corresponds with a larger sensor capacitance value than setpoint 1 (SP1= -0.553V) and results in a larger amplitude of the control voltage. However, the pid-control voltage has been limited to 28V in Fig.A3 - 15 because of possible side-pull-in of the sense-actuators for higher voltages.

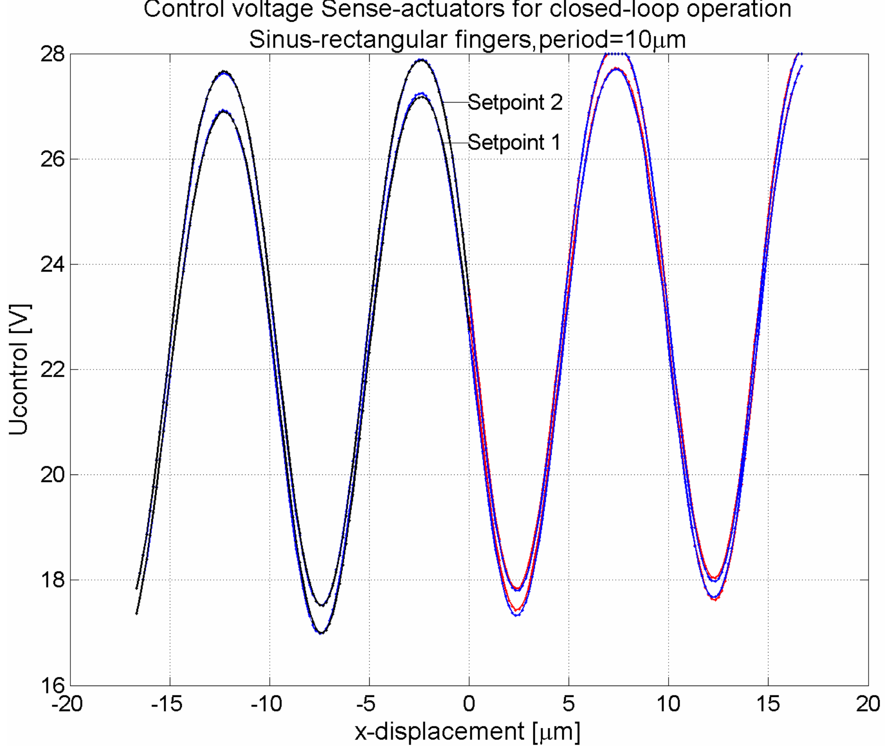

Fig.A3 - 15 : The measured control voltage for the sense-actuators in closed-loop operation for two different setpoints. The sensor-capacitance value for setpoint 2 is larger than for setpoint 1.

The average differential change dV/dx in control voltage $U_{control} \approx 2V\ \mu m^{-1}$ and $|dV/dx|_{max} = 3.8V\ \mu m^{-1}$ around x=0. With the same procedure as for open-loop the mean difference between up- and down sweep (1 cycle) is $|\Delta U_c|_{mean}$ (1) ≈78.5 mV, $|\Delta U_c|_{mean}$ (2) ≈37 mV and corresponds to estimated displacement uncertainties $\Delta e_x(1)$ = 40nm and $\Delta e_x(2)$ = 18nm.
However, part of the increase in U_c may be caused by changes in relative humidity H_r and not solely on the change in setpoint value of δU_{set} = 1 mV.

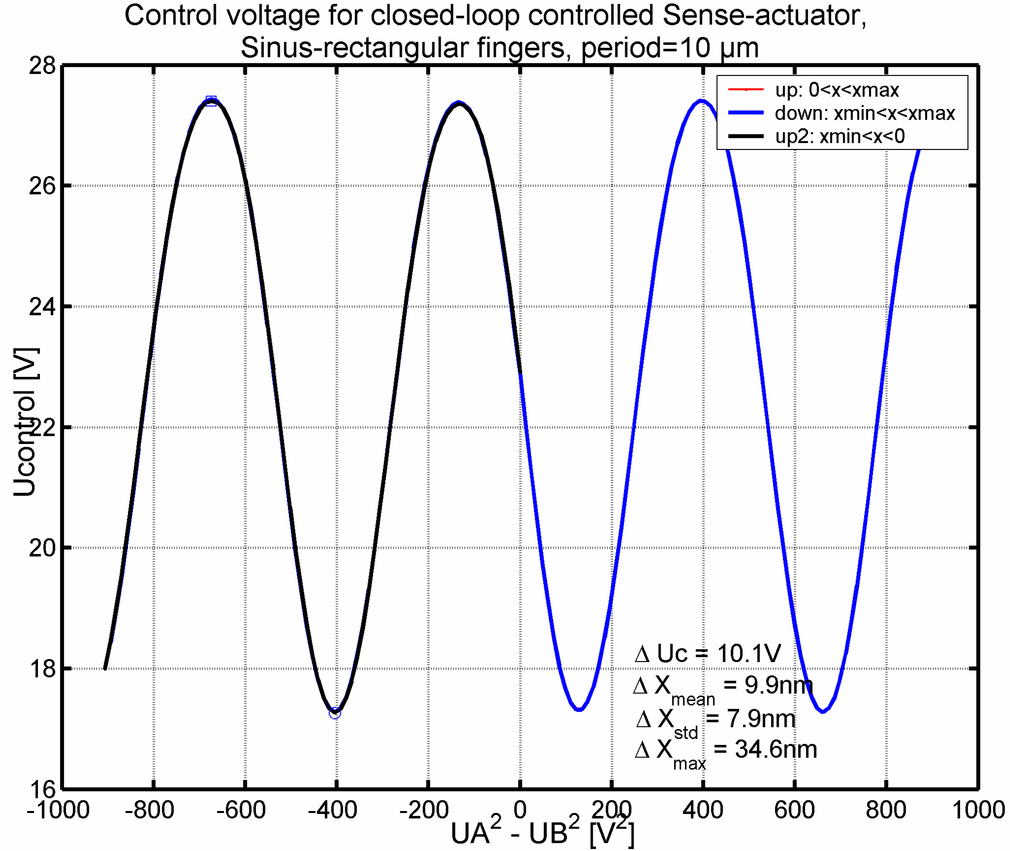

Fig.A3 - 16: Another CCMM result showing the control voltage U_c

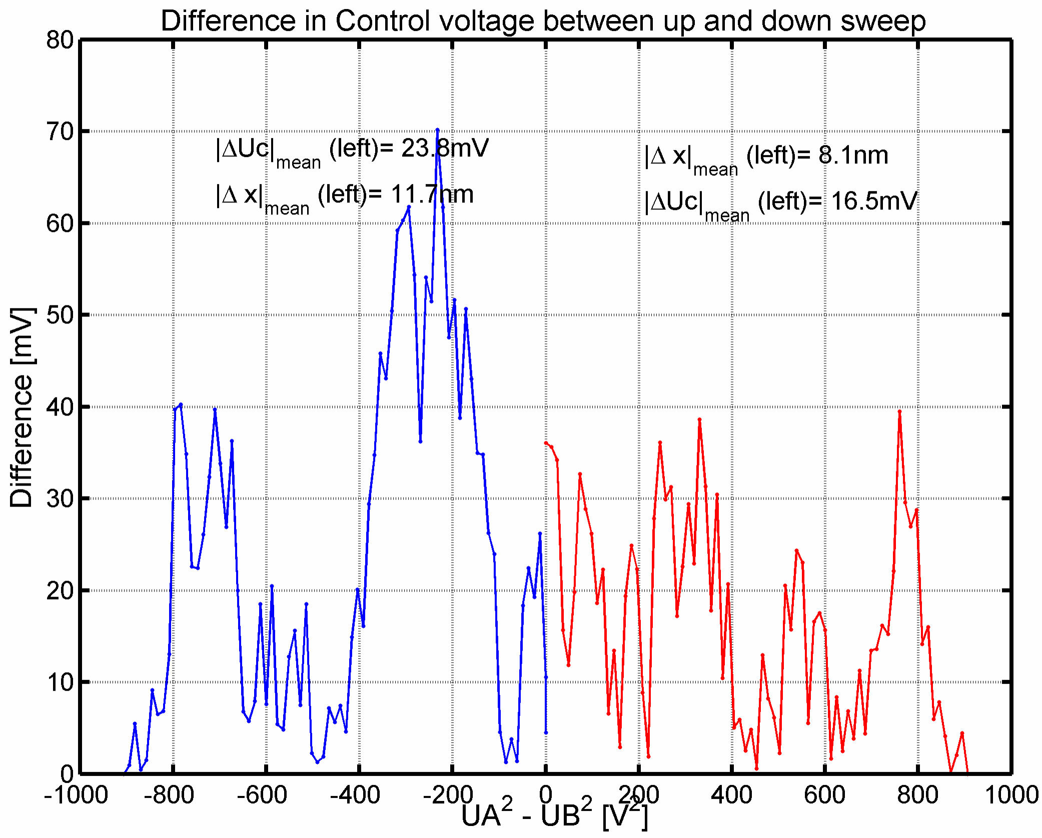

Fig.A3 - 17: Difference in U_c between up – and down sweep.

3.6 Frequency response pull-pull actuation electronics

However, in Fig.A3 - 18 is depicted, the measured gain-phase response for the pull-pull electronics. Also here the oscillation voltage V_{osc} = 0.5V is added to a bias voltage Ubias = 12 V. In Fig.A3 - 19 the difference in gain and phase between the two outputs is given. From these gain-phase measurements it is clear that the difference in gain and phase is minimal and it is unlikely that this could solely cause the 2-ω component with the dynamic response as present in the results of Fig. 47.

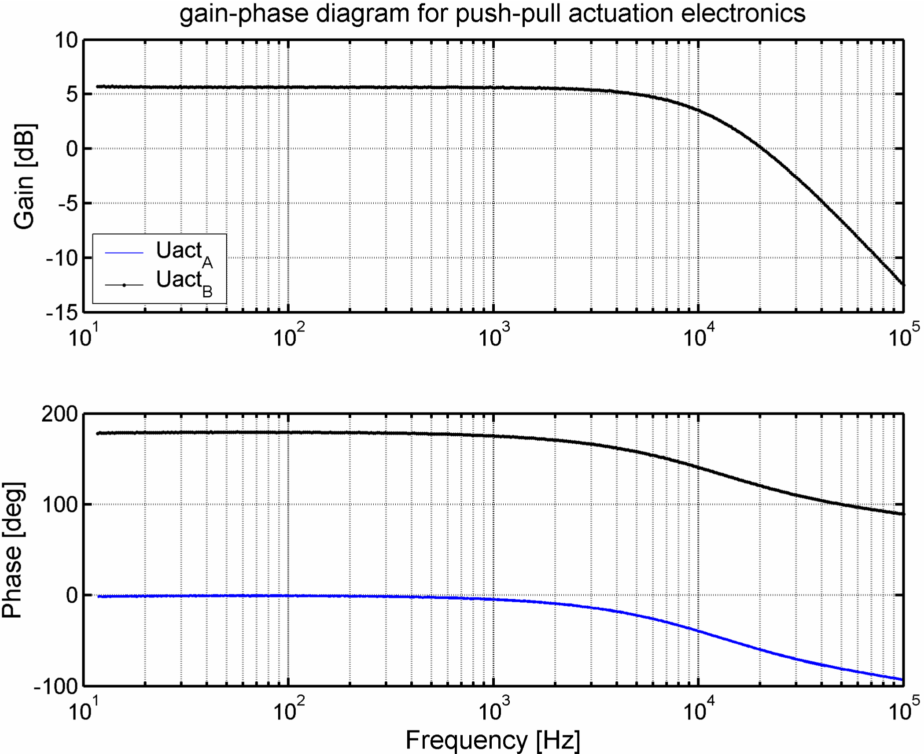

Fig.A3 - 18 : The gain-phase diagram for the pull-pull actuation electronics with two actuation voltages Uact_A and Uact_B.

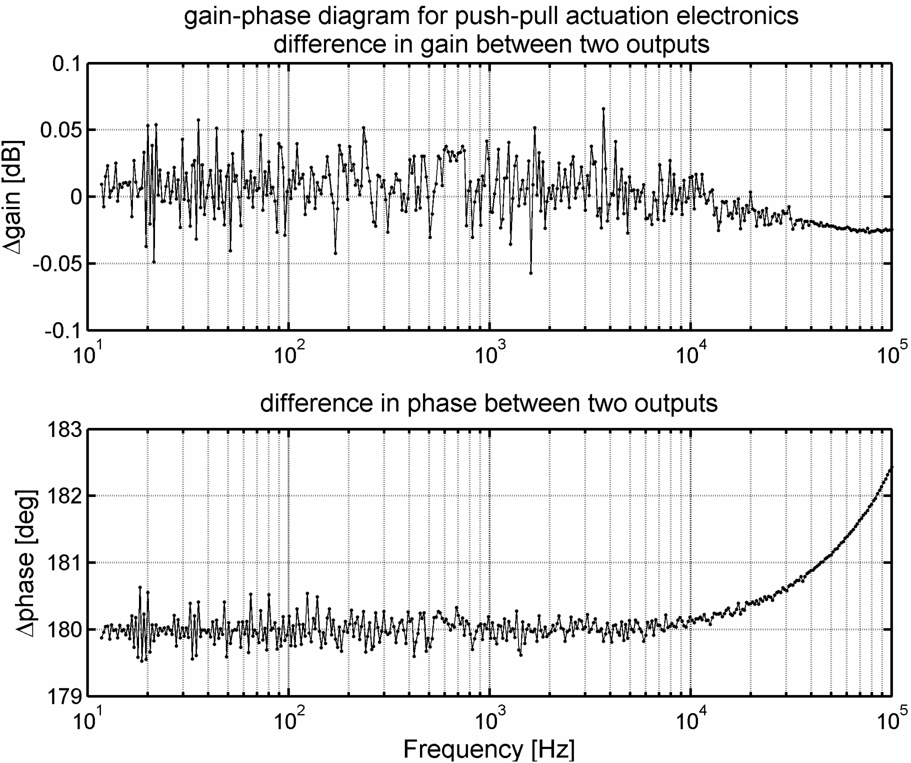

Fig.A3 - 19 : The difference for the two actuation voltages in gain and phase.

Summary

This thesis is about a "Micromachined capacitive long-range displacement sensor for nano-positioning of microactuator systems".

Possible applications of such microsystems are found in future probe-based datastorage, scanning probe microscopy, microbiology, optical lens manipulation, microgrippers and microrobots, etc. These applications require positioning with nanometer precision over a long range (ten's of micrometers) and benefit from further miniaturization and the application of sub-mm sized Micro Electro Mechanical Systems (MEMS). In many cases open-loop operation is not sufficient and a form of system control is required to combine nanometer accuracy with a large dynamic range and to obtain better system performance. In order to make such systems both economically viable as well as compact, on-chip position sensing appears to be a requirement. The aim is therefore, to obtain optimal performance through an integration of sensor and actuator with micromachining fabrication technology without additional micro assembly.

The target specifications for the microsensor were to obtain 1-10 nm accuracy in a range of X_{max} ~ 100 µm or more i.e. dynamic measurement range of ~ 10^5 or more.

An incremental measurement principle is investigated because in contrast with a non-incremental principle, it decouples resolution and range and thus reduces the demands for dynamic range. With two periodic sensor output signals with period P, a quadrature detection principle can be employed. Counting the number of $P/4$-sized increments in position, in combination with an analog interpolation technique (e.g. arctan calculation) gives a high precision position measurement.

Using repetitive patterns with periods down to e.g. P = 8 micrometer and application of quadrature detection, can reduce the dynamic range requirement of 10^5 by a factor of $4 \cdot X_{max} / P$ = 50x. For a velocity of v = 50 mm/s, a bandwidth of at least v / P = 6.25 KHz would be required for each periodic sensor.

Various sensing principles were considered to be applicable as an incremental displacement sensor. A capacitive sensing principle has been chosen because it can have good performance in terms of accuracy, range, bandwidth and has a wide range of electronic interfacing possibilities. Moreover, it offers relative easy integration through micromachining technology of a capacitive sensor and an electrostatic microactuator system. The problematic aspect of this principle may be the influence of the ever present electrostatic forces and the parasitic capacitance.

This thesis presents two related concepts for an incremental capacitive position sensor. Both concepts are based on the change in capacitance ΔC_s between two periodic geometries S1 and S2 for a relative displacement between the two. One geometry is on a slider-structure movable in x-direction, the other is on sense-structures at both sides of the slider, which are movable in y-direction. In Incremental Capacitive Measurement Mode (ICMM) the position of the slider in x-direction is determined by measuring the periodic change in capacitance $\Delta C_s(x)$ between slider geometry and sense-structure. The gap between slider and sense-structure can be reduced by additional sense-actuators to

increase the signal-to-noise ratio (SNR).

In Constant Capacitance Measurement Mode (CCMM) the sense-actuators are closed-loop controlled in order to keep the capacitance C_s constant, equal to a setpoint value C_{setp}. (i.e. $C_s(x)=C_{setp}$). As a result the sense-structures with a finger-like geometry will move in y-direction, closely following the (sine) pattern on the slider. The required control voltage $U_c(x)$ becomes a sine-signal and a measure for the slider displacement. For typical conditions theoretical analysis predicts an increase in SNR of 320x relative to ICMM.

For experimental assessment various devices with various periodic geometries were designed for a surface micromachining process. The design integrates electrostatic actuators with a capacitive position sensor in a 5 µm-high poly-silicon structural layer, using one mask. The capacitance between the two geometries on sense-structures and slider is converted to a voltage and measured using a charge amplifier and a synchronous detection technique. All experiments were done without compensation for changes in humidity or temperature (e.g. through a reference capacitance).

Quasi-static experiments in ICMM mode show reasonable good agreement with 2D-Finite Element simulations with capacitance variations in the order of $\Delta C/\Delta x$ ~ 1-2 fF μm^{-1}. It is further demonstrated for a sine – rectangular finger geometry with 10 µm period, that a gap-reduction gives an increase in maximum voltage variation to $|\Delta U|_{max}$ ~ 12 mV per 5 µm displacement and a reduction in estimated position uncertainty to ~$|\Delta x|_{max}$ = 24 nm over a total displacement range of ~ 32 µm. This includes a systematic position uncertainty of $|\Delta x|_{mean_hyst}$ = 12 nm due to hysteresis.

For CCMM an estimated position uncertainty below 10 nm is demonstrated, although far from real-time operation. However, a position uncertainty of 1 nm or less appears feasible. CCMM can improve the non-linearity due to higher order spatial harmonics resulting ideally in a pure sine-shaped voltage $U_c(x)$.

Dynamic experiments for ICMM demonstrate that operation at frequencies above the resonance frequency of the test-device f_r = 1.7 KHz is possible with an estimated resolution of about 2 nm and an equivalent bandwidth of 1 Hz.

New experiments are anticipated in the near future with devices made with a novel bulk micromachining process called TWIN. These devices have an increase in structure height by a factor of 5 - 20x. This is expected to give an increase in SNR in the order of 25 - 200. With some further improvements in electronics and experimental setup, actual positioning with nanometer precision over a long range will be attainable. Characterization using e.g. image analysis techniques will be carried out to fully demonstrate nano-position capabilities.

Samenvatting

Dit proefschrift gaat over een “Micromachined capacitive long-range displacement sensor for nano-positioning of microactuator systems”.

Mogelijke applicaties van zulke microsystemen worden gevonden in toekomstige probe- of tipgebaseerde data-opslag systemen, scannende probe microscopie, microbiologie, optische lens-manipulatie, micro-grijpers en microrobots, etc. Deze applicaties vereisen positionering met nanometer precisie over een groot bereik (decades van micrometers) en profiteren van verdere miniaturisatie en de toepassing van Micro Electro Mechanische Systemen (MEMS) met sub-mm afmetingen. In veel gevallen is open-lus bedrijf niet toereikend en een vorm van systeemregeling of terugkoppeling is nodig om nanometer nauwkeurigheid te combineren met een groot dynamisch bereik en om betere systeem prestaties te verkrijgen. Op-de-chip positie detectie lijkt een vereiste, teneinde dit soort systemen zowel compact als economisch uitvoerbaar te maken. Het doel daarom is, een optimale prestatie niveau te verkrijgen door integratie van sensor en actuator door *micromachining* fabricage technologie zonder aanvullende micro assemblage of fijnmechanische bewerkingen.

De gewenste specificaties voor de microsensor waren: het behalen van een 1 – 10 nm nauwkeurigheid in een bereik van X_{max} ~ 100 µm of meer, d.w.z een dynamisch meetbereik van 10^5 of meer.

Een incrementeel meetprincipe is onderzocht, omdat in tegenstelling tot een niet-incrementeel principe, de resolutie en het bereik worden ontkoppeld en daarmee de eisen aan dynamisch bereik worden gereduceerd. Met twee periodieke sensor-uitgangssignalen met periode P kan een kwadratuur detectie principe worden ingezet. Het tellen van incrementele positieveranderingen ter grootte van $P/4$, in combinatie met een analoge interpolatie techniek (b.v. door een arctan berekening) geeft een positiemeting met hoge-precisie.

Het gebruik van periodieke patronen met periodes tot b.v. $P = 8$ µm en toepassing van kwadratuur detectie kan de eisen aan het dynamische bereik van 10^5 verkleinen met een factor $4 \cdot X_{max} / P = 50$x. Voor een snelheid van $v = 50$ mm/s zou een bandbreedte van minstens $v / P = 6.25$ KHz nodig zijn voor elk van de periodieke sensoren.

Verschillende fysische meetprincipes zijn beschouwd op toepasbaarheid als incrementele verplaatsingssensor. Een capacitief detectie principe is gekozen omdat het een goed prestatieniveau kan hebben wat betreft nauwkeurigheid, bereik en bandbreedte en vele mogelijkheden voor elektronische connectie en manipulatie. Verder biedt dit principe relatief eenvoudige integratie van een capacitieve sensor en een elektrostatische *microactuator* door *micromachining* technologie. Een problematisch aspect van dit principe kan de invloed zijn van de altijd aanwezige elektrostatische krachten en parasitaire capaciteiten.

Dit proefschrift presenteert twee gerelateerde concepten voor een incrementele capacitieve positie sensor. Beide concepten zijn gebaseerd op de verandering in capaciteit ΔC_s tussen twee periodieke geometriën S1 en S2 voor een relatieve onderlinge verplaatsing. Eén geometrie is deel van een *slider*-structuur, bewegende in x-richting. De

andere is deel van *sense*-structuren aan weerszijden van de *slider* en beweegbaar in y-richting. In Incrementele Capacitieve Meet Modus (ICMM) wordt de positie van de *slider* bepaald, door de periodieke capaciteitsverandering $\Delta C_s(x)$ tussen *slider*-geometrie en *sense*-structuur te meten. De spleet of *gap* tussen *slider* en *sense*-structuren kan worden verkleind door additionele *sense*-actuators om daarmee de signaal-ruis ratio (SNR) te vergroten.

In Constante Capaciteit Meet Modus (CCMM) worden de *sense*-actuators in een terugkoppelings-lus geregeld, teneinde de capaciteit C_s constant en gelijk te houden aan een instel-waarde of *setpoint* C_{setp}. (d.w.z. $C_s(x)=C_{setp}$). Als gevolg daarvan zullen de *sense*-structuren met een op vingers lijkende geometrie in y-richting bewegen en het sinus-patroon op de *slider* met (zeer) kleine afstand volgen. De benodigde regelspanning $U_c(x)$ wordt sinusvormig en een maat voor de *slider*-verplaatsing. Voor typische condities voorspelt een theoretische analyse een verhoging in SNR van 320x in vergelijking met ICMM.

Voor experimentele evaluatie zijn verschillende microsystemen met verschillende periodieke geometriën ontworpen. Het ontwerp integreert elektrostatische actuators met een capacitieve positie sensor in een 5 μm dikke poly-silicium structuur laag met gebruik van één masker. De capaciteit tussen de *sense*-structuren en de *slider* wordt geconverteerd naar een spanning en gemeten door een trans-impedantie of ladingsversterker en een synchroon-detectie techniek. Alle experimenten zijn gedaan zonder compensatie voor veranderingen in relatieve luchtvochtigheid of temperatuur (bv. door middel van een referentie-capaciteit).

Quasi-statische experimenten in ICMM bedrijf laten redelijk goede overeenkomst zien met 2D-eindige elementen simulaties met capaciteitsvariaties ter grootte van $\Delta C/\Delta x \sim$ 1-2 fF μm^{-1}. Verder wordt gedemonstreerd voor een sinus-rechthoekige vinger geometrie met 10 μm periode, dat een *gap*-verkleining een toename geeft van de maximale spanningsvariatie $|\Delta U|_{max} \sim$ 12 mV per 5 μm verplaatsing en een reductie in geschatte positie onzekerheid tot $\sim|\Delta x|_{max}$ = 24 nm over een totaal verplaatsings-bereik van ~32 μm. Dit omvat een systematische onzekerheid van $|\Delta x|_{mean_hyst}$ = 12 nm door hysterese.

Voor CCMM bedrijf wordt een geschatte positie-onzekerheid van minder dan 10 nm gedemonstreerd, hoewel verre van *real-time*. Echter, een positie-onzekerheid van 1 nm of kleiner lijkt haalbaar. CCMM kan de niet-lineariteit door hogere-orde spatiele harmonischen verbeteren, wat idealiter resulteert in een puur sinusvormige spanning $U_c(x)$.

Dynamische experimenten voor ICMM demonstreren dat het mogelijk is om de huidige implementatie te bedrijven op frequenties hoger dan de resonantie-frequentie van het test-microsysteem van f_r = 1.7 KHz met een geschatte resolutie van circa 2 nm bij een equivalente bandbreedte van 1 Hz.

Nieuwe experimenten worden verwacht in de nabije toekomst met microsystemen die gemaakt zijn met een nieuw *bulk-micromachining* proces, genaamd TWIN. Deze microsystemen hebben een toename in structuur-hoogte met een factor 5 tot 20x. De verwachting is dat dit een toename in SNR geeft in de orde van 25 – 200 x. Met enkele verdere aanpassingen in elektronica en experimentele opstelling zal feitelijke nano-positionering met nanometer-precisie over een groot bereik haalbaar zijn. Karakterisatie door middel van b.v. beeld analyse technieken zal worden uitgevoerd om daarmee nano-positionering volledig te demonstreren.

Dankwoord

Ik wil beginnen met iedereen te bedanken die een positieve bijdrage heeft geleverd aan de totstandkoming van dit proefschrift en de resultaten van mijn onderzoek. Ik ga nu een poging doen om een aantal mensen in het bijzonder te noemen. Allereerst mijn promotor Miko Elwenspoek. Ik hoop dat je tevreden bent over de besteding van jouw Simon Stevin prijs, het voelde als een eer. Ik bewonder je manier van leiding geven. De cultuur van vrijheid is heel bijzonder en kent een zekere mate van chaos beheerst door 'organizers' maar bevordert daardoor creativiteit, flexibiliteit en zelfdiscipline. En ik bewonder je lesgeven en denk met veel plezier terug aan de trimesters (2-3) waarin ik je mocht assisteren voor het vak Elektromagnetische veldtheorie. Ik zou eigenlijk willen vragen, wanneer mag ik weer? Je korte lezingen over ruis, gravitatie en relativiteitstheorie waren zeer boeiend en ik hoop 't vervolg graag mee te maken. Als laatste wil ik je bedanken voor de persoonlijke steun en het vertrouwen die je gegeven hebt tijdens de meest moeilijke periode eerder dit jaar.

Gijs ben ik zeer dankbaar voor de stimulerende, kritische begeleiding, steun en geregeld gezellige bijeenkomsten. Als bij-produkt van deze bijeenkomsten kwamen we er na 2 jaar achter dat we onze interesse in muziek van 'Van der Graaf generator' en 'Peter Hammill' deelden. De analyse in hoofdstuk 3 heb ik direct aan jou te danken en dit heeft als een leidraad voor dit proefschrift gewerkt. Dankzij jou hebben we extra middelen en tijd van de STW gehonoreerd gekregen en ik wil me de komende tijd na mijn promotie sterk inzetten om tot nieuwe resultaten en artikelen te komen.

Remco W. wil ik graag bedanken voor de 'maak je niet (te) druk' adviezen en voor de hulp en inzet (ssst) bij de electronica ontwikkeling. Zo ook Theo, enorm ideeën kanon, bedankt voor de steun, je kennis, de geregeld fysisch filosofische beschouwingen en het oeverloos 'gezwam', weejewel. En dan was daar op jouw kamer ineens het moment van serendipiteit waarin het idee voor constante capaciteit naar voren kwam.

Erwin en Meint moet ik ook bijzonder bedanken voor hun adviezen en hulp, zowel in de clean room als daarbuiten en 'voor de weg er naar toe' als de finish steeds nabij lijkt. Meint is dus het voorbeeld van operator afhankelijke ambachtelijke vriesdroog resultaten. De devices, of eigenlijk bleek 1 device (met SinP10 geometrie) voldoende, waarmee de metingen zoals opgenomen in dit proefschrift zijn gedaan, heb ik aan jou te danken. Helaas bleek het niet eerder dan in het begin van m'n vierde jaar mogelijk te zijn, maar het is dan toch gelukt.

Om even bij de clean room te blijven, wil ik gelijk alle medewerkers bedanken in 't bijzonder Peter, Huib, Gerard, Eddy, Hans, Marion, Samantha, Dominique,

Niels en Henrie bedankt voor de adviezen en sfeer (sneeuwballen gevecht), en ik kijk uit naar het uitwisselen van muziek, waar ik nu eindelijk tijd voor kan nemen.

Ik wil Remco S. (oftewel Pino) zeer bedanken als vriend, collega, stemmingsmaker, katalysator en natuurlijk in het bijzonder voor het aanvaarden van het paranimfschap. Ooit zul jij vast ook 'mijn' films waarderen.

Vervolgens wil ik Henk vW en Dick bedanken voor hun ondersteuning wbt PC's, buro's, mic's etc. Ook de secretaresses Judith, Ingrid en Marieke wil ik bedanken voor hun persoonlijke steun, en het helpen bij administratieve zaken.

Mijn collega's nieuw en oud bedankt voor de bijzondere, vrije, gezellige groepssfeer. Dennis, Doekle, Boudewijn (Bob), Dannis, Jeroen, Roald (succes! Zal geregeld terugdenken aan deze gezamenlijke ploetertijd), Joost (bedankt voor Guimaraes en je hulp), John (fietsen?), Marcel, Phillip, Hans-Elias, Duy, Laura (Lola), Winfried, Edwin O., Willem T., Regina, Petra, Stefan, Henk W., Jasper, Theo V., Han. Ook Mink bijzonder hartelijk bedankt. Zal geregeld aan de MEMS conferentie in Maastricht en dat maffe rouge hotel terugdenken.

I'ld like to thank my foreign colleagues; Saravanan thanks for the stories about India, humans and humanity, the help with SEM and the mensa dinners, Srinivas and Imran thanks for your help and support, discussions and the delicious Indian and Pakistan dinner, Luis thanks for the laughs, drinks and small talk, Hien and Hanh, I admire your friendliness and devotion, Sartya thanks for the pleasant (lunch) conversations, Maryanna and Antonella thanks for the support and interest (party?), Deladi (thanks for your support, fun, tennis, safari), Vitaly thanks for the conversations about Sologub, Tarkovski, art, physics, life, women etc.
Zacharia thank you very much for the nice time during your stay with our group and later at the Eurosensors conference in Guimaraes. Thanks for your kind email last summer.
Verder wil ik Edin en Aïda zeer bedanken voor hun steun en vriendschap, Portugal, Maastricht, en de afgelopen moeilijke periode. Wietze bedankt, ik hoop dat er nu eindelijk tijd komt voor muziek maken. Zo ook Marcoen, tijd voor films en de ideale muziek-CD, 'there is always music in the air'.
Timco en Yvonne wil ik ook bijzonder bedanken voor de vriendschap,steun door dik en dun, kattenoppas, spelletjesavonden etc. En Timco, ook jij bedankt voor het aanvaarden van het paranimfschap.
Fam. Versteegh bedankt, Jacob bedankt, ik hoop dat je gelijk hebt, Martijn en Maaike bedankt, tijd voor beta proefjes en muziek?
Ook B enorm bedankt voor de meest boeiende intellectuele ervaringen, erftennis, weekend ping-pong, tovermuziek, de witte waan, etc.
En dan ben ik aangekomen bij het punt waar ik nooit had kunnen komen zonder mijn directe familie, bovenal mijn ouders, Karel en Christina en co, Taco en Marjan en co, Boukje en Rutger en Sofietje, zij lieten me telkens stukjes blauwe lucht zien zodat ik volhield.

If we have gained, how do we now meet the cost?
What have we bargained, and what have we lost?
What have we relinquished, never knowing it was there?
(P.Hammill)

Toon Kuijpers,
Haerst, 7-11-04,
(Miles from Nowhere)

Biografie

Toon Kuijpers werd geboren in Zwolle op 27 September 1970 maar groeide op in Haerst. Hij doorliep op de Thorbecke Scholengemeenschap te Zwolle, Mavo, Havo en ging vervolgens naar de MTS en HTO Windesheim. In sept. 1996 begon hij met de verkorte universitaire opleiding Electrotechniek aan de Universiteit van Twente. Deze studie rondde hij af in maart 2000, met een afstudeeropdracht bij de leerstoel 'Regeltechniek', naar Limit-cycle gedrag in een simulatie systeem voor een ruimte robot-arm. Hierna startte hij gelijk met het promotieonderzoek "Microactuators for Nano-position control" bij de vakgroep TST onder leiding van professor Miko Elwenspoek.

Toon heeft interesse in vele zaken Natuurwetenschappen, Filosofie, Psychologie, politiek, Literatuur, Film, kunst en in sterke mate: muziek. Hij speelt gitaar en drums, uiteenlopende muziek. In de overige vrije tijd zijn er nog enkele sportieve momenten die zeker wel fanatiek kunnen zijn, maar niet zijn gericht op de ultieme prestatie (ten koste van een ander) maar op de 'roes'. Hij denkt daarbij aan erf-tennis in storm, ping-pong bij stallicht, hard fietsen in veel grondwind,